Modeling of Heat Generation in Cryogenic Turbopump Bearing

Hiromitsu Kakudo

2023

Acknowledgement

I would like to express my sincere gratitude to Professor Tomoko Hirayama for giving me opportunities to work on this research project at Kyoto University and helpful guidance throughout this project.

I am also deeply grateful to Dr. Satoshi Takada at Japan Aerospace Exploration Agency for encouraging me to commit innovative research works and giving me a lot of great advice for everything at any time.

I received technical support for conducting all difficult experiments from Mr. Masataka Kikuchi, Mr. Tomoyuki Takano, and Mr. Takashi Yokoyama at Kakuda Space Center.

I would like to thank Dr. Koji Matsumoto and Mr. Yohsuke Hagiwara for supporting me in conducting chemical analysis at Chofu Aerospace Center.

I also thank Dr. Tomoya Nakamura at Honda R&D Co., Ltd. for giving me kind advice and discussing bearing research with me.

Finally, I would like to thank my family for their support.

Table of contents

Lists of figures

Lists of tables

Chapter 1. Introduction

1.1. Liquid rocket propulsion

A liquid rocket is one of the most advanced space transportation systems and essential technologies for modern society. Rocket systems composed of liquid rocket technologies have provided access to space for numerous satellites which help information-based society by their communication capabilities, various spacecrafts aiming to explore deep-space beyond the Moon, and human explorations. History of liquid rocket technologies has started since V-2 development leaded by Von Braun. Since then, Unites States and Russia have leaded rocket development through manned exploration activities to the Moon, the construction of the International Space Station, transportations of commercial satellites to the low Earth orbit, and so on. Representative launch vehicles of these histories are Saturn V, Soyuz, and Space Shuttle shown in Fig. 1. They were mainly powered by liquid rocket propulsion systems to meet the demand of their much efficient propulsion capabilities.

Liquid propulsion systems essentially need turbopump systems to pressurize propellant stored in tanks and feed it to the main combustion chamber that generates thrust power [1, 2]. High-thrust liquid rocket engines are designed to improve their thrust-weight ratio (T/W) by increasing the system pressure. Since turbopumps can efficiently increase the engine system pressure, turbopump design capability is one of the most essential technologies. Turbopumps which can perform fluid suction and pressurizing also reduce the pressure of the propellant tank storage, which decreases the tank weight by reducing the wall thickness. Therefore, turbopumps play very important roles not only in improving the T/W of liquid rocket engines but also in increasing the structural efficiency of the entire rocket system.

Fig. 1 Representative launch vehicles (Saturn V, Soyuz, and Space Shuttle) ©NASA.

1.2. Ball bearing for rocket engine turbopump

As examples of rocket turbopumps, schematics of a liquid oxygen (LOX) turbopump and a liquid hydrogen (LH_2) turbopump are shown in Fig. 2 and Fig. 3, respectively. A typical rocket turbopump is composed of many rotational components such as an axial inducer which suction propellant, radial impellers which boost propellant pressure, axial turbines which drive the main shaft and so on. Bearings support the main shaft which connect all the rotational components. There is wide pressure distribution inside a turbopump by the rotating fluid devices, which results in axial and radial load on the shaft. Typically, balance piston systems can balance or reduce the axial load [3]. On the other hand, radial load cannot be balanced by using fluid devices such as the balance piston. Therefore, the bearings are required to support such forces generated by pressure distribution inside the turbopump while rotating. Bearing failures such as bearing seizure can cause the turbopump to shut down and have significant impacts not only on the rocket engine but also on the entire rocket system. Therefore, the turbopump bearing is one of the most important elements in the entire propulsion system.

Since, as explained above, technologies related to the turbopump bearings have been considered as key technologies of rocket engines, each country's space agency has confidentially conducted its own

research and development for a long time. Therefore, available information to the public has been limited. European Space Agency (ESA) has developed its own bearing technologies through rocket engine developments such as Vulcain engine and HM7 engine [4]. Dry lubrication film which is composed of a nickel and silver electrolytic layer with molybdenum disulfide powder had been developed to improve LH_2 bearings performance for such engines. National Aeronautics and Space Administration (NASA) has conducted advanced bearing studies for satisfying challenging demand by Space Shuttle Main Engine (SSME) which was the only large reusable, liquid rocket engine before 2011 [5]. For developing the High Pressure Oxidizer Turbopump (HPOTP), ball material of its bearing was changed from stainless steel to Si_3N_4 to reduce the bearing elements' wear and improve its life [6-8]. In addition, the fluid flow characteristics of the bearing coolant had been researched [9]. This research proposed to apply a jet nozzle to improve the bearing cooling capability and enhance the bearing life. Japan has also developed bearing technologies through development of its flagship launch vehicles and fundamental research. For developing LE-5 rocket engine which was the upper stage engine of H-I launch vehicle, a self-lubricating ball bearing with glass cloth reinforced Polytetrafluoroethylene (PTFE) retainer shown in Fig. 4 was developed [10]. The research clarified that Hydrofluoric acid (HF) chemical etch treatment on the retainer and rf-sputtered PTFE film coating on bearing elements greatly decreased frictional heat generation and significantly lowered wear rate of bearing components. In the development of LE-7 rocket engine that powered the first stage of H-2 launch vehicle, ball bearings for high-thrust liquid rocket engine were developed, and the durability was tested [11-14]. Fundamental research aiming to demonstrate high-speed ball bearing technologies had been conducted [15]. The research resulted in succeeding development of a hybrid ceramic ball bearing which have a capability of rotating under 120,000 rpm and 3 million DN value. In addition, the performance of the ball bearing under several cryogenic environment such as LH_2, LOX, and liquid nitrogen (LN_2) was experimentally investigated in parametrically ways [16].

Since almost all turbopump bearing studies mentioned above were experimental investigations under cryogenic environment which needs special facilities for testing, it has taken numerous time and cost to evaluate bearing performance. Furthermore, it is difficult to measure a variety of bearing data to comprehend bearing motion and situation under cryogenic environment and high-speed rotating operation because of the limitations of measurement technologies. Therefore, it is necessary to model the physical phenomena of rotating bearings for further understanding of the turbopump bearing physics and more advanced bearing design. Additionally, the modeling capability contributes to optimization of turbopump system design which is significantly influenced by bearing performance such as the heat generation and the coolant conditions.

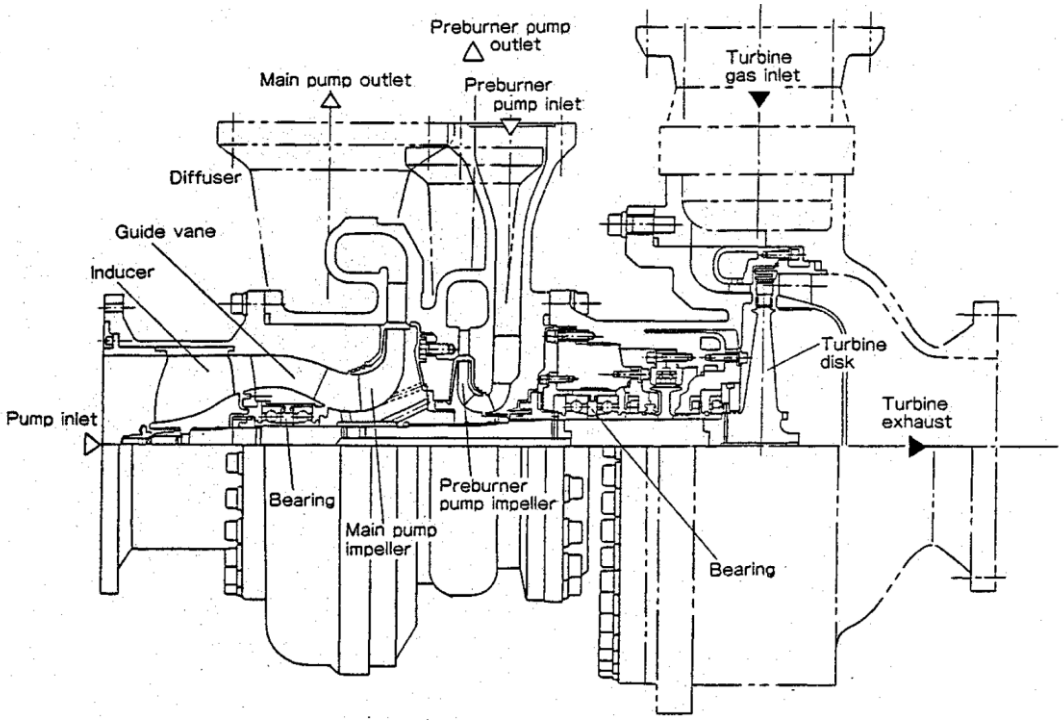

Fig. 2 LE-7 LOX turbopump schematic [17].

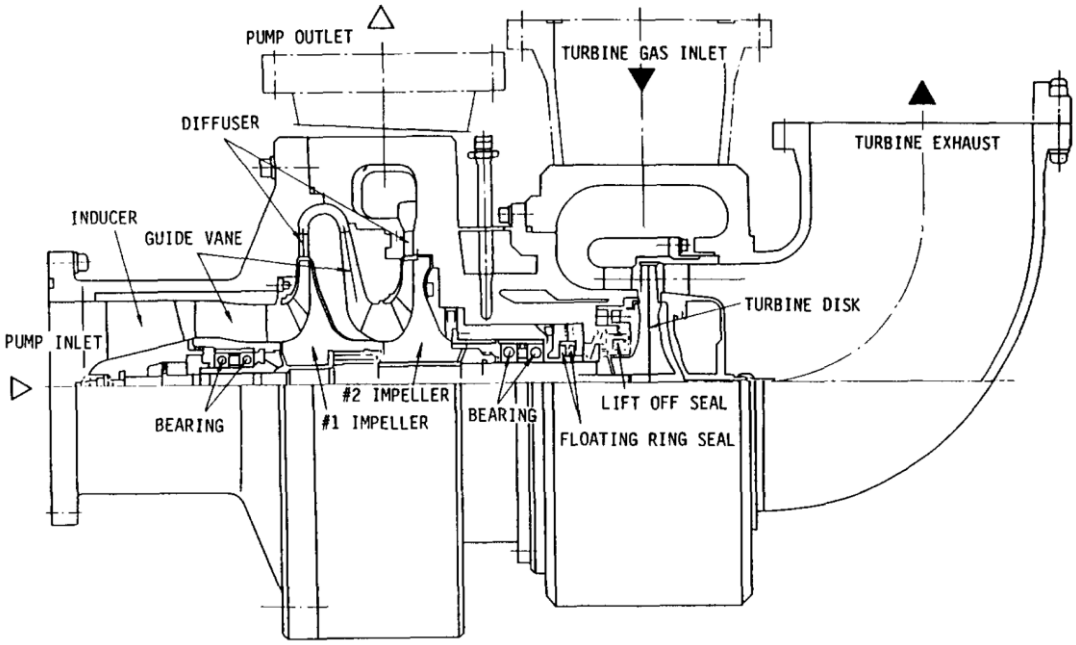

Fig. 3 LE-7 LH_2 turbopump schematic [18].

Fig. 4 Self-lubricating ball bearing with glass cloth reinforced PTFE retainer.

1.3. Research background of modeling for rotating ball bearings

Modeling of rotating ball bearings have been studied for a long time. As the first step of the bearing modeling, it is necessary to comprehend the bearing motion. The bearing motion had been studied analytically using multiple equations by Jones, A. B. [19, 20]. Harris, T. A. also had researched the bearing motion focusing on high-speed ball bearings [21, 22]. These studies used quasi-static models, such as simple kinematic relations, to obtain the ball contact loads and surface velocities. By this approach, it is difficult to understand the dynamic phenomena such as influences of dynamic behavior on contact friction and thermal coupling between bearing components considering heat generation of rotating bearing. Therefore, research on dynamic modeling of bearing motion has also been conducted. The representative research on the dynamic model has been studied by Gupta, P. K. [23-29]. In recent years, as computer calculation speeds have been improved, more specialized dynamic models incorporating much more complex phenomena inside rotating bearings, such as the characteristics of bearing wear, have been developed for each bearing design to improve the fidelity of the modeling [30-33].

Unlike ordinary bearings for general purposes, no faithful modeling of cryogenic ball bearings such as turbopump bearings has been constructed. There are two unique points which are different from ordinary bearings. One is their lubricant. While oil based lubricant is applied to ordinary bearings because of its excellent lubricating performance, oil cannot be used to cryogenic bearings because the environment is extremely cold. Furthermore, since cryogenic fluids such as LOX, LH_2, LCH_4, and LN_2 are not viscous enough, hydrodynamic lubrication is not performed in the bearing contact area [34]. Therefore, a solid material such as polytetrafluoroethylene (PTFE) is used for the lubricant. However, the lubrication mechanism and the friction characteristics under cryogenic environment have not been clarified yet. There have been several studies aiming to clarify tribology characteristics of rotating bearings under turbopump operating environment. Naerheim et al. confirmed the presence

of metal fluoride on the surface of bearings used in SSME HPOTP after hot firing engine tests by performing X-ray Photoelectron Spectroscopy (XPS) analysis [35]. This study concluded that PTFE decomposed and reacted with the bearing steel to form fluorides and that PTFE did not appear to function directly as a lubricant under LOX turbopump environment. Nosaka also conducted surface analysis on bearings used in turbopump operating environment [14, 36, 37]. Though several studies aiming to clarify the lubrication mechanisms of cryogenic ball bearings used in turbopump environment have been conducted by performing surface analysis, a modeling on the friction characteristics has not completed yet.

The other unique point of turbopump bearing is that the bearing cavity is filled with the propellant such as cryogenic fluids. The propellant performs cooling of the bearing by flowing through the bearing cavity. As mentioned above, the bearing coolant flow pattern was researched to improve cooling capability by using jet nozzles for extending the bearing life. However, it is typical to cool bearings by simply supplying coolant through the bearing cavity without cooling devices such as the jet nozzles because the cooling devices can complexify turbopump systems. The fluid flow characteristics of bearing coolant flowing through the cavity is much complex since a bearing consists of several components, such as balls, races, and a retainer, which rotate around different axes at different velocities, respectively. This complex fluid flow generates pressure difference between the upstream and downstream of the bearing, which have influences on turbopump inner flow pattern [38]. Furthermore, the fluid flow also produces heat generation due to drag and churning loss, which is unique physical phenomena of turbopump bearings. To comprehend performance characteristics of turbopump bearings, it is necessary to model this fluid flow characteristics.

As mentioned above, there are difficulties to model turbopump bearings' performance. However, there has been a study of modeling cryogenic turbopump bearings, in which the characteristics of friction and fluid flow were modeled roughly. Gupta has constructed a dynamic modeling of heat

generation in LOX turbopump bearings [39]. In the paper, it was pointed out that there were errors between predicted values and experimental data. Therefore, it is considered that the rough model of friction and fluid flow can cause the errors and the fidelity of the modeling is not enough to simulate the bearing behavior under turbopump operational environment.

1.4. Purpose of this study

This study aims to clarify the friction characteristic of bearing material under cryogenic environment and the fluid flow characteristics of the bearing coolant and to finally construct a high-fidelity modeling of heat generation in turbopump bearings.

This paper is organized as follows. The background of the study is introduced in Chapter 1.

In Chapter 2, a calculation method of bearing motion analysis that is applied to this research is summarized. As the first step of construction of high-fidelity modeling for cryogenic turbopump bearings, quasi-static models of bearing motion studied by Jones, A. B. and Harris, T. A. are adopted in order to predict much accurately constant performance on several operating conditions. Influences of dimension changes due to extremely low temperature, tightly interference fitting and high-speed centrifugal force are considered. In addition, factors of heat generation are introduced and theoretical calculation methods of them are explained.

In Chapter 3, experimental results of bearing testing conducted under turbopump operating environment are discussed. Heat generation data of several turbopump bearings were measured in various conditions of rotational speed, bearing load, bearing coolant and so on. The bearing performance characteristics are evaluated parametrically.

In Chapter 4, the fluid flow characteristics of bearing coolant are studied for improving fidelity of the model. The fluid flow characteristics are studied by using 3D computational fluid dynamics (CFD) analysis because it is difficult to evaluate the complex fluid flow by experimentation. Influences of

bearing operating condition, such as bearing coolant, flow rate and rotational speed, are investigated in terms of bearing performance.

In Chapter 5, the friction characteristics of bearing material under cryogenic environment are investigated experimentally. Friction tests using bearing material were conducted at high contact pressure conditions as well as bearing contact conditions to acquire the friction coefficient. The influence of contact pressure which seems to be the most dominant factor on the friction characteristic is evaluated.

In Chapter 6, a model of heat generation in cryogenic ball bearing is constructed, considering bearing motion and the characteristics of the fluid flow and the friction coefficient. The model is compared with experimental results to evaluate the fidelity. The quality of this model is discussed.

In the last chapter, the results of this study are summarized, and the conclusions are mentioned.

Chapter 2. Bearing motion analysis and heat generation factors

2.1. Introduction

Turbopump bearings are operated on higher speed and larger load conditions with requirement of much more sufficient reliability than ordinary bearings. In addition, they are needed to be stiff enough to minimize the shaft vibration and instabilities, which enable to design the highest efficiency of pumps and turbines with minimum clearances between blades and stators. To enhance the bearing stiffness, the bearing axial preload is set in larger load. This preload condition increases the contact pressure of friction areas. Furthermore, spinning motion would occur in the friction areas on higher-speed conditions since there would be differences in the contact angles of races and balls between outer race and inner race. Centrifugal forces loading on balls increase the contact pressure in the friction areas of the outer race with the rotational speed. The severe friction condition due to the larger load and higher speed would be one of the causes of bearing failures such as insufficient lubrication and lubrication film breakdown. Therefore, it is necessary for bearing designers to accurately predict bearing friction conditions such as relative velocity and contact pressure in the friction areas of races and balls by conducting bearing motion analyses.

The bearing motion analysis was theorized by Jones, A. B. In his studies, the loads and velocities of balls of rotating bearings were formulized considering elastic deformation on the friction areas of angular contact ball bearings [19, 20]. Harris formulized bearing motion of high-speed ball bearings by using multiple equations. The studies have enabled to calculate the displacement of balls in high-speed bearings and evaluate the bearing stiffness [21, 22]. In addition, rapid calculation methods by using digital computers were demonstrated to solve the bearing analyses including multiple equations [40]. Since then, improvement of digital computing speed has made it possible to calculate much more complex bearing calculations. Recently, there have been several studies for evaluation of bearing dynamics, which aim to clarify influences of various conditions on bearing motion in detail.

In this research, calculation codes of the bearing motion analysis for turbopump ball bearings were

implemented, considering not only the characteristics of high-speed ball bearings that have been clarified by previous studies but also several influences of cryogenic environment. In this chapter, the analysis method and several calculation examples are introduced. Furthermore, the heat generation factors due to such bearing motion are discussed.

2.2. Influences of cryogenic environment

2.2.1. Thermal expansion model

The dimensions of cryogenic ball bearings' elements change to much smaller under operational conditions than room temperature environment because they are operated in extremely low temperature environment such as LOX (90.2 K at 1 atm), LCH_4 (112 K at 1 atm), and LH_2 (20.3 K at 1 atm). In addition, the amount of the dimension changes depends on the material characteristics. The performance characteristics and operating conditions of ball bearings are significantly affected by each element's dimension. This is the reason why a ball bearing's dimension is strictly controlled in manufacturing processes. Therefore, the dimension changes by temperature environment also need to be predicted accurately to evaluate ball bearings' performance. In this study, each element's dimension under operating conditions is calculated by referencing a material handbook [41] including several material information under cryogenic environment. The thermal expansion ratio of Inconel 718 and SUS440C used in this study is shown in Fig. 5. Because material data of Si_3N_4 under cryogenic environment could not be found in open publications, the thermal expansion ratio of Si_3N_4 was measured in our laboratory. The data was acquired by directly measuring the amount of shrinkage at LN_2 temperature. Since the thermal expansion ratio of Si_3N_4 is much smaller than metals, the influence of its change with temperature conditions on bearing motion analysis is negligible. Therefore, the thermal expansion ratio of Si_3N_4 is assumed to be constant value 3.40×10^{-6} in this study.

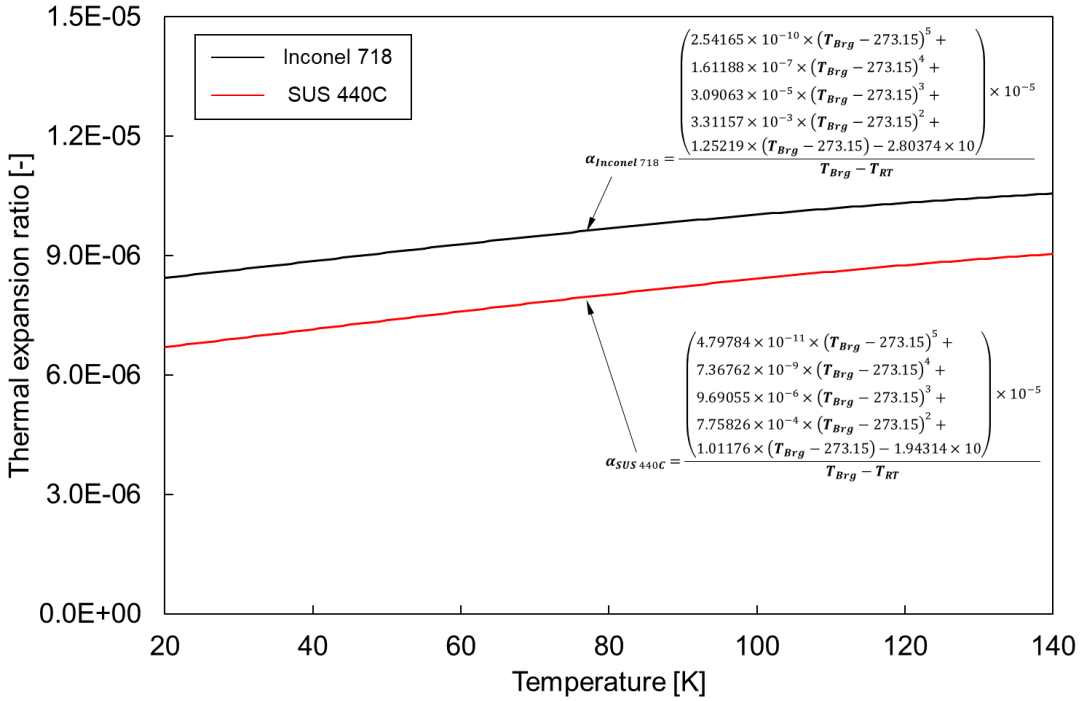

Fig. 5 Thermal expansion ratio of Inconel 718 and SUS440C in cryogenic environment.

2.2.2. Interference fitting model including an effect of centrifugal force

High precision of rotating performance is required for turbopump bearings. For improving the precision, the inner race is tightly fit to the main shaft, which is interference fitting. Interference fitting between the inner race and the main shaft can minimize a position gap between their axial center lines and enable them to rotate together without any slip in the interface even on high-speed conditions. In interference fitting conditions, the main shaft would shrink, and the inner race would expand due to pressure in the fitting interface. The expansion of the inner race would have significant influences on contact angle against rotating elements. Therefore, the expansion amount needs to be evaluated accurately. In addition, the dimension changes of the inner race and the main shaft due to centrifugal force under high-speed conditions are also important to the bearing motion analysis. In this study, the interference fitting model including an effect of centrifugal force, shown in Fujii's research about high-

speed ball bearings [42], is referred. The outline of the model is as follows.

Dimension changes of an inner race and a shaft are calculated by solving a simplified problem of interference fitting about a cylinder and a shaft. Hence, an inner race needs to be approximated as a simple cylinder. Dimensions of an inner race are shown in Fig. 6. This inner race is assumed to be a cylinder of outer diameter D_i and inner diameter d_i in the interference fitting model of this study. D_i is expressed as an average of the groove diameter d_{mi} and the shoulder diameter d_{si}:

$$D_i = \frac{d_{mi} + d_{si}}{2} \tag{1}$$

The relationship between the interference δ_i, the expansion of the inner race Δd_i, and the shrinkage of the shaft ΔD_s is:

$$\delta_i = \Delta d_i + \Delta D_s \tag{2}$$

The balance of pressure between the interface and the shaft is:

$$p_{si} + \frac{E_s}{1-\nu_s} A_s - \frac{E_s}{1+\nu_s} \frac{4}{{D_s}^2} B_s - \frac{3+\nu_s}{32} \rho_s {\omega_i}^2 {D_s}^2 = 0 \tag{3}$$

p_{si} is the interface pressure, E_s is the Young's modulus of the shaft, ν_s is the Poisson's modulus of the shaft, A_s and B_s are the integration constant values of the shaft, D_s is the outer diameter of the shaft, ρ_s is the density of the shaft material, and ω_i is the rotational velocity.

The expansion of the shaft is:

$$\Delta D_s = -\left(D_s A_s + \frac{4}{D_s} B_s - \frac{1-{\nu_s}^2}{32} \frac{\rho_s}{E_s} {\omega_i}^2 {D_s}^3 \right) \tag{4}$$

The balance of pressure between the interface and the inner race is:

$$p_{si} + \frac{E_i}{1-\nu_i} A_i - \frac{E_i}{1+\nu_i} \frac{4}{{d_i}^2} B_i - \frac{3+\nu_i}{32} \rho_i {\omega_i}^2 {d_i}^2 = 0 \tag{5}$$

E_i is the Young's modulus of the inner race, ν_i is the Poisson's modulus of the inner race, A_i and B_i is the integration constant of the inner race, d_i is the inner diameter of the inner race, and ρ_i is the density of the inner race material.

The balance of pressure on the outer side of the inner race is:

$$p_{bi} + \frac{E_i}{1-\nu_i} A_i - \frac{E_i}{1+\nu_i} \frac{4}{{D_i}^2} B_i - \frac{3+\nu_i}{32} \rho_i {\omega_i}^2 {D_i}^2 = 0 \tag{6}$$

$$p_{bi} = \frac{Z P_i \cos\theta_i}{W \pi d_{mi}} \tag{7}$$

p_{bi} is the outer side pressure loaded by rolling elements, Z is the number of rolling elements, P_i is the contact force of a rolling element, θ_i is the contact angle of a rolling element, and W is the width of the inner race.

The expansion of the inner race's inner diameter is:

$$\Delta d_i = d_i A_i + \frac{4}{D_i} B_i - \frac{1-{\nu_i}^2}{32} \frac{\rho_i}{E_i} {\omega_i}^2 {d_i}^3 \tag{8}$$

The expansion of the inner race's outer diameter is:

$$\Delta D_i = D_i A_i + \frac{4}{D_i} B_i - \frac{1-{\nu_i}^2}{32} \frac{\rho_i}{E_i} {\omega_i}^2 {D_i}^3 \tag{9}$$

Solving the simultaneous equations about Equation (1) to Equation (9), the dimensions considering the interference fitting including an effect of centrifugal force are obtained.

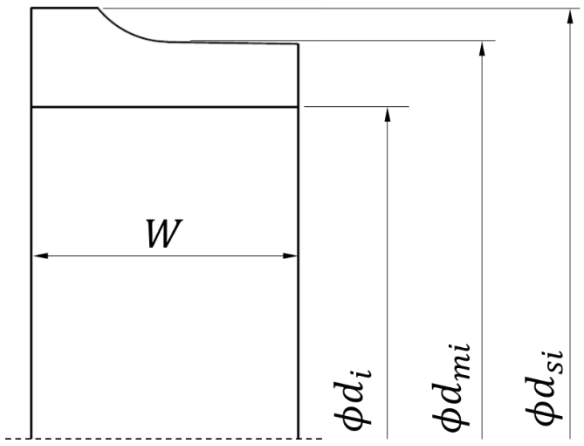

Fig. 6 Dimensions of inner race.

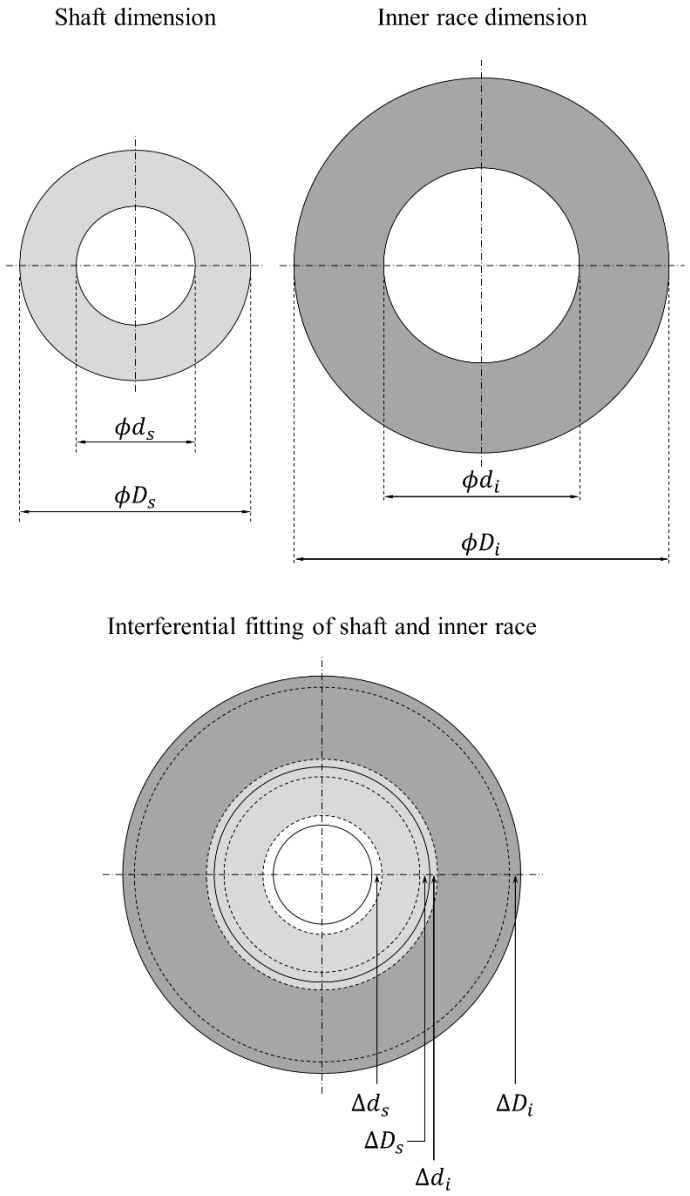

Fig. 7 Interference fitting model of inner race and shaft.

2.3. Analysis Method of bearing motion

2.3.1. Force calculation

Force balances inside a bearing are calculated to acquire the contact load between races and rolling elements. In this study, analysis modeling of a high-speed angular ball bearing, which was proposed by Jones[19] and Harris[21], is adopted. The calculation outline is as follows.

An inner race is displaced from the initial position due to bearing loading. The displacements are shown in Fig. 8. These displacements values are a part of outputs by bearing motion analysis. Rolling elements are equally allocated as shown in Fig. 9. At first, force balance of a rolling element at position j is calculated. Considering bearing loading and centrifugal force due to high-speed rotating, the ball center position is displaced from the initial position as shown in Fig. 10. The line of action between the raceway groove curvature centers is not collinear with a line connecting these centers since the rolling elements' center moves out of the line due to centrifugal force loading. In Fig. 10, it is assumed that the inner raceway groove curvature center moves relative to the fixed centers of the outer raceway groove curvature.

The axial distance between the raceway groove curvature centers A_{1j} is:

$$A_{1j} = BD \sin \alpha^0 + \delta_a + \theta R_i \cos \psi_j \tag{10}$$

BD is the initial distance between the raceway groove curvature centers, α^0 is the initial contact angle, δ_a is the axial displacement of the inner raceway groove curvature center, θ is the displacement of the inner race, ψ_j is the angle between the top and the position j as shown in Fig. 9. R_i is the distance between the shaft center and the inner raceway groove curvature center:

$$R_i = \frac{d_m}{2} + \left(r_i - \frac{D}{2}\right) \cos \alpha^0 \tag{11}$$

d_m is the distance between the shaft center and the ball center, r_i is the radii of the inner raceway groove curvature, and D is the ball diameter.

The radial distance between the raceway groove curvature centers A_{2j} is:

$$A_{2j} = BD \cos \alpha^0 + \delta_r \cos \psi_j \tag{12}$$

δ_r is the radial displacement of the inner raceway groove curvature center.

The ball final position $\left(X_{1j}, X_{2j}\right)$ is expressed as:

$$\cos \alpha_{oj} = \frac{X_{2j}}{(f_o - 0.5)D + \delta_{oj}} \tag{13}$$

$$\sin \alpha_{oj} = \frac{X_{1j}}{(f_o - 0.5)D + \delta_{oj}} \tag{14}$$

$$\cos \alpha_{ij} = \frac{A_{2j} - X_{2j}}{(f_i - 0.5)D + \delta_{ij}} \tag{15}$$

$$\sin \alpha_{ij} = \frac{A_{1j} - X_{1j}}{(f_i - 0.5)D + \delta_{ij}} \tag{16}$$

f_o is the ratio of the outer race curvature radii to the ball diameter, f_i is the ratio of the inner race curvature radii to the ball diameter, δ_{oj} is the contact deformation on the outer race interface, and δ_{ij} is the contact deformation on the inner race interface.

Considering the Pythagorean Theorem:

$$\left(A_{1j} - X_{1j}\right)^2 + \left(A_{2j} - X_{2j}\right)^2 = \left\{(f_i - 0.5)D + \delta_{ij}\right\}^2 \tag{17}$$

$$X_{1j}{}^2 + X_{2j}{}^2 = \left\{(f_o - 0.5)D + \delta_{oj}\right\}^2 \tag{18}$$

The ball loading at position j is shown in Fig. 11. Q_{oj} is the normal loading between the outer raceway and the ball. Q_{ij} is the normal loading between the inner raceway and the ball. M_{gj} is the gyroscopic moment at the ball:

$$M_{gj} = J\left(\frac{\omega_B}{\omega}\right)_j \left(\frac{\omega_m}{\omega}\right)_j \omega^2 \sin \beta \tag{19}$$

J is the ball's mass moment of inertia which is expressed as:

$$J = \frac{1}{6}\rho\pi D^2 \tag{20}$$

ω_B is rotational speed of the ball about its center, ω_m is orbital speed of the ball, ω is rotational speed of the shaft, β is direction of the ball's rotation.

λ_{oj} and λ_{ij} are the resisting balance of the friction force due to the moment. For example, $\lambda_{oj} = 1$ and $\lambda_{ij} = 1$ in the case where the moment is resisted equally at the ball-inner and ball outer raceway contacts. $\lambda_{oj} = 2$ and $\lambda_{ij} = 0$ if the moment is resisted entirely by friction force at the ball-outer raceway contact. In this study, since the analysis cases are extremely high-speed conditions where the boll motion is assumed to be outer raceway control, $\lambda_{oj} = 2$ and $\lambda_{ij} = 0$

are adopted. F_{cj} is the centrifugal force loading on the ball due to rotating motion:

$$F_{cj} = \frac{1}{2} m_b d_m {\omega_m}^2 \tag{21}$$

m_b is the ball mass. α_{oj} and α_{ij} are contact angles at outer and inner raceway, respectively. Considering the equilibrium of forces in the horizontal and vertical directions:

$$Q_{ij} \sin \alpha_{ij} - Q_{oj} \sin \alpha_{oj} - \frac{M_{gj}}{D} (\lambda_{ij} \cos \alpha_{ij} - \lambda_{oj} \cos \alpha_{oj}) = 0 \tag{22}$$

$$Q_{ij} \cos \alpha_{ij} - Q_{oj} \cos \alpha_{oj} - \frac{M_{gj}}{D} (\lambda_{ij} \sin \alpha_{ij} - \lambda_{oj} \sin \alpha_{oj}) + F_{cj} = 0 \tag{23}$$

Considering Hertzian contact, the normal load is expressed:

$$Q_{oj} = K_{oj} {\delta_{oj}}^{1.5} \tag{24}$$

$$Q_{ij} = K_{ij} {\delta_{ij}}^{1.5} \tag{25}$$

K_{oj} and K_{ij} are coefficients that can be calculated in accordance with Hertzian contact theory.

The conditions of equilibrium of forces applying the entire bearing are:

$$F_a = \sum_{j=1}^{Z} \left(Q_{ij} \sin \alpha_{ij} - \frac{\lambda_{ij} M_{gj}}{D} \cos \alpha_{ij} \right) \tag{26}$$

$$F_r = \sum_{j=1}^{Z} \left(Q_{ij} \cos \alpha_{ij} + \frac{\lambda_{ij} M_{gj}}{D} \sin \alpha_{ij} \right) \cos \psi_j \tag{27}$$

$$M = \sum_{j=1}^{Z} \left\{ \left(Q_{ij} \sin \alpha_{ij} - \frac{\lambda_{ij} M_{gj}}{D} \cos \alpha_{ij} \right) R_i + \frac{\lambda_{ij} M_{gj}}{D} r_i \right\} \cos \psi_j \tag{28}$$

F_a is the axial load, F_r is the radial load, and M is the moment.

Solving the simultaneous equations about Equation (10) to Equation (28), the normal loads and the contact angles of high-speed ball bearings are obtained.

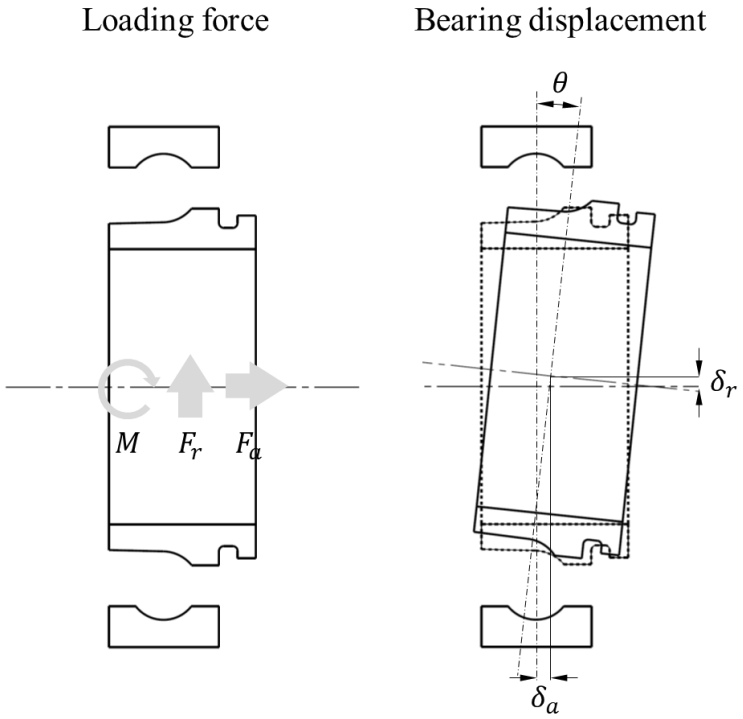

Fig. 8 Displacements of an inner ring due to combined radial, axial, and moment loading.

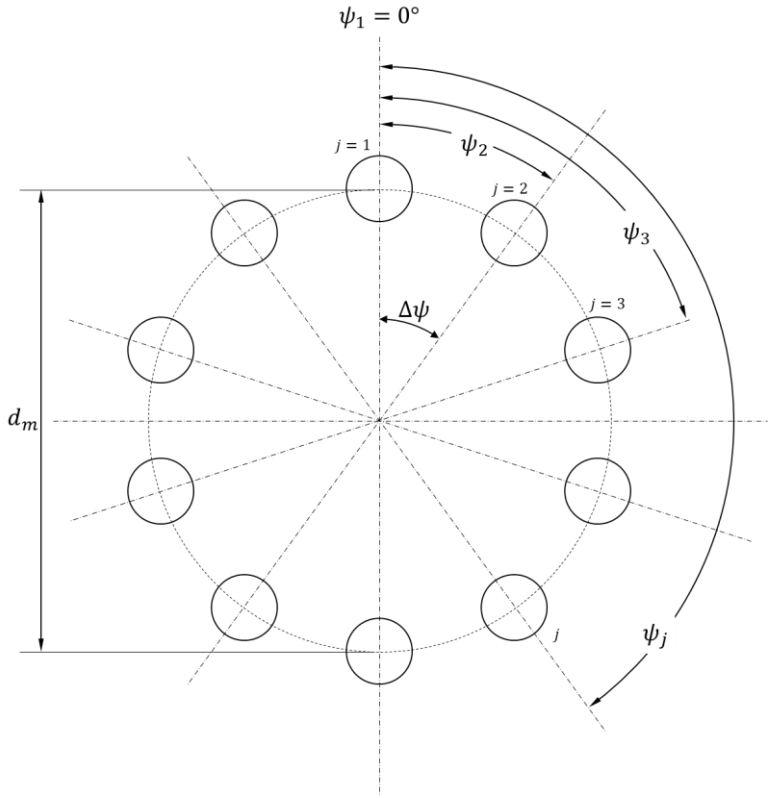

Fig. 9 Angular position of rolling elements.

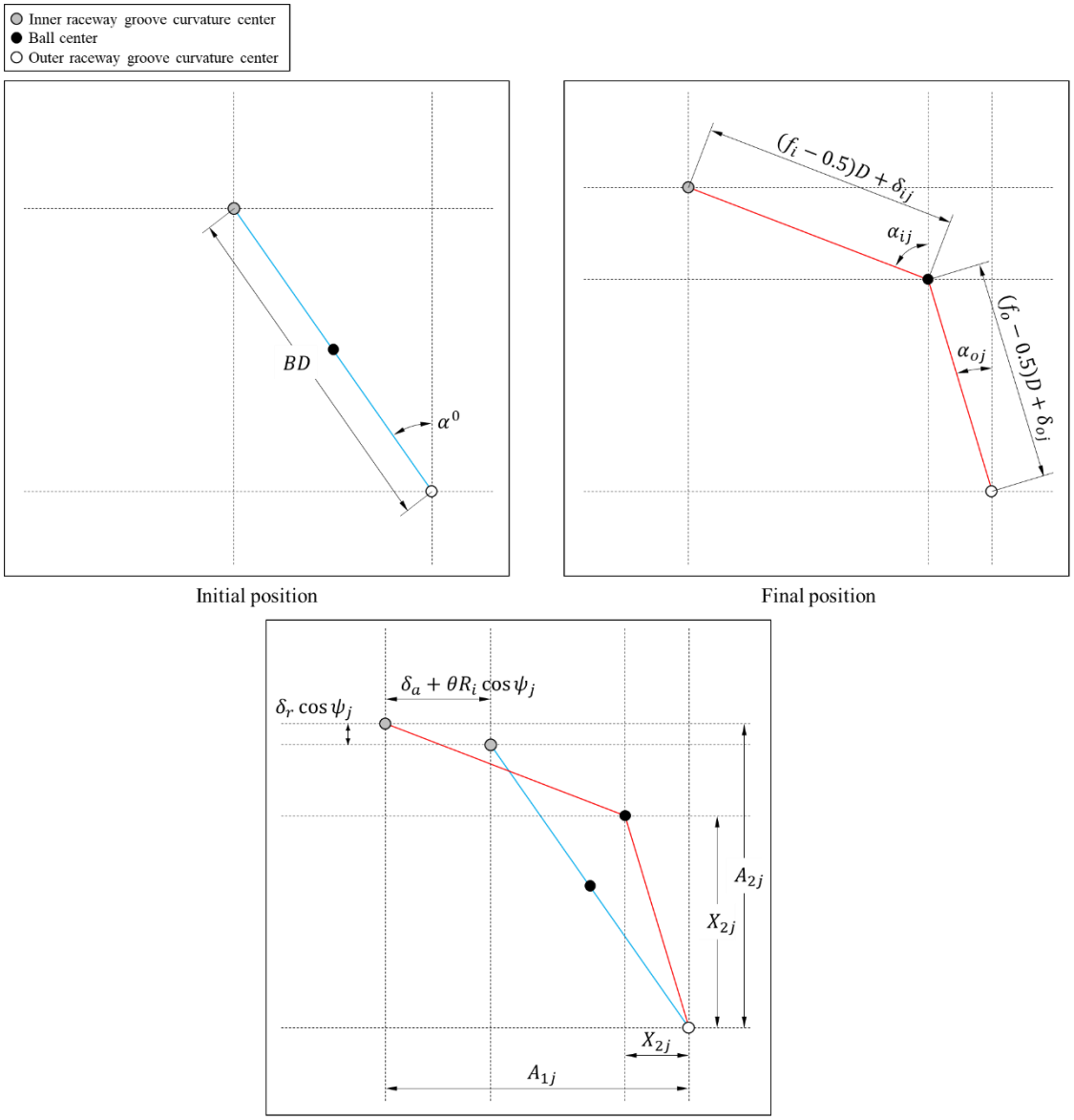

Fig. 10 Positions of ball center and raceway groove curvature centers at position *j*.

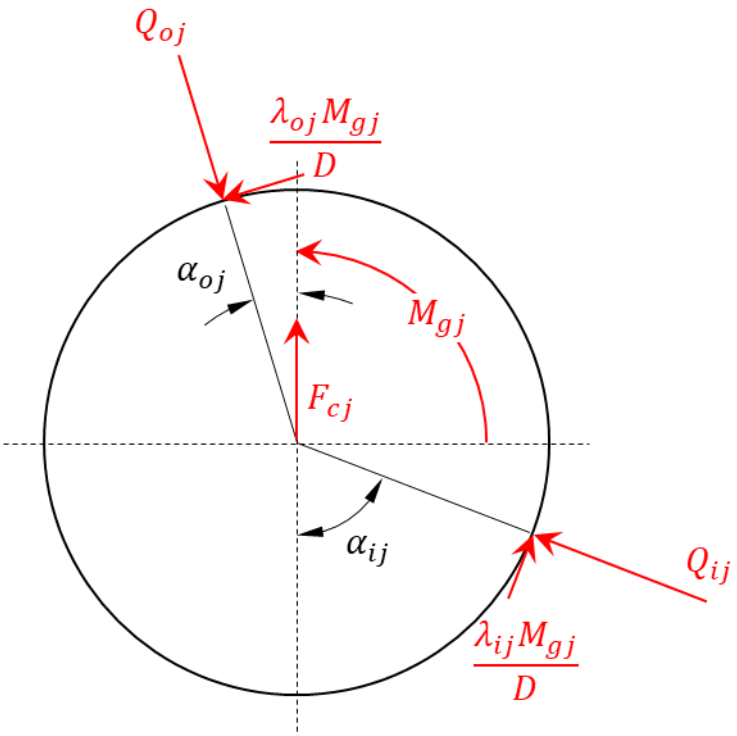

Fig. 11 Ball loading at position j.

2.3.2. Velocity calculation

The relative velocity of the ball to the raceways needs to be calculated to analyze the bearing motion. In this study, the calculation method proposed by Jones [19] is referred. The detailed calculation process is shown in [19]. The raceway contacts are shown in Fig. 12 and Fig. 13. Equations used in the bearing analysis are as follows.

The relative angular velocity of the inner race ω_i is:

$$\omega_i = \frac{\omega}{1 + \frac{r'_o \left(\frac{d_m}{2} - r'_i \cos\alpha_i\right)(\cos\beta \cos\beta' \cos\alpha_o + \sin\beta \sin\alpha_o)}{r'_i \left(\frac{d_m}{2} - r'_o \cos\alpha_o\right)(\cos\beta \cos\beta' \cos\alpha_i + \sin\beta \sin\alpha_i)}} \tag{29}$$

r'_o and r'_i are the effective rolling radius of the ball where the transition of the ball is identical to that of each raceway, β is the angle defining direction of the ball's rotation, and β' is the initial contact angle. β is shown in Fig. 14. Considering outer raceway control:

$$\tan\beta = \frac{\sin\theta_o}{\cos\theta_o - \frac{D}{d_m}} \tag{30}$$

The relative angular velocity of the outer race ω_o is:

$$\omega_o = \frac{-\omega}{1 + \frac{r'_i\left(\frac{d_m}{2} - r'_o\cos\alpha_o\right)(\cos\beta\cos\beta'\cos\alpha_i + \sin\beta\sin\alpha_i)}{r'_o\left(\frac{d_m}{2} - r'_i\cos\alpha_i\right)(\cos\beta\cos\beta'\cos\alpha_o + \sin\beta\sin\alpha_o)}} \tag{31}$$

The angular velocity of the ball about its center ω_B is:

$$\omega_B = \frac{-\omega}{1 + \frac{r'_o(\cos\beta\cos\beta'\cos\alpha_o + \sin\beta\sin\alpha_o)}{\frac{d_m}{2} + r'_o\cos\alpha_o} + \frac{r'_i(\cos\beta\cos\beta'\cos\alpha_i + \sin\beta\sin\alpha_i)}{\frac{d_m}{2} - r'_i\cos\alpha_i}} \tag{32}$$

Using these relative velocities, the velocity distribution of each contact area, which is needed to calculate the heat generation of ball-raceway friction can be obtained.

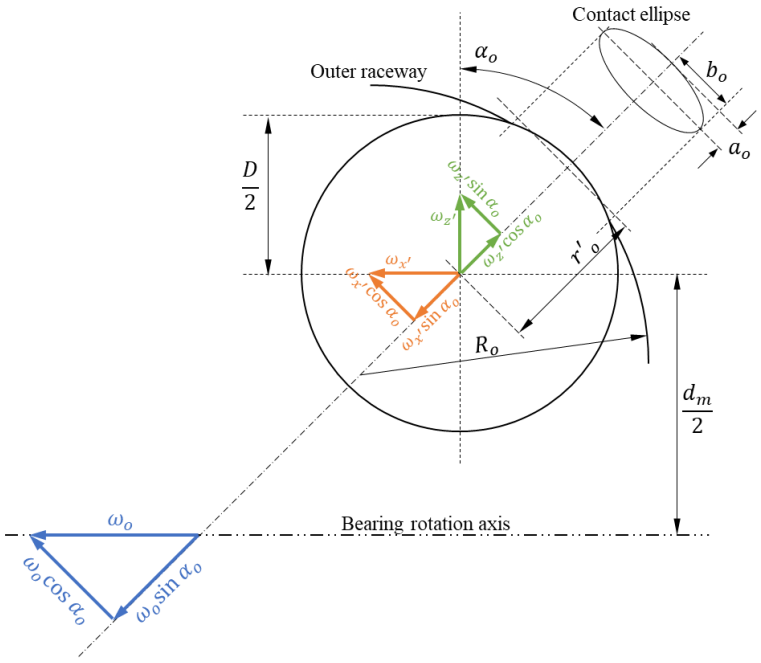

Fig. 12 Outer raceway contact.

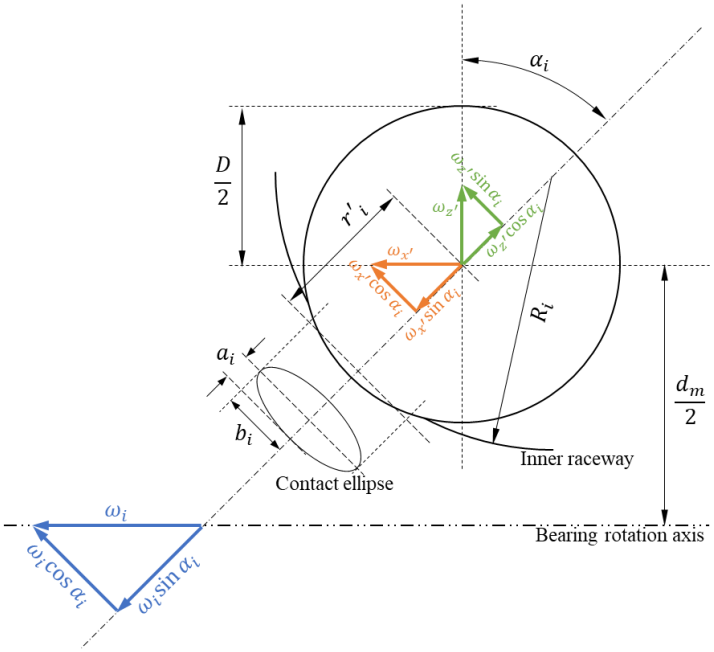

Fig. 13 Inner raceway contact.

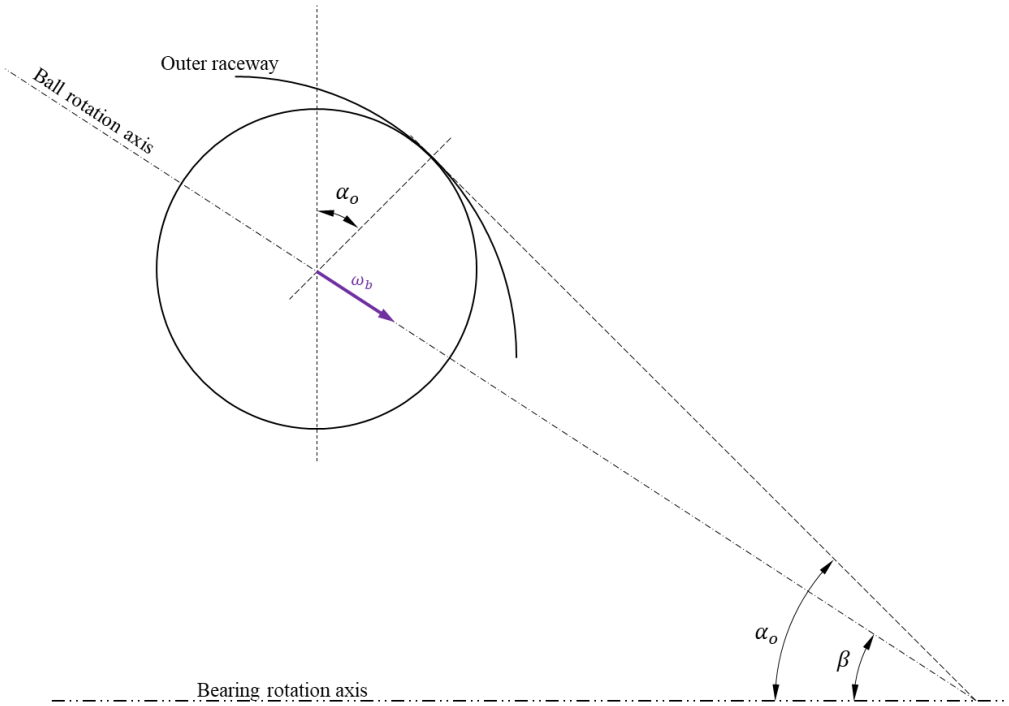

Fig. 14 Direction angle of ball rotation.

2.3.3. Contact pressure calculation of ball-raceway friction

The contact pressure of ball-raceway friction is calculated to assess the friction characteristics and evaluate the heat generation. In this study, the Hertz contact theory is adopted. The calculation method of the Hertz pressure for the ball-raceway contact is summarized in [43].

2.3.4. Calculation examples

Theoretical calculation of bearing motion and contact condition was conducted by using the method described in this chapter. The results are needed for more detailed analysis such as CFD of bearing coolant and calculation of friction heat generation. In this study, two types of bearings are used as the research target. Their design parameters are shown in Table 1. The material of ball, races, and shaft for both bearings is Si_3N_4, SUS440C, and Inconel 718, respectively.

Table 1 Design parameter of Bearing X and Y.

Parameter	Bearing X	Bearing Y
D, ball diameter	7.938 mm	11.113 mm
f_i, ratio of inner race curvature to ball diameter	0.56	0.56
f_o, ratio of outer race curvature to ball diameter	0.51	0.52
Z, number of balls	10	13
α^0, initial contact angle	20 deg	25 deg
W, bearing width	15 mm	18 mm
D_s, shaft outer diameter	25 mm	45 mm
d_i, inner diameter of inner race	25 mm	45 mm
d_m, ball pitch diameter	38.5 mm	65 mm
m_b, ball mass	0.848 g	2.329 g

E_b, elastic modulus of ball material	308000 MPa	308000 MPa
ν_b, Poisson's ratio of ball material	0.29	0.29
E_s, elastic modulus of shaft material	199000 MPa	199000 MPa
ν_s, Poisson's ratio of shaft material	0.225	0.225
ρ_s, density of shaft material	8221 kg/m^3	8221 kg/m^3
E_i, elastic modulus of inner race material	206022 MPa	206022 MPa
ν_i, Poisson's ratio of inner race material	0.284	0.284
ρ_i, density of inner race material	7750	7750
E_o, elastic modulus of outer race material	206022 MPa	206022 MPa
ν_o, Poisson's ratio of outer race material	0.284	0.284
δ_i, amount of inner race-shaft interference	0.040 mm	0.051 mm

2.3.4.1. Calculation results of Bearing X

Calculation conditions for Bearing X are shown in Table 2. The calculation was conducted by significantly changing rotational speed as a parameter since Bearing X is operated in much wider range of rotational speed conditions. The same conditions as the experiments described in Chapter 3 are included.

Calculation results of Bearing X are shown in Fig. 15. The bearing stiffness is shown in Fig. 15 (a). Both the axial stiffness and the radial stiffness were not as dependent on the rotational speed as Bearing Y results described later, and Bearing X performed more stable stiffness characteristics in wide range of rotational speed conditions. This is because Bearing X is designed for higher speed conditions. In the design, the initial contact angle is set at 20 deg which is much smaller than ordinary angular contact bearings, and the change of contact angle from the initial contact due to high-speed rotation is reduced by using low density material Si_3N_4 for balls. The contact angle is shown in Fig. 15 (b). Contact angle

changes of Bearing X from the initial contact at 120000 rpm were -7.8 deg in the outer race and around -0.2 deg in the inner race which were much smaller Bearing Y. It indicates that the contact angle of Bearing X did not easily change with the rotational speed. The small change of the contact angle reduced the change of stiffness performance and spinning motion occurred in the contact area of inner race, which contributes to mitigating the severe friction conditions there.

The ball load, maximum contact pressure, maximum SV value, and contact area are shown in Fig. 15 (c), Fig. 15 (d), Fig. 15 (e), and Fig. 15 (f). The figures show the influences of the centrifugal forces at higher speed conditions even though the material of balls was Si_3N_4 which is significantly lighter than SUS440C, which contributed to reducing the centrifugal forces loaded on balls. For example, the ball load of the outer race at 120000 rpm was 2.3 times larger than 0 rpm, which contributed to nonlinear increase of contact pressure, SV value, and contact area on the outer race. On the other hand, since the ball load of the inner race did not change as significantly as outer race, there was almost no nonlinear change of parameters relating to contact load.

From the above, severe friction-resistance capabilities are demanded for the bearing operation at 120000rpm even though Bearing X is designed to reduce spinning motion in inner race contact and contact pressure in outer race. Since the SV value at 120000 rpm was 5937 MPa-m/s in the inner race and 4065 MPa-m/s in the outer race which were remarkably severe, sufficient lubrication performance is needed for the contact area of raceways.

Table 2 Calculation conditions for Bearing X.

Parameter	Value
Rotational speed	20000, 40000, 60000, 80000, 100000, 120000 rpm
Thrust load	1000 N
Ball material	Si_3N_4

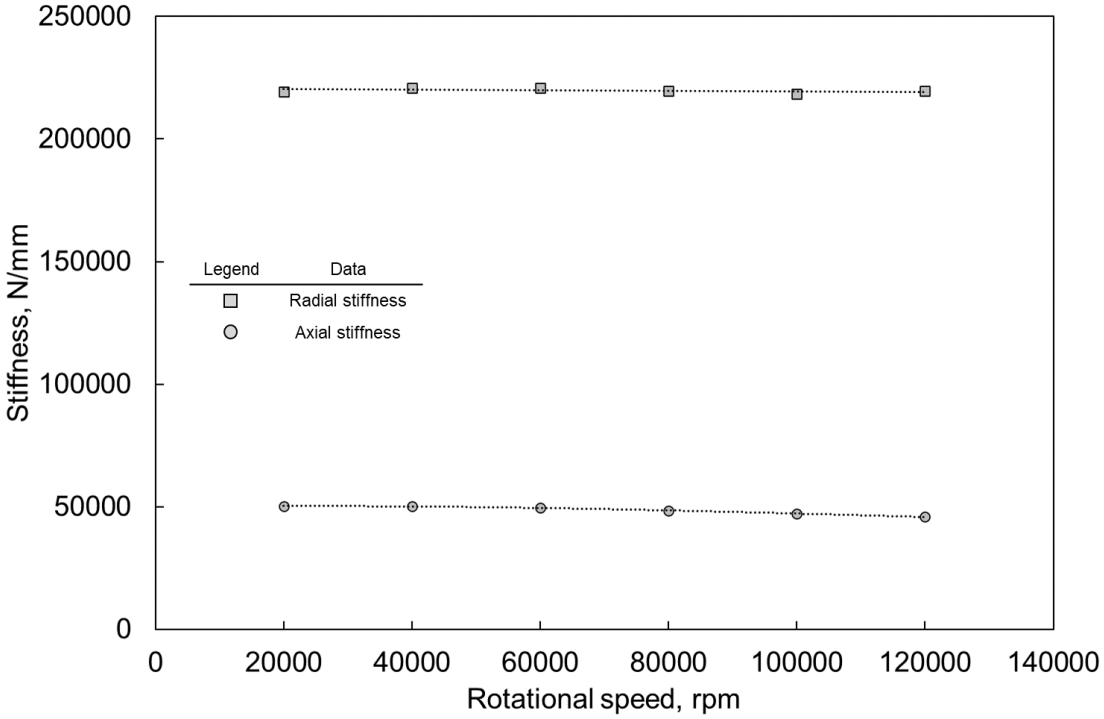

Fig. 15 (a) Bearing stiffness.

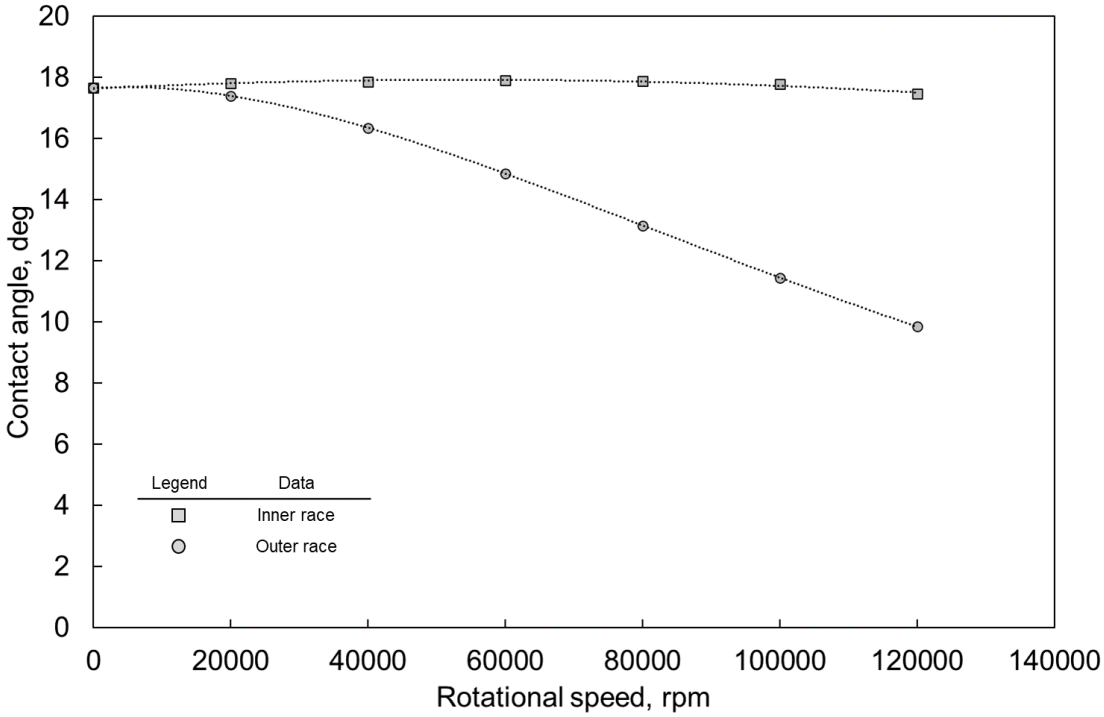

Fig. 15 (b) Contact angle.

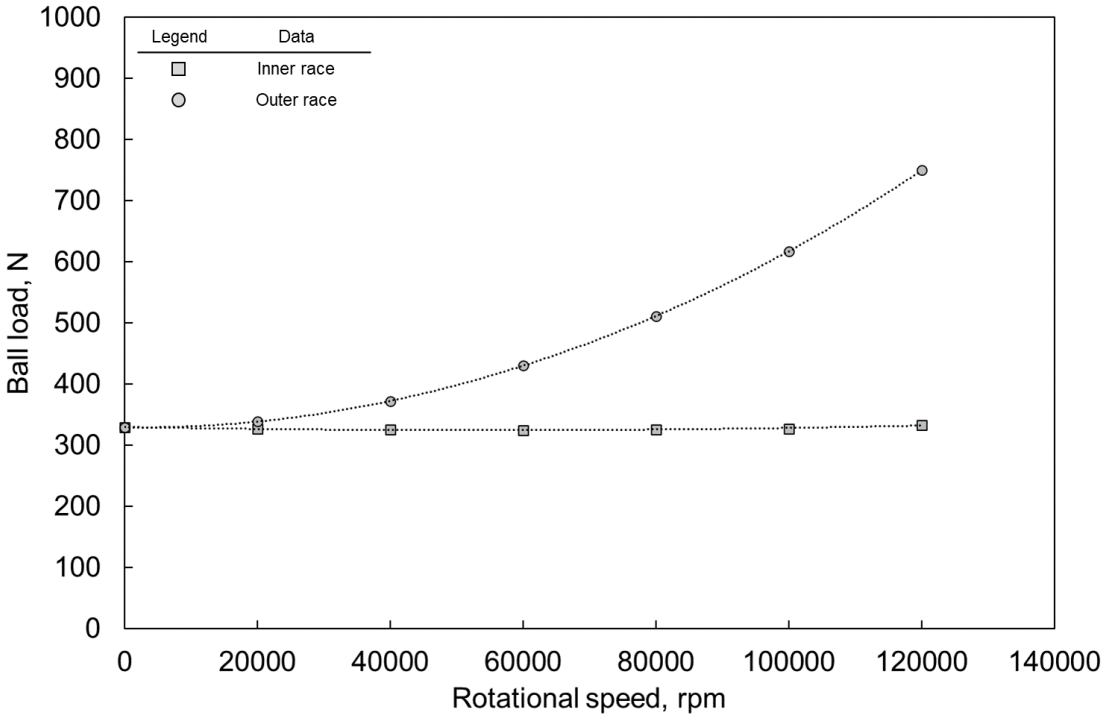

Fig. 15 (c) Ball load.

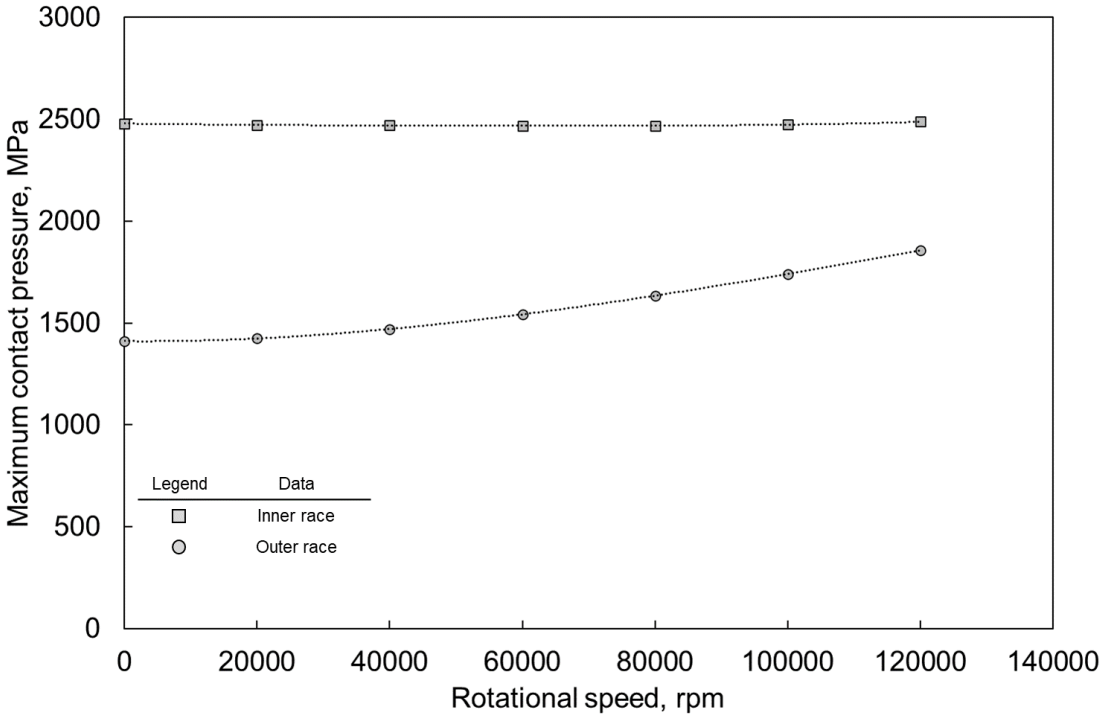

Fig. 15 (d) Maximum contact pressure.

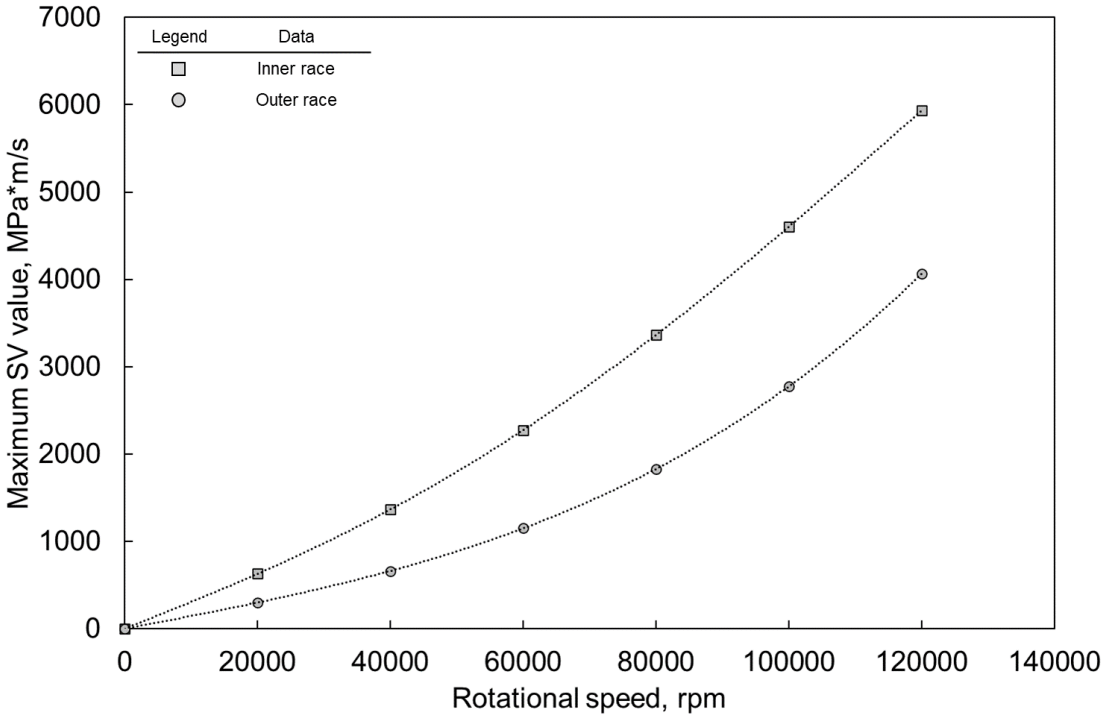

Fig. 15 (e) Maximum SV value.

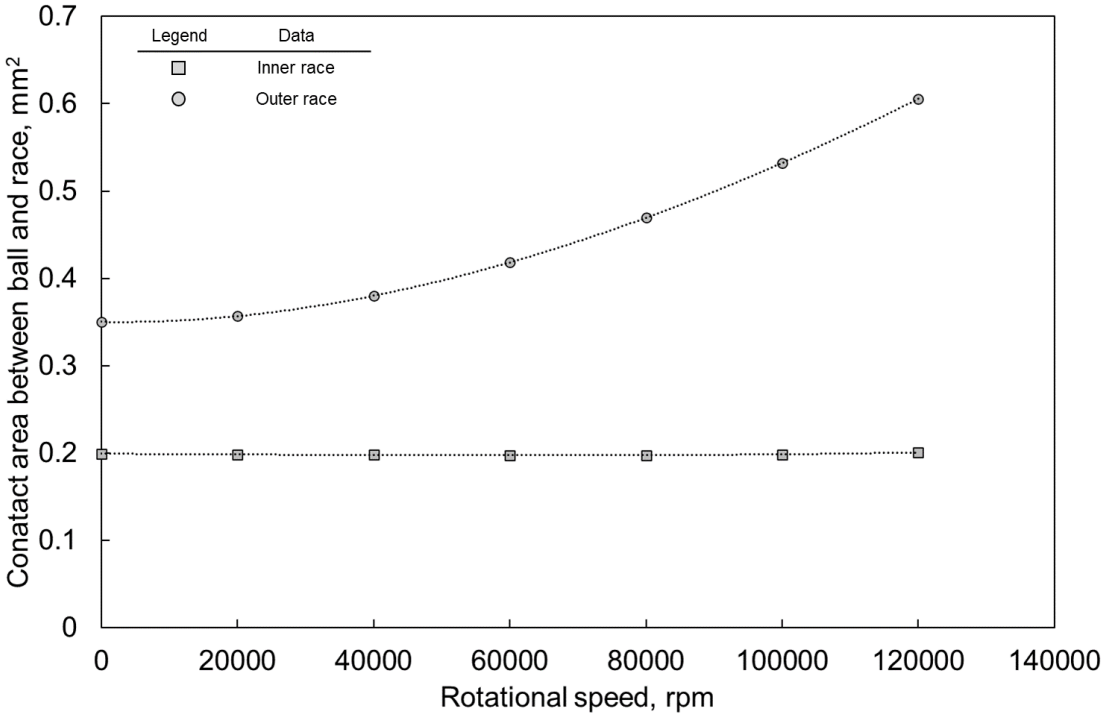

Fig. 15 (f) Contact area.

Fig. 15 Calculation results of Bearing X with Si_3N_4 balls as a function of rotational speed.

2.3.4.2. Calculation results of Bearing Y

Calculation conditions for Bearing Y are shown in Table 3. The calculation was conducted by changing rotational speed, thrust load, and ball material as parameters since they significantly influence bearing motion and contact condition. The same conditions as the experiments described in Chapter 3 are included.

Calculation results of Bearing Y are shown in Fig. 16. The contact angles of Bearing Y with Si_3N_4 balls on each condition are shown in Fig. 16 (a). The contact angle at 0 rpm increased with thrust load although it was smaller than the initial contact angle without thrust load due to dimensional changes by thermal expansion. The contact angle on the inner race slightly increased with the rotational speed while the contact angle on the outer race remarkably decreased with the rotational speed. It is due to centrifugal force loading on balls, which is proportional to the square of rotational speed and compresses balls to outer side. The contact angle changes due to the rotational speed were smaller in larger thrust load condition.

The ball loading results are shown in Fig. 16 (b). The ball load on the inner race slightly decreased with the rotational speed, and ball load on the outer race remarkably increased with the rotational speed. It is due to centrifugal force loading on balls as well as the influence of the rotational speed on the contact angle. The thrust load conditions independently affect the ball loading because the centrifugal force was not influenced by them.

The bearing stiffness is shown in Fig. 16 (c). The bearing stiffness in both radial direction and axial direction was higher in larger thrust load condition. This is because the dimensional changes due to elastic deformation by bearing load would get smaller when the thrust load is larger. The radial stiffness and the axial stiffness decreased with the rotational speed. It is caused by the contact angle changes with the rotational speed. Especially the outer race contact angle was significantly influenced by the rotational speed. In smaller angle of outer race contact, larger contact deformation on the outer

race interface (δ_{oj}) would be needed for a certain deformation in radial direction, which contributes to smaller radial stiffness. Also, in smaller angle of outer race contact, ball load on outer race (Q_{oj}) would change lesser for a certain deformation in axial direction, which contributes to smaller axial stiffness.

The maximum contact pressure, the maximum SV value, and the contact area are shown in Fig. 16 (d), Fig. 16 (e), and Fig. 16 (f). The contact pressure changes with the rotational speed were dependent on the ball load that was shown in Fig. 16 (b). Although the ball load on inner race was smaller than that on outer race especially on higher-speed conditions because of the centrifugal force loading on ball, the contact pressure on inner race was much larger than that on outer race. This is because of the geometric relationship between raceway and ball where inner raceway has concave groove curvature and outer raceway has convex groove curvature, which contributes to much larger contact area on outer race as shown in Fig. 16 (f). As a result, the SV value which is one of evaluation indexes for friction condition was much larger on inner race than outer race, which indicates that the friction condition is more severe on inner race. However, since outer race had much larger contact area with balls, friction heat generation from there would be larger as well. From the above, in the range of the calculation conditions, enough lubrication performance would be needed for more severe friction conditions on inner race. In addition, enough cooling capability would be needed for large friction heat generation on outer race.

To evaluate influences of ball material on bearing motion, calculation results of Bearing Y with SUS440C balls are shown in Fig. 17. The ball material would influence centrifugal force on balls, balls' thermal expansion, and balls' elastic deformation. Due to these influences, the contact angle changes were much larger than the results with Si_3N_4 balls. Especially, contact angle of outer race on higher speed conditions was significantly smaller. This is mainly caused by much larger ball load on outer race due to centrifugal force on balls as shown in Fig. 17 (b), which contributes to larger contact

pressure on outer race as shown in Fig. 17 (d). As a result, the bearing stiffness was smaller than the results with Si_3N_4 balls as shown in Fig. 17 (c).

Table 3 Calculation conditions for Bearing Y.

Parameter	Value
Rotational speed	10000, 20000, 30000, 40000, 50000 rpm
Thrust load	1000, 1900, 3000 N
Ball material	Si_3N_4, SUS440C

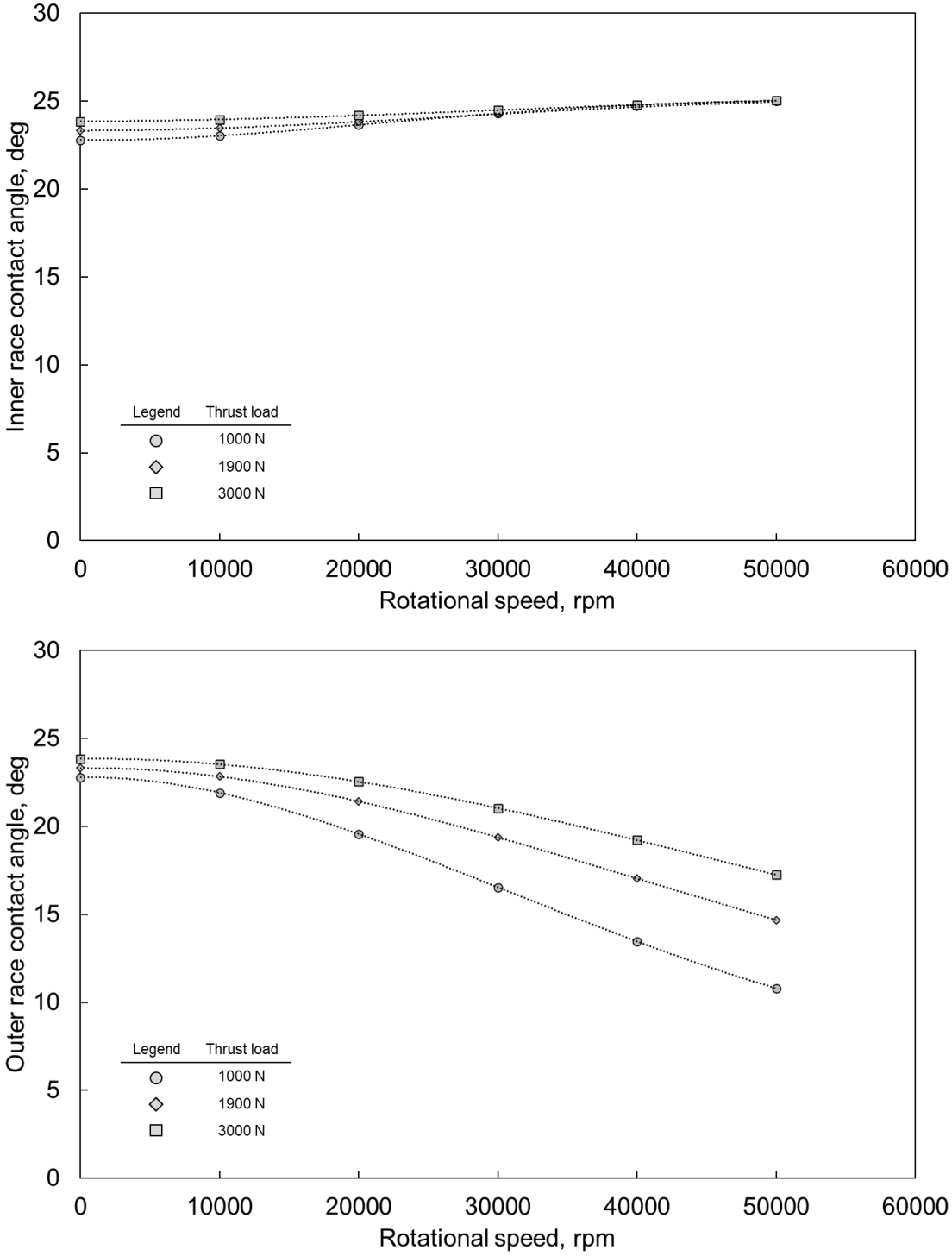

Fig. 16 (a) Contact angle.

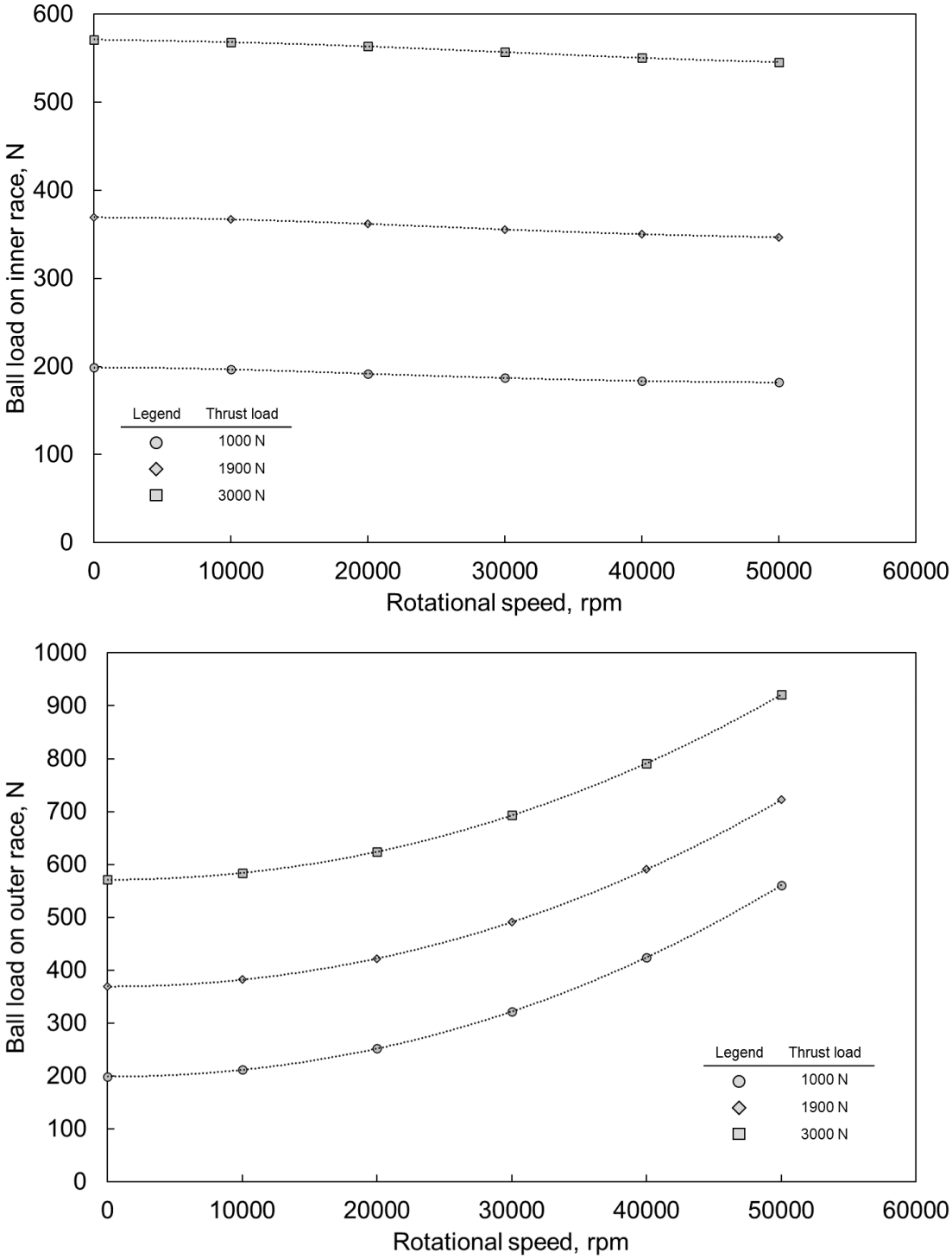

Fig. 16 (b) Ball load.

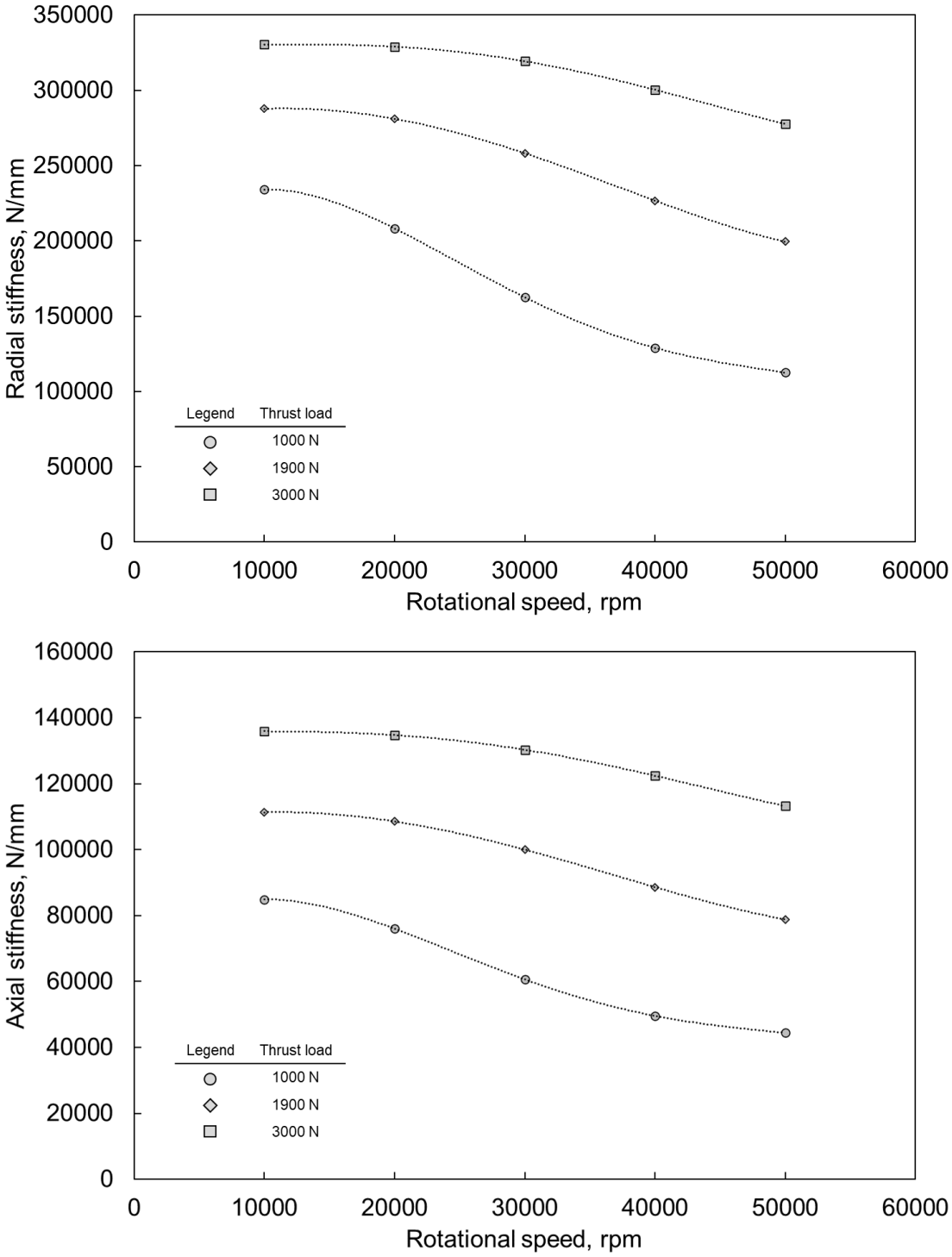

Fig. 16 (c) Bearing stiffness.

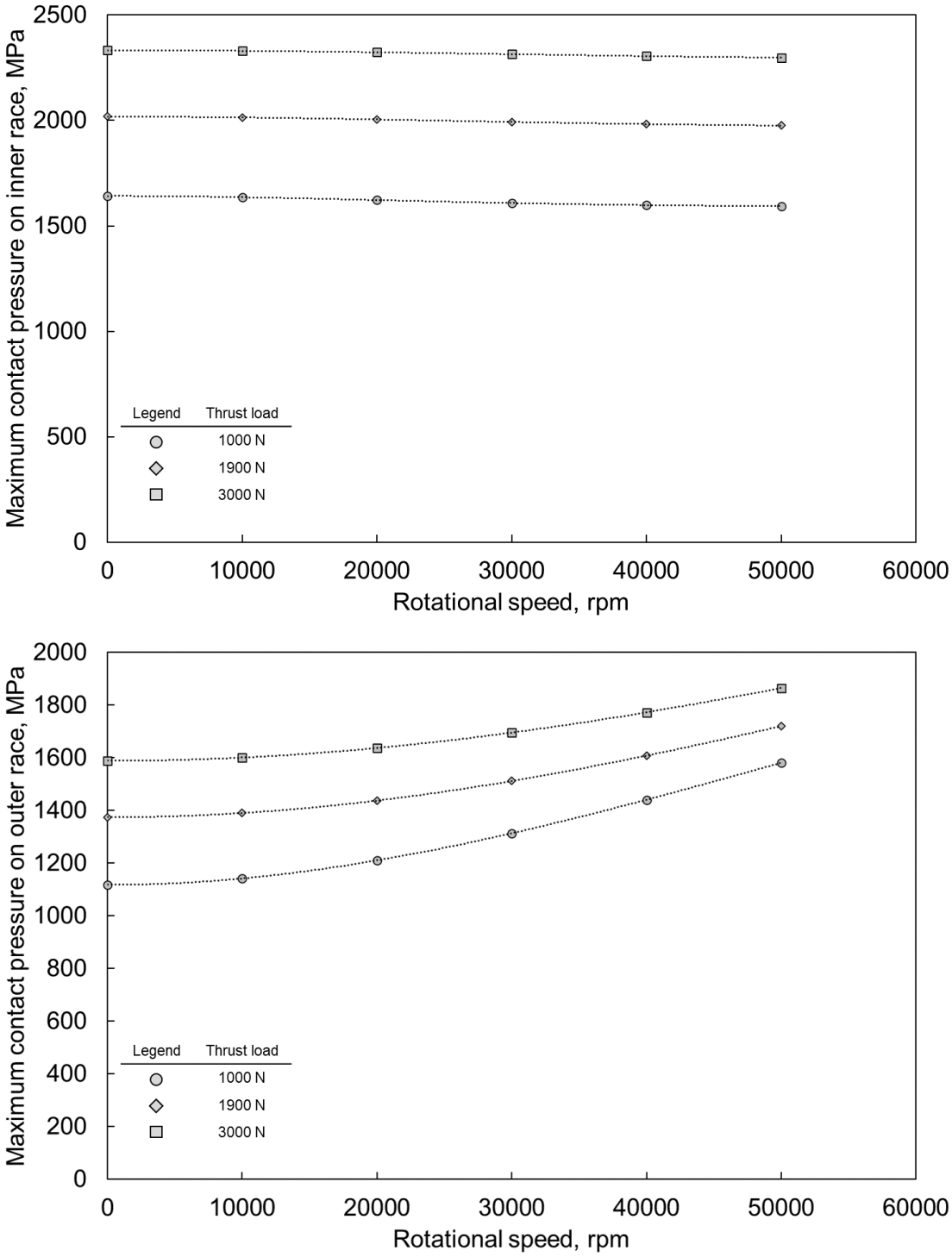

Fig. 16 (d) Maximum contact pressure of friction area between ball and raceway.

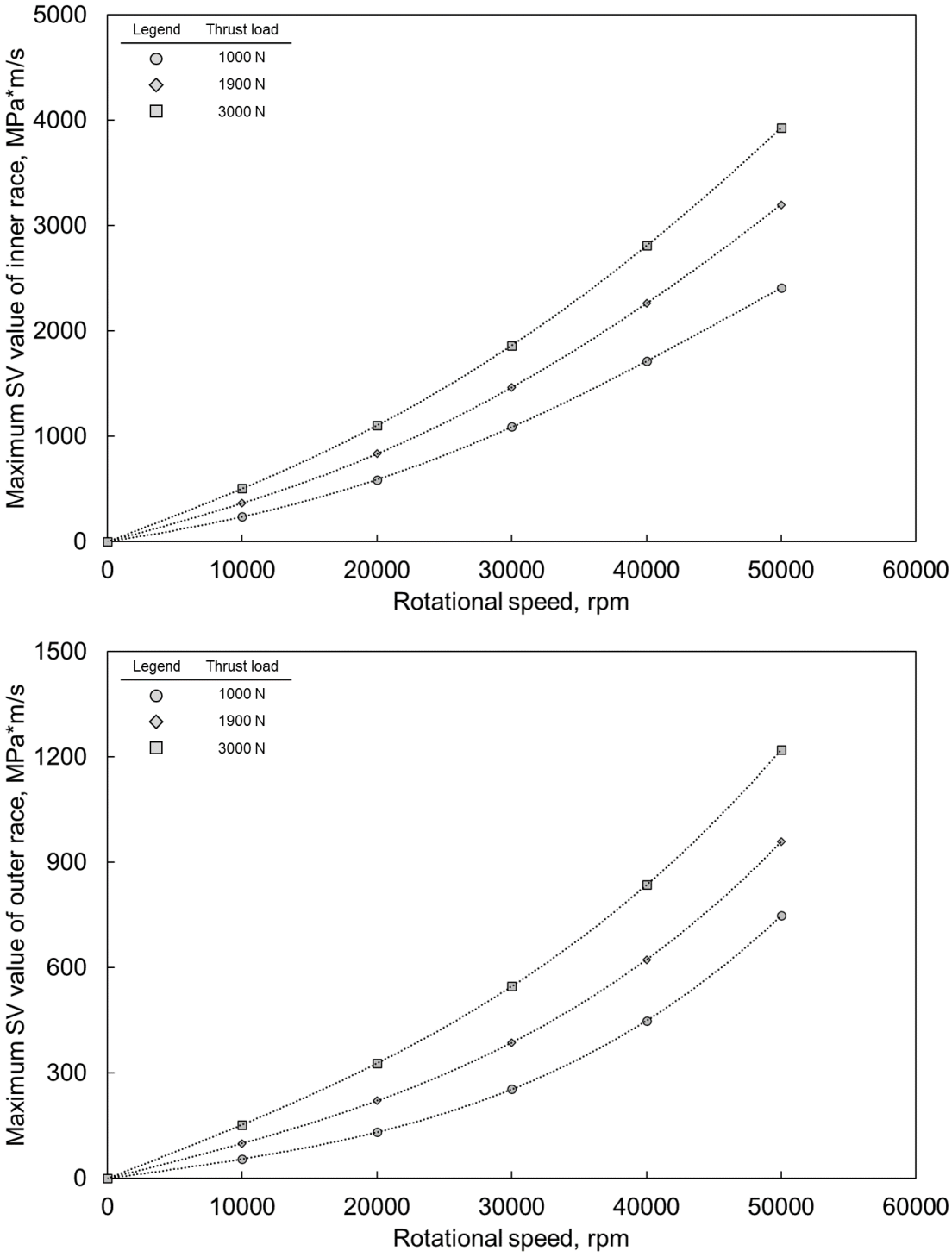

Fig. 16 (e) Maximum SV value of friction area between ball and raceway.

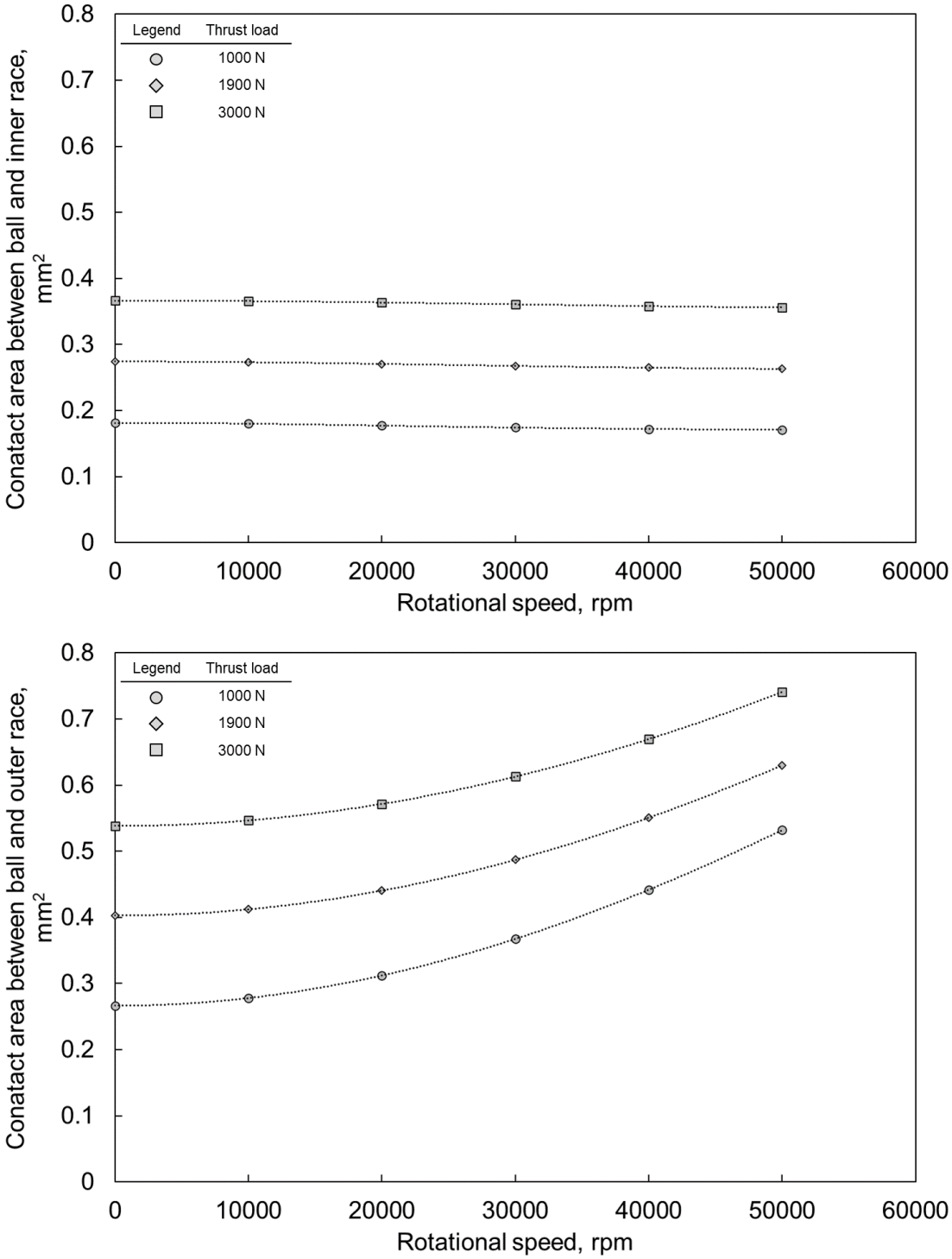

Fig. 16 (f) Contact area between ball and raceway.

Fig. 16 Calculation results of Bearing Y with Si_3N_4 balls as a function of rotational speed and thrust load.

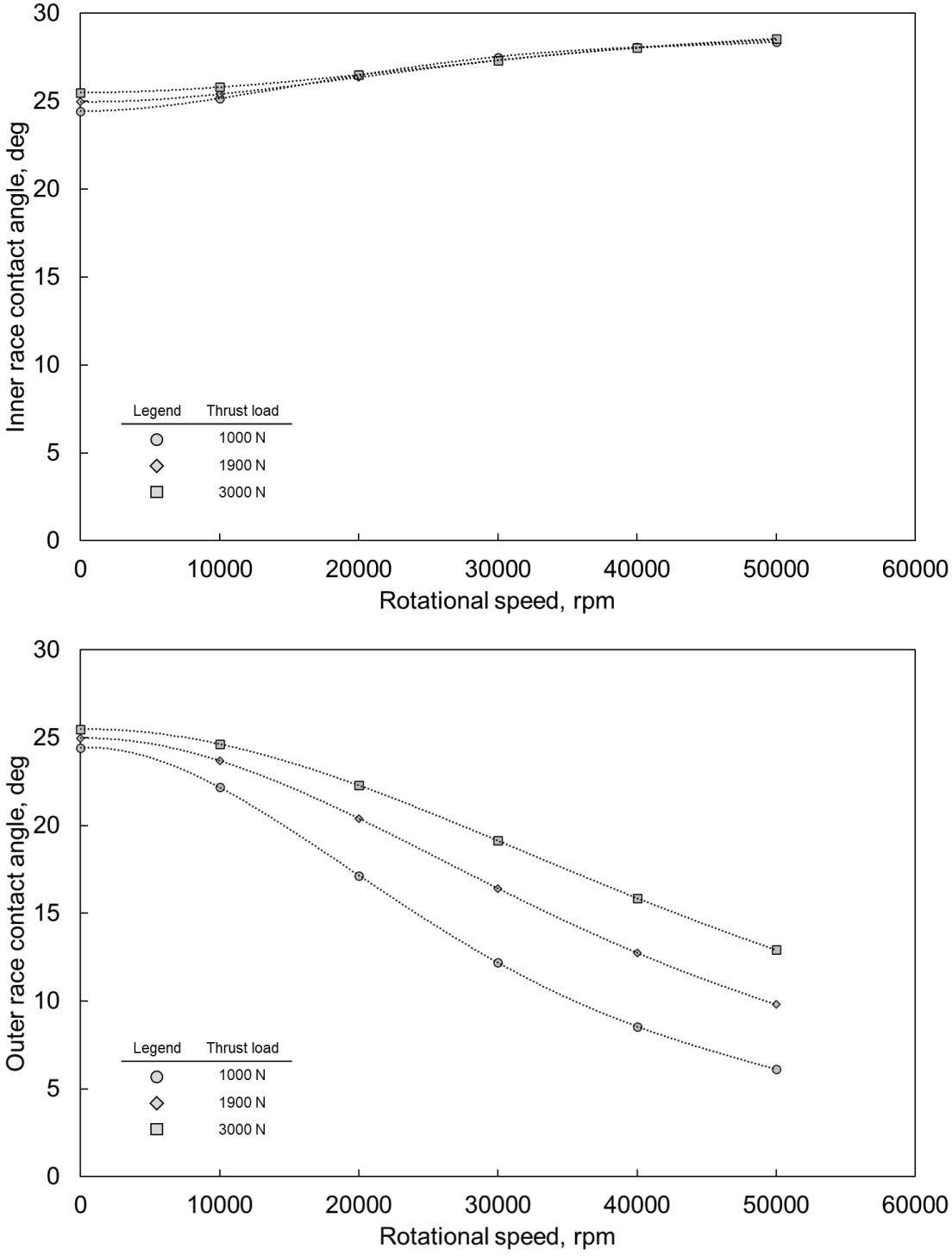

Fig. 17 (a) Contact angle.

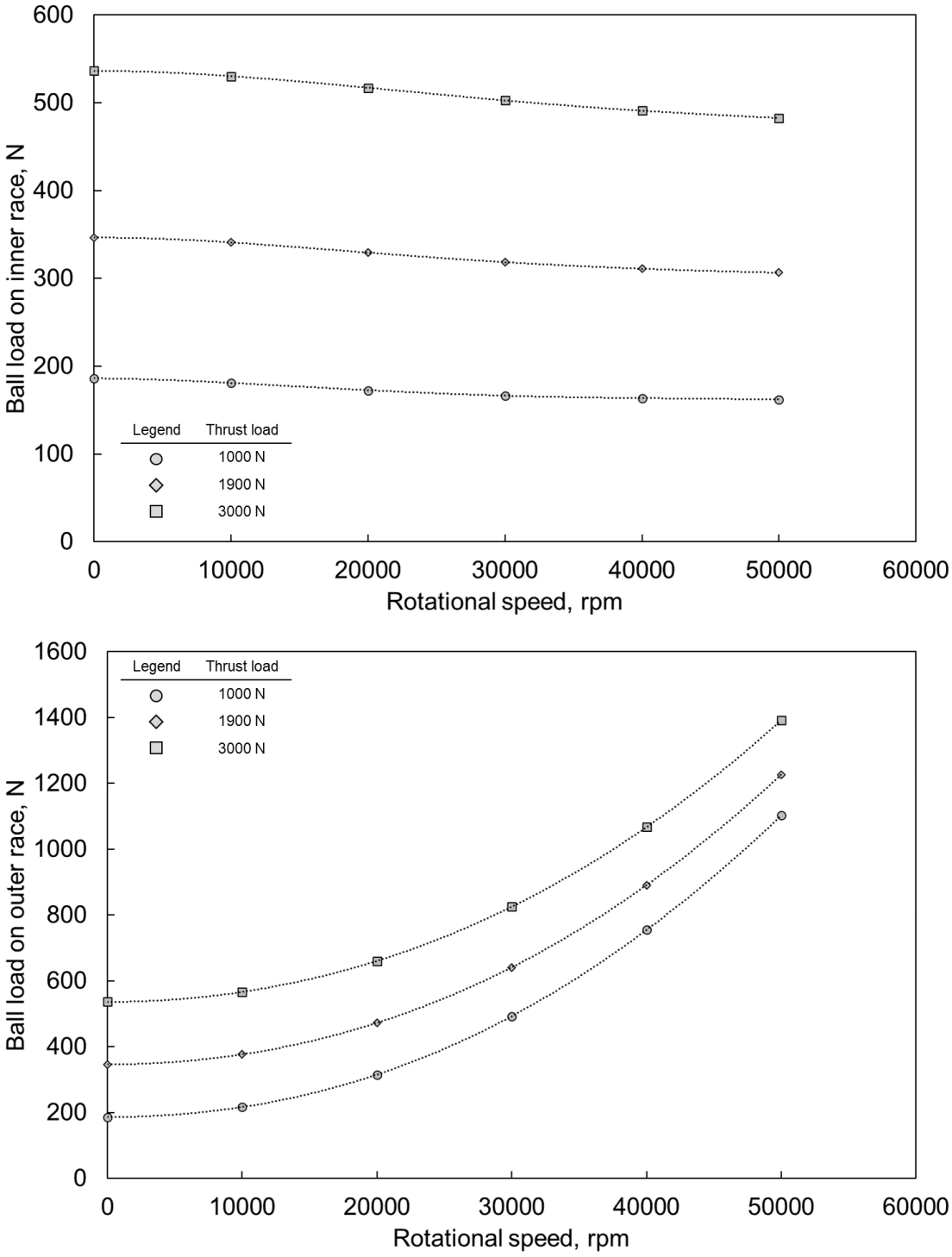

Fig. 17 (b) Ball load.

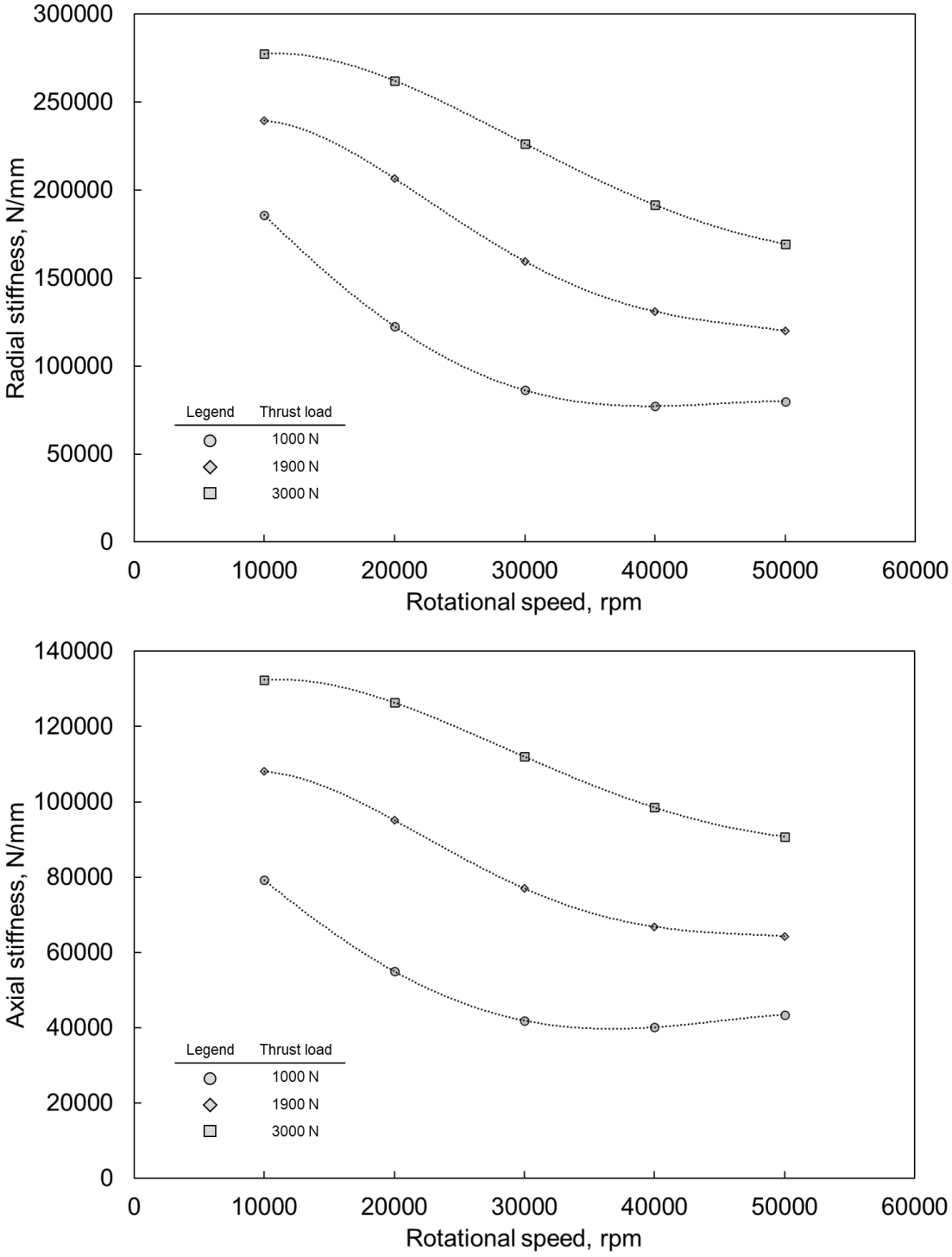

Fig. 17 (c) Bearing stiffness.

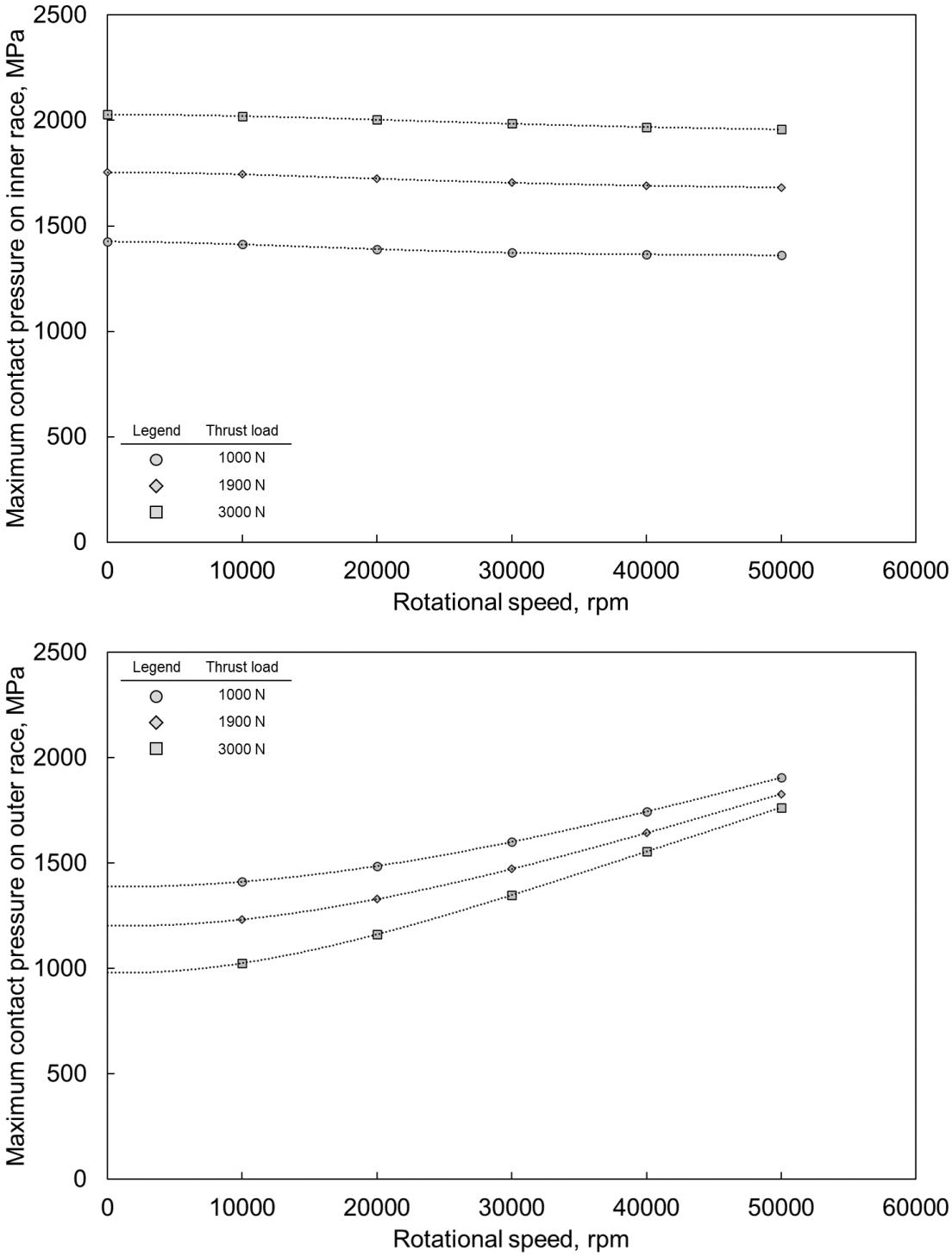

Fig. 17 (d) Maximum contact pressure of friction area between ball and raceway.

Fig. 17 Calculation results of Bearing Y with SUS440C balls as a function of rotational speed and thrust load.

2.4. Factors of heat generation in turbopump bearing

To clarify quantitatively the heat generation mechanism of cryogenic turbopump bearings, each significant factor needs to be modeled. The factors are classified as (A) friction heat generation on contact area in bearing elements and (B) fluid heat generation of coolant fluid flow due to rotational motion of bearing elements. These factors are shown in Fig. 18. (A) is composed of (a), (b), and (c) which are the friction heat generation of balls-race contacts, retainer-balls contacts, and outer race-retainer contacts. (B) is composed of (d), (e), and (f) which are fluid heat generation on surface of the inner race, the balls, and the retainer.

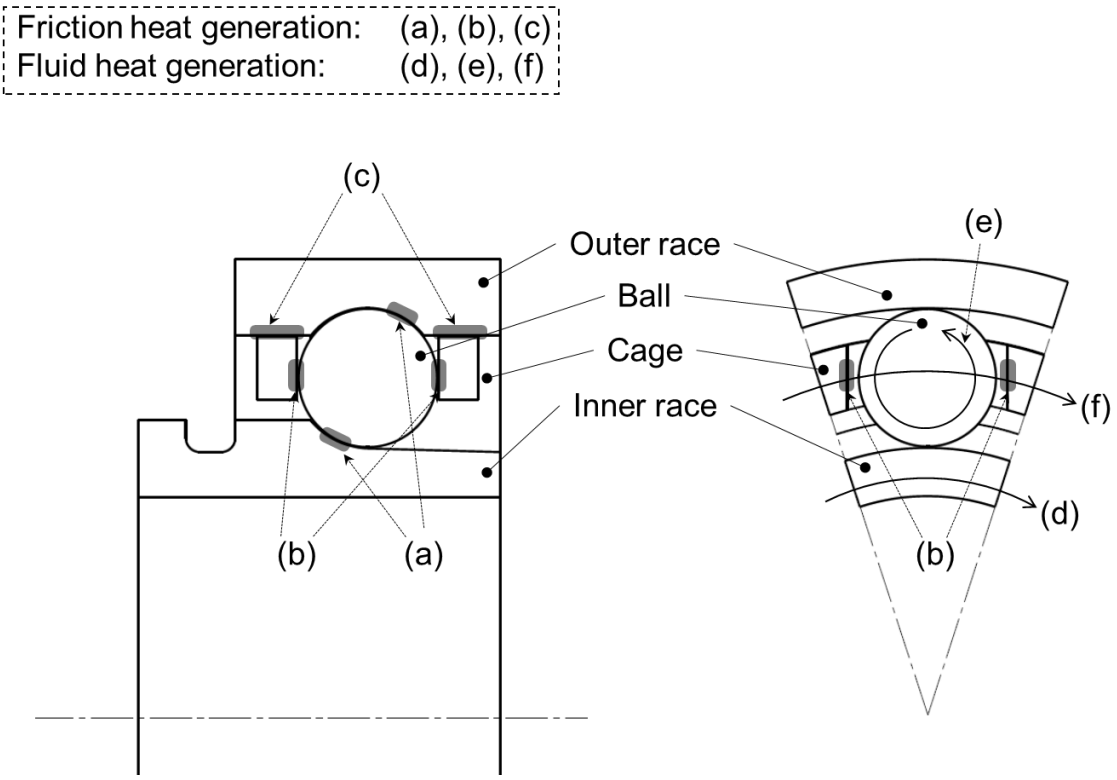

Fig. 18 Factors of heat generation in turbopump bearing.

2.4.1. Friction heat generation

In a ball bearing, shaft load is transferred from the inner race to balls and to the stationary outer race. Therefore, since the contact pressure of contact areas between balls and raceways would be the maximum in entire bearing elements, it is necessary to provide sufficient lubrication capabilities at the contact areas. An example of friction conditions in the contact area is shown in Fig. 19. The figure shows friction conditions of Bearing X inner race in 1000 N thrust load at 120,000 rpm. Based on Hertzian contact theory, the shape of the contact areas between spherical balls and curved surfaces of races is an ellipse that has pressure distribution. In addition, since there is a velocity distribution there, the contact is a rolling-sliding type. Therefore, the lubrication performance on the contact area significantly impacts the high-speed performance of the ball bearing. Considering the solid lubrication used for cryogenic turbopump bearings, temperature on the contact area significantly influences the strength of PTFE transfer film and the lubrication performance. Thus, it is important to understand accurately how much heat generation would be occurred at the contact areas.

The schematic of the balls-races contact area is shown in Fig. 20. The friction heat generation of this area is calculated from a surface integral of area ΔA at each arbitrary point (x, y). Heat generation at the balls-inner race contact, balls-outer race contact, and the sum of them are calculated as follows.

$$W_a(Inner\ race) = \sum_{n=1}^{N} \int \mu_n(x,y) \cdot P_n(x,y) \cdot v_n(x,y) dA_{n,Inner\ race} \tag{33}$$

$$W_a(Outer\ race) = \sum_{n=1}^{N} \int \mu_n(x,y) \cdot P_n(x,y) \cdot v_n(x,y) dA_{n,Outer\ race} \tag{34}$$

$$W_a = W_a(Inner\ race) + W_a(Outner\ race) \tag{35}$$

N is the number of balls, $P_n(x,y)$ is the contact pressure, $v_n(x,y)$ is relative velocity, $\mu_n(x,y)$ is the friction coefficient at the point (x,y), $A_{n,Inner\ race}$ is the contact area on the inner race, and $A_{n,Outer\ race}$ is the contact area on the outer race. Contact pressure, relative velocity, and contact area are calculated by the method described in section 2.3. The friction coefficient $\mu_n(x,y)$ of the balls-

races contact is an unknown factor that there has almost no research about. Therefore, the friction characteristic there was studied in detail in this study and shown in Chapter 5.

A retainer is used as a separator preventing a ball rotating at high speed from colliding with the other balls. In cryogenic ball bearings, the retainer also acts as a lubricant supplier. When radial force is loaded on a ball bearing, ball speed variation (BSV) occurs. Under such conditions, an excessive contact load would occur between a retainer and balls if the BSV is greater than a retainer's pocket gap against the balls [44]. Therefore, the gap of the test bearing is designed to be much larger than the BSV. A retainer contact on balls in the axial direction is shown in Fig. 18 (b) on the left side and in the circumferential direction as shown in Fig. 18 (b) on the right side. Since the axial gap is designed to be enough large to not contact the test bearing, contact in the axial direction is not considered in this study.

The heat generation at (b) is calculated as follows.

$$W_b = \sum_{n=1}^{N} \mu_b \cdot F_n \cdot v_n \tag{36}$$

μ_b is the friction coefficient of retainer-ball contact, F_n is the contact load and v_n is relative velocity. In the analysis, the contact of each ball with the retainer is not judged, and F_n is assumed to be the sum of normal forces on retainer-ball contact. The sum is assumed to be the fluid drag force loaded to the retainer considering the equilibrium of forces.

The test bearing retainer is guided by the inner surface of outer race. Considering that the retainer size could change due to thermal expansion and hoop stress expansion at operating conditions, the gap between the retainer and outer race is designed to be small during operation. When the retainer contact on the outer race is considered, the heat generation at (c) is calculated as follows.

$$W_c = \sum_{n=1}^{N} \mu_c \cdot F_c \cdot v_c \tag{37}$$

μ_c is the friction coefficient of the retainer-to-outer-race contact, F_c is the contact load and v_c is relative velocity.

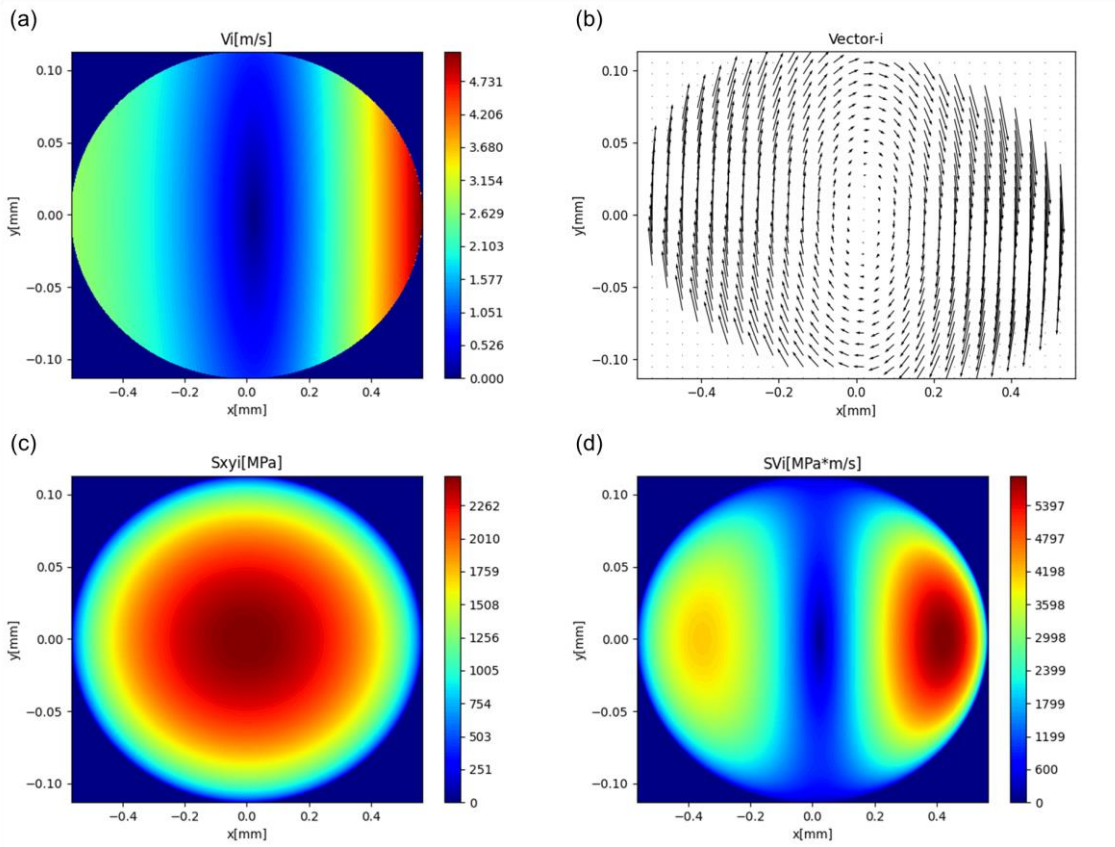

Fig. 19 Friction conditions in contact area of Bearing X inner race in 1000 N thrust load at 120,000 rpm. (a) Velocity distribution. (b) Velocity vector. (c) Contact pressure distribution. (d) SV value distribution.

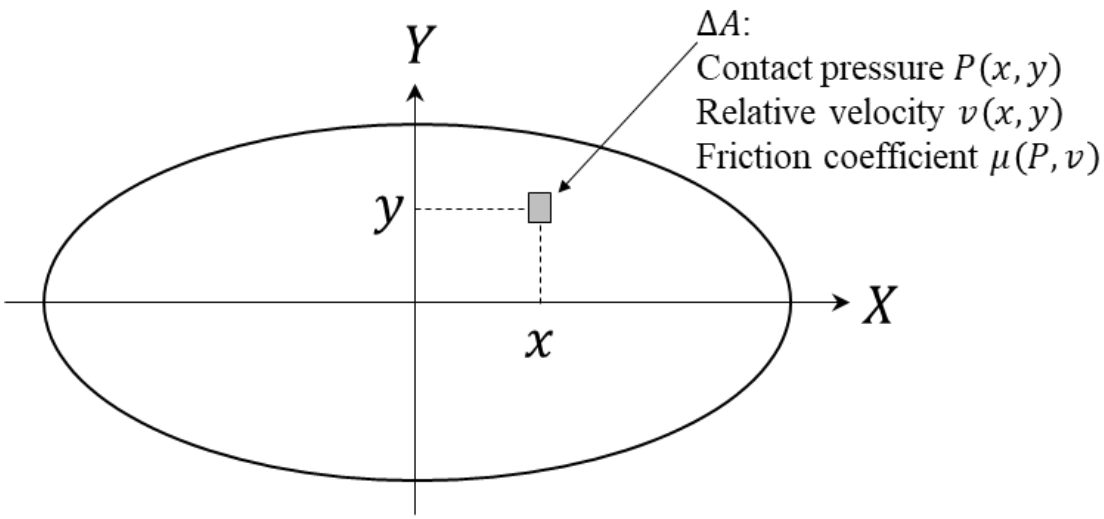

Fig. 20 Schematic of the ball-to-races contact area.

2.4.2. Fluid heat generation

Each element of an angular contact ball bearing rotates at each rotational velocity around each rotational axis. With a stationary outer race, the inner race rotates synchronously with the shaft rotation. The balls have complex motion where revolution around the shaft axis and rotation around the ball axis are synthesized. The retainer rotates synchronously with the balls' revolution motion. The rotational velocities of the bearing elements are shown in Fig. 21. The data were calculation results of Bearing Y with Si_3N_4 on the conditions of 1000 N thrust load. All velocities linearly increased with the rotational speed. The balls' rotational velocity was around 2.9 times faster than the shaft rotation because balls' diameter is significantly smaller than inner race. The retainer's rotational velocity was around 0.42 times the shaft rotation.

Cryogenic ball bearings rotate inside bearing coolant with such complex motion. Fluid friction heat is generated due to fluid drag caused by shear forces between moving elements' wall and surrounding fluid. The shear force depends on the relative velocity between the walls and the fluid. Since the bearing has complex motion with each element's velocity around their own rotation axes, it is significantly difficult to predict the fluid velocity and the fluid heat generation by using simple

equations. Therefore, fluid analysis with CFD was applied in this study. The results are shown in Chapter 4.

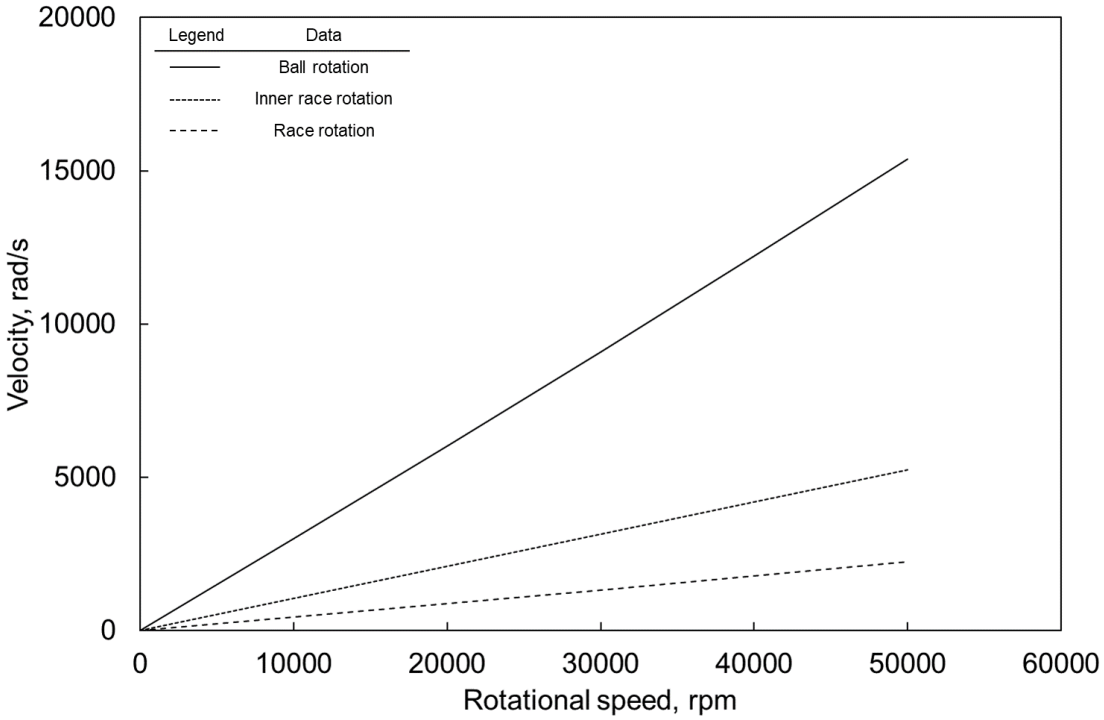

Fig. 21 Rotational velocities of each bearing element in Bearing Y with Si_3N_4 balls on the conditions of 1000 N thrust load.

2.5. Lubrication condition of race-ball contact

As described in section 1.3., it is considered that cryogenic propellants which are used as bearing coolant are not viscous enough to perform hydrodynamic lubrication in bearing contact areas. To verify this, film thickness of elastohydrodynamic lubrication (EHL) between race-ball contact area was calculated assuming that EHL is performed there. For the calculation of EHL film thickness, prediction equation proposed by Dowson and Higginson was used [45]:

$$\frac{h_{min}}{R_x} = 2.65G^{0.54}U^{0.7}W^{-0.13} \tag{38}$$

h_{min} is minimum lubricant gap, R_x is effective radius, G is material parameter in EHL calculation, U is velocity parameter in EHL calculation, W is load parameter in EHL calculation.

Calculation results of EHL film thickness is shown in Fig. 22. In all cases, the film thickness is much less than 110 nm which is surface roughness of the bearing contact area. Therefore, races and balls would contact directly without any lubrication film in the contact area. This calculation result quantitatively shows that cryogenic bearing coolant is not viscous enough to perform EHL.

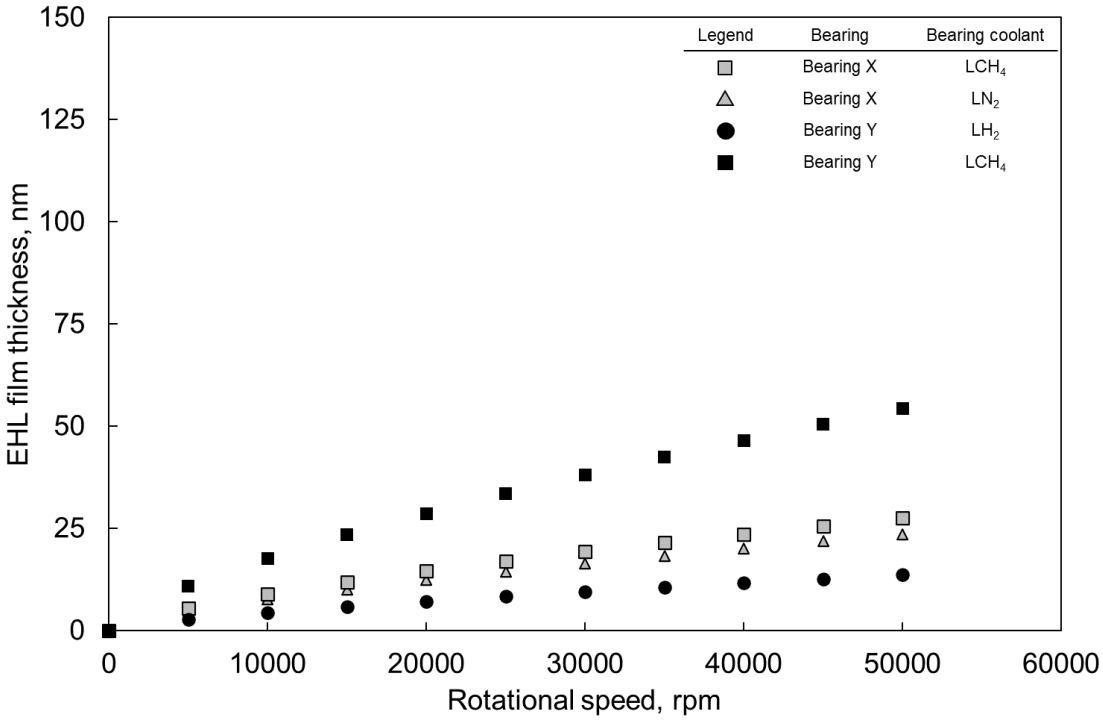

Fig. 22 EHL film thickness of Bearing X and Bearing Y.

2.6. Summary

Analytical method for calculation of bearing motion and factors of heat generation in cryogenic ball bearings were discussed in this chapter. The analytical method considered the influences of thermal expansion, centrifugal forces, and interference fitting which are unique characteristics of cryogenic

ball bearings. Calculation with Bearing X and Y were conducted on several conditions. The results indicated that the bearing performance and the bearing motion conditions such as bearing stiffness, contact angle, ball load, and SV value were significantly dependent on bearing geometry, thrust load, rotational speed, and ball material. Therefore, the bearings' parameters need to be designed for meeting demands of bearing performances, considering operating environment and conditions. Also, it is necessary to confirm that lubrication capability of the bearings is enough to operate the friction conditions which are determined by the bearing parameters and operating conditions. In addition, the quantitative information of the bearing motion is necessary for conducting theoretical calculation of bearing heat generation, and the accurate prediction of the bearing heat generation enables to set optimum operating conditions such as cooling flowrate of bearing coolant. Finally, the factors and mechanisms of the heat generation are introduced. For detail calculation of the friction heat generation, the friction characteristics of bearing material in operating conditions need to be clarified. It is also necessary to study the fluid flow characteristics of bearing coolant surrounding the bearing elements.

Chapter 3. Measurement of heat generation in cryogenic ball bearing

3.1. Introduction

Performances of elementary technologies composing a rocket engine system have been evaluated by conducting experimental testing under the same environment as rocket engines. This is because experimental data acquired in the operating conditions have been emphasized in rocket engine technologies to ensure enough reliability for launch capability and safety [2]. Therefore, it has been considered necessary to confirm that there is no problem after several tests at each phase of engine development such as elementary parts testing, component testing, sub-system testing and system testing conducted under more severe conditions than the actual ones in rocket engines. Also in Japan, significant technologies related to LOX/LH_2 rockets have been researched by conducting experimental testing to develop its flagship launch vehicles based on the philosophy described above [46-49]. Turbopump bearings have also been studied by acquiring data from several testing such as material tests, bearing tests, turbopump tests and engine tests. In research phase, the bearing performance is evaluated in detail by conducting bearing tests using bearing testers that can simulate the same environment as turbopumps. The bearing testers equip enough sensors to monitor the bearing data in detail and can acquire more data than turbopump tests and engine-system tests.

As described in Chapter 1, each space agency has researched bearing technologies although the public information has been limited. Because of these previous studies, a lot of knowledges have been acquired. However, most of these studies mainly focused on durability to be operated in actual turbopumps and engines, not on acquiring bearing data to construct a bearing performance model. This is why there has been little research case which contributes to clarifying heat generation of cryogenic turbopump bearings which is one of the most important design parameters.

Therefore, this research conducted experimental studies that focused on obtaining heat generation data parametrically to construct a model for heat generation in cryogenic turbopump bearings. The heat generation is considered to be strongly influenced by several conditions such as bearing load,

rotational speed, bearing coolant flowrate and physical properties of bearing coolant. In this research, bearing tests were conducted by changing these conditions as much as possible. Since this study aims to construct a detailed and precise quasi-steady modeling of the heat generation as the first step, steady state bearing data were accumulated on sufficiently static conditions to eliminate transitional influences. Finally, these data were evaluated parametrically and organized as a database for improving the cryogenic bearing model.

This chapter is organized as follows. In section 3.2, test results of Bearing X were explained. Experiments using Bearing Y were described in section 3.3 as well. Finally, influences of several factors on the heat generation were summarized in section 3.4.

3.2. Measurement of heat generation with a hybrid ceramic ball bearing of 25 mm inner diameter

3.2.1. Experiment P: LCH_4 and LN_2 environment

3.2.1.1. Test objective

In this test, a hybrid ceramic ball bearing of 25 mm inner diameter was evaluated to investigate the characteristics of its heat generation in LCH_4 and LN_2 environment. The bearing coolant was supplied in supercooled conditions from a pressurized tank to prevent from evaporating and perform enough cooling capabilities.

3.2.1.2. Test bearing (Bearing X)

Design parameters of the test bearing are shown in Table 1. The bearing is an angular contact ball bearing. The material of balls is Si_3N_4. It is a self-lubricating ball bearing with a retainer made of glass-cloth-PTFE laminate [10].

3.2.1.3. Bearing tester

The bearing tester is shown in Fig. 23. The tester can simulate the same environment for the test bearing and the shaft seals as in rocket engine turbopumps. The main shaft was supported by two bearings loaded by disk springs and rotated by an electrical motor which was controlled by an inverter. The coolant was supplied from a pressurized tank into the tester and flowed through the two bearings then drained out of the tester. Shaft seals were set outside bearings to prevent leakage of the bearing coolant from its main flow. A bellows mechanical seal was set at the upstream of the test bearing and a kind of non-contacting mechanical face seals [50, 51] which perform dynamic seal by lifting off the rotor surface to a few micro-meters gap in rotating conditions and have no thermodynamic impact on the bearing coolant. The flowrate was controlled by using a control valve set in the downstream of the drain line.

Temperature and pressure of the bearing coolant were measured at the upstream and downstream of the test bearing. The coolant temperature and pressure are indicated as T_0 and P_0 upstream of the test bearing and T_1 and P_1 downstream of the test bearing, respectively. Temperature was measured by using Type T thermocouples which perform high sensitivity and linearity in LCH_4 and LN_2 environment. Pressure was measured by using pressure transducers set outside of the tester at room temperature, which were connected to the measurement point by pipes. The flow rate of the bearing coolant was measured using a turbine flowmeter set in supply system of the coolant.

Heat generation of the rotating bearing was calculated by Equation (39). In this study, energy increase of the coolant flowing through a bearing was defined as the bearing heat generation.

$$W_{ex} = (H_1 - H_0) \cdot \dot{m}_f \tag{39}$$

H_0 is specific enthalpy of the coolant upstream of the test bearing, H_1 is specific enthalpy of the coolant downstream of the test bearing, and $\dot{m}_f$ is the mass flow rate of the coolant. The specific enthalpy was calculated from the measurement data of T_0, P_0, T_1, and P_1 by REFPROP [52].

Measurement uncertainty is described as follows. Accuracy of the temperature sensors used in the experiments was within ± 0.5 K of the measured temperature. However, the sensors were calibrated by using LN_2 which is cryogenic fluid as well as the bearing coolant. The accuracy of the calibrated sensors was within 0.07 K at LN_2 saturated temperature of the atmospheric pressure. Since the differential temperature of the bearing coolant between the upstream and downstream was around 2.0 K, the error of the temperature sensors was about 3.5 % of measured differential temperature which is the most influential factor for the bearing heat generation. Regarding accuracy of the pressure sensors, the nonlinearity, hysteresis, and repeatability was within ± 0.01 MPa, ± 0.01 MPa, and ± 0.005 MPa which corresponded to less than 2.0 % of the coolant pressure. Accuracy of the turbine flowmeter which was calibrated by using LN_2 was within ± 0.0022 L/s which corresponded to less than 0.7 % of the coolant flowrate.

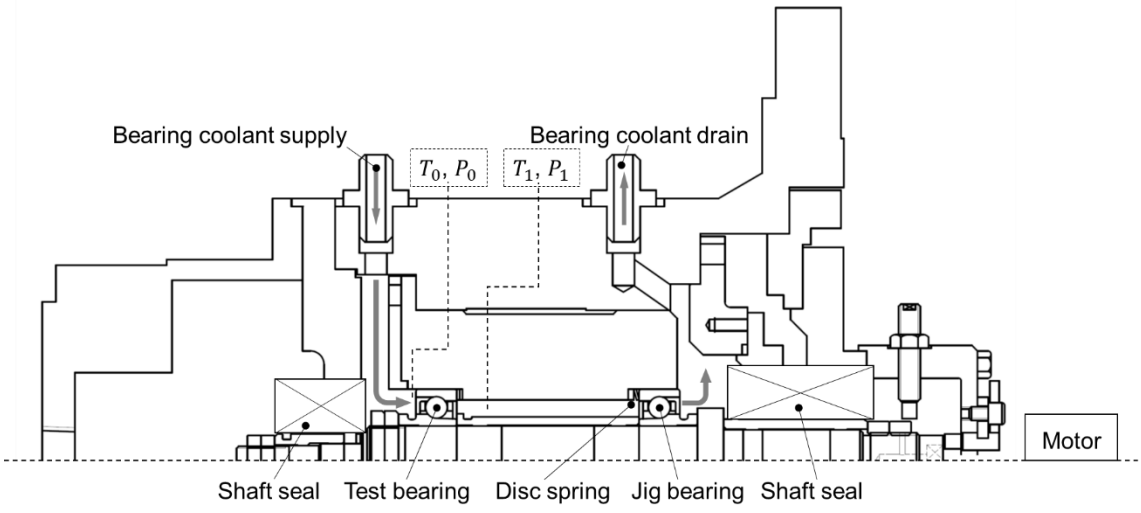

Fig. 23 Bearing tester for evaluating Bearing X in LCH_4 and LN_2 environment.

3.2.1.4. Test conditions

The test conditions are summarized in Table 4. Bearing tests were conducted by changing the rotational speed as a main test parameter. The maximum rotational speed in each coolant environment

was set by the limitation of motor power.

A typical test sequence is shown in Fig. 24 with variations in rotational speed, temperature, pressure, and mass flowrate as a function of time. Several conditions were arranged to meet desired test conditions at lower rotational speed, and then the shaft speed was raised step by step. At each rotational speed, the speed was kept constant to stabilize all conditions such as temperature and flowrate. Time-averaged data for more than 5 s where all conditions were stabilized were used for evaluation. One test sequence took around 1000 s. Several tests were conducted under different conditions to acquire stable condition data. Before the bearing tests, the bearing coolant was fed into the bearing tester to precool it until the tester filled with the coolant, which was confirmed by monitoring temperature data inside the tester.

Table 4 Test conditions of Experiment P.

Parameter	Value	
Coolant	LCH_4	LN_2
Coolant pressure	1.16 ~ 1.60 MPa	1.03 ~ 1.15 MPa
Coolant inlet temperature	120.2 ~ 121.7 K	95.3 ~ 96.5 K
Coolant flow rate	0.129 ~ 0.154 kg/s	0.300 ~ 0.330 kg/s
Rotational speed	15203 ~ 51787 rpm	19917 ~ 40222 rpm
Thrust load	1000 N	1000 N

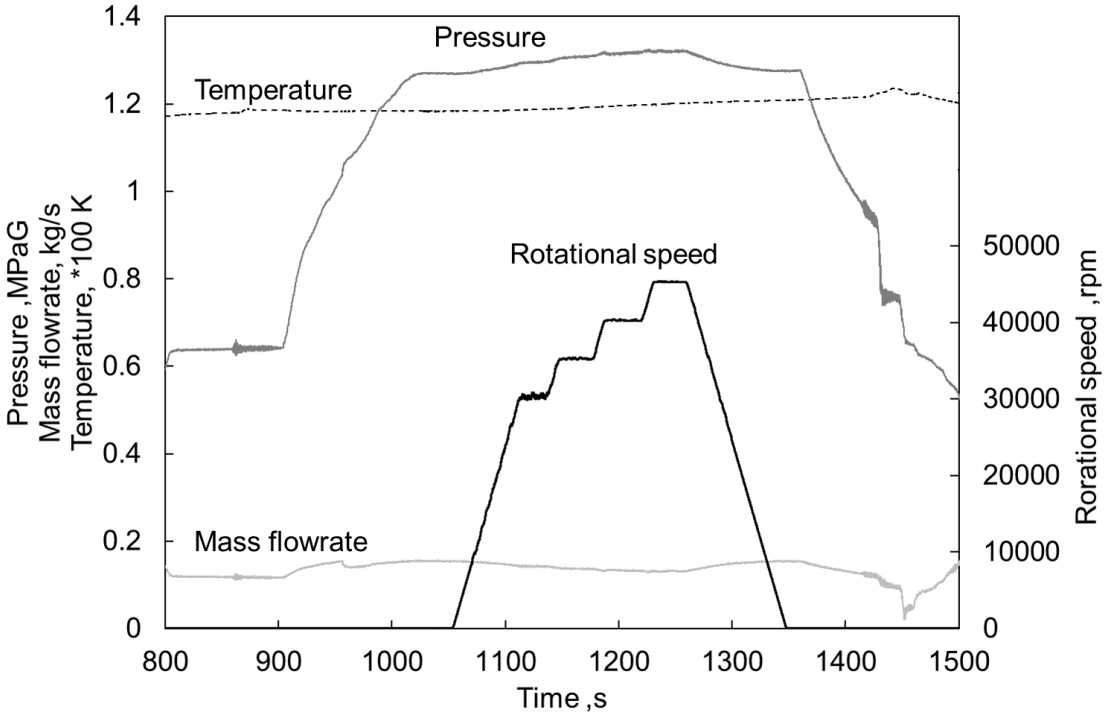

Fig. 24 Typical test sequence of LCH_4 experiments showing variation in rotational speed, temperature, pressure, and flow rate as a function of time.

3.2.1.5. Test results

Heat generation data in LCH_4 and LN_2 experiments are shown in Fig. 25. The plots show the experimental data, and the lines indicate regression curves of the plots. In both conditions of coolants, the heat generation exponentially increased with the rotational speed. This tendency on the speed is caused by the characteristics of the heat source factors described in Chapter 2. The factors are composed of friction heat generation and fluid heat generation, and both increase with the rotational speed, considering their mechanisms.

In comparison between LCH_4 and LN_2, increase of the heat generation with the rotational speed was clearly lager in LN_2 than in LCH_4. For example, the heat generation at 40000 rpm was 1381 W in LN_2 and 1110 W in LCH_4, which indicates definite difference at the same rotational speed. As described in

section 3.2, the friction heat generation at the same rotational speed should be the same regardless of the coolant, considering the mechanism. In this test results, the friction heat generation at 40000 rpm in both environments was less than 1110 W in LCH_4 environment which included both the friction heat generation and the fluid heat generation. The 271 W of differential heat generation should be caused by the characteristics of fluid heat generation due to the difference of the fluid properties. For instance, the density of the operating condition was 409.9 kg/m^3 for LCH_4 at 120.9 K and 1.32 MPa and 720.4 kg/m^3 for LN_2 at 95.1 K and 1.03 MPa, respectively. Since the difference of the heat generation between LCH_4 and LN_2 with the rotational speed, the fluid generation would account for much larger portion of the entire heat generation in higher speed conditions.

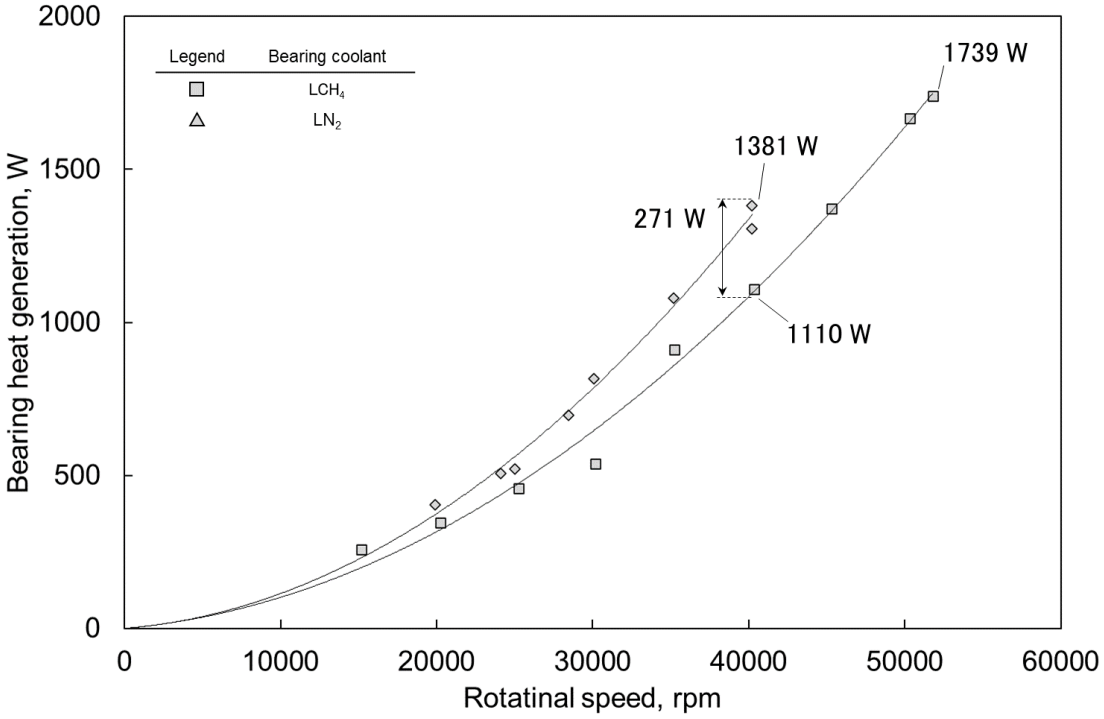

Fig. 25 Heat generation of Bearing X in Experiment P as a function of rotational speed.

3.2.2. Summary of the heat generation in hybrid ceramic ball bearing of 25 mm inner diameter

In all environments, the heat generation increased with the rotational speed. Comparing between the coolant types, heat generation in LN_2 environment were larger than LCH_4 environment since the gradients to the rotational speed were dependent on the environment and larger in LN_2. Comparing heat generation at the same rotational speed condition by using the regression curves, the heat generation data in LCH_4 and LN_2 are 316 W and 374 W at 20000 rpm, and 1638 W and 2041 W at 50000 rpm. This indicates that the differences between the coolant types become larger in higher-speed conditions. Considering the mechanisms of the heat generation, the differences should be caused by the fluid heat generation since the friction heat generation would be almost the same value regardless of the environment. As stated above, the differences of fluid heat generation are caused by the differences of fluid properties such as density and viscosity. Each density and viscosity of the coolants at the operating conditions are 724.1 kg/m^3 and 90.7 μPa-s for LN_2 and 410.0 kg/m^3 and 98.8 μPa-s for LCH_4. Although the densities are much different in the environments, the viscosity of LN_2 is cloth to LCH_4.

The relationship between the heat generation estimated with the regression curves and the density is shown in Fig. 26. The heat generation has positive correlation with the density. The bearings are immersed in coolant while rotating, which contribute to improving the coolant's kinetic energy in the vicinity of the rotating bearing. In higher density environment, the kinetic energy improved by the rotating bearing would be larger, which results in larger fluid heat generation. The relationship between the heat generation estimated with the regression curves and the viscosity is shown in Fig. 26. Comparing between LN_2 and LCH_4, the heat generation in LN_2 were larger even though the viscosity is smaller. It indicates that the heat generation is dependent on the other parameter beside viscosity, which led to larger heat generation in LN_2 that is less viscous. In this case, the influence of density

which is described above could be much more than that of viscosity. From the above, it is significantly difficult to predict in simple relationship with fluid properties. For high-fidelity modeling of bearing heat generation, the influences of fluid properties need to be considered in detail.

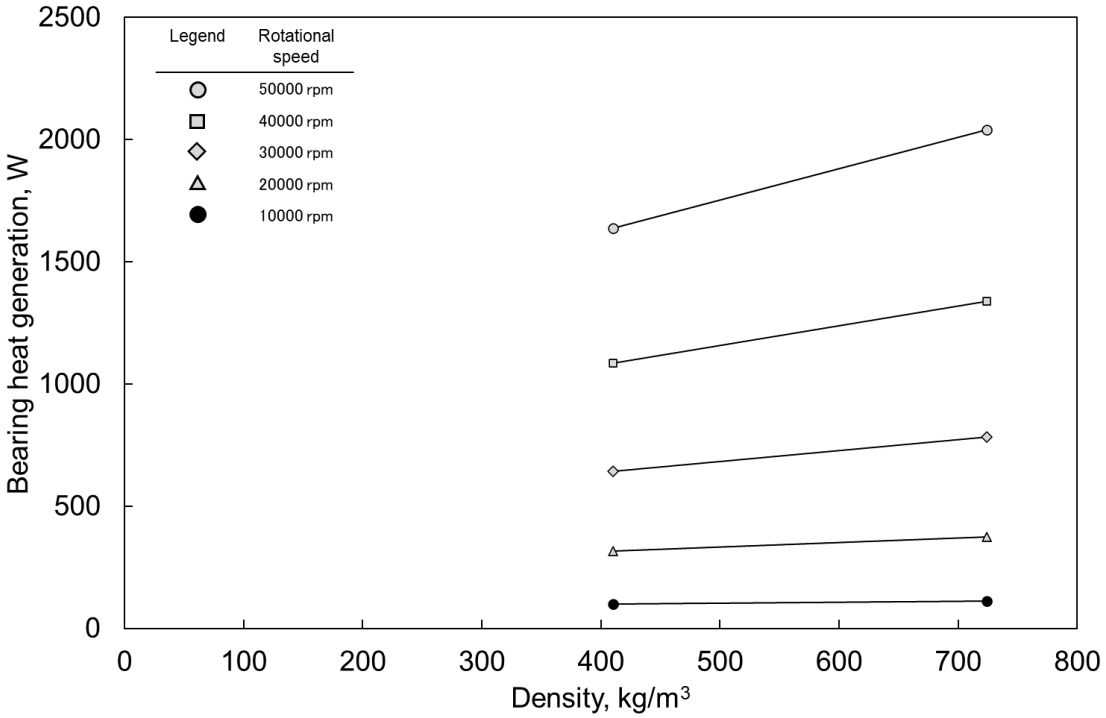

Fig. 26 Heat generation of Bearing X in Experiment P as a function of density.

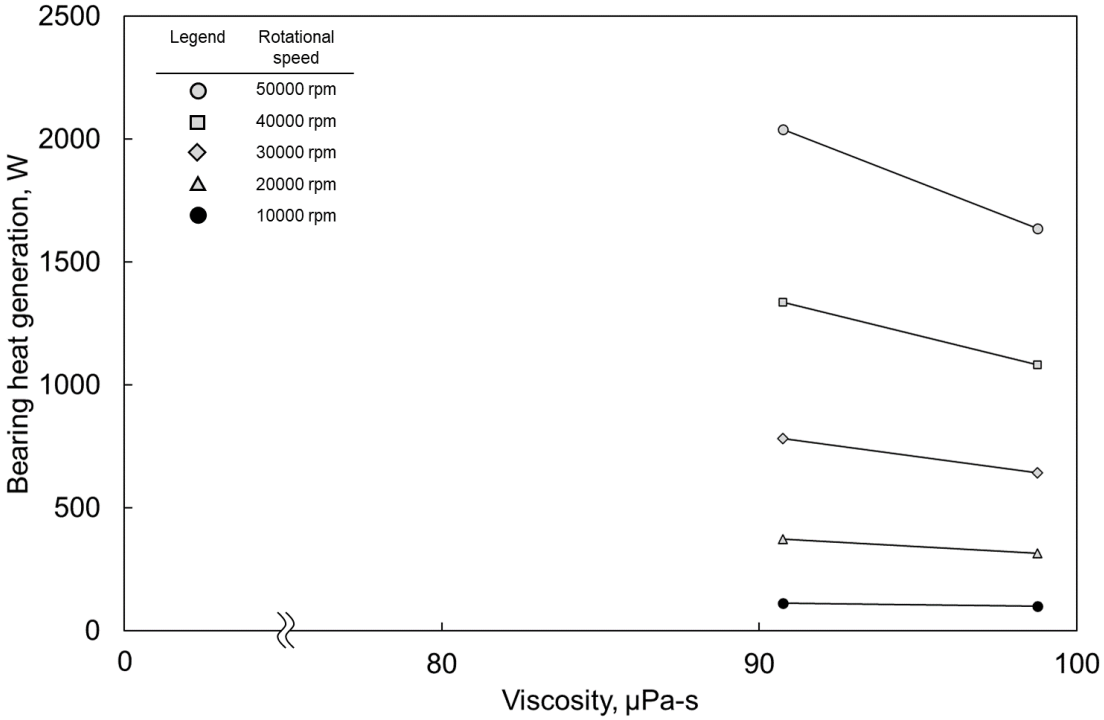

Fig. 27 Heat generation of Bearing X in Experiment P as a function of viscosity.

3.3. Measurement of heat generation with hybrid ceramic ball bearing of 45 mm inner diameter

3.3.1. Experiment Q: LCH_4 and LH_2 environment

3.3.1.1. Test objective

In this test, a hybrid ceramic ball bearing of 45 mm inner diameter was evaluated to investigate characteristics of its heat generation in LCH_4 and LH_2 environment. The bearing coolant was supplied in supercooled conditions from a pressurized tank to prevent from evaporating and perform enough cooling capabilities.

3.3.1.2. Test bearing (Bearing Y)

Design parameters of the test bearing are shown in Table 1. The bearing is an angular ball bearing.

The material of balls is Si_3N_4. It is a self-lubricating ball bearing with a retainer made of glass-cloth-PTFE laminate [10].

3.3.1.3. Bearing tester

Bearing tester is shown in Fig. 28. Structure of the tester is almost the same as tester used in Experiment P that is shown in Fig. 22. The only thing different is the shaft diameter.

Temperature was measured in LH_2 experiments using chromel-gold/iron alloy thermocouples which perform high sensitivity and linearity in cryogenic environment. Type T thermocouples whose measurement range include LN_2 temperature (around 77K) were used for LCH_4 experiments.

The evaluation method of heat generation in the test bearing and the measurement uncertainty are the same as described in section 3.2.1.3.

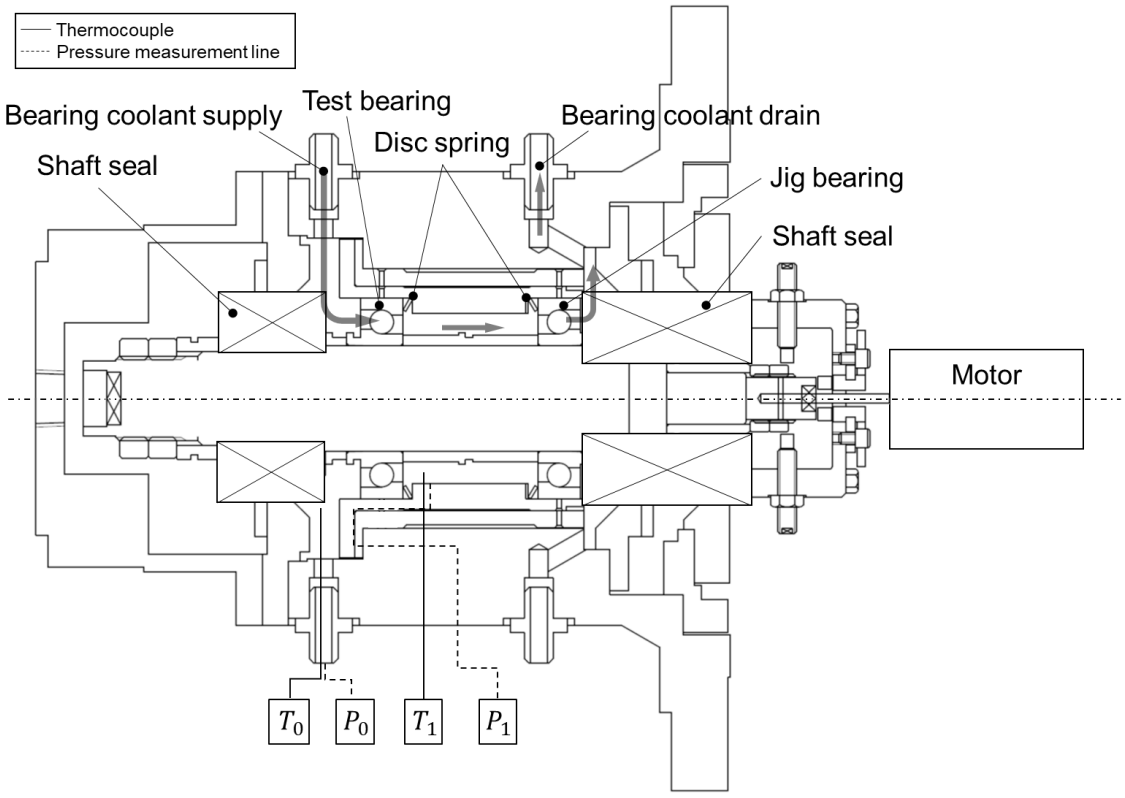

Fig. 28 Bearing tester for evaluating Bearing Y in LCH_4 and LH_2 environment.

3.3.1.4. Test conditions

The test conditions are summarized in Table 5. Bearing tests were conducted by changing the rotational speed as a main test parameter. The maximum rotational speed in each coolant environment was set by the limitation of motor power.

A typical test sequence is shown in Fig. 29 with variations in rotational speed, temperature, pressure, and mass flowrate as a function of time. Test conditions were arranged to meet desired test conditions at lower rotational speed, and then the shaft speed was raised step by step. At each rotational speed, the speed was kept constant to stabilize all conditions such as temperature and flowrate. Time-averaged data for more than 5 s where all conditions were stabilized were used for evaluation in this study. One test sequence took around 1000 s. Several tests were conducted under different conditions to acquire stable condition data. Before the bearing tests, the bearing coolant was fed into the bearing tester to precool it until the tester filled with the coolant, which was confirmed by monitoring temperature data inside the tester.

Table 5 Test conditions of Experiment Q.

Parameter	Value	
Coolant	LCH_4	LH_2
Coolant pressure	1.11 ~ 2.15 MPa	0.63 ~ 2.11 MPa
Coolant inlet temperature	117.6 ~ 122.6 K	26.3 ~ 30.2 K
Coolant flow rate	0.232 ~ 0.268 kg/s	0.0371 ~ 0.0575 kg/s
Rotational speed	10136 ~ 25195 rpm	4552 ~ 35155 rpm
Thrust load	1000 N	1000 N

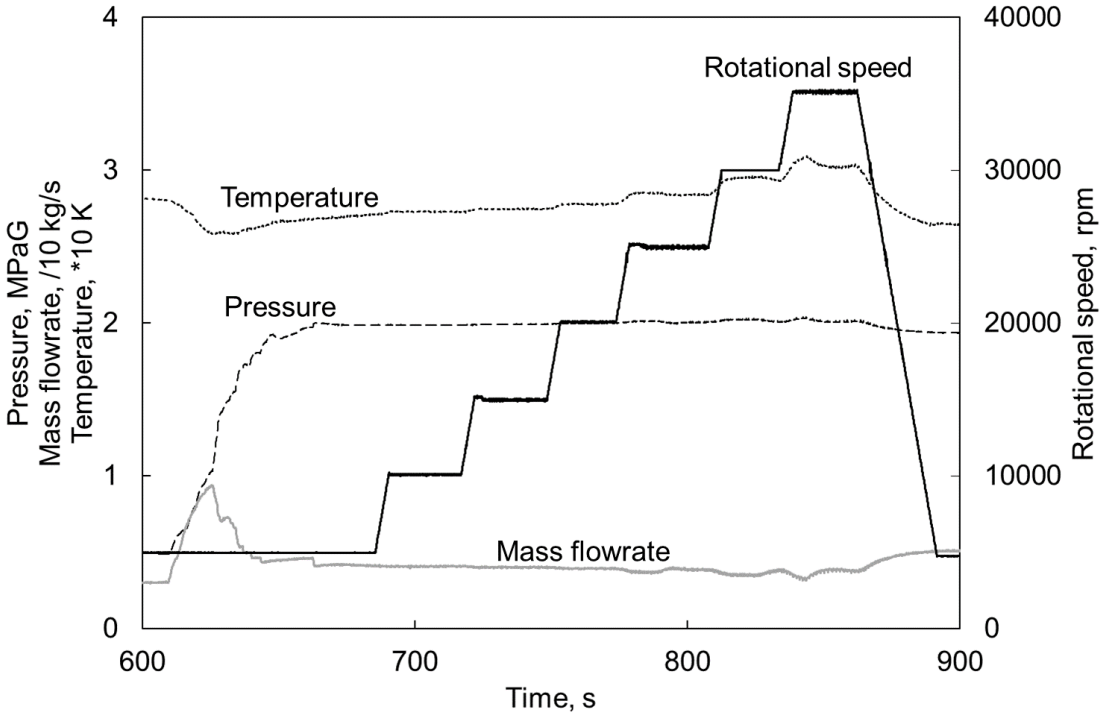

Fig. 29 Typical test sequence of Experiment Q showing variation in rotational speed, temperature, pressure, and flow rate as a function of time.

3.3.1.5. Test results

Heat generation data in LCH_4 and LH_2 experiments are shown in Fig. 30. In both conditions of coolants, the heat generation exponentially increased with the rotational speed. This tendency on the speed is caused by the characteristics of the heat source factors described in Chapter 2. They are composed of friction heat generation and fluid heat generation, and both increase with the rotational speed, considering their mechanisms.

In comparison between LCH_4 and LH_2, increase of the heat generation with the rotational speed was much larger in LCH_4 than in LH_2. For example, the heat generation at 25000 rpm was 1572 W in LCH_4 and 563 W in LH_2, which indicates around 2.79 times difference at the same rotational speed. The friction heat generation at the same rotational speed should be the same regardless of the coolant,

considering the mechanism. In this test results, the friction heat generation at 25000 rpm should be less than 563 W in LH_2 environment which included both the friction heat generation and the fluid heat generation. Since the friction heat generation in LCH_4 environment should be also less than 563 W as well, the fluid heat generation would be more than 1009 W which contributes to more than 64.2 % of the entire heat generation. Furthermore, since the difference of the heat generation between LH_2 and LCH_4 exponentially increased with the rotational speed, the fluid generation would account for much larger percentage of the entire heat generation in higher speed conditions. Therefore, these results indicate that it is much significant to precisely predict the fluid heat generation.

The difference induced by coolant type could be explained by the characteristics of fluid heat generation that should be influenced by fluid properties such as density and viscosity as described in section 3.2. For instance, the density of the operating condition was 414.3 kg/m^3 for LCH_4 at 117.8 K and 1.11 MPa and 63.0 kg/m^3 for LH_2 at 26.4 K and 0.63 MPa, respectively. This indicates that the density of LCH_4 is around 6.58 times as much as LH_2 and their fluid properties are significantly different, which could result in difference of heat generation between coolant types.

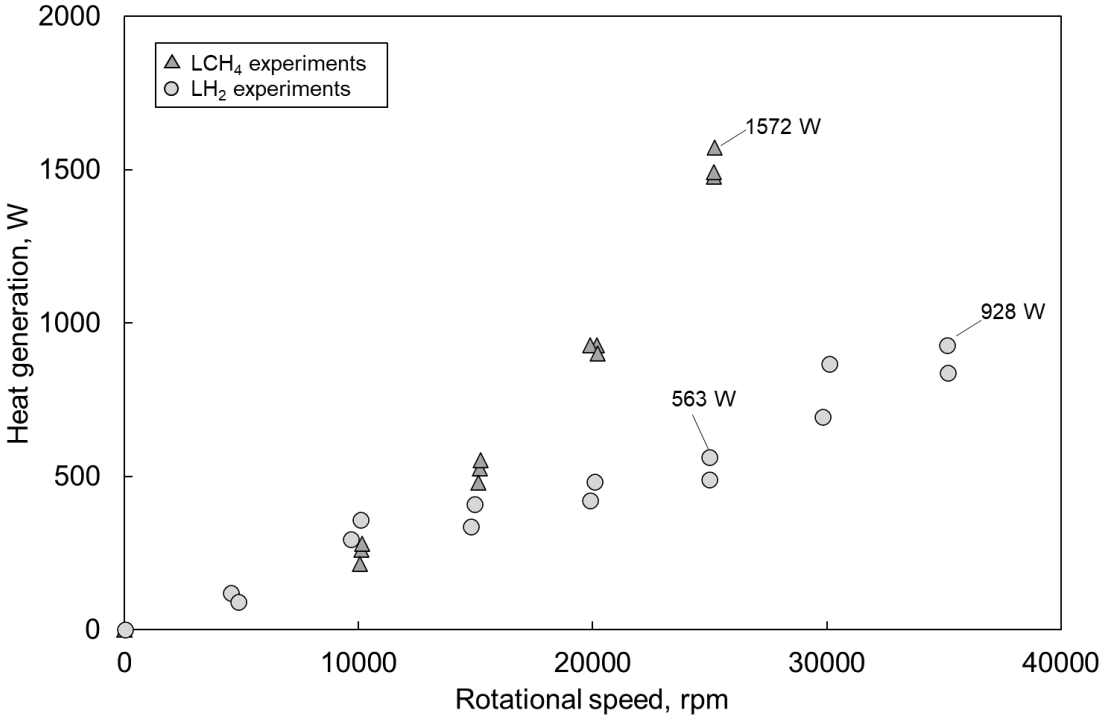

Fig. 30 Heat generation of Bearing Y in Experiment Q as a function of rotational speed.

3.3.2. Experiment R: High-temperature and high-pressure hydrogen environment (warmed and pressurized LH_2)

3.3.2.1. Test objective

In this test, a hybrid ceramic ball bearing of 45 mm inner diameter was evaluated to investigate the characteristics of its heat generation in high-temperature and high-pressure hydrogen environment which was supercritical condition because turbopump bearings are operated in such condition. This is because temperature and pressure of bearing coolant that is bled from main propellant flow pumped by an impeller are usually larger than LH_2 which is in supercooled or saturated state as stored in propellant tanks since the total energy of the fluid is extensively gained by the impeller rotation. In such supercritical condition, the property of hydrogen is easy to significantly change with temperature and pressure. As described above, it is apparent that the property of bearing coolant has significant

influences on heat generation. Therefore, in this bearing test, influences of bearing coolant property on bearing heat generation in hydrogen were investigated by changing the coolant's temperature and pressure.

3.3.2.2. Test bearing

The same bearing as described in section 3.2.1.2 was used in this test.

3.3.2.3. Bearing tester

The same bearing tester as described in section 3.3.1.3 was used in this test as well. Pressure of the bearing coolant was controlled by changing pressurizing gas pressure of a storage tank for the coolant. Temperature of the coolant was increased by a heat exchanger set in the supply line of the bearing coolant.

3.3.2.4. Test conditions

Test conditions are summarized in Table 6. Bearing tests were conducted by changing the coolant temperature and pressure in addition to the rotational speed. The bearing thrust load by the disc springs was larger than Experiment Q to investigate the influence of the load on the heat generation. The coolant pressure and temperature were much higher than Experiment Q. In addition, their ranges were much wider to change extensively the coolant properties such as density and viscosity. Color maps indicating the phase diagram of hydrogen, the test conditions, and the fluid properties are shown in Fig. 31. The maps show that the fluid properties substantially changed between test cases due to large variation of the fluid temperature and pressure.

A typical test sequence is shown in Fig. 32 with variations in rotational speed, temperature, pressure, and mass flowrate as a function of time. Several conditions were arranged to meet desired test

conditions at lower rotational speed, and then the shaft speed was raised step by step. At each rotational speed, the speed was kept constant to stabilize all conditions such as temperature, pressure, and flowrate. Time-averaged data for more than 5 s where all conditions were stabilized were used for evaluation in this study. One test sequence took around 800 s, and several tests were conducted under different conditions to acquire stable condition data. Before the bearing tests, the bearing coolant was fed into the bearing tester to precool it until the tester filled with the coolant, which was confirmed by monitoring temperature data inside the tester.

Table 6 Test conditions of Experiment R.

Parameter	Value
Coolant	LH_2
Coolant pressure	1.06 ~ 3.61 MPa
Coolant inlet temperature	30.5 ~ 46.6 K
Coolant flow rate	0.0184 ~ 0.0685 kg/s
Rotational speed	12700 ~ 46300 rpm
Thrust load	1900 N

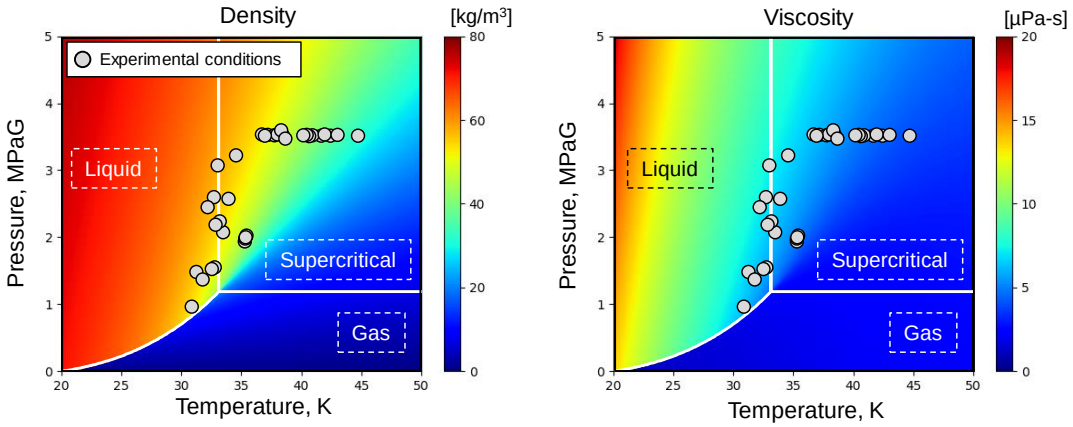

Fig. 31 Color maps of density and viscosity with plots indicating experimental conditions.

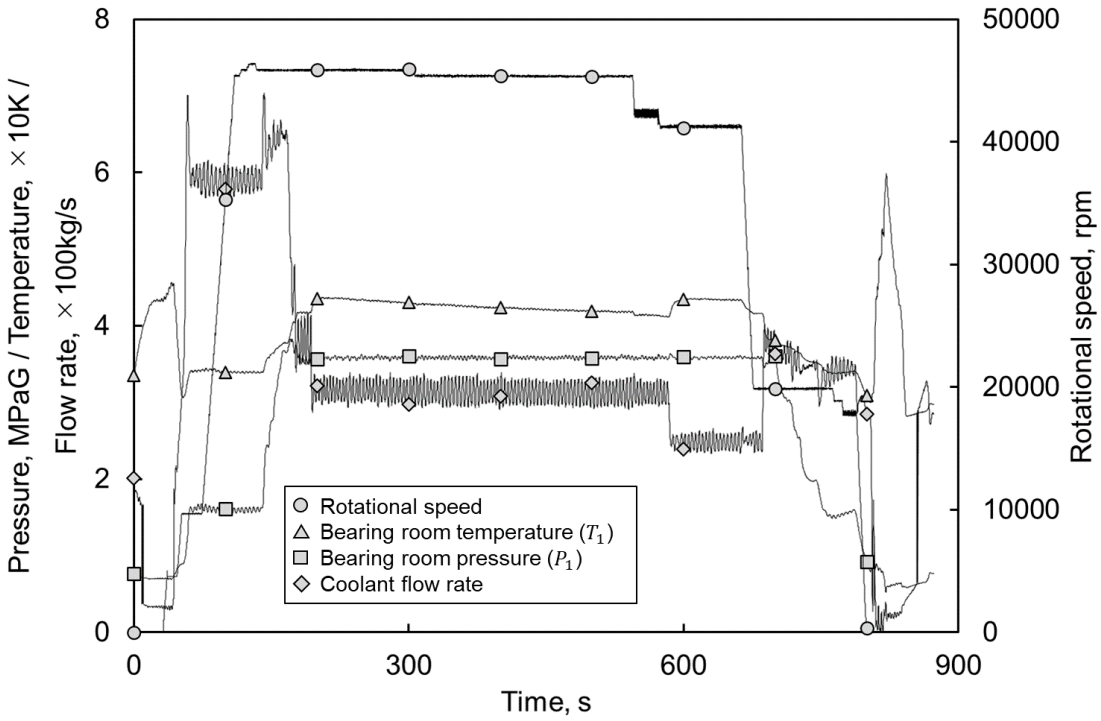

Fig. 32 Typical test sequence Bearing Y in Experiment R showing variation in rotational speed, temperature, pressure, and flow rate as a function of time.

3.3.2.5. Test results

Heat generation data in high-temperature and high-pressure hydrogen experiments are shown in Fig.

33. The heat generation increased with the rotational speed to the maximum value of 3149 W at 46000 rpm. This tendency on the speed can be explained by the characteristics of the heat source factors as well as the results of Experiment Q. However, these test results were different with Experiment Q in terms of the larger differences of the heat generation at the same rotational speed that was 905 W at 46000 rpm and 776 W at 42000 rpm. Such differences should be caused by factors other than rotational speed conditions. In this test, the heat generation was evaluated by changing the coolant's fluid properties that were controlled by conditions of fluid temperature and pressure. Therefore, the test results implies that the differences of the bearing heat generation were caused by the change of the fluid properties.

Relationships of the heat generation with the density and the viscosity which are possible factors to influence on the heat generation are shown in Fig. 34 and Fig. 35. It is apparent that these figures show the definite correlation between these fluid properties and the heat generation and that the heat generation increased with these properties. Moreover, the slope is larger in high-speed conditions. This indicates that the influences of the properties' changes had more significant impacts on the heat generation in high-speed conditions. This characteristic was confirmed in Experiment Q. In this test, the fluid properties were controlled by warming and pressurizing LH_2. Since the density and viscosity change at the same time in such operation, the most critical parameter for the bearing heat generation cannot be distinguished only by this test. However, at least it is apparent that the fluid heat generation caused by fluid friction force due to shear force between moving wall and fluid changed with the fluid properties, considering the mechanisms of the heat generation. From the above, the clarification of mechanisms on the fluid heat generation and the precise prediction are important for construction of the model on the bearing heat generation.

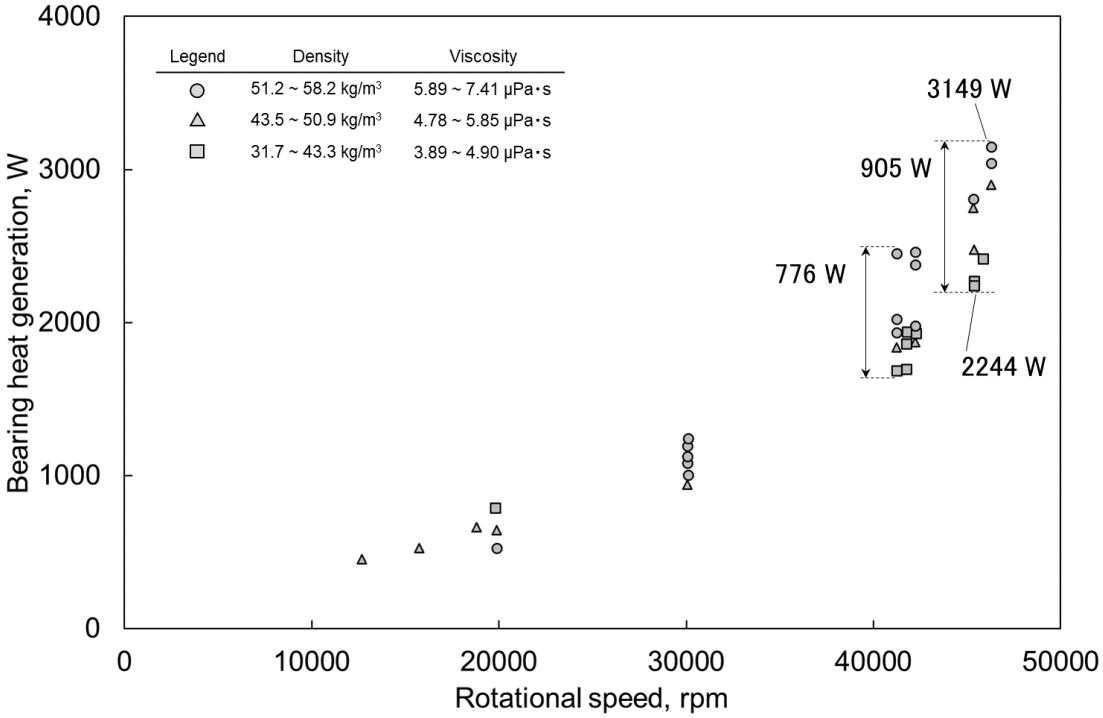

Fig. 33 Heat generation Bearing Y in Experiment R as a function of rotational speed.

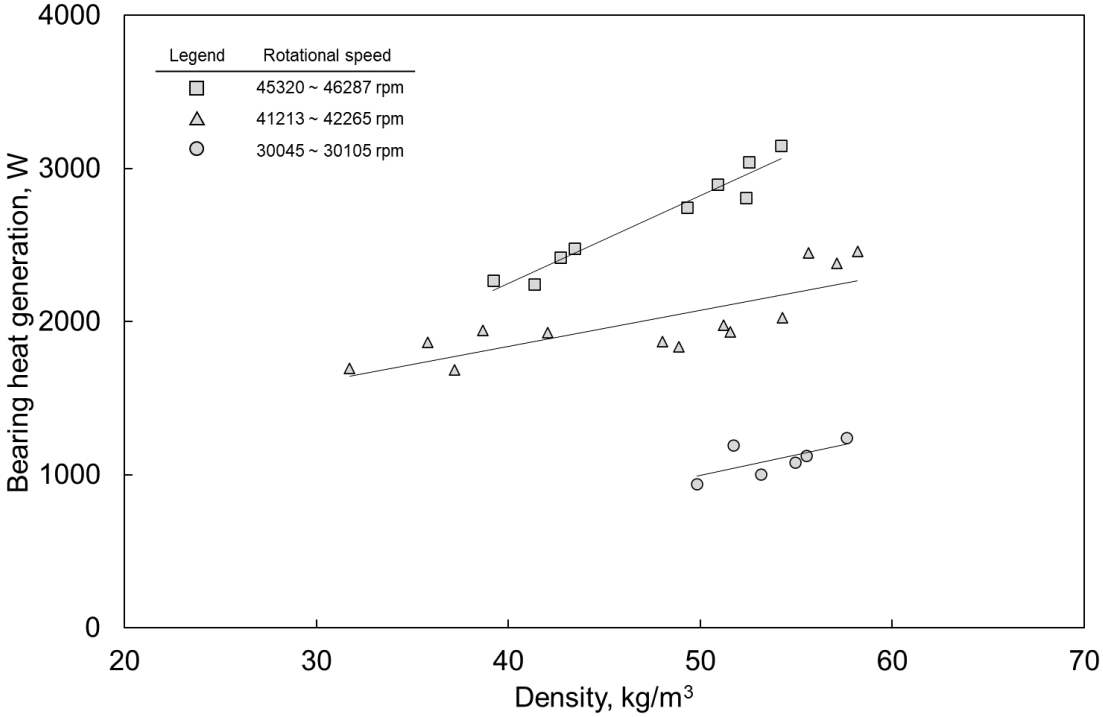

Fig. 34 Heat generation Bearing Y in Experiment R as a function of the fluid density.

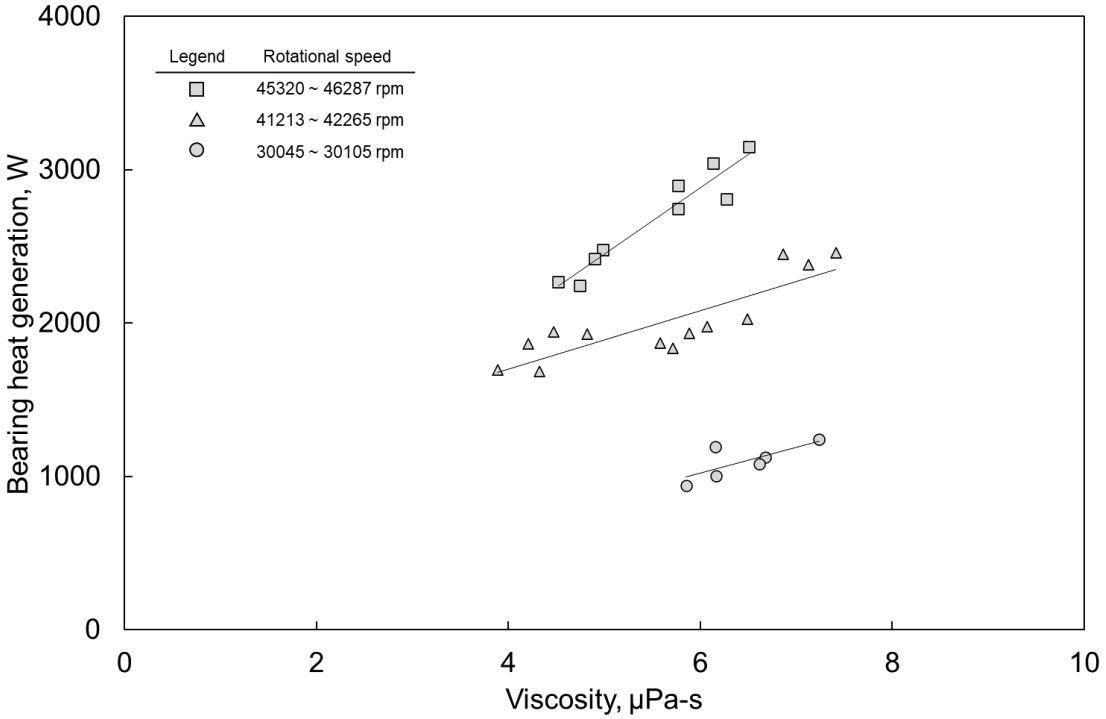

Fig. 35 Heat generation of Bearing Y in Experiment R as a function of the fluid viscosity.

3.3.3. Summary of the heat generation in hybrid ceramic ball bearing of 45 mm inner diameter

The summary of heat generation data measured by using Bearing Y is shown in Fig. 36. As described above, each heat generation exponentially increased with the rotational speed regardless of the other conditions such as the coolant fluid, the fluid properties, and the thrust load. For hydrogen environment, the heat generation data measured in Experiment R was larger than Experiment Q. This is because the friction heat generation was larger in Experiment R since the condition of the thrust load by the disc springs was larger. As described in Chapter 2, ball load is higher in the bearing on larger thrust-load conditions. The high load condition resulted in larger friction forces between races and balls, which contributed to larger friction heat generation. In addition, the heat generation data measured in LCH_4 were larger than Experiment R. As described in section 3.3.1, this is because the fluid properties are

significantly different between LCH_4 and LH_2.

The relationship between the density and the heat generation estimated with regression curves from experimental data plots is shown in Fig. 37. The heat generation had positive correlation with the density as well as the results of Bearing X as shown in Fig. 26. The relationship between the viscosity and the heat generation estimated with the regression curves is shown in Fig. 38. The heat generation also had positive correlation with the viscosity contrary to the results of Bearing X as shown in Fig. 27. Comparing between LCH_4 and LH_2, both the density and viscosity are remarkably different. Therefore, only with these test results, it is difficult to identify which is the more influential factor to the heat generation. However, considering the results with Bearing X, the density would be more influential factor.

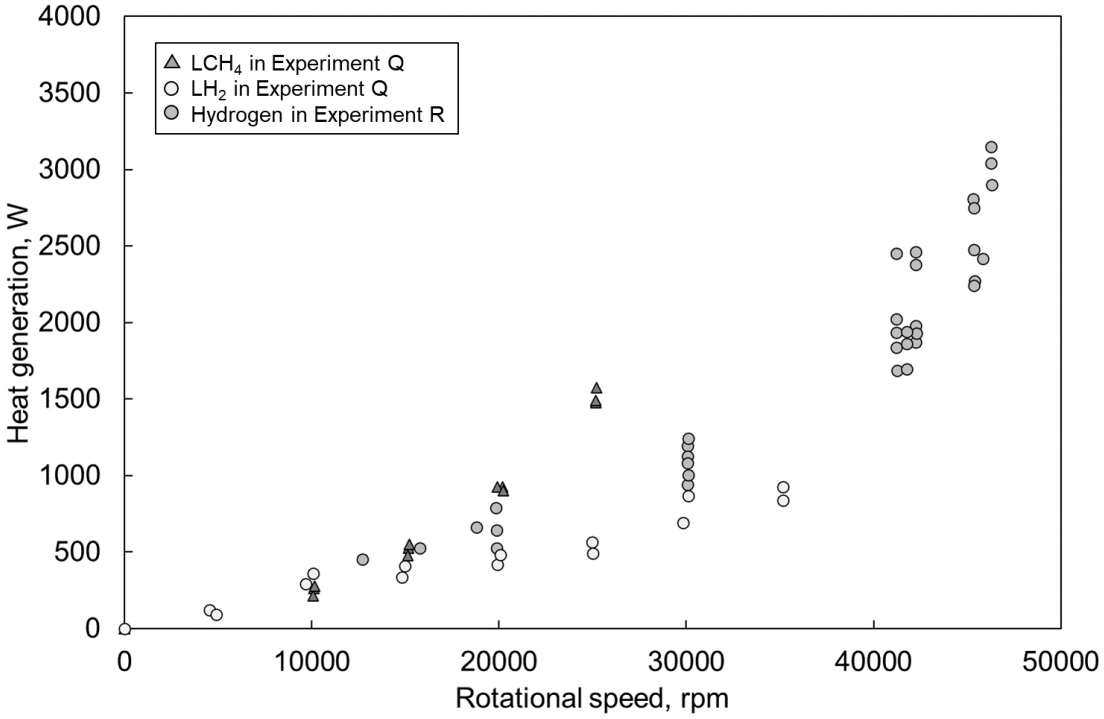

Fig. 36 Heat generation of Bearing Y in Experiment Q and Experiment R as a function of rotational speed.

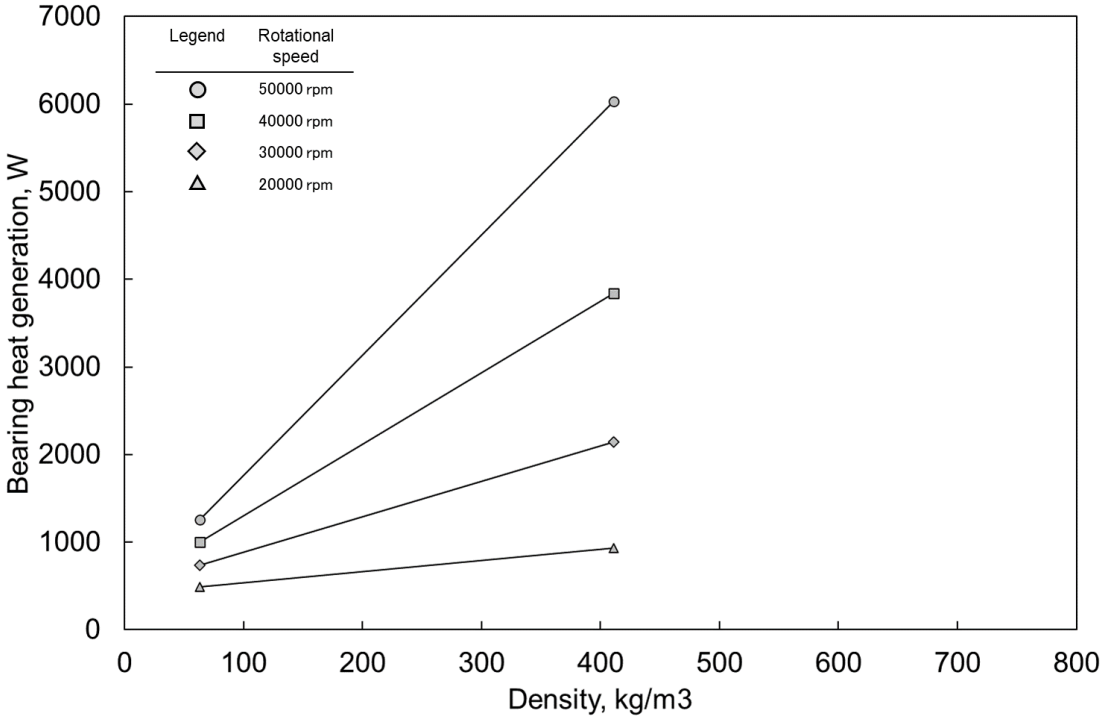

Fig. 37 Heat generation of Bearing Y in Experiment Q as a function of density.

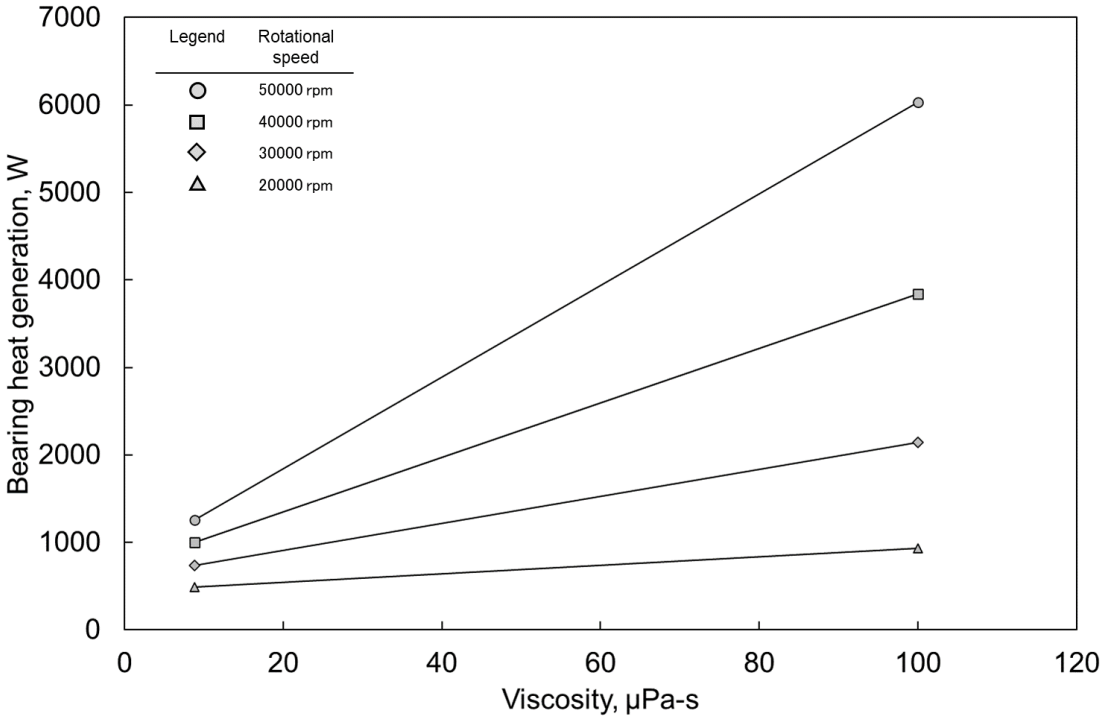

Fig. 38 Heat generation of Bearing Y in Experiment R as a function of viscosity.

3.4. Summary

Results of experiments which investigated the bearing heat generation in cryogenic environment were parametrically evaluated and summarized in this chapter. Two types of bearings were tested in LH_2, LCH_4, and LN_2 environment and the bearing heat generation was measured. In all bearing types and environments, the heat generation increased with the rotational speed. The gradient to the rotational speed depended on the coolants and increased with the fluid density. This characteristic would cause larger bearing heat generation in higher density fluid. The results of Bearing X experiments under LCH_4 and LN_2 environment identified that density of bearing coolant would have strong relationship with the fluid heat generation. By conducting bearing tests under hydrogen environment of several pressure and temperature conditions with Bearing Y, it was identified that density and viscosity significantly influenced the fluid heat generation. In addition, it is considered that the friction heat generation also significantly influences the entire heat generation especially in lower density coolant since the fluid heat generation does not account more portion of heat generation than higher density coolant. From the above, to construct high-fidelity modeling of heat generation in cryogenic bearing, the mechanisms of not only fluid heat generation but also friction heat generation need to be clarified quantitatively.

Chapter 4. Fluid flow characteristics of bearing coolant for cryogenic ball bearings

4.1. Introduction

Turbopump ball bearings are operated inside propellant that is supplied as bearing coolant. This indicates that bearing cavity is completely filled with the fluid. Therefore, the propellant in the vicinity of the baring cavity is churned by rotating motion of the bearing elements. Fluid heat generation due to drag and churning loss would occur with the bearing motion inside the coolant and contribute to gaining the coolant energy and the rotational torque of the main shaft. In this study, the energy increase is defined as fluid heat generation which is one of main heat generation factors of cryogenic ball bearings.

In a few of previous studies about a modeling of heat generation in turbopump bearings, the fluid heat generation is estimated by adopting simple empirical models of fluid drag force occurring on a flat surface, which was studied in [53]. In [39], there were test cases where the difference between experimental results and predicted values was clear, and the reason was not explained in the paper. It can be considered that the simple models for the fluid heat generation are not enough accurate to predict the fluid heat generation of cryogenic ball bearings. Also, in [54], there was a significant difference between the experimental results and the numerical results on specific conditions. It was pointed out that the difference could be caused by errors of the empirical models, and that fluid flow in the vicinity of bearing elements was too complicated to calculate by using the simple models. Even though there was one previous research by NASA which conducted ball bearing tests focusing on the fluid heat generation of RP-1 turbopump bearing [55] , there has been no research performing CFD analysis to predict the fluid heat generation of the cryogenic turbopump bearing coolant. Although previous research conducted by NASA and JAXA performed CFD analysis of the bearing coolant fluid flow, both studies focused on the differential pressure of the fluid flow between upstream and downstream of rotating ball bearing, not on the fluid heat generation [9, 38].

Therefore, CFD analysis was performed in this study to clarify mechanisms of the fluid flow

characteristics and to predict more accurately the fluid heat generation. The bearing models of Bearing X and Y were adapted for the analysis. The calculation was conducted on several conditions to clarify influences of bearing operating conditions, such as coolant types, coolant flowrate, and rotational speed, on the fluid heat generation. Finally, the calculation results were parametrically summarized.

4.2. CFD analysis method

ANSYS FLUENT 2020 R1 was used as the CFD analysis solver in this study. Realizable k-epsilon model was adopted as the turbulence model. Bearing coolant was considered as incompressible fluid. The fluid properties that were needed for CFD analysis, such as density, viscosity, specific heat capacity, and thermal conductivity, were calculated by using polynomial regression curves of data from REFPROP [52]. The CFD analysis did not take into account phase change of the fluid.

Governing equations are as follows. Mass conservation equation:

$$\frac{\partial \rho}{\partial t} + \nabla \cdot (\rho \vec{v}) = 0 \tag{40}$$

Momentum conservation equation:

$$\frac{\partial}{\partial t}(\rho \vec{v}) + \nabla \cdot (\rho \vec{v} \vec{v}) = -\nabla p + \nabla \cdot (\bar{\bar{\tau}}) + \vec{F} \tag{41}$$

Energy equation:

$$\frac{\partial}{\partial t}(\rho E) + \nabla \cdot \left(\vec{v}(\rho E + p)\right) = \nabla \cdot \left(k_{eff} \nabla T - \sum_j h_j \overrightarrow{J_j} + \left(\overline{\overline{\tau_{eff}}} \cdot \vec{v}\right) \right) \tag{42}$$

ρ is density, v is velocity, p is static pressure, $\bar{\bar{\tau}}$ is stress tensor, $\vec{F}$ is external body force, k_{eff} is effective conductivity, E is internal energy, T is temperature, h is enthalpy, and $\overrightarrow{J_j}$ is diffusion flux of species.

4.3. CFD analysis on Bearing X

4.3.1. Analysis model

3D models used for CFD analysis are shown in Fig. 39. One ball was included in the calculation domain which corresponds to 36 degrees for Bearing X out of the whole fluid geometry. Periodic boundary conditions were applied to the side walls. It was considered that all walls had no slip with the fluid at their surfaces. Virtual gaps that do not exist in real bearings were set in the contact region between the races and the ball to simplify the mesh generation. The gaps would not significantly influence calculation results of fluid heat generation because volume occupied by the gap is slight. Steady-state calculation was performed in the rotational coordinate system which rotated at the same velocity as the ball revolution motion. The inlet boundary condition was defined as constant pressure. The outlet boundary condition was defined as constant flowrate. Friction heat and the wall heat transfer were not taken account in this calculation to evaluate only the fluid heat generation.

The mesh quality was evaluated in terms of grid dependency on the fluid heat generation. The calculation results are shown in Fig. 40. The fluid heat generation asymptotically approached to around 850 W with mesh quality. Considering efficiency of the analysis in terms of solving time and mesh quality, 6.9 E-12 m^3 averaged element size which contributes to less than 0.25 % difference of heat generation from the minimum element size condition was selected in this study.

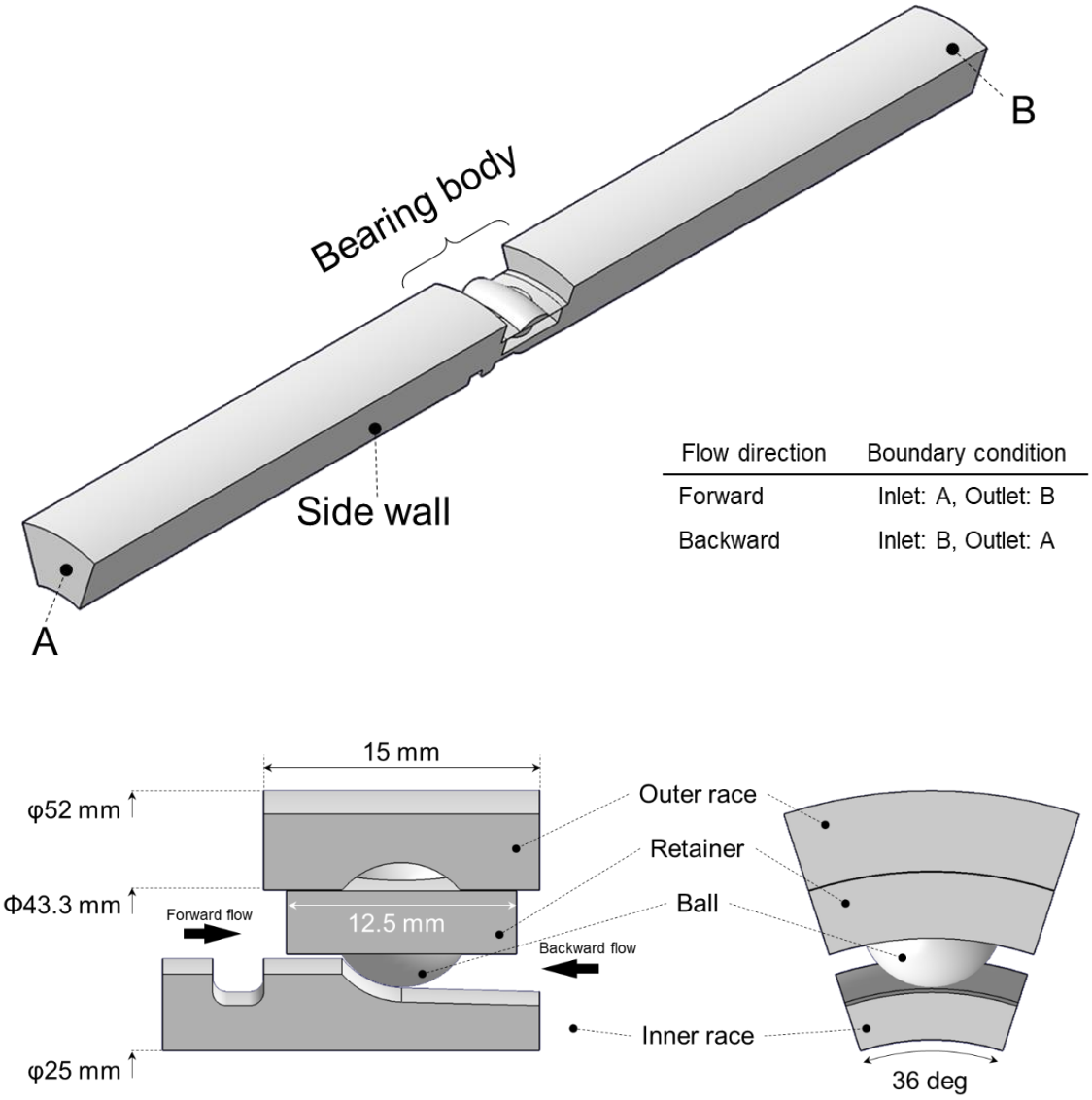

Fig. 39 3D models used for CFD analysis for Bearing X.

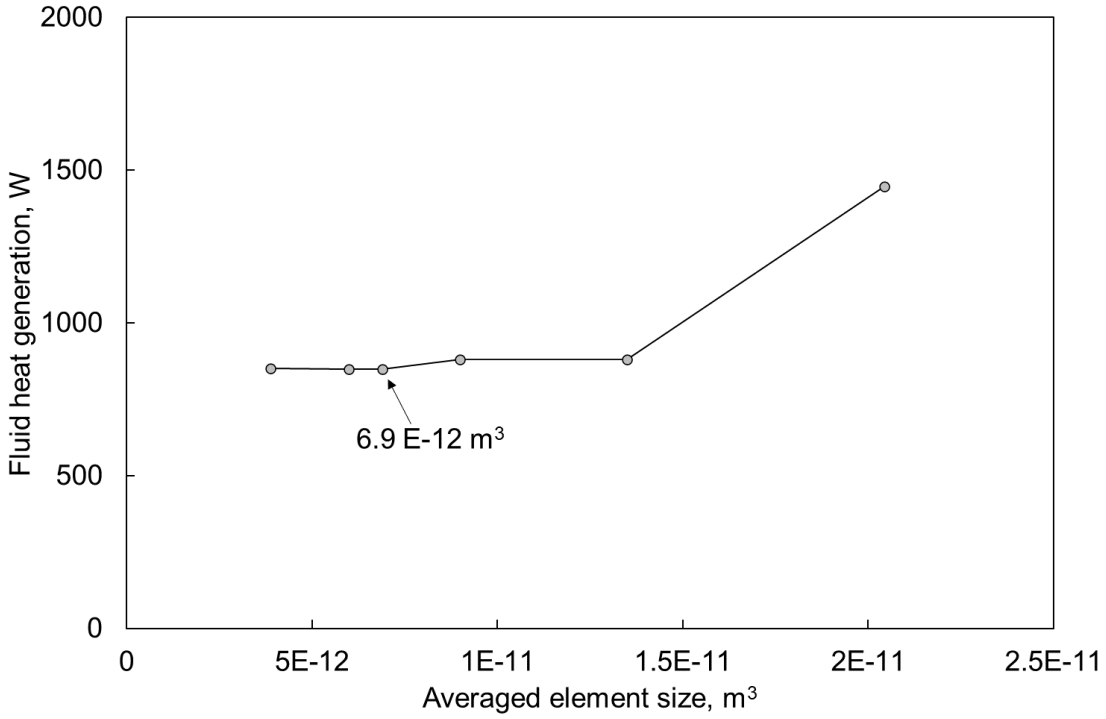

Fig. 40 Influence of Bearing X's mesh quality on fluid heat generation.

4.3.2. Analysis condition

Analysis conditions are listed in Table 7. The bearing test results mentioned in Chapter 3 indicate that the heat generation in turbopump bearings strongly depends on the rotational speed and the fluid properties such as fluid density. Therefore, LH_2, LCH_4, and LN_2 were set as the bearing coolant in this analysis to simulate the experimental conditions. The cases X-1 to X-8 were calculated in LH_2 environment to investigate differences from Bearing Y. The cases X-8 to X-15 were calculated on close conditions with the experimental conditions to compare the analysis results with the experimental ones. The case X-16 were calculated by changing the flow directions from X-7 to investigate an influence of flow direction. The cases X-17 to X-20 were calculated by changing the mass flowrate from X-15 to investigate an influence of mass flowrate.

Table 7 Analysis conditions of Bearing X.

Analysis case	Bearing coolant	Mass flowrate [kg/s]	Inlet pressure [MPa]	Inlet temperature [K]	Rotational speed [rpm]	Flow direction
X-1	LH_2	0.00503	1.25	24.8	0	Forward
X-2	LH_2	0.00503	1.25	24.8	20000	Forward
X-3	LH_2	0.00503	1.25	24.8	40000	Forward
X-4	LH_2	0.00503	1.25	24.8	60000	Forward
X-5	LH_2	0.00503	1.25	24.8	80000	Forward
X-6	LH_2	0.00503	1.25	24.8	100000	Forward
X-7	LH_2	0.00503	1.25	24.8	120000	Forward
X-8	LCH_4	0.0139	1.43	120.9	0	Forward
X-9	LCH_4	0.0139	1.43	120.9	20000	Forward
X-10	LCH_4	0.0139	1.43	120.9	40000	Forward
X-11	LCH_4	0.0139	1.43	120.9	60000	Forward
X-12	LN_2	0.0307	1.11	94.5	0	Forward
X-13	LN_2	0.0307	1.11	94.5	20000	Forward
X-14	LN_2	0.0307	1.11	94.5	40000	Forward
X-15	LN_2	0.0307	1.11	94.5	60000	Forward
X-16	LH_2	0.00503	1.25	24.8	120000	Backward
X-17	LN_2	0.06	1.11	94.5	60000	Forward
X-18	LN_2	0.09	1.11	94.5	60000	Forward
X-19	LN_2	0.12	1.11	94.5	60000	Forward
X-20	LN_2	0.15	1.11	94.5	60000	Forward

4.3.3. Analysis results

4.3.3.1. Fluid flow characteristics

CFD results of velocity distribution of Bearing X in LH_2 environments are shown in Fig. 41. The color maps show the tangential velocity distribution, and the arrows show the meridional velocity. The tangential velocity near moving wall such as the shaft, the inner race, the retainer, the ball tended to be higher due to effects of viscosity while the velocity near the stationary outer race was lower. The fluid flow near the contact area between the inner race and the ball was extensively accelerated since

the walls moving fast were facing with each other. 6 points described as (a) ~ (f) in the figure show recirculation zones in the vicinity of the bearing. Recirculation zones (a) and (b) in the upstream of the bearing were caused by rotational flow accelerated by the moving walls and converging to outer side due to its centrifugal force. Recirculation zone (c) was the fluid flow entering into the inner race's groove and did not have significant influences on the main coolant flow since the recirculation flow was closed only inside the groove. Recirculation zones (d) and (e) in the downstream of the bearing originated from tangential flow accelerated by passing through the rotating ball bearing which contributed to centrifugal force. Although (d) and (e) were similar flow structure to the recirculation zones (a) and (b), they were more developed vortexes since the color maps indicated that the tangential flow of the downstream was faster than the upstream. Recirculation zone (e) which was one of the developed vortexes resulted in reverse flow that went from the downstream to the ball and the inner race, which contributed to generating recirculation zone (f). The fluid flow in the downstream of the bearing indicated that the inner race and the ball would be cooled by such reverse fluid flow. The fluid flow characteristics described above were common among all rotational speed conditions although the CFD results showed that the tangential flow which contributed to generating centrifugal force causing the recirculation zones was developed in higher-speed conditions. Averaged tangential velocity data at several axial positions in X-7 are shown in Fig. 42. The tangential velocity increased from 35.7 m/s at the upstream to 97.2 m/s at the center of the bearing and decreased to 58.8 m/s at the downstream. This result indicates that the tangential flow was accelerated from 35.7 m/s to 58.8 m/s by passing through the rotating ball bearing, which contributed to generating the recirculating zone stated above and gaining the kinetic energy of the fluid flow.

Temperature distribution data of Bearing X in LH_2 environment are shown in Fig. 43. The temperature of the fluid increased in the vicinity of moving walls such as the shaft, the inner race, the retainer, the ball. This is because the fluid was heated near the walls by fluid friction of shear force

occurring between the fluid and the moving walls which were rotating much faster than the surrounding fluid due to the fluid viscosity. Additionally, the figures show that temperature increased near the stationary outer race. The temperature rise was also caused by fluid friction of shear force occurring between the stationary wall and the fluid which was accelerated by the moving walls due to the fluid viscosity. These fluid friction phenomena caused by the differential velocity between the fluid and the walls contributed to raising temperature of the fluid passing through the rotating ball bearing. The figure shows that this temperature rise increased with the rotational speed, which contributed to increasing the internal energy of the fluid flow. Averaged temperature data of the tangential flow at several axial positions in X-7 are shown in Fig. 44. The temperature drastically increased at the center of the rotating ball bearing, which contributed to 2.1 K increase from 26.1 K at the upstream to 28.1 K at the downstream.

Pressure distribution data of Bearing X in LH_2 environment are shown in Fig. 46. Although the distribution at the upstream was relatively uniform, the fluid pressure at the downstream increased in the radial direction. The pressure distribution at the downstream was caused by the tangential fluid flow stated above which contributed to generating centrifugal force and pressurizing the fluid toward outer side of the rotation. The pressure in the region near the contact area between the ball and the inner race was decreased. This was caused by much faster fluid flow which contributed to decreasing the static pressure by Bernoulli's principle. The figures indicate that there was high-pressure region inside the retainer pocket. This is because the fluid flow in the vicinity of the rotating bearing was extensively accelerated by moving walls inside the pocket, which contributed to gaining the fluid energy that increased the static pressure. Averaged pressure data of the rotational flow at several axial positions in X-7 are shown in Fig. 46. The pressure at the upstream gradually decreased near the rotating bearing from 1.15 MPa at Z = -20 to 1.13 MPa at Z = -5, which was caused by the increased velocity in both the rotational direction and the axial direction decreasing the static pressure. At the

center of the rotating bearing, the pressure drastically increased to 1.18 MPa because of the high-pressure region inside the retainer pocket described above. The pressure at Z = 5 that was just downstream of the bearing rapidly decreased to 1.09 MPa due to the accelerated fluid flow by the rotating bearing. In the downstream of Z = 5, the static pressure was recovered because the passage area of the cross section increased, and the fluid velocity was decelerated. The net pressure change of the fluid flow was 0.01 MPa drop from 1.15 MPa to 1.14 MPa by passing through the rotating bearing. From the above, it was found that the uniformity of the pressure distribution significantly changed from the upstream to the downstream although the averaged value of the pressure was not significantly changed.

The fluid heat generation of Bearing X is shown in Fig. 47. The heat generation exponentially increased with the rotational speed to 1269 W at 120000 rpm. The regression curve shown as dotted line in the graph indicates that the heat generation was approximately proportional to the cube of the rotational speed, which can be explained by the mechanisms of the fluid heat generation as follows. The fluid heat generation was caused by shear force occurring between bearing elements' walls and the surrounding fluid. Therefore, it is equal to energy loss generated by fluid drag force on rotating bearing elements. The energy E_{Fluid} is expressed as follows.

$$E_{Fluid} = T_{Elemts} \times \omega_{Elements} \tag{43}$$

$T_{Elements}$ is torque on bearing elements around their rotational axes, and $\omega_{Elements}$ is angular velocity of bearing elements.

$$T_{Elements} = R_{Elements} \times F_{Fluid\ drag} \tag{44}$$

$R_{Elements}$ is radius of bearing elements. $F_{Fluid\ drag}$ is drag force on bearing elements and can be expressed as follows because it is proportional to the square of the differential velocity between wall and fluid according to [53].

$$F_{Fluid\ drag} \propto \rho {\omega_{Elements}}^2 \tag{45}$$

From the above,

$$E_{Fluid\ loss} \propto \rho {\omega_{Elements}}^3 \tag{46}$$

Considering these physical mechanisms of fluid energy loss, main factor of fluid heat generation should be torque of bearing elements about their rotational axes. The torque data of Bearing X' elements in LH_2 environment are shown in Fig. 48. Each torque increased with the rotational speed. The torque of the inner race whose velocity was the maximum in all elements was the largest, followed in order by the outer race, the retainer, and the ball. The torque of the ball was the smallest because the surface area was much smaller than the others although the rotational velocity was the maximum as well as the inner race. The outer race generated comparable torque with the inner race and the retainer due to differential velocity with surrounding fluid although it is a stationary element.

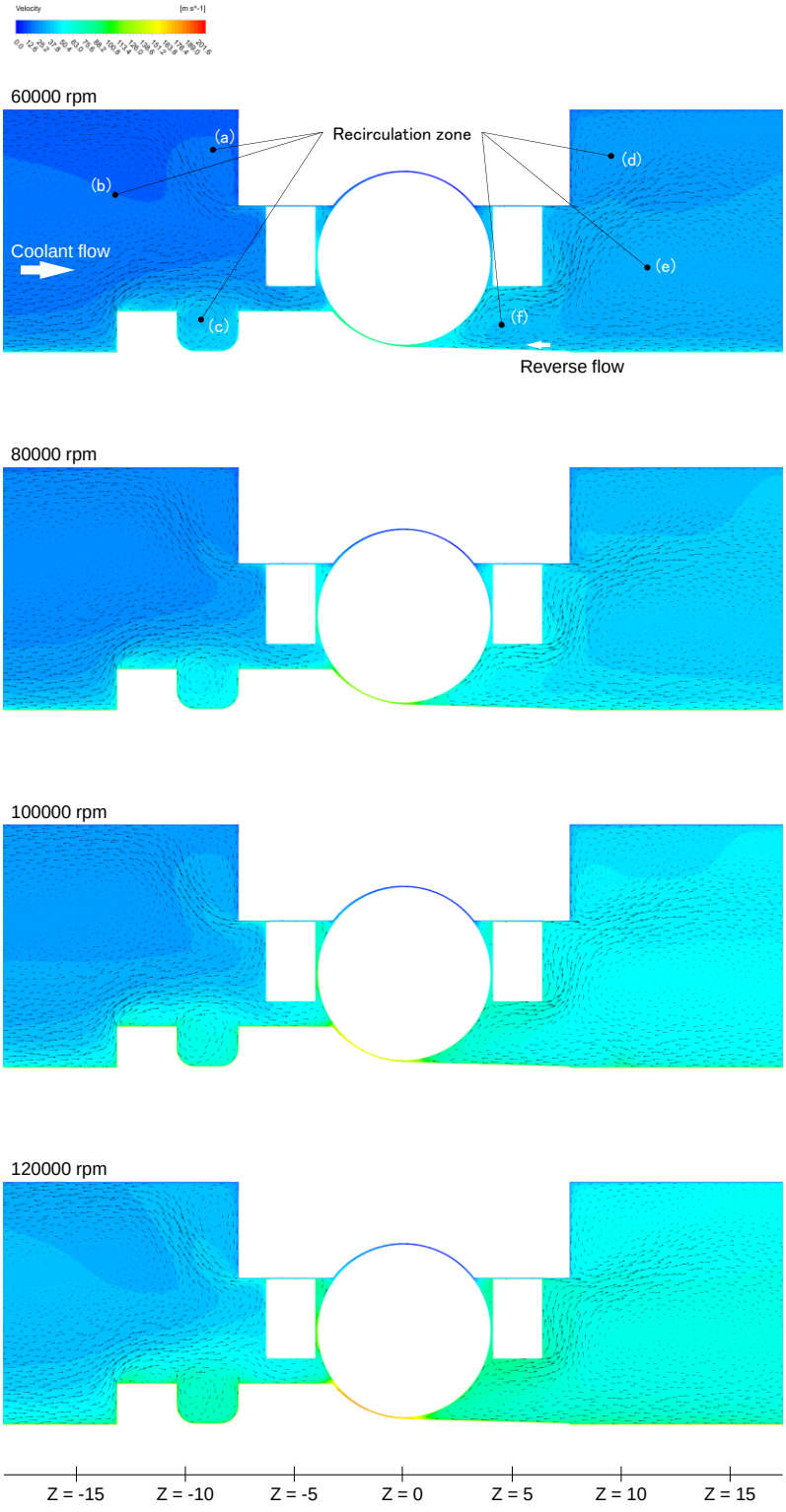

Fig. 41 Velocity distribution of LH_2 around Bearing X (color maps: tangential velocity, arrows: meridional velocity) (CFD results).

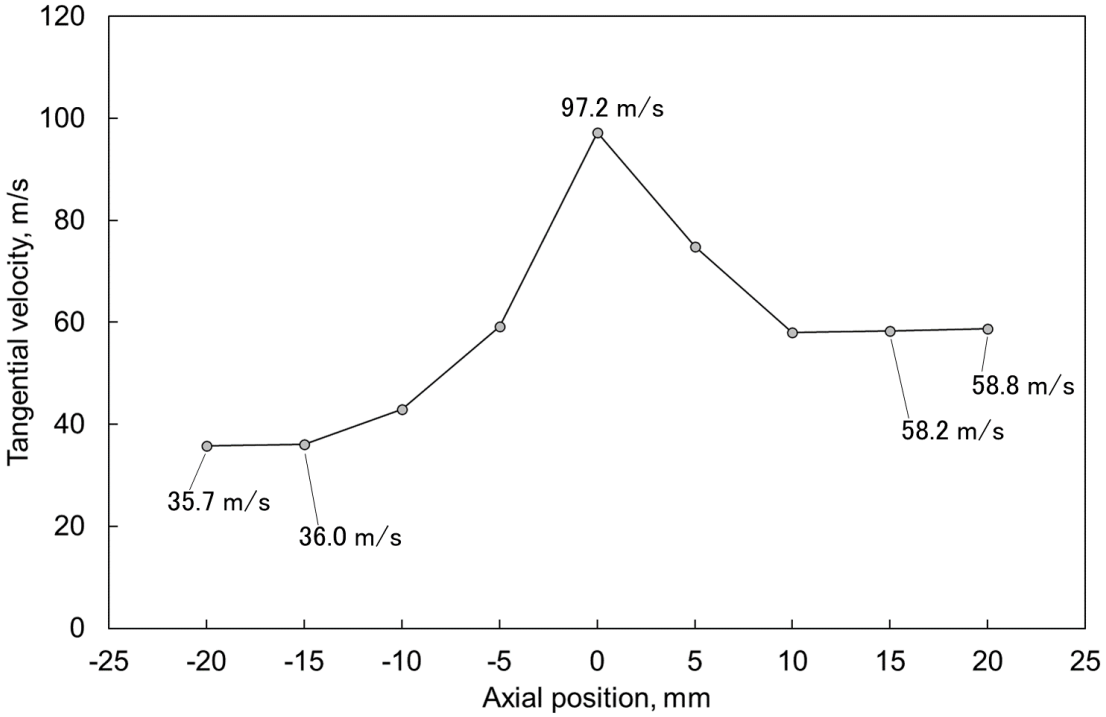

Fig. 42 Averaged velocity of the tangential flow in X-7 as a function of axial position (CFD results).

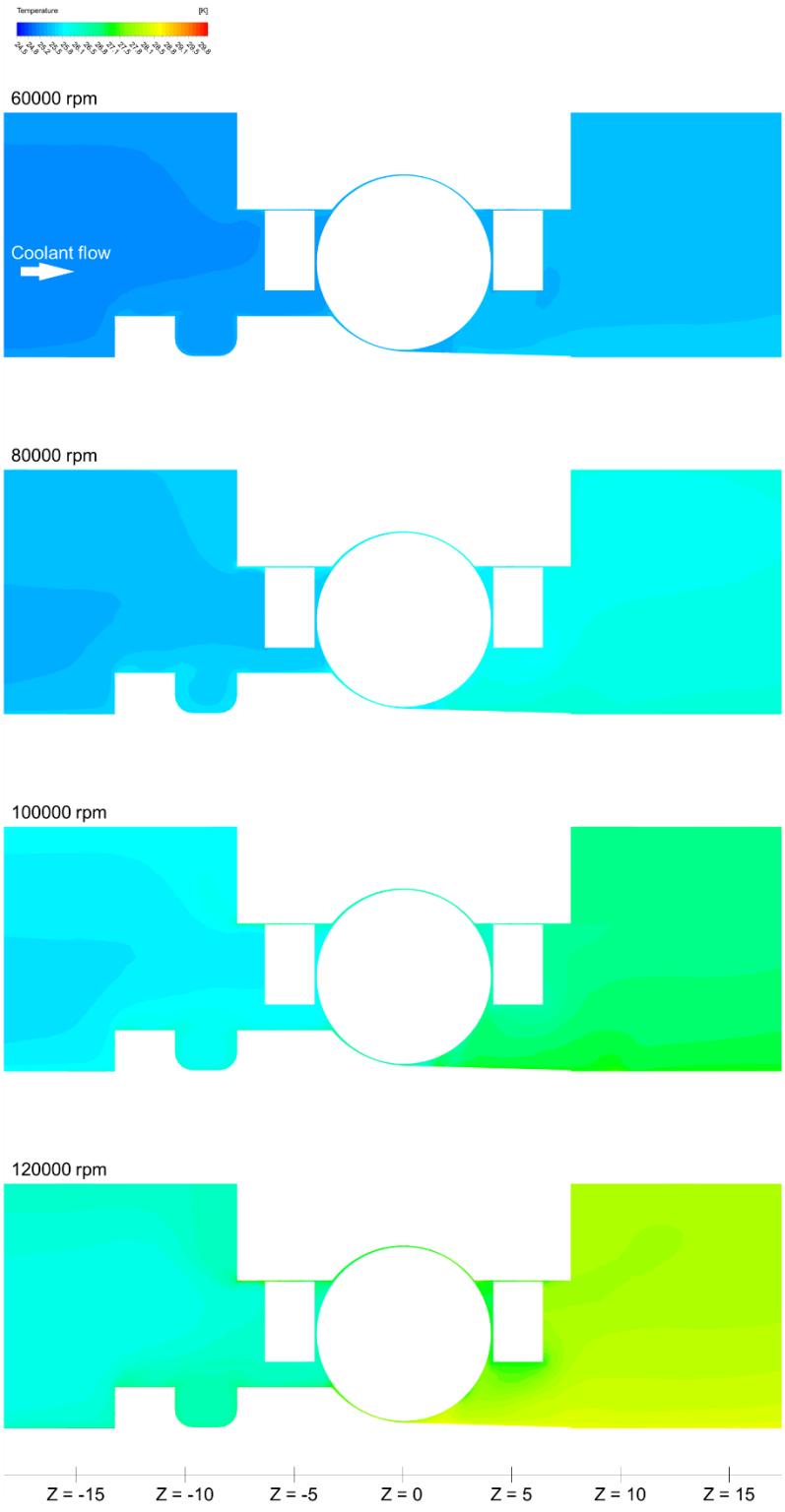

Fig. 43 Temperature distribution of LH_2 around Bearing X (CFD results).

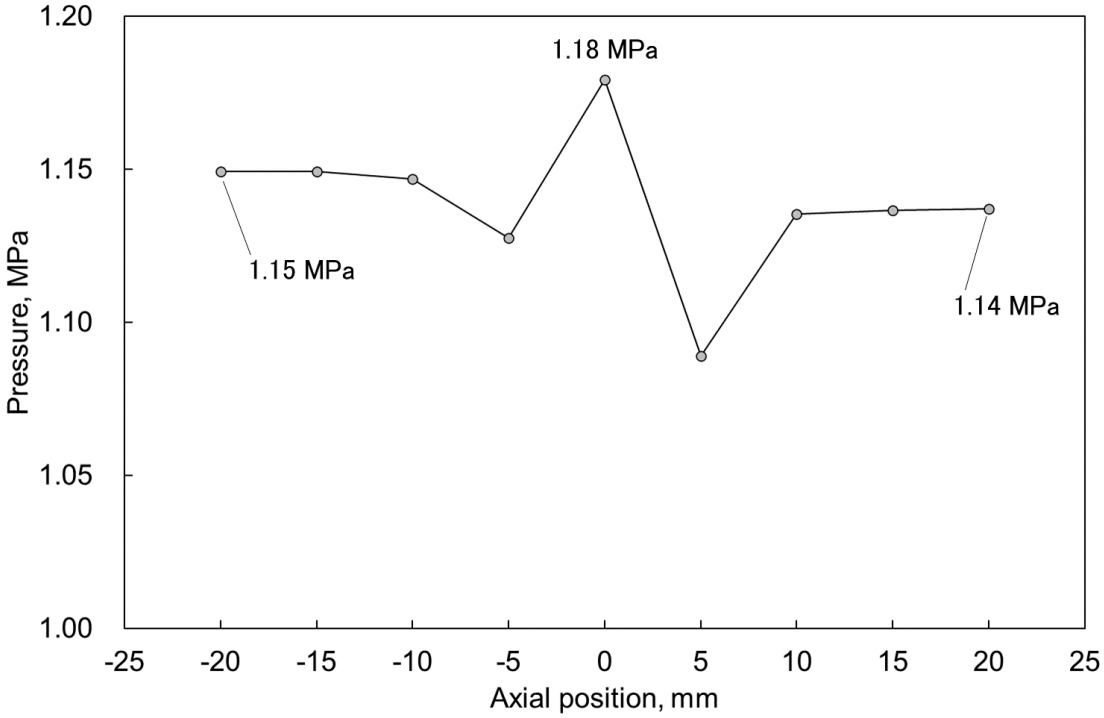

Fig. 44 Averaged temperature of the fluid flow in X-7 as a function of axial position (CFD results).

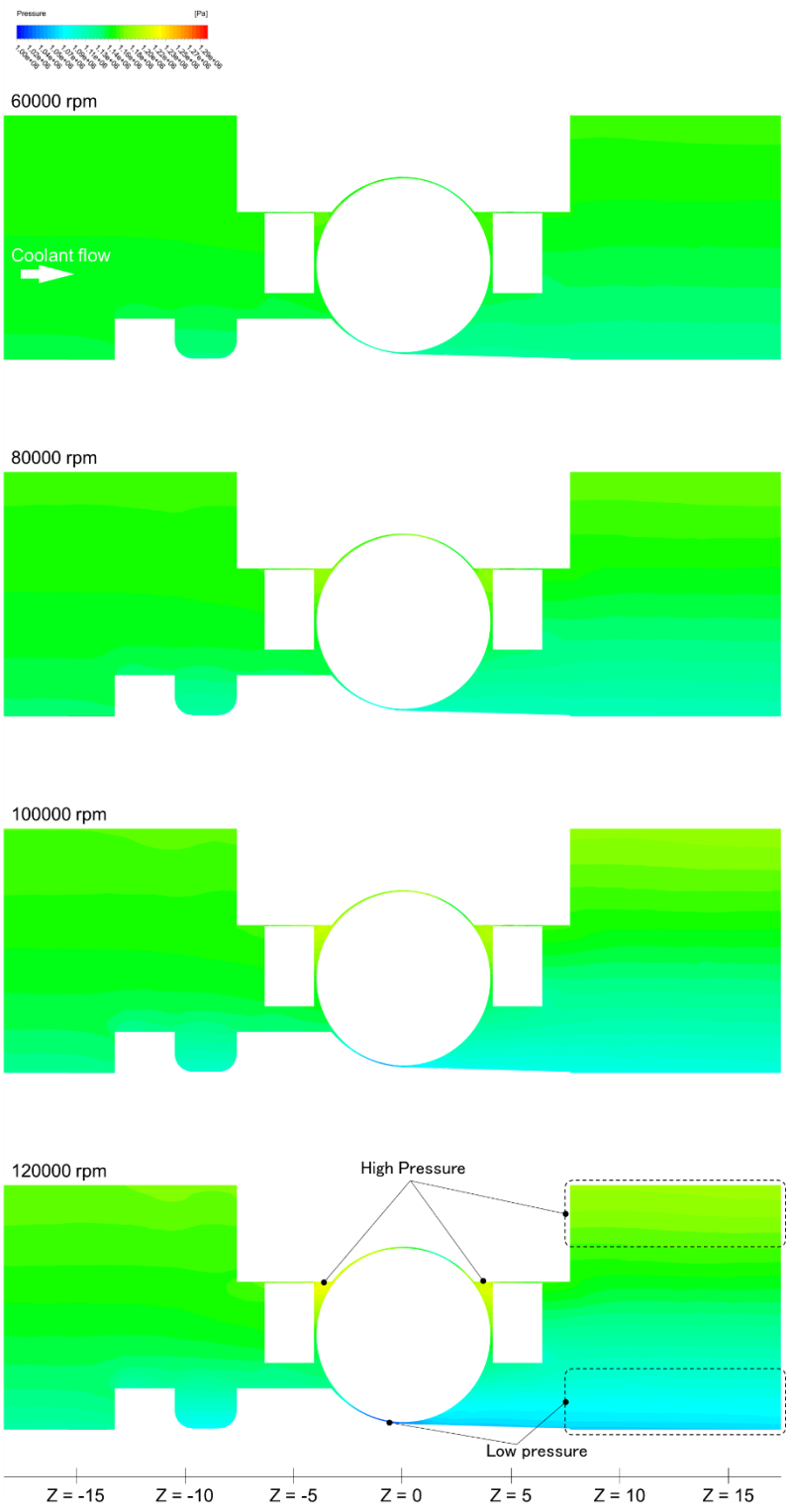

Fig. 45 Pressure distribution of LH_2 around Bearing X (CFD results).

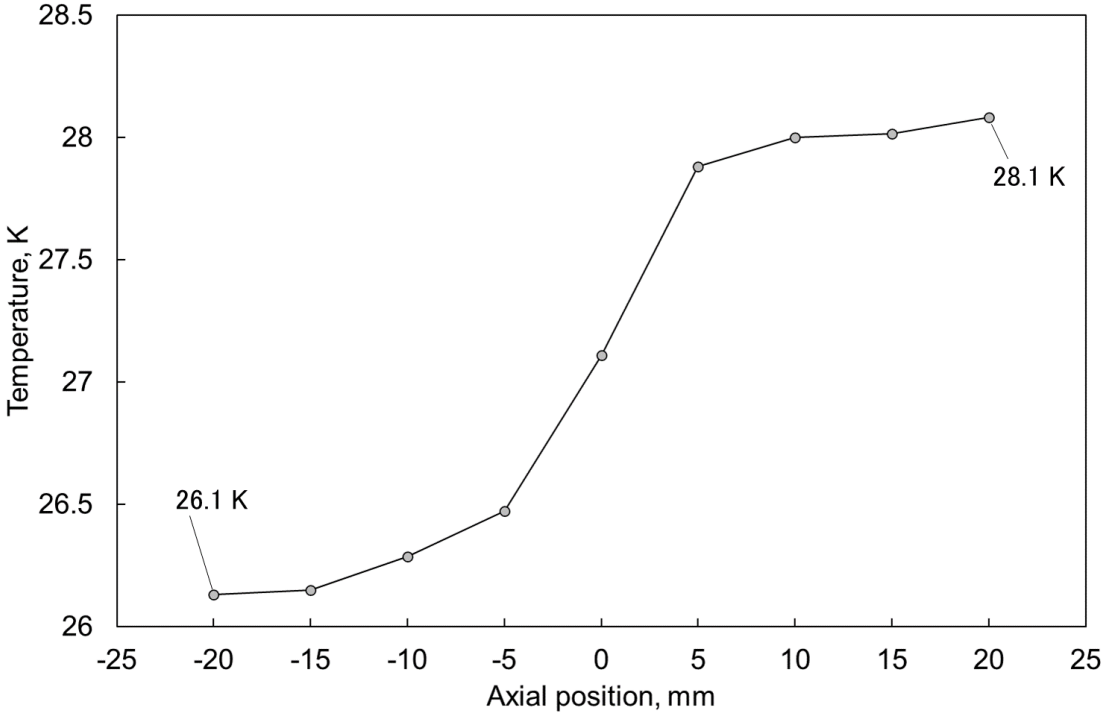

Fig. 46 Averaged pressure of the fluid flow in X-7 as a function of axial position (CFD results).

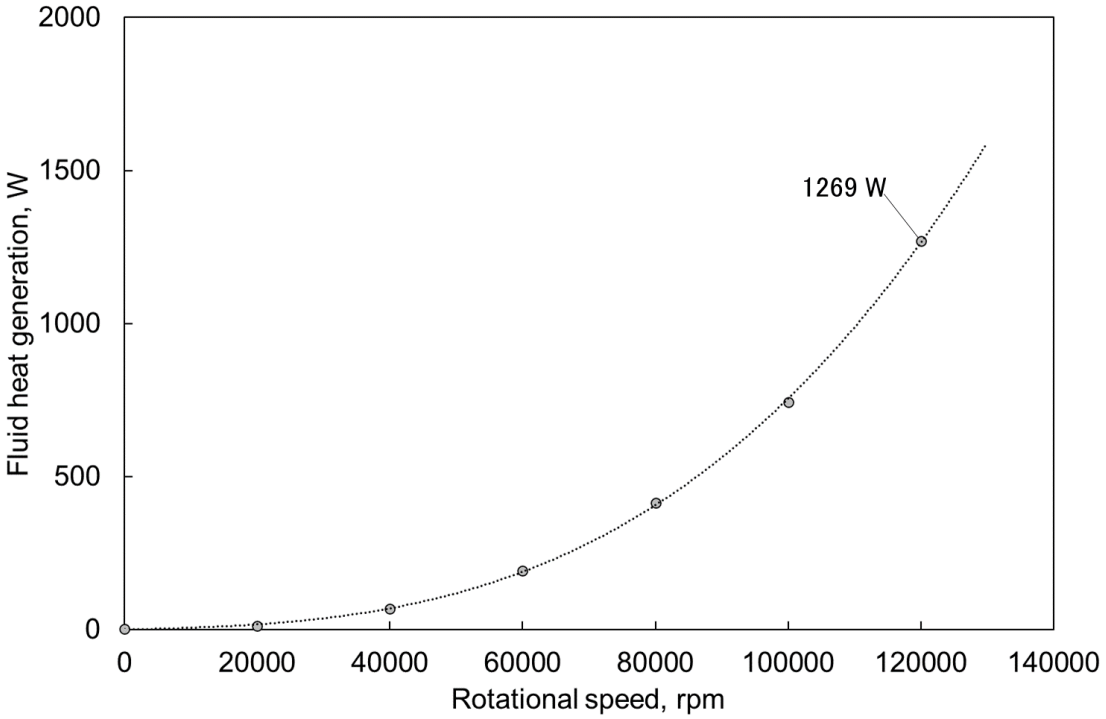

Fig. 47 Fluid heat generation of Bearing X in LH_2 as a function of the rotational speed (CFD results).

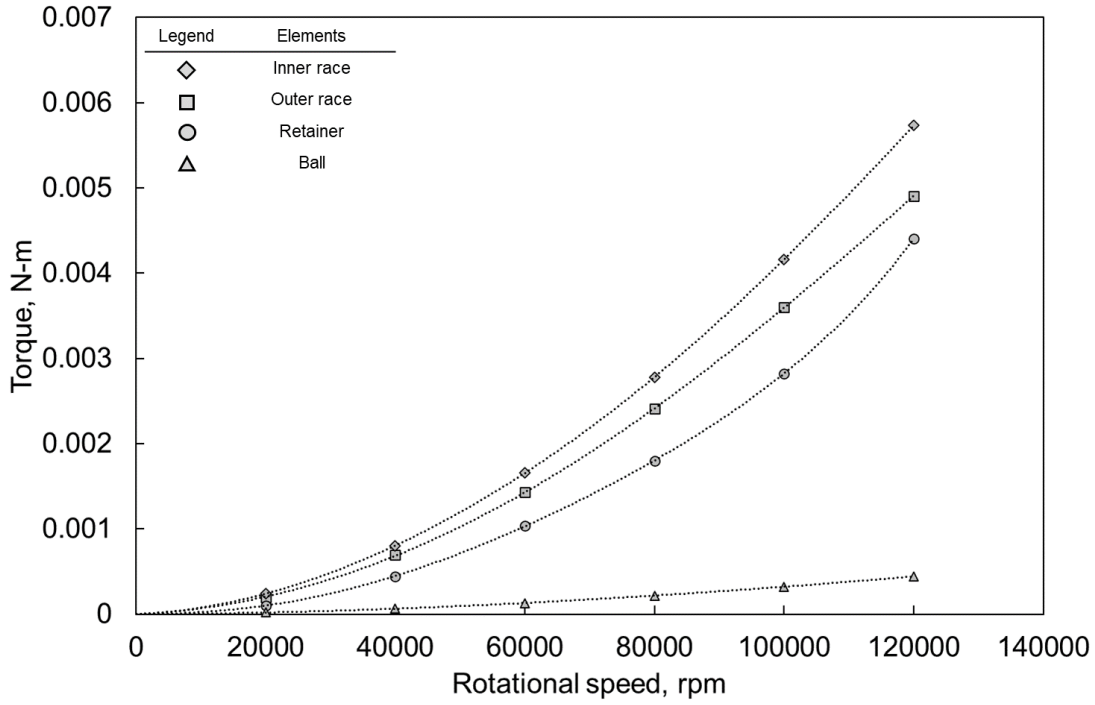

Fig. 48 Torque of Bearing X's elements about their rotational axes (CFD results).

4.3.3.2. Influences of bearing coolant fluid

CFD results of velocity distribution of Bearing X in LH_2, LCH_4, and LN_2 environments are shown in Fig. 53. The distribution of the tangential velocity and the meridional velocity was almost the same in all fluid conditions, which contributed to the same fluid flow characteristics of the recirculation zones and the reverse flow described in section 4.3.3.1. This result indicates that the coolant fluid conditions had little influences on the velocity field characteristics. Averaged tangential velocity data at several axial positions in X-4, X-11, and X-15 are shown in Fig. 50. The averaged tangential velocity was not significantly influenced by the coolant fluid conditions as well as the velocity field characteristics.

Averaged temperature data at several axial positions in X-4, X-11, and X-15 are shown in Fig. 51. The graph shows temperature differences from Z = 20 in each fluid condition to evaluate temperature

increase due to flowing through the rotating bearing because the fluid absolute temperature is significantly different from each other. In all fluid conditions, the fluid temperature suddenly increased when flowing through the rotating bearing, which is the same characteristic as stated in section 4.3.3.1. The increase amounts were dependent on the fluid conditions. The increase from Z = -20 to Z = 20 was 3.07 K in LN_2, 2.51 K in LCH_4, and 0.34 K in LH_2, respectively. This indicates that the temperature increase was larger in higher density fluid. It was caused by the characteristics of the fluid heat generation which was described in Equation (46).

Averaged pressure data at several axial positions in X-4, X-11, and X-15 are shown in Fig. 52. The graph shows pressure differences from Z = 20 in each fluid condition to evaluate pressure change due to flowing through the rotating bearing. In all fluid conditions, fluid pressure was significantly low in the vicinity of the rotating bearing (Z = -5 and Z = 5) and suddenly increased at the center of the bearing (Z = 0), which is almost the same characteristic as stated in in section 4.3.3.1. The pressure difference from Z = -20 to Z = 20 is -0.021 MPa in LN_2, -0.012 MPa in LCH_4, and -0.004 MPa in LH_2, respectively. The pressure differences due to flowing through the rotating bearing were dependent on the fluid conditions, and the changes were larger in higher density fluid. This is because the pressure changes were influenced by pressure loss due to fluid drag. In general, pressure loss due to fluid drag is proportional to $\rho\omega_{Elements}{}^2$. Considering that the characteristics of velocity distribution were almost the same regardless of the fluid conditions as shown in Fig. 53, the pressure loss should be proportional to ρ, which was consistent with the CFD results.

Fluid heat generation data in all fluid conditions are shown in Fig. 53. The fluid heat generation exponentially increased with the rotational speed in all fluid conditions. The increase amounts significantly depended on the fluid conditions. The fluid heat generation at 60000 rpm is 2128 W in LN_2, 1256 W in LCH_4, and 209 MPa in LH_2, which indicates that the heat generation was larger in higher density fluid. This is because the fluid drag force was proportional to fluid density according

to Equation (45). Therefore, according to Equation (46), the fluid heat generation is proportion to the fluid density and the cube of the rotational speed. The characteristics of the fluid heat generation should influence the temperature increase stated above.

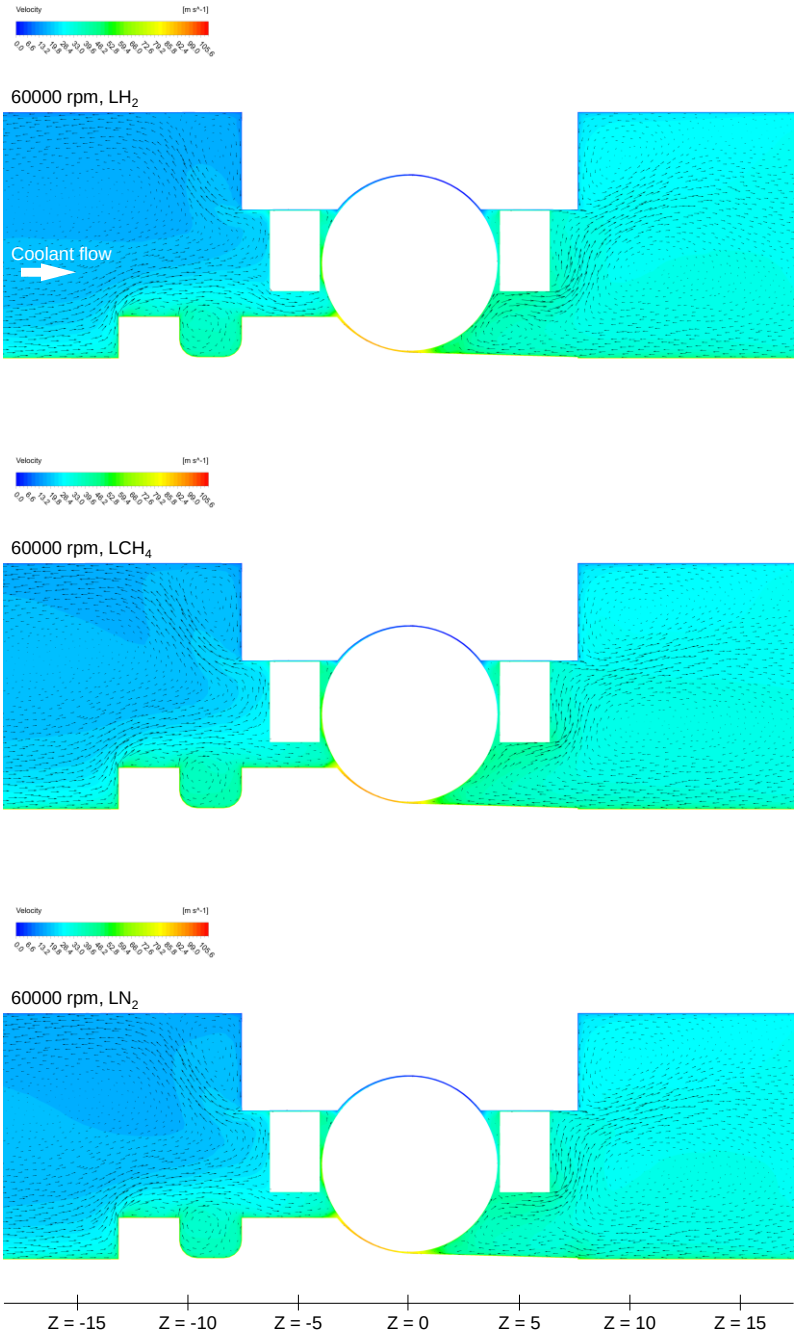

Fig. 49 Velocity distribution of Bearing X coolant in LH_2, LCH_4, and LN_2 (color maps: tangential velocity, arrows: tangential velocity) (CFD results).

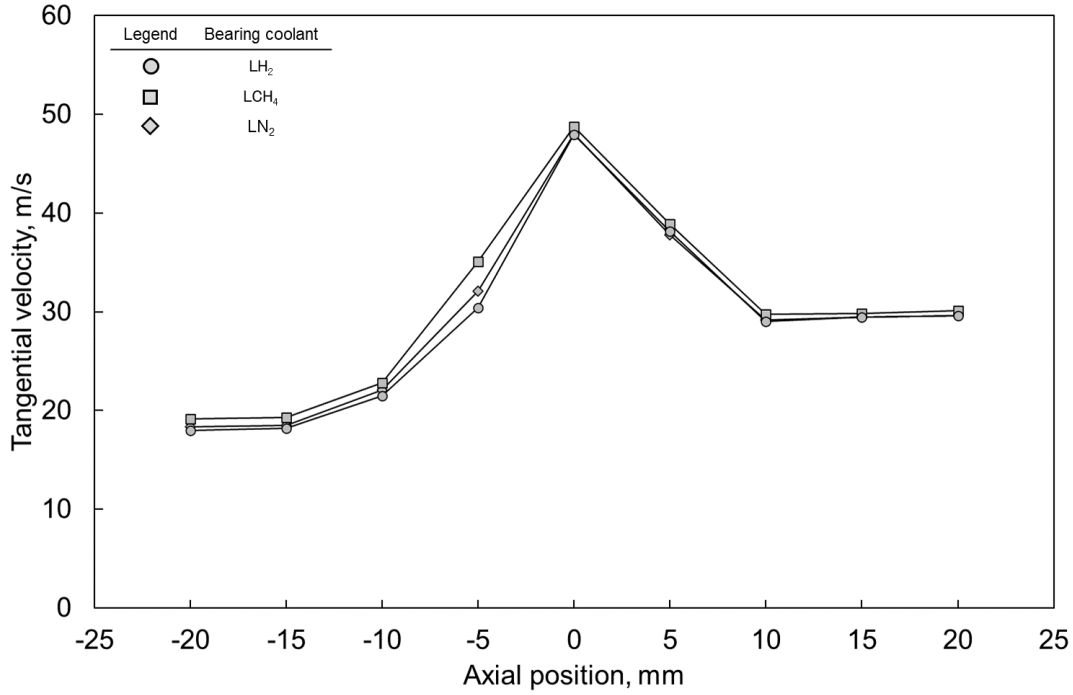

Fig. 50 Averaged tangential velocity in X-4, X-11, and X-15 as a function of axial position (CFD results).

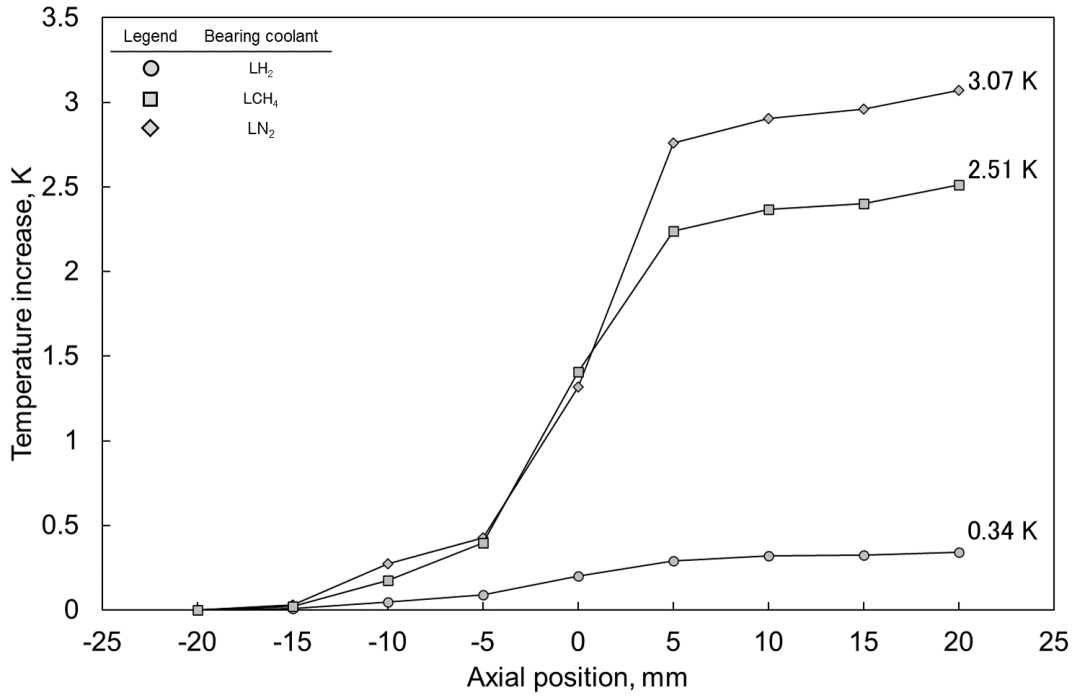

Fig. 51 Averaged temperature difference from Z = -20 in X-4, X-11, and X-15 as a function of axial position (CFD results).

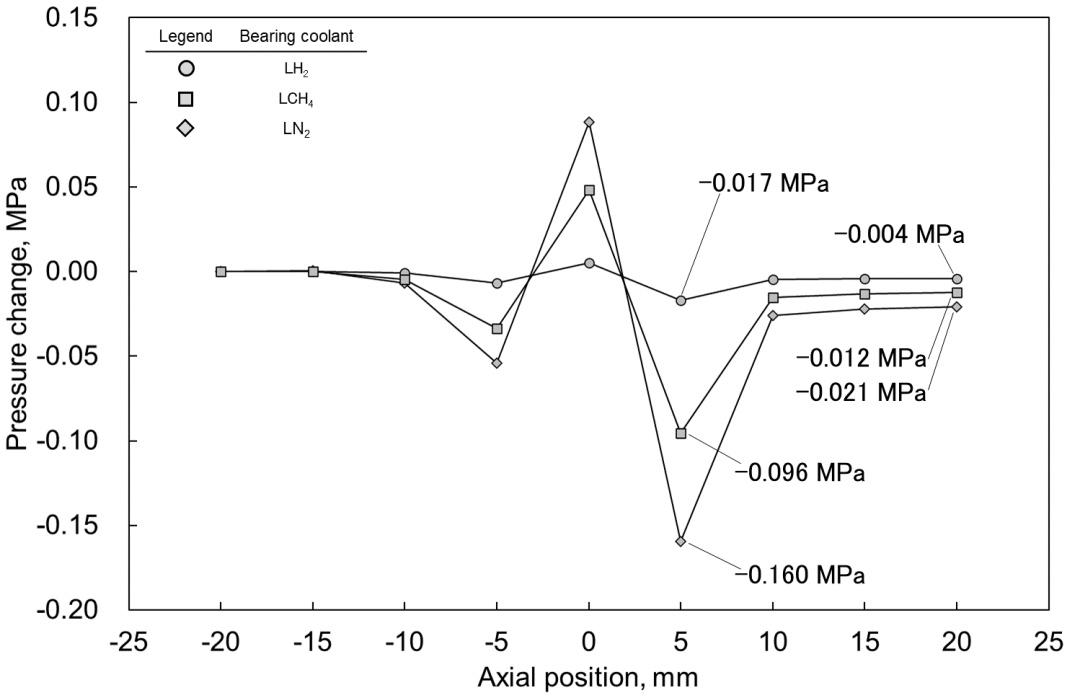

Fig. 52 Averaged pressure difference from Z = -20 in X-4, X-11, and X-15 as a function of axial position (CFD results).

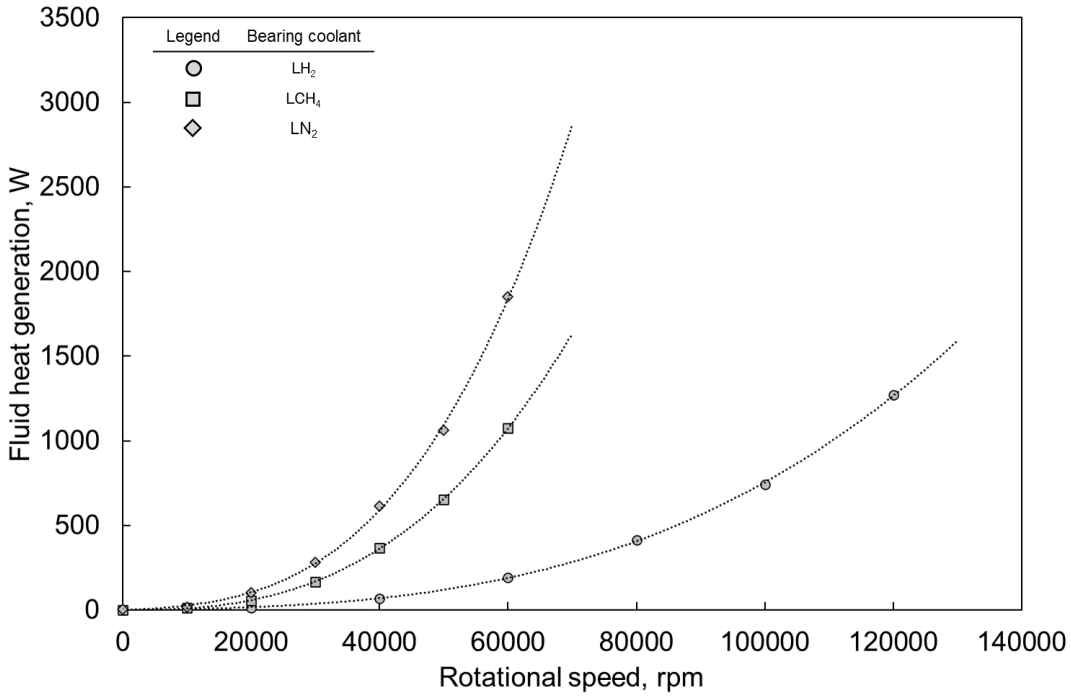

Fig. 53 Fluid heat generation of Bearing X in LH_2, LCH_4, and LN_2 environments as a function of rotational speed (CFD results).

4.3.3.3. Influences of flow direction

CFD results of velocity distribution of LH_2 around Bearing X in X-7 and X-16 are shown in Fig. 54. The color maps show the tangential velocity distribution, and the arrows show the meridional velocity. The fluid flow structure on the backward condition was similar to the forward condition described in section 4.3.3.1. 5 points described as (a) ~ (e) in the figure show recirculation zones in the vicinity of the bearing. Recirculation zones (a) and (b) in the upstream of the bearing were caused by rotational flow which was accelerated by the moving walls and heading towards outer side due to its centrifugal force. The recirculation zone (b) generated reverse flow between the retainer and the inner race in the upstream of the bearing. Recirculation zone (c) was the fluid flow entering into the inner race's groove and did not have significant influences on the main coolant flow since the recirculation flow was closed only inside the groove. Recirculation zones (d) and (e) in the downstream of the bearing originated from tangential flow accelerated by passing through the rotating ball bearing which contributed to centrifugal force. Although (d) and (e) were similar flow structure to the recirculation zones (a) and (b), they were more developed vortexes since the color maps indicate that the tangential flow of the downstream was faster than the upstream. As described in section 4.3.3.1, reverse flow was generated in the downstream of the bearing on the forward condition although no reverse flow was generated there on the backward condition. This suggests that the cooling capability on the backward condition would be superior to the forward condition since higher-temperature fluid in the downstream would not reverse to the bearing friction area which needs cooling capability of the coolant.

Averaged tangential velocity data at several axial positions in X-7 and X-16 are also shown in Fig. 54. The tangential velocity increased by flowing through the rotating bearing on both forward and backward conditions, which contributed to generating the recirculating zone stated above and gaining kinetic energy of the fluid flow. Although the tangential velocities in the vicinity of the bearing were

different between those conditions, the increase amount of the velocity was almost the same.

Temperature distribution and averaged temperature data at several axial positions in X-7 and X-16 are shown in Fig. 55. The temperature suddenly increased by flowing through the rotating bearing on both forward and backward conditions, which contributed to increasing internal energy of the fluid flow. The increase amount of the temperature on the backward condition was almost the same as the forward condition.

Pressure distribution and averaged pressure data at several axial positions in X-7 and X-16 are shown in Fig. 56. Although the pressure slightly decreased by flowing through the rotating bearing on the forward condition as described in section 4.3.3.1, the pressure increased on the backward condition. The distribution indicates that the un-uniformity of the pressure in the downstream was stronger on the backward condition. This is because the coolant flow heading towards outer side of the cavity was formed due to the inner race groove shape on the backward condition. Additionally, the flow velocity as accelerated because the passage area decreases along with the flow direction due to the inner race shape. It is considered that flow structure accelerated towards outer side as the backward flow condition contributed to increasing the fluid flow pressure due to the same mechanism as centrifugal pumps. This is why the pressure on the backward condition increased from the upstream to the downstream, which contributes to increasing the fluid energy.

The fluid heat generation was 1269 W on the forward condition and 1290 W on the backward condition, respectively. The heat generation on the backward condition was slightly larger than the forward condition because the fluid energy was increased on the backward condition due to the inner race groove shape as stated above. However, the difference between the conditions was just 1.69 %.

From the above, it was found that the flow direction condition influenced the pressure distribution especially in the downstream of the bearing although an impact on the fluid heat generation was slight.

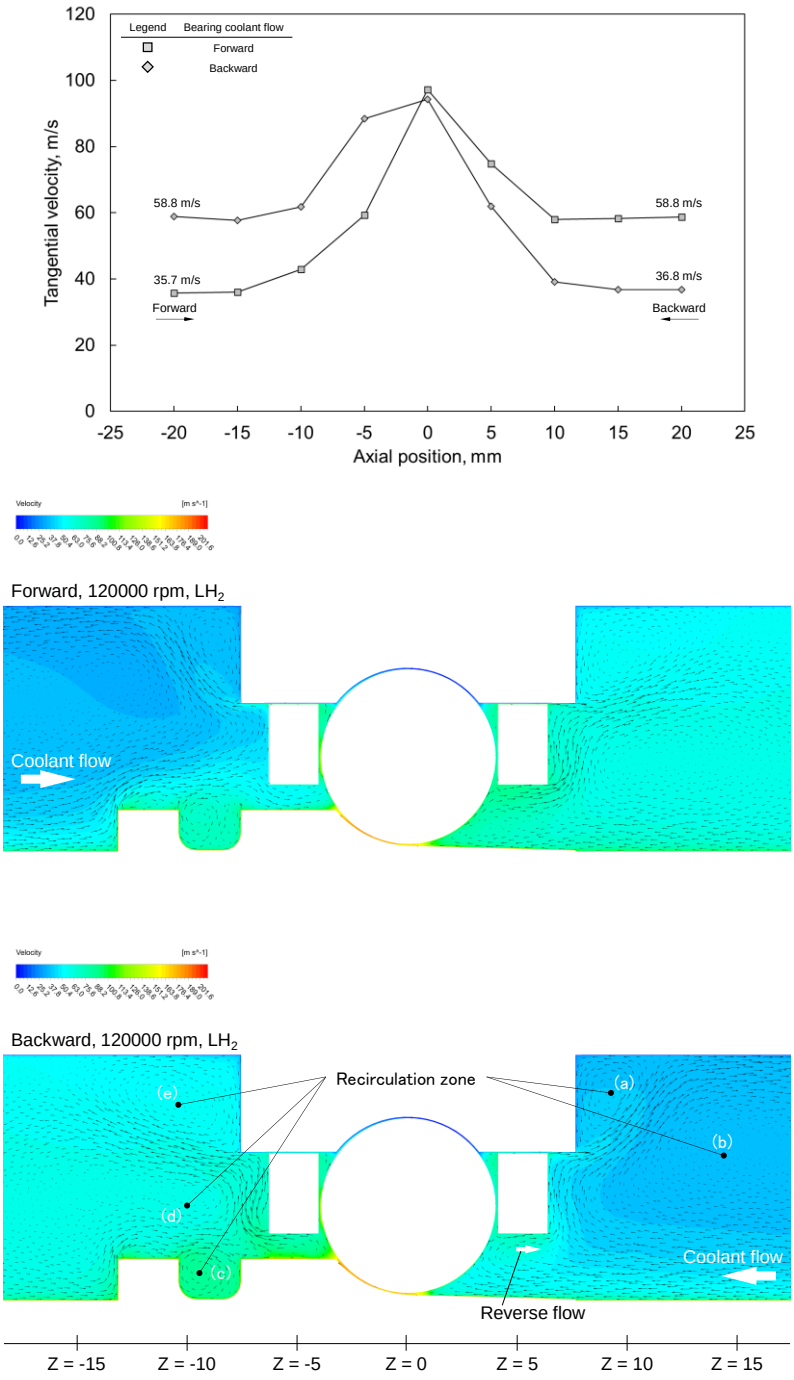

Fig. 54 Velocity distribution of LH_2 around Bearing X in X-7 and X-16 (color maps: velocity, arrows: meridional velocity) (CFD results).

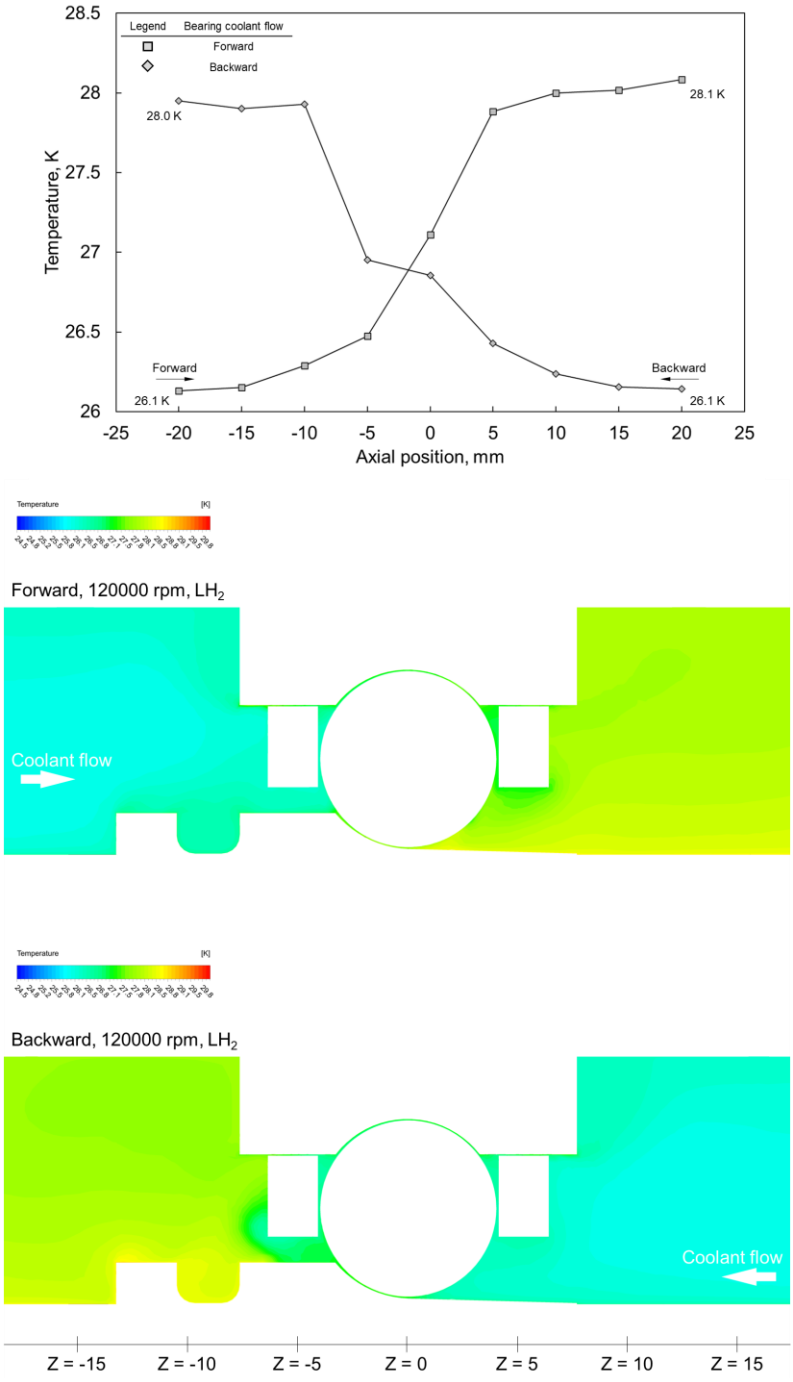

Fig. 55 Temperature distribution of LH_2 around Bearing X in X-7 and X-16 (CFD results).

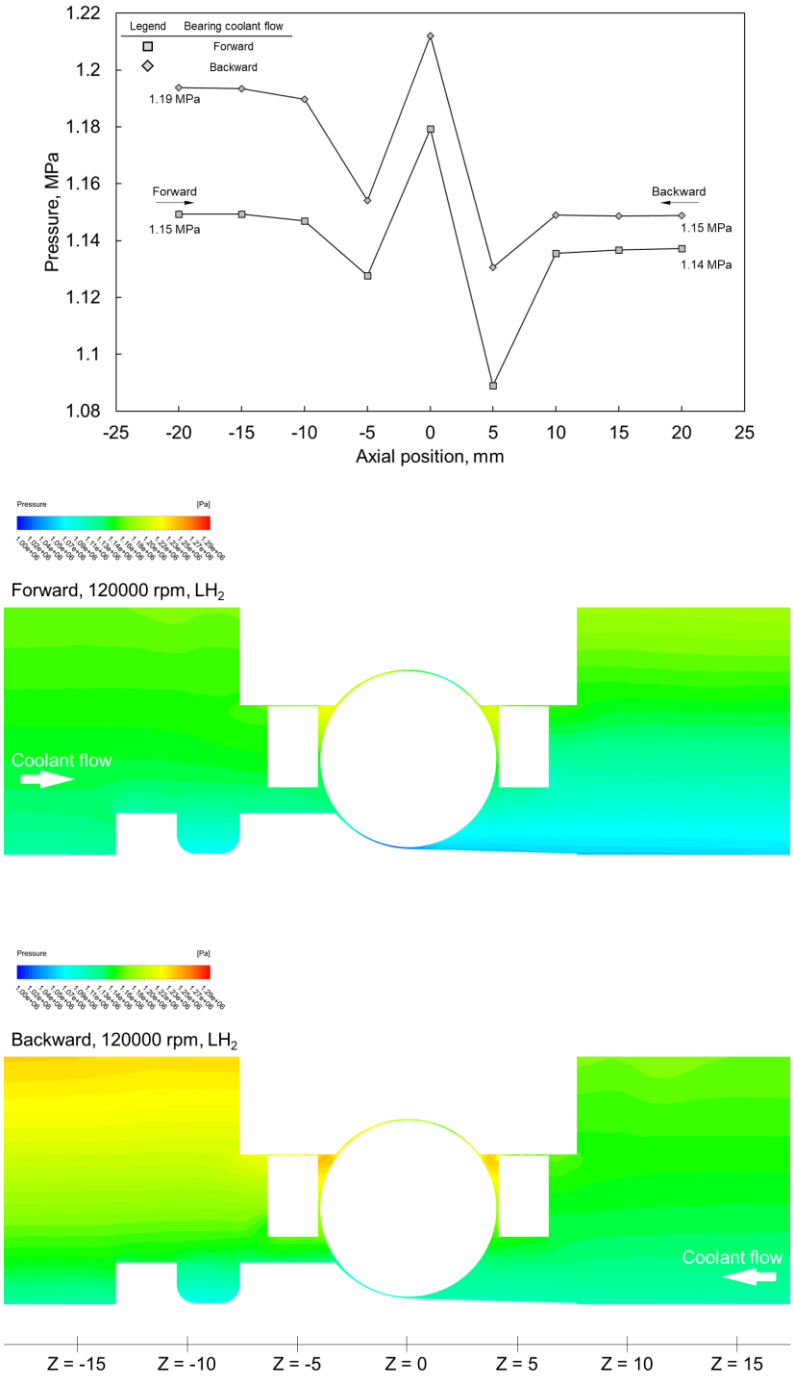

Fig. 56 Pressure distribution of LH_2 around Bearing X in X-7 and X-16 (CFD results).

4.3.3.4. Influences of coolant's mass flowrate

The fluid heat generation of Bearing X in X-15, -17, -18, -19, and -20 is shown in Fig. 57. The heat generation increased with the flowrate, and the increase amount was roughly proportion to the flowrate.

This is caused by the flow velocity which contributes to the fluid drag. Averaged axial velocity data at several axial positions in X-15, -17, -18, -19, and -20 are shown in Fig. 58. The velocity on larger flowrate condition was higher because the flow passage area was the same. It is considered that the characteristics of the velocity should influence the fluid heat generation. Additionally, the increase of the fluid heat generation with flowrate was also caused by increase of fluid momentum, considering Equation (41). This is because the momentum which is gained by the rotating bearing is proportion to the flowrate.

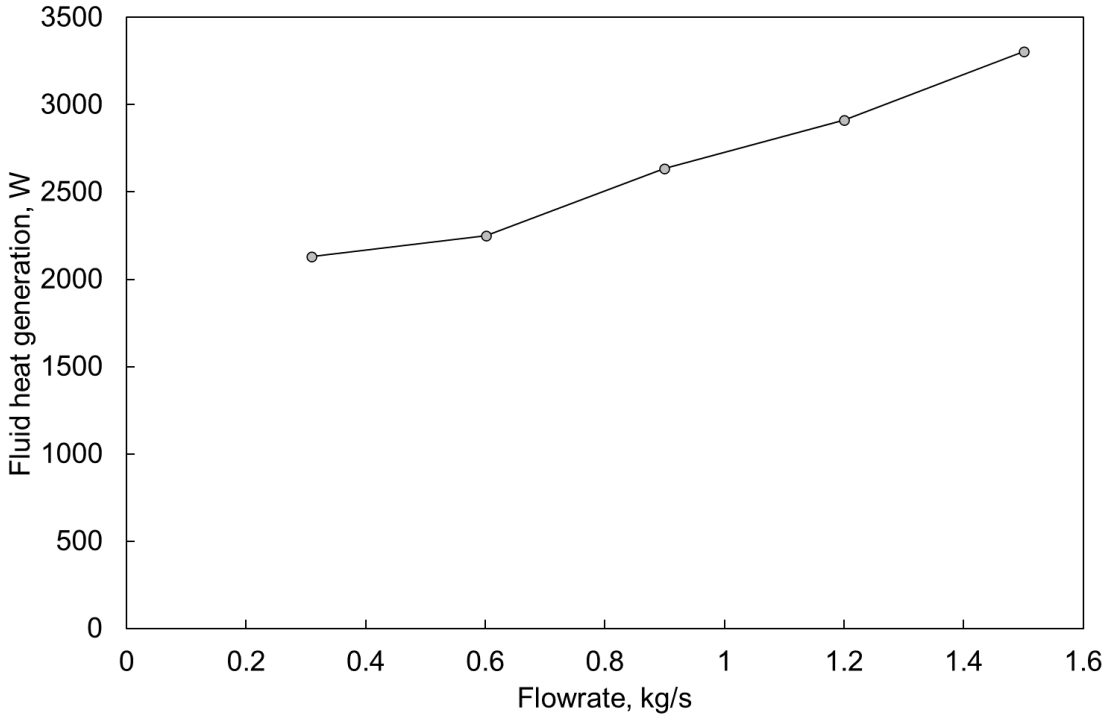

Fig. 57 Fluid heat generation of Bearing X in X-15, -17, -18, -19, and -20 as a function of coolant flowrate.

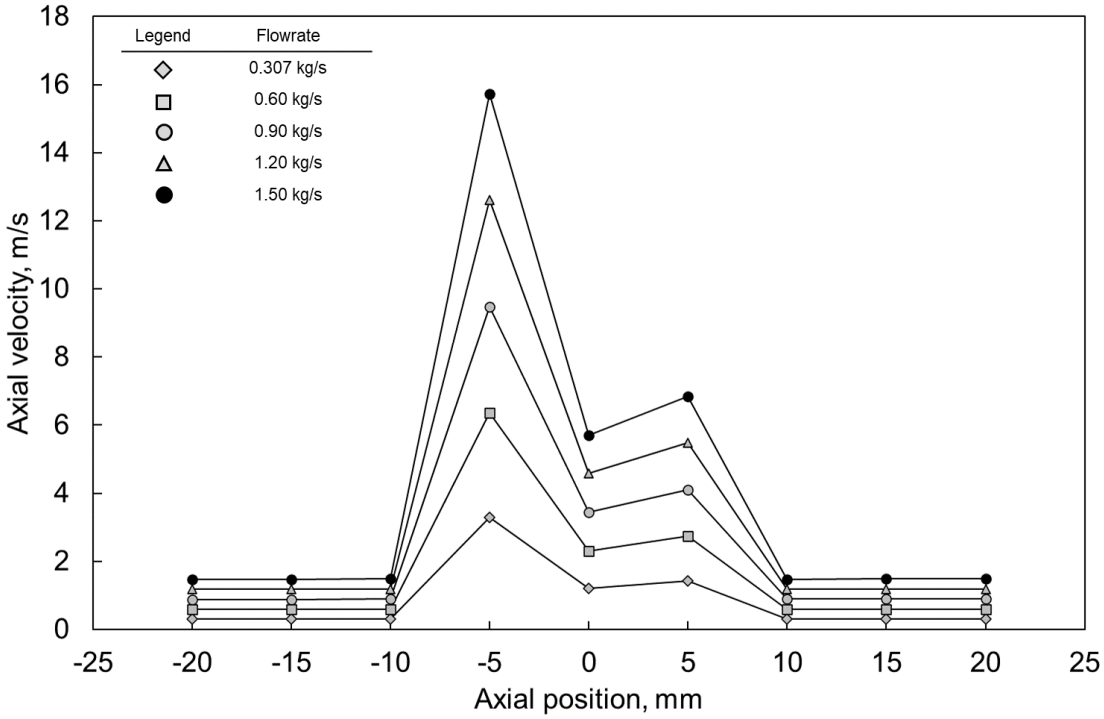

Fig. 58 Averaged axial velocity of LH_2 around Bearing X in X-15, -17, -18, -19, and -20 as a function of axial position (CFD results).

4.4. CFD analysis on Bearing Y

4.4.1. Analysis models

3D models used for CFD analysis is shown in Fig. 59. One ball was included in the calculation domain which corresponded to 36 degrees for Bearing Y out of the whole fluid geometry. The periodic boundary condition was applied to the side wall. Virtual gaps that do not exist in real bearings were set in the contact region between the races and the ball to simplify the mesh generation. The gaps would not significantly influence calculation results of fluid heat generation because volume occupied by the gap is slight. The steady-state calculation was performed in the rotational coordinate system which rotated at the same velocity as the ball revolution motion. The inlet boundary condition was defined as the constant pressure. The outlet boundary condition was defined as the constant flowrate.

The friction heat and the wall heat transfer were not taken account in this calculation to evaluate only the fluid heat generation.

The mesh quality was set in the same element size as Bearing Y analysis.

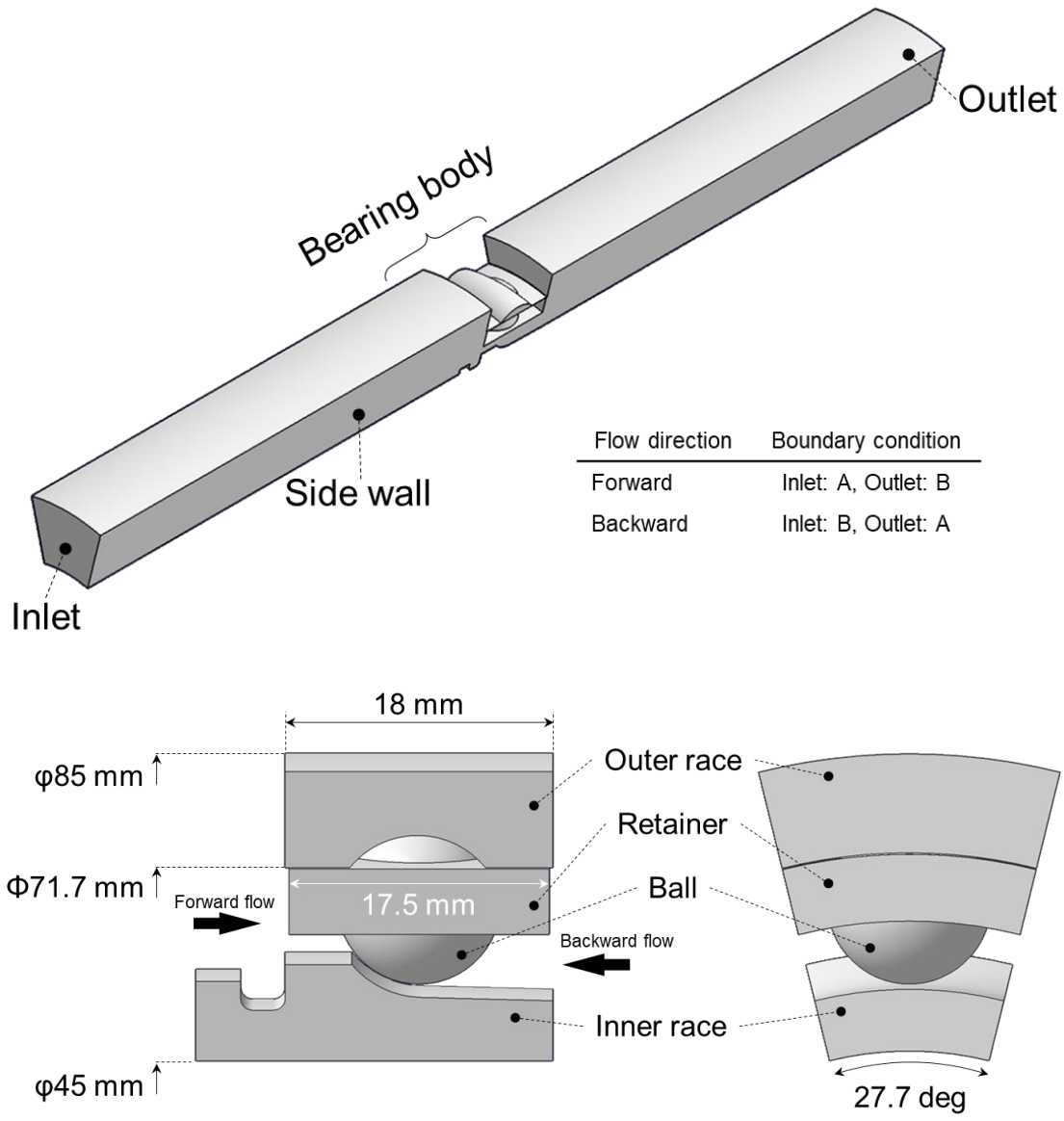

Fig. 59 3D models used for CFD analysis for Bearing Y.

4.4.2. Analysis condition

The analysis conditions are listed in Table 8. The bearing test results mentioned in Chapter 3 indicate that the heat generation in turbopump bearings strongly depended on the rotational speed and the fluid properties such as fluid density. Therefore, LH_2 and LCH_4 were set as the bearing coolant in this analysis to simulate the experimental conditions. The cases Y-1 to Y-12 were calculated on close conditions with the experimental conditions to compare the analysis results with the experimental ones.

Table 8 Analysis conditions of Bearing Y.

Analysis case	Bearing coolant	Mass flowrate [kg/s]	Inlet pressure [MPa]	Inlet temperature [K]	Rotational speed [rpm]	Flow direction
Y-1	LH_2	0.00327	1.66	27.8	0	Forward
Y-2	LH_2	0.00327	1.66	27.8	10000	Forward
Y-3	LH_2	0.00327	1.66	27.8	20000	Forward
Y-4	LH_2	0.00327	1.66	27.8	30000	Forward
Y-5	LH_2	0.00327	1.66	27.8	40000	Forward
Y-6	LH_2	0.00327	1.66	27.8	50000	Forward
Y-7	LCH_4	0.0198	1.52	120.2	0	Forward
Y-8	LCH_4	0.0198	1.52	120.2	10000	Forward
Y-9	LCH_4	0.0198	1.52	120.2	20000	Forward
Y-10	LCH_4	0.0198	1.52	120.2	30000	Forward
Y-11	LCH_4	0.0198	1.52	120.2	40000	Forward
Y-12	LCH_4	0.0198	1.52	120.2	50000	Forward

4.4.3. Analysis results

4.4.3.1. Fluid flow characteristics

CFD results of velocity distribution of Bearing Y in LH_2 environments are shown in Fig. 60. The color maps show the tangential velocity distribution, and the arrows show the meridional velocity. The tangential velocity near moving wall such as the shaft, the inner race, the retainer, the ball tended to be higher due to effects of viscosity although the velocity near the stationary outer race was lower.

The fluid flow near the contact areas between the raceways and the ball was extensively accelerated since the walls moving fast were facing with each other. 5 points described as (a) ~ (e) in the figure show recirculation zones in the vicinity of the bearing. Recirculation zone (a) in the upstream of the bearing was caused by rotational flow that was accelerated by the moving walls and heads towards outer side due to its centrifugal force. Recirculation zone (b) was the fluid flow entering into the inner race's groove and did not have significant influences on the main coolant flow since the recirculation flow was closed only inside the groove. Recirculation zone (c) was formed by the fluid flow colliding with the rotating ball and also had few impacts on the main coolant flow since the size was significantly small. Recirculation zones (d) and (e) in the downstream of the bearing originated from tangential flow accelerated by passing through the rotating ball bearing which contributed to centrifugal force. Although (d) and (e) were similar flow structure to the recirculation zones (a) and (b), they were more developed vortexes since the color maps indicate that the tangential flow of the downstream was faster than the upstream. Recirculation zone (e) which was one of the developed vortexes results in reverse flow that went from the downstream to the ball and the inner race. Averaged tangential velocity data at several axial positions in Y-2, -4, and -6 are also shown in Fig. 60. The tangential velocity was accelerated by passing through the rotating ball bearing, which contributed to generating the recirculating zone stated above and gaining the kinetic energy of the fluid flow. The tangential velocity was larger in higher speed conditions. On 50000 rpm condition, the velocity was accelerated from 28.0 m/s at Z = - 20 to 50.8 m/s at Z = 20.

Temperature distribution data of Bearing Y in LH_2 environment are shown in Fig. 61. The temperature increases in the vicinity of the bearing were caused by differential velocity between the fluid and the walls of the rotating bearing elements. The figure shows that this temperature rise increased with the rotational speed, which contributed to increasing the internal energy of the fluid flow. Averaged temperature data of the tangential flow at several axial positions in Y-2, -4, -6 are also

shown in Fig. 61. The temperature drastically increased near the center of the ball, which contributed to 1.24 K increase on the 50000 rpm condition.

Pressure distribution data of Bearing Y in LH_2 environment are shown in Fig. 62. Although the distribution at the upstream was relatively uniform, the fluid pressure at the downstream increased in the radial direction. The pressure distribution at the downstream was caused by the tangential fluid flow stated above which contributed to generating centrifugal force and pressurizing the fluid toward outer side of the rotation. The pressure near contact areas between the ball and the raceways was decreased. This was caused by much faster fluid flow there which contributed to decreasing the static pressure by Bernoulli's principle. The figures indicate that there was high-pressure region inside the retainer pocket. This is because the fluid flow in the vicinity of the rotating bearing was extensively accelerated by moving walls inside the pocket, which contributed to gaining the fluid energy that increased the static pressure. Averaged pressure data of the rotational flow at several axial positions in Y-2, -4, -6 are also shown in Fig. 62. The graph shows pressure differences from Z = - 20 in each condition to evaluate pressure change due to flowing through the rotating bearing. The pressure at the upstream did not change until the fluid flow enters narrow area between the inner race and the retainer. At Z = -7.5, the pressure differences decreased by the increased velocity in both the rotational direction and the axial direction decreasing the static pressure. Near the ball center, the pressure differences drastically increased to +0.018 MPa because of the high-pressure region inside the retainer pocket described above. The pressure differences at Z = 7.5 that was just downstream of the bearing rapidly decreased due to the accelerated fluid flow by the rotating bearing. In the downstream of Z = 7.5, the static pressure was recovered because the passage area of the cross section increased, and the fluid velocity was decelerated. The net pressure difference of the fluid flow was +0.010 MPa increase by passing through the rotating bearing. It was the opposite result to CFD analysis of Bearing X which indicated pressure drop as described in section 4.3.3.1. As stated above, there are two factors of the

fluid flow characteristics which have impact on the fluid pressure. One is passing through narrow area between the inner race and the retainer, which contributes to pressure loss. The other one is acceleration of the tangential velocity by flowing through the rotating bearing, which contributes to increasing the fluid energy and pressure. Both factors would be considered by the analysis results of the pressure, resulting in pressure rise at the downstream of Bearing Y. It is considered that the pressure rise is dominantly caused by the bearing geometry. The size of Bearing Y is larger than Bearing X, which could contribute to larger area between the inner race and the retainer and relatively smaller pressure loss there. It was found that the bearing geometry had influences on the fluid flow pressure which has significant impacts on turbopump inner flow field.

The fluid heat generation of Bearing Y is shown in Fig. 63. The heat generation exponentially increased with the rotational speed to 777 W at 50000 rpm. The regression curve shown as dotted line in the graph indicate that the heat generation was proportional to the cube of the rotational speed, which was explained by the mechanisms of the fluid heat generation in section 4.3.3.1. The torque data of Bearing X' elements in LH_2 environment are shown in Fig. 64. Each torque increased with the rotational speed. The torque of the inner race was the maximum in all elements is the largest, followed in order by the outer race, the retainer, and the ball. The torque of the ball was the smallest because the surface area was much smaller than the others although the rotational velocity was the maximum as well as the inner race. The outer race generated comparable torque with the inner race due to differential velocity with surrounding fluid although it was a stationary element.

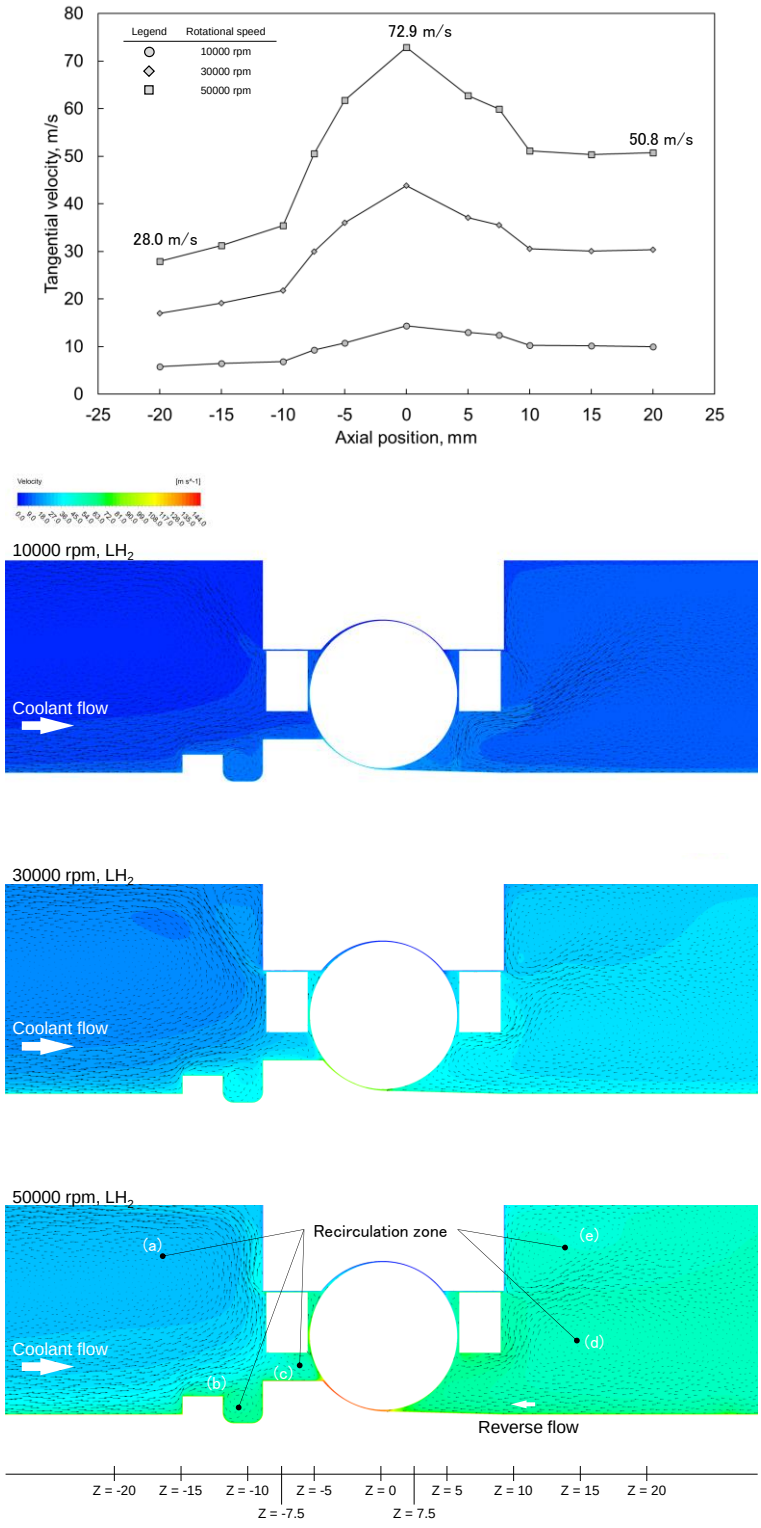

Fig. 60 Velocity distribution of LH_2 around Bearing Y in Y-2, -4, and -6 (color maps: tangential velocity, arrows: meridional velocity) (CFD results).

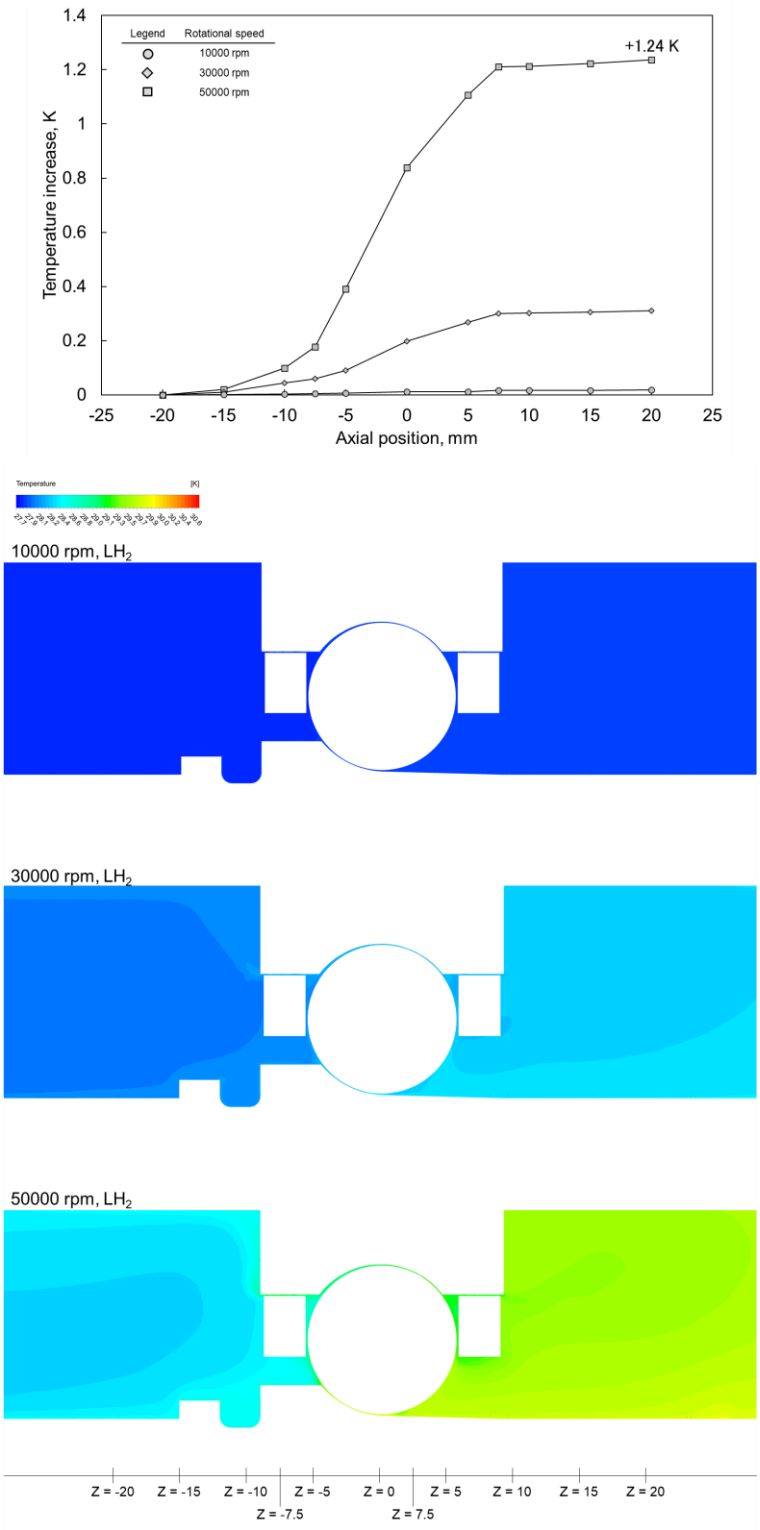

Fig. 61 Temperature distribution of LH_2 around Bearing Y in Y-2, -4, and -6 (CFD results).

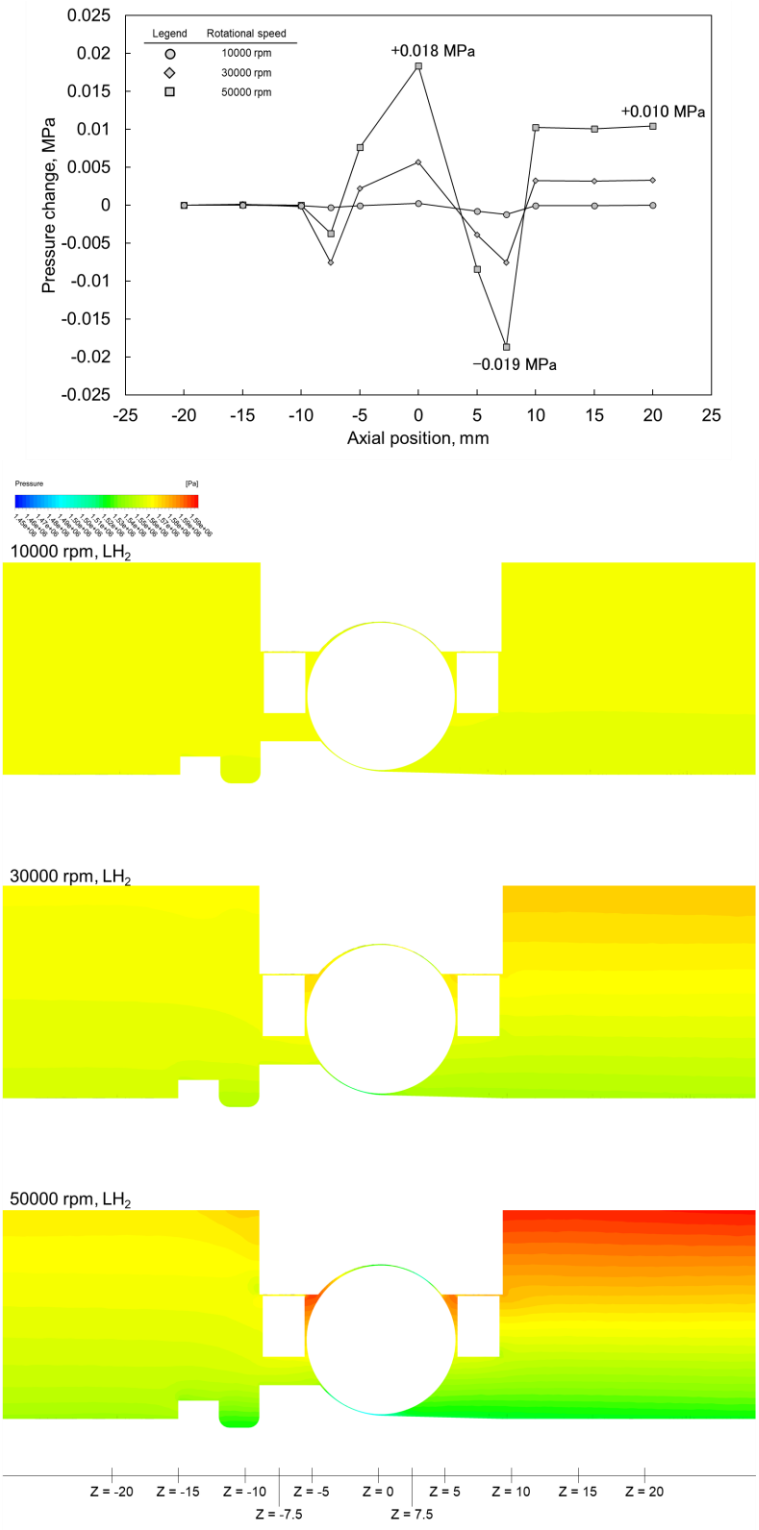

Fig. 62 Pressure distribution of LH_2 around Bearing Y in Y-2, -4, and -6 (CFD results).

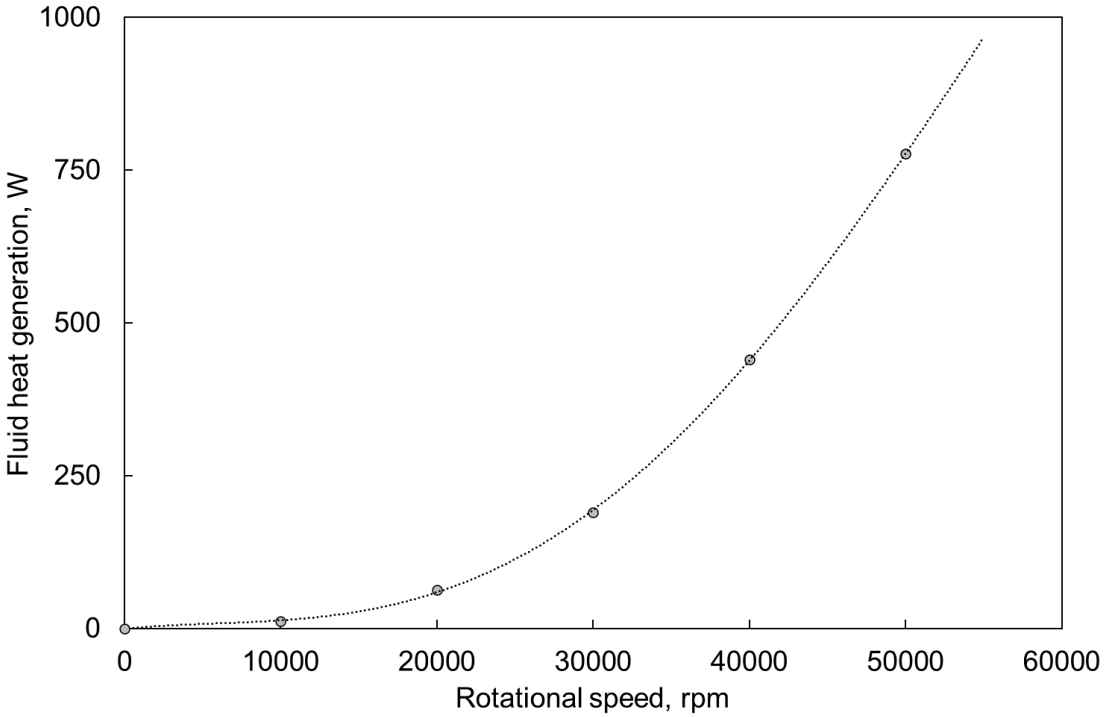

Fig. 63 Fluid heat generation of Bearing Y in LH_2 as a function of the rotational speed (CFD results).

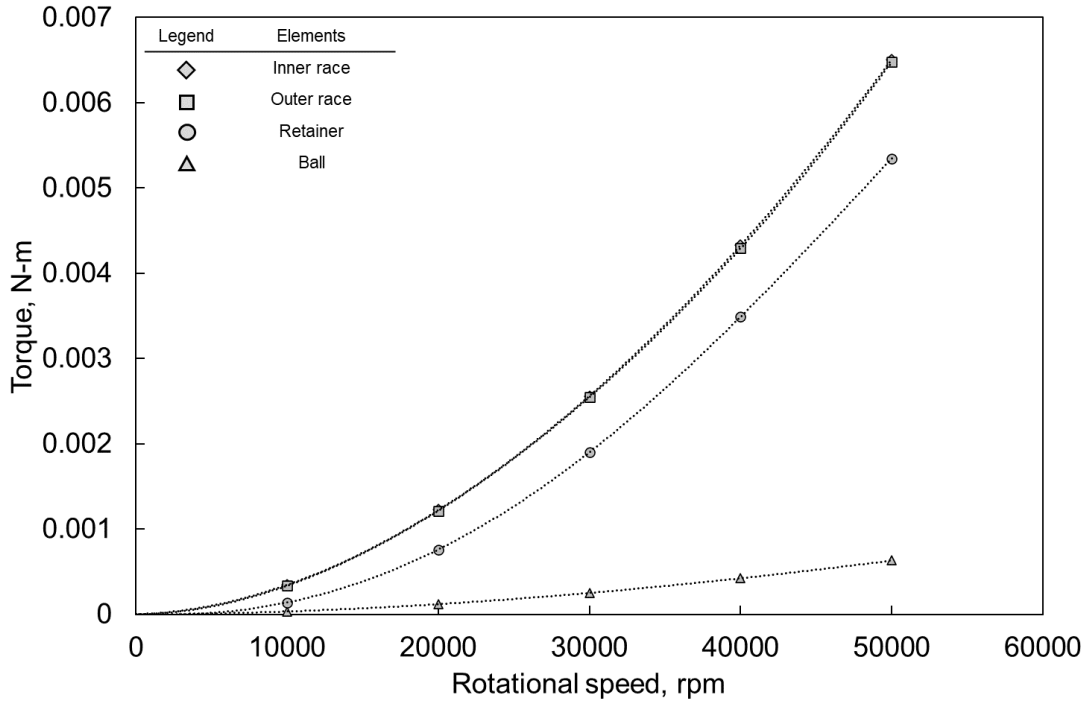

Fig. 64 Torque of Bearing Y's elements about their rotational axes (CFD results).

4.4.3.2. Influences of bearing coolant

Averaged temperature data at several axial positions in Y-6 and Y-12 are shown in Fig. 65. The graph shows temperature differences from Z = 20 in each fluid condition to evaluate temperature increase due to flowing through the rotating bearing because the fluid absolute temperature is significantly different from each other. In both fluid conditions, the fluid temperature suddenly increased when flowing through the rotating bearing, which was the same characteristic as stated in section 4.3.3.1. The increase amounts were dependent on the fluid conditions. The increase from Z = -20 to Z = 20 was +6.12 K in LCH_4, and +1.24 K in LH_2, respectively. This indicates that the temperature increase was much larger in higher density fluid as well as the analysis results of Bearing X.

Averaged pressure data at several axial positions in Y-6 and Y-12 are shown in Fig. 66. The graph shows pressure differences from Z = 20 in each fluid condition to evaluate pressure change due to flowing through the rotating bearing. In both fluid conditions, fluid pressure was significantly low in the vicinity of the rotating bearing (Z = -7.5 and Z = 7.5) and suddenly increased at the center of the bearing (Z = 0), which was almost the same characteristic as stated in in section 4.4.3.1. The pressure difference from Z = -20 to Z = 20 was +0.067 MPa in LCH_4, and +0.010 MPa in LH_2, respectively. The pressure differences due to flowing through the rotating bearing were dependent on the fluid conditions were larger in higher density fluid as well as the analysis results of Bearing X.

Fluid heat generation data in both fluid conditions are shown in Fig. 67. The fluid heat generation exponentially increased with the rotational speed in both conditions. The increase amounts significantly depended on the fluid conditions. The fluid heat generation at 50000 rpm was 5723 W in LCH_4, and 777 MPa in LH_2, which indicates that the heat generation was much larger in higher density fluid as well as the analysis results of Bearing X.

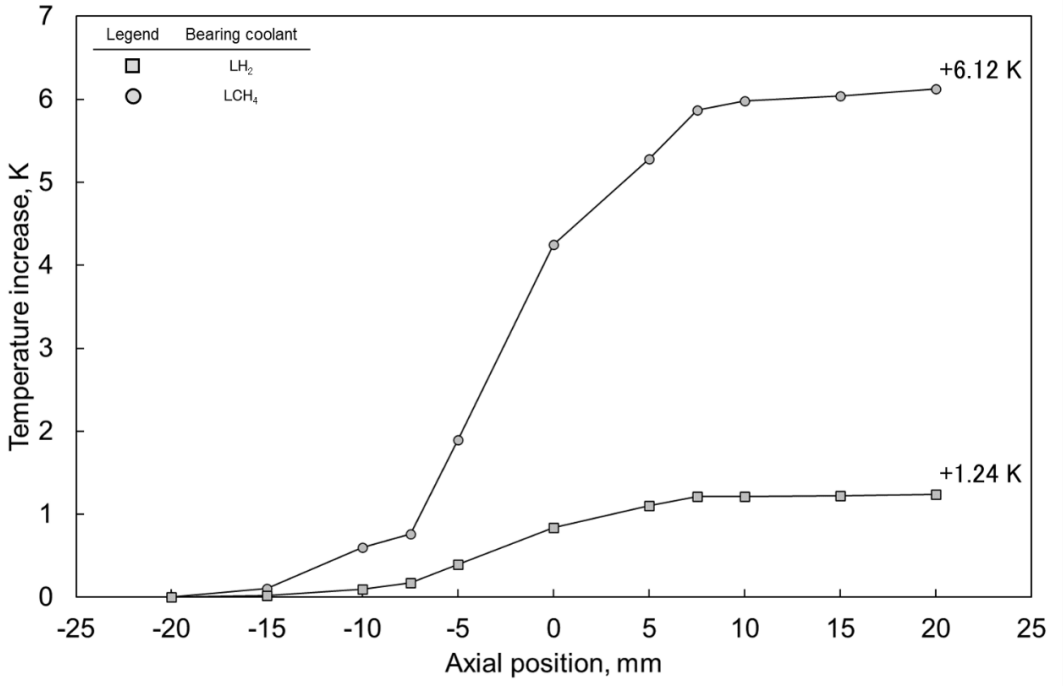

Fig. 65 Averaged temperature difference from Z = -20 in Y-6 and Y-12 as a function of axial position (CFD results).

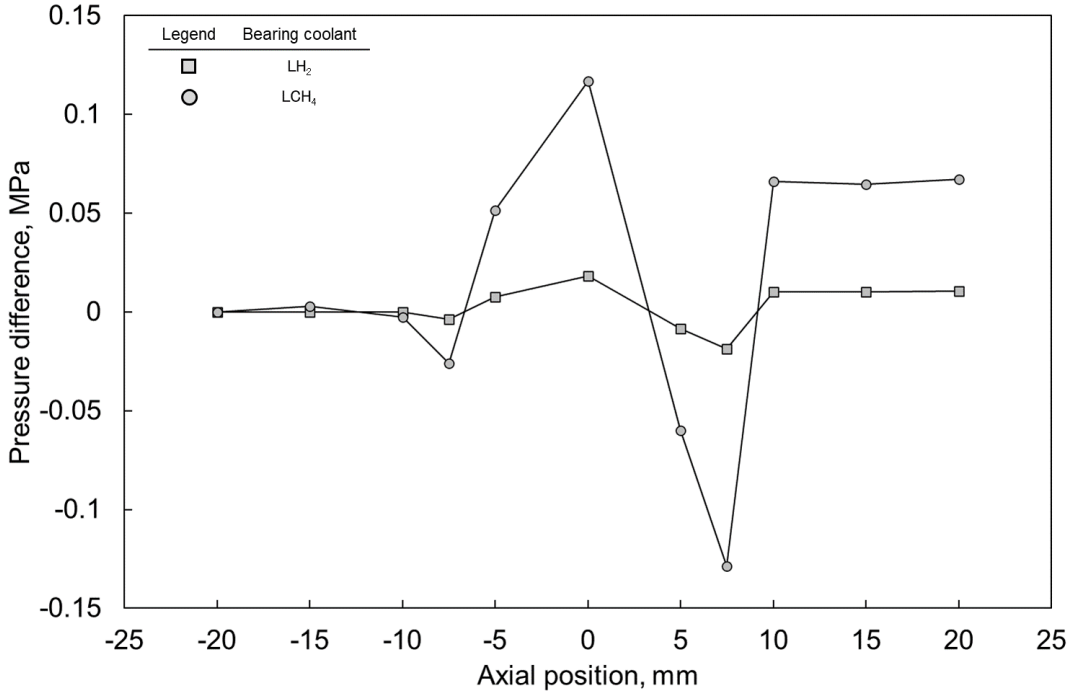

Fig. 66 Averaged pressure difference from Z = -20 in Y-6 and Y-12 as a function of axial position (CFD results).

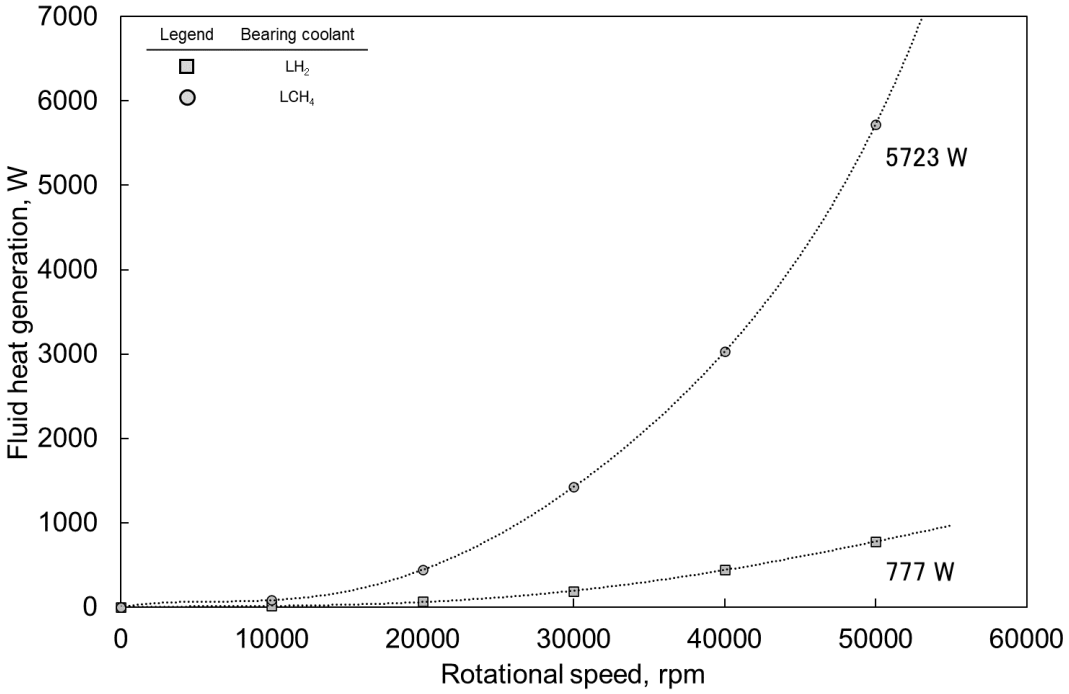

Fig. 67 Fluid heat generation of Bearing Y in LH_2 and LCH_4 environments as a function of rotational speed (CFD results).

4.5. Comparison between 25 mm bearing and 45 mm bearing

Fluid heat generation data of Bearing Y and B in LH_2 and LCH_4 are shown in Fig. 68. The fluid heat generation exponentially increased with the rotational speed in all conditions. The increase amounts significantly depended on both the bearing size and the fluid conditions. The influence of the bearing size was significantly larger in higher density fluid conditions. Fluid heat generation in LCH_4 environment at 50000 rpm was 5723 W for Bearing Y and 654 W for Bearing X, which indicates 8.75 times difference by the bearing size. This significant difference was caused by surface areas which had linear relationship with fluid drag force according to [53].

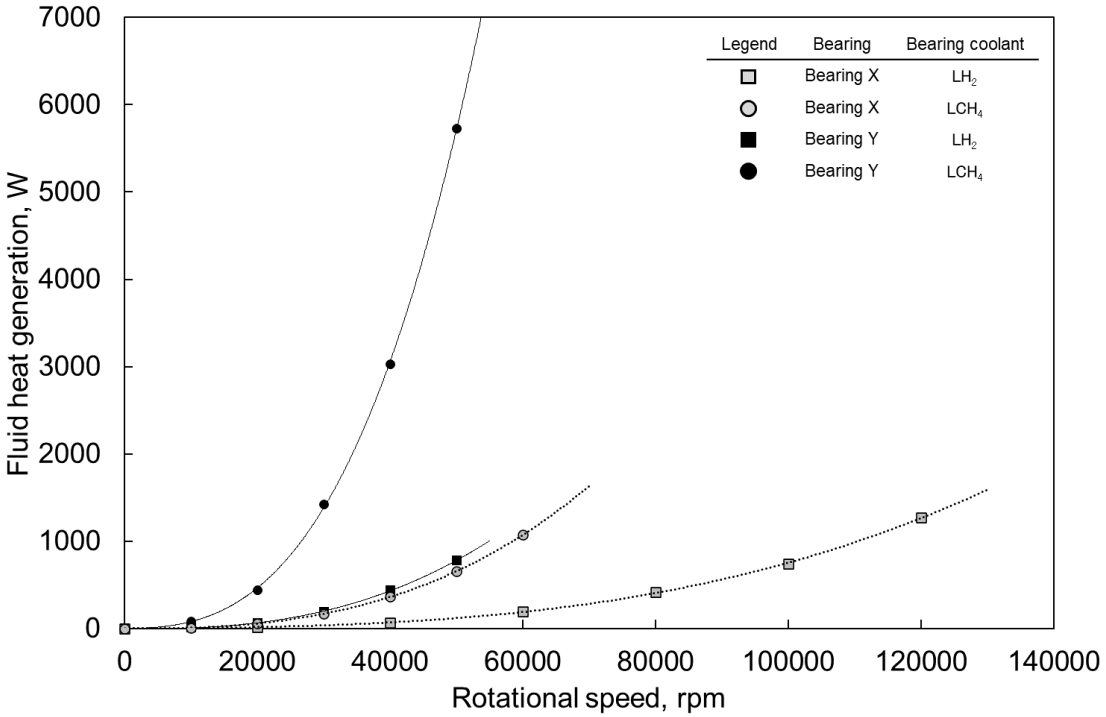

Fig. 68 Fluid heat generation of Bearing Y and Bearing X in LH_2 and LCH_4 environments as a function of rotational speed (CFD results).

4.6. Summary

The fluid heat generation which is one of the heat generation factors in cryogenic bearings was quantitatively investigated by performing CFD analysis in this chapter. Since the characteristics of the fluid heat generation would be influenced by several conditions such as bearing size, rotational speed, coolant fluid, fluid flow direction, and coolant flowrate, the analysis conditions were set by changing these conditions. Bearing X and Bearing Y were used as the calculation models to compare with experimental results in later chapter. Bearing operating conditions were set on several values including the experimental conditions.

Distribution of velocity, temperature, and pressure which have significant impact on fluid heat generation were remarkably complicated and changed with operating conditions. The CFD results

visualized complex characteristics of the fluid flow in the vicinity of bearing cavity. In particular, recirculation zones were formed in the downstream and upstream of the bearing cavity on all conditions. Therefore, the bearing coolant flow was too complicated to predict by adopting simple empirical equations for flat surfaces' fluid flow.

The method for evaluation of the fluid heat generation mentioned in this chapter contributes to improving fidelity of the model for the heat generation of turbopump bearings and optimization of the geometry design in terms of the fluid heat generation.

Chapter 5. Friction characteristics of bearing material under cryogenic environment

5.1. Introduction

Polytetrafluoroethylene (PTFE) is well-known as a solid lubricant because of its excellent lubrication performance. Many studies have been conducted to clarify the wear and friction characteristics against the other material such as metals [56-61]. Makinson et al. conducted PTFE friction experiments and identified that when PTFE slides on clean surfaces there is strong adhesion at the interface [62]. This adhesion leads to transfer of polymer from PTFE to the other surface. Consequently, the friction characteristics are dominated by the shearing phenomena of the slices within PTFE's crystal structure clarified by Bunn [63] and Speerschneider [64] as shown in Fig. 69 and Fig. 70. Therefore, the PTFE transfer to the counterface is considered as the significant characteristics for the friction and wear property. This is why the transfer mechanism has been studied. Cadman et al. identified the presence of metal fluoride on the metal surface after rubbing against PTFE by conducting X-ray Photoelectron Spectroscopy (XPS) analysis [65]. De-Li also researched the wear and transfer mechanisms [66-68] and clarified that the binding between PTFE transfer film and metallic surface is chemical binding and not of a von der Waals nature. Furthermore, the bonds to the metal is via fluorine atoms of the metal fluoride formed on the metal surface during rubbing with PTFE. Also, his experimental results suggest that the fluorine atoms in PTFE possess enough ability to react with active metallic atom in the metal oxide and to form active metal fluoride under the friction test conditions. The chemical reaction process of PTFE friction was discussed by Jintang [60] and Zuo [69]. In the process, PTFE is deformed and broken due to the friction energy, producing molecule radicals. F-ions generated from the breakdown process react with metal oxide or fresh metal surface to form metal fluorides.

The friction characteristics under cryogenic environment have also been studied [70, 71]. This is because PTFE is applied to cryogenic machines in which general lubricants including oil cannot be used since they would freeze due to the low temperature environment. Hübner et al. constructed a cryogenic tribometer that can conduct friction tests under low temperature gaseous or liquid

environment in the temperature range from 4.2 K to room temperature and obtained data on the friction and wear properties [72]. Theiler et al. investigated tribological behavior of PTFE composites at low temperature and the test pieces were examined by conducting chemical surface analyses [73]. They revealed that iron fluorides were formed at the steel surface during the friction under cryogenic environment as well as the studies in room temperature stated above.

Cryogenic turbopumps used in liquid rocket engines are one of such cryogenic machines. Cryogenic ball bearings supporting the main shaft of the turbopump are lubricated by PTFE because adequate loading capability and high-speed performance are required, considering the severe operating conditions of rocket engine turbopumps [12, 13]. They are self-lubricating ball bearings which use a glass cloth-PTFE laminate retainer [10] and one of the most significant parts in an entire rocket system because turbopump bearing failures can cause catastrophic problems involving rocket engine systems. This is why turbopump bearings have been intensively researched by each space agency for a long time. In the Space Shuttle program, NASA had deeply conducted bearing research regarding bearing coolant flow pattern and rolling element material for improving the bearing's wear-resistance performance [6, 7, 9]. JAXA has researched cryogenic ball bearing technologies for development of Japanese flagship launch vehicles [11, 14]. However, these studies were heavily based on experimental approaches that take numerous time and costs. Therefore, performance models of turbopump bearings have been constructed by NASA[39] and JAXA[54] as well as conventional bearings [31-33, 74] in recent years in order to design and evaluate the bearing performance more properly and efficiently than the conventional approach where many experiments are conducted. The models are based on previous studies of bearing analysis [23-25] and can estimate the turbopump bearing performances such as heat generation without carrying out any experiments. To improve the fidelity of the model, the friction characteristics of cryogenic ball bearings under several friction conditions need to be precisely clarified.

Turbopump ball bearings are operated in cryogenic propellant such as liquid oxygen (LOX), liquid hydrogen (LH_2), and liquid methene (LCH_4). Viscosity of such cryogenic propellant is too low to perform hydrodynamic lubrication [34]. Therefore, the rolling elements and races contact directly with each other at friction areas unlike hydrodynamic lubrication conditions. Hence, boundary lubrication is considered as the dominant contact condition in the friction areas even on high-speed conditions. This is why PTFE is used as solid lubricant to perform adequate lubrication and prevent from bearing failures, such as bearing seizure, on several operating conditions. Although there have been numerous studies about the phenomena of PTFE-metals friction and its low-friction characteristics as described above, the friction mechanisms between bearing materials under PTFE lubrication in cryogenic environment have not been researched well. There have been studies conducting chemical surface analyses on rolling elements after cryogenic turbopump testing. Naerheim et al. confirmed the presence of metal fluoride on the surface of bearings used in Space Shuttle main engine turbopump after hot firing engine tests by performing XPS analysis [35]. This study concluded that PTFE decomposed and reacted with the bearing steel to form fluorides under liquid oxygen environment. Nosaka et al. revealed that metal fluoride is formed on the rolling elements operated in LOX, LH_2, and liquid nitrogen (LN_2) [14, 36, 37, 75, 76]. These studies concluded that the formation of metal fluoride prevent form adhesion between rolling elements and races and hold transfer PTFE film on the bearing contact areas leading to low friction characteristics. However, the formation process of metal fluoride that is considered as the significant phenomena of cryogenic bearing lubrication has not been clarified yet. In addition, the friction coefficient between bearing materials under PTFE lubrication has not been quantitatively identified yet.

This research experimentally investigated the friction coefficient of bearing materials via PTFE lubrication under cryogenic environment to clarify the friction characteristics of cryogenic turbopump ball bearings by using a fundamental cryogenic tribometer. The data on the friction coefficient will

contribute to improving the fidelity of the bearing performance models. Since the friction condition is considered to be boundary lubrication, friction experiments were conducted on several contact pressure conditions which are influential on the friction coefficient in such situation. These experiments revealed the dependance of the contact pressure on the friction coefficient. Finally, various analyses were performed after testing to clarify the lubrication mechanisms.

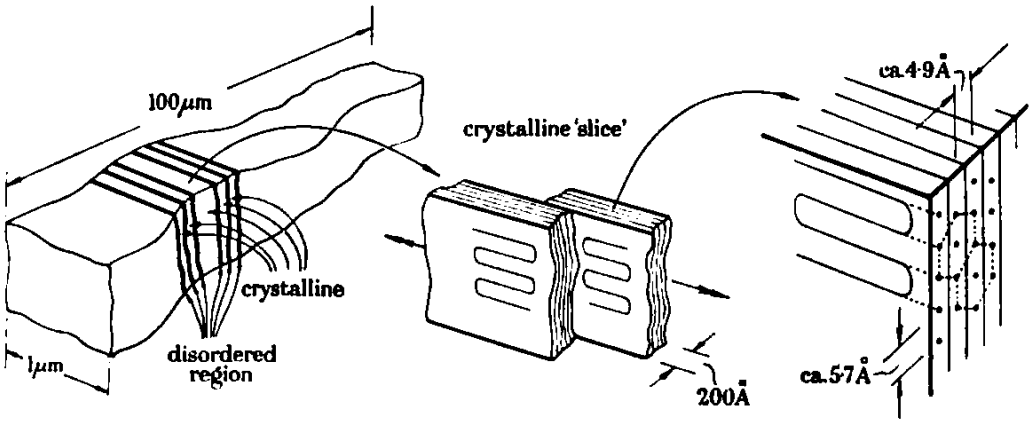

Fig. 69 PTFE structure [62].

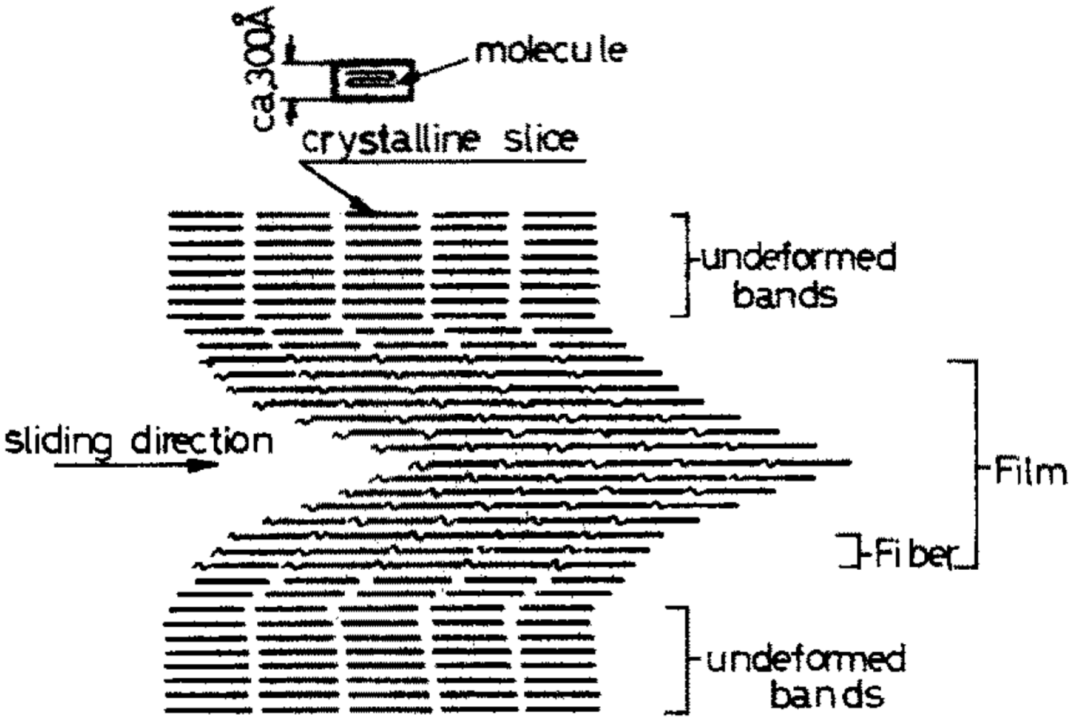

Fig. 70 Banded structure of PTFE film [77].

5.2. Tribometer

In this study, a four ball tribometer that can simulate low-temperature environment and high-contact-pressure friction characterizing the operating conditions of ball bearings used in rocket engine turbopumps was used to precisely evaluate the friction characteristics of bearing materials under cryogenic environment. The tribometer is shown in Fig. 71. A rotating ball contacts and slides against three stationary balls. The stationary balls are loaded identically by the rotating ball. The contact pressure is controlled by changing the normal force loaded by deadweight. LN_2 is supplied to the tribometer and cool the contact areas inside the test chamber. The test chamber is filled with LN_2 during friction tests, which is confirmed by measuring the chamber room temperature. The friction coefficient is calculated by using measured data of normal load and friction force.

The process of friction experiments is shown in Fig. 72. At first, a rotating pin made of the same material as the turbopump bearings' retainer is rubbed against stationary balls made of the bearing races material under cryogenic environment to form PTFE transfer film on their surface. Secondly, the pin is changed to a ball made of the bearing rolling element material. Finally, the rotating ball is rubbed against the stationary balls under cryogenic environment. This process simulates the friction between ball bearing materials under PTFE lubrication occurring inside self-lubricating ball bearings used in cryogenic turbopumps.

The material of the balls is SUS440C for the stationary balls and Si_3N_4 for the rotating ball, respectively. Material properties of SUS440C and Si_3N_4 used in this study are shown in Table 9. Since they are the same materials as the hybrid ceramic ball bearings used in rocket engine turbopumps, the friction characteristics of the bearings' contact can be evaluated by the friction experiments in this study.

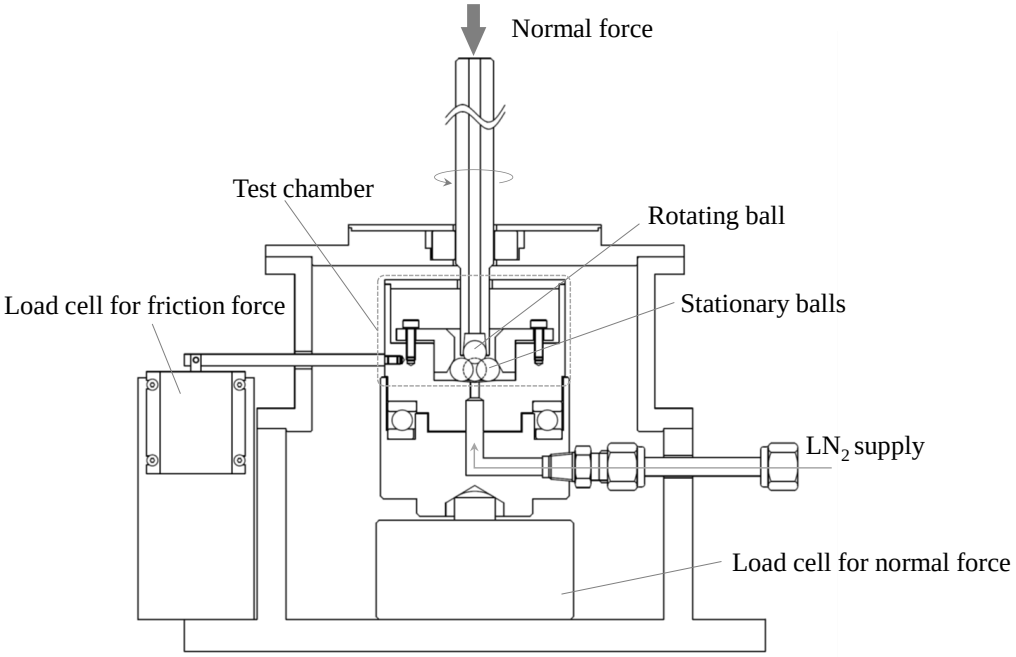

Fig. 71 Four ball tribometer for friction testing under cryogenic environment.

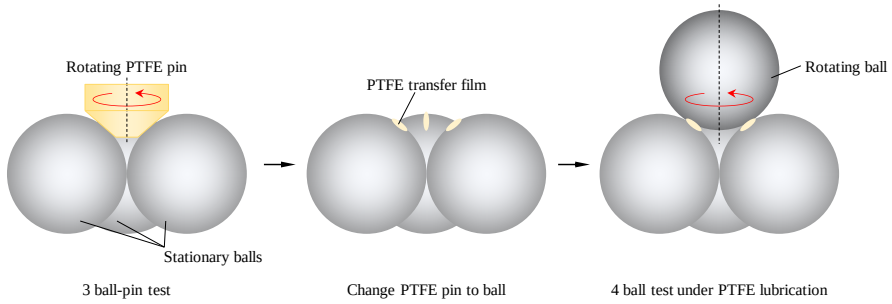

Fig. 72 Process of friction experiments for evaluating friction characteristics of cryogenic ball bearings.

Table 9 Material properties of SUS440C and Si_3N_4

Material property	SUS440C	Si_3N_4
Chemical compositions	C 0.97wt.% Si 0.23 wt.% Mn 0.41 wt.% P 0.022 wt.% S 0.001 wt.% Ni 0.11 wt.% Cr 16.62 wt.% Mo 0.41 wt.% Co 0.03 wt.% Fe Balance	Y 3.4 wt.% Al 4.2 wt.% Ti 0.78 wt.% Si_3N_4 Balance
Ultimate strength	671 MPa	1053 MPa
Vickers Hardness	728	1550

5.3. Test condition

The normal load of the three ball-pin tests before each four ball test was set around 100 N which contributes to enough PTFE transfer on the stationary balls' surface. Four ball tests conditions are listed in Table 10. Initial contact pressure was changed as a main parameter of the four ball friction tests in the pressure range from 979 MPa to 2645 MPa as calculated values of the maximum hertz contact pressure. The pressure range is comparable with contact conditions of hybrid ceramic ball bearings for cryogenic turbopumps [16]. Rotational speed in the three ball-pin tests and four ball tests was set at 60 rpm.

LN_2 which is a simulant of the turbopump bearing coolant was supplied to the tribometer as coolant fluid. The flowrate was set to perform enough cooling capability on the contact area and maintain the test chamber condition filled with LN_2. The flowrate was not measured by a flowmeter although it can be estimated to be around 0.014 kg/s by calculating from the amount of LN_2 used during tests and the tests' duration. The chamber room temperature during tests was around -195.8 deg C regardless of

friction conditions which showed that the chamber was maintained filled with LN_2. This temperature condition simulates one in the vicinity of ball bearings used in rocket engine turbopumps which show temperature of liquid-phase cryogenic coolant. Although rocket engine propellant is supplied as the bearing coolant in turbopumps, the simulant was used in this study because it is much difficult to conduct tribology experiments under safe operation of rocket engine propellants which easily lead combustion reaction. Since LN_2 is often used as a simulant for several tribology tests to evaluate the performance of turbopump's parts such as bearings and shaft seals under cryogenic environment, the friction characteristics can also be evaluated properly in this study.

As described in section 5.2, three ball-pin tests were conducted before all four ball tests listed in Table 1. For comparison, four ball test using fresh balls without PTFE transfer film by three ball-pin test was conducted in one test case defined as CASE-0. In CASE-0, the normal force for each stationary ball was intended to be set around the same condition of contact pressure as CASE-3 for comparison. The force resulted in 9.74 N which was 1.32 N different from CASE-3 since it is significantly difficult to control the force accurately in the range of lighter force in this tester.

Table 10 Four ball tests conditions.

CASE No.	Normal force for each stationary ball, N	Maximum Hertz contact pressure, MPa
CASE-1	2.59	979
CASE-2	5.67	1271
CASE-3	8.42	1451
CASE-4	13.52	1699
CASE-5	17.72	1859
CASE-6	23.23	2035
CASE-7	25.96	2112
CASE-8	28.72	2184
CASE-9	32.47	2275
CASE-10	41.62	2472
CASE-11	51.03	2645

5.4. Test result

5.4.1. Friction coefficient

The friction coefficients from CASE-1 to CASE-10 are shown in Fig. 73. Each plot shows time-averaged data for 5 seconds during steady state condition in the friction tests, and error bars indicate the standard deviation of time history data. The friction coefficients of CASE-0 and CASE-11 were much higher than the other test cases and 0.911 for CASE-0 and 1.274 for CASE-11, respectively. In CASE-0, since there was no lubrication in contact area, SUS440C and Si_3N_4 contacted directly with each other, which contributed to higher friction coefficient. In CASE-11, the contact pressure seemed to exceed the load capacity of lubrication film originated by PTFE transfer. Consequently, the lubrication film was broken, and bearing materials contacted directly with each other. This result was consistent with studies by Du et al. which showed that tribological damage phenomenon and failure type in multilayer tribology systems with polymer is affected by normal contact load [78, 79]. Furthermore, according to [16], the limitation of load capacity in hybrid ceramic ball bearings for

cryogenic turbopumps was about 2690 MPa in LH_2 environment. The test results in CASE-11 showed good agreement with these results in terms of the limitation of load capacity.

In the test cases from CASE-1 to CASE-10, PTFE transfer film seemed to perform lubrication within its load capacity unlike CASE-0 and CASE-11. The results of the friction coefficient range from 0.241 to 0.469 which are remarkably smaller than CASE-0 and CASE-11. These definite low-friction characteristics are caused by PTFE lubrication. According to [80], friction coefficient of pure PTFE-steel at LN_2 environment is about 0.05. The friction condition in this study is SUS440C-Si_3N_4 sliding under PTFE lubrication and clearly different from PTFE-steel sliding conditions which have been comparatively studied. This should be the reason why the friction coefficient range in this study was different from the PTFE-steel sliding.

As shown in Fig. 73, the friction coefficient had a clear dependency on the normal force. The friction coefficient decreased with normal force on the conditions up to 25.96 N which contributes to 2112 MPa of Hertz contact pressure. To the contrary, it increased on the conditions more than 25.96 N. This dependency seems to be caused by friction and lubrication mechanisms. Therefore, several surface analyses were conducted to clarify the mechanisms. Test cases of CASE-3, -5, -7, and -9 were selected for the analyses because test results of those cases characterized the dependency.

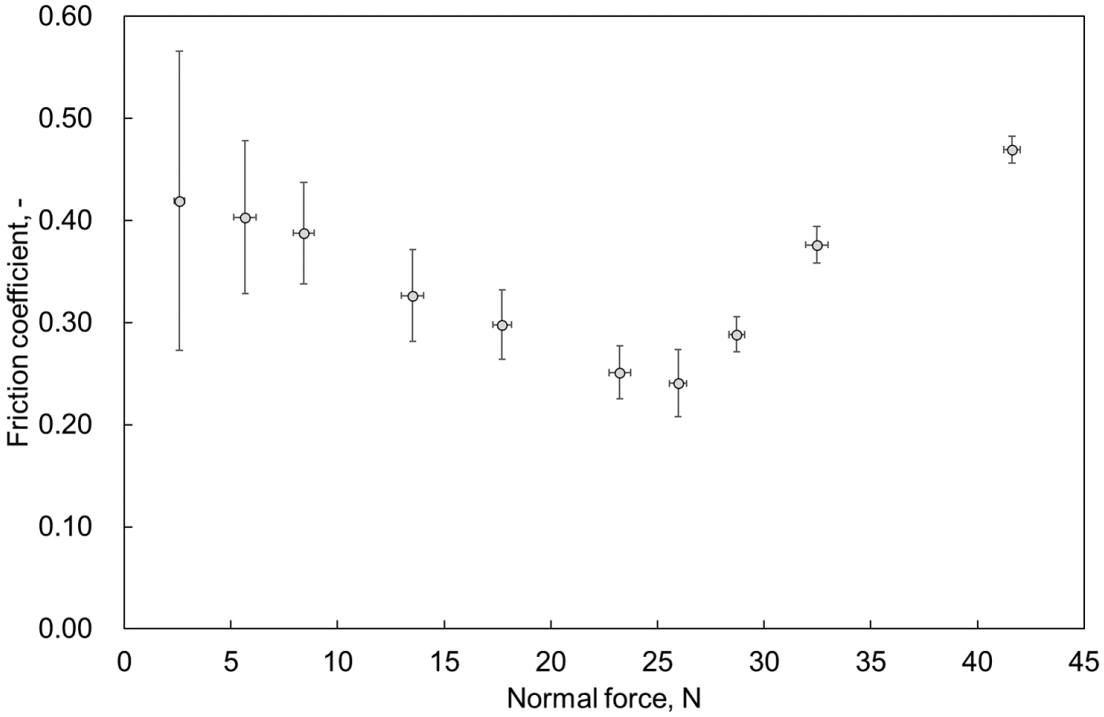

Fig. 73 Friction coefficient of four ball tests under LN_2 environment as a function of normal force.

5.4.2. Surface analyses

5.4.2.1. Microscopic analysis

Microscopic images of friction areas on the stationary balls of representative cases are shown in Fig. 74. In all cases, round-shape marks were observed in the friction areas. The marks indicate the sliding and contact areas with the rotating ball. The contact between the stationary balls and the rotating ball was elastic contact because the normal force applied was low enough not to cause any plastic deformation. Therefore, the mark's diameter is larger in test cases of higher normal force.

As shown in (A) of Fig. 74, some amount of polymer accumulates upstream of the friction area. This was carried and transferred from the rotating ball. Since there is contact pressure in the friction area, the lump of polymer would be ground and broken into thin fragments due to the friction under the

contact pressure. Consequently, the fragments of the polymer (B) would entry into the friction area, and the remaining (A) stay in the upstream edge. Therefore, the fragments should be polymer originating from PTFE transfer film and adhere on the friction area of the stationary ball. These substances should perform lubrication and will be identified by XPS analysis described later. Although there is no visible film in the friction area in CASE-3, extremely thin lubrication film should exist on the friction area, considering the better lubrication performance in CASE-3 than CASE-0.

Microscopic images of friction areas on the rotating balls are shown in Fig. 5. Friction marks on the rotating balls are not clear as the round-shape marks on the stationary balls. The adhesion of polymer (C) is observed in CASE-5, 7, and 9. In addition, the density of the polymer is higher in lower friction coefficient cases. Therefore, the amount of lubrication film adhering on the friction area may relate with lubrication performance. There is no visible film in the friction area in CASE-3 unlike the other cases, and this can contribute to higher friction coefficient.

From the above, transfer film formed by the friction in the three ball-pin test is a significant factor to perform lubrication between bearing materials in the four ball test under cryogenic environment. Furthermore, because the remaining lubrication film on the contact area even during the friction process seems to relate with the friction characteristics, the mechanism of the film adhesion is needed to be clarified.

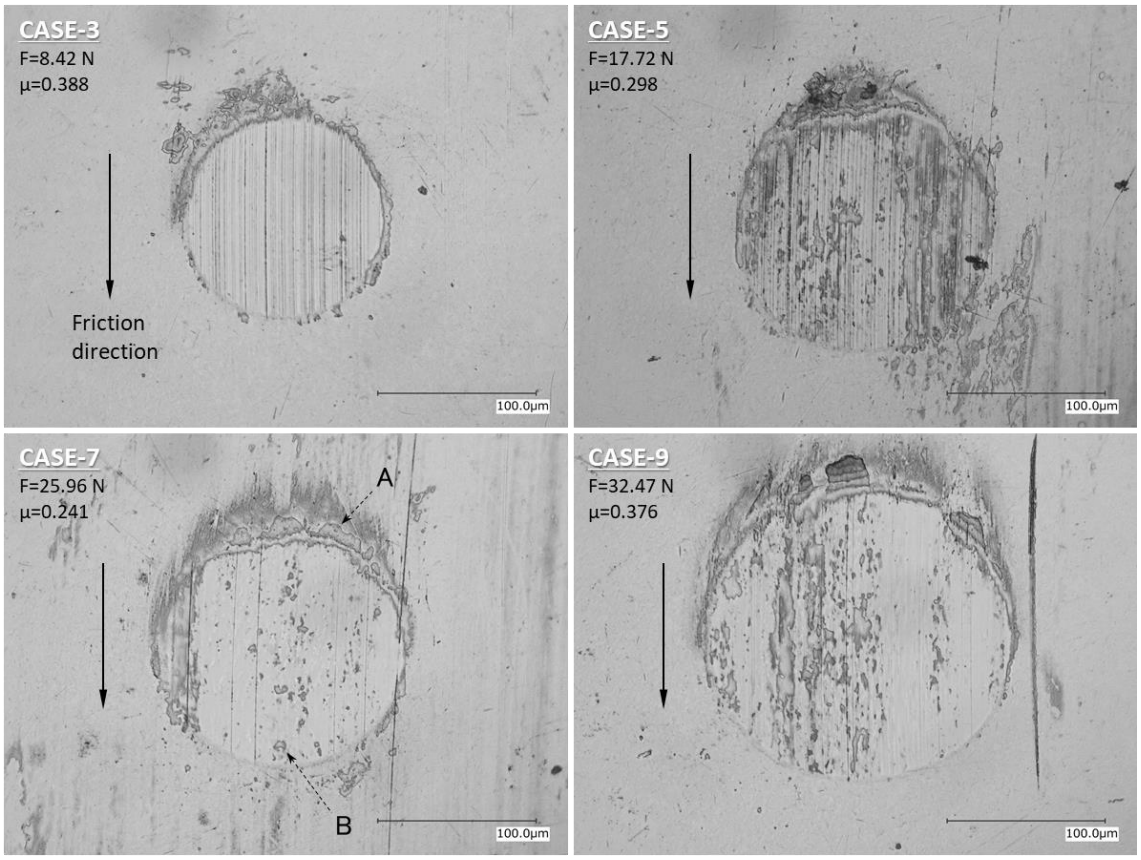

Fig. 74 Microscopic images of friction areas on SUS440C balls.

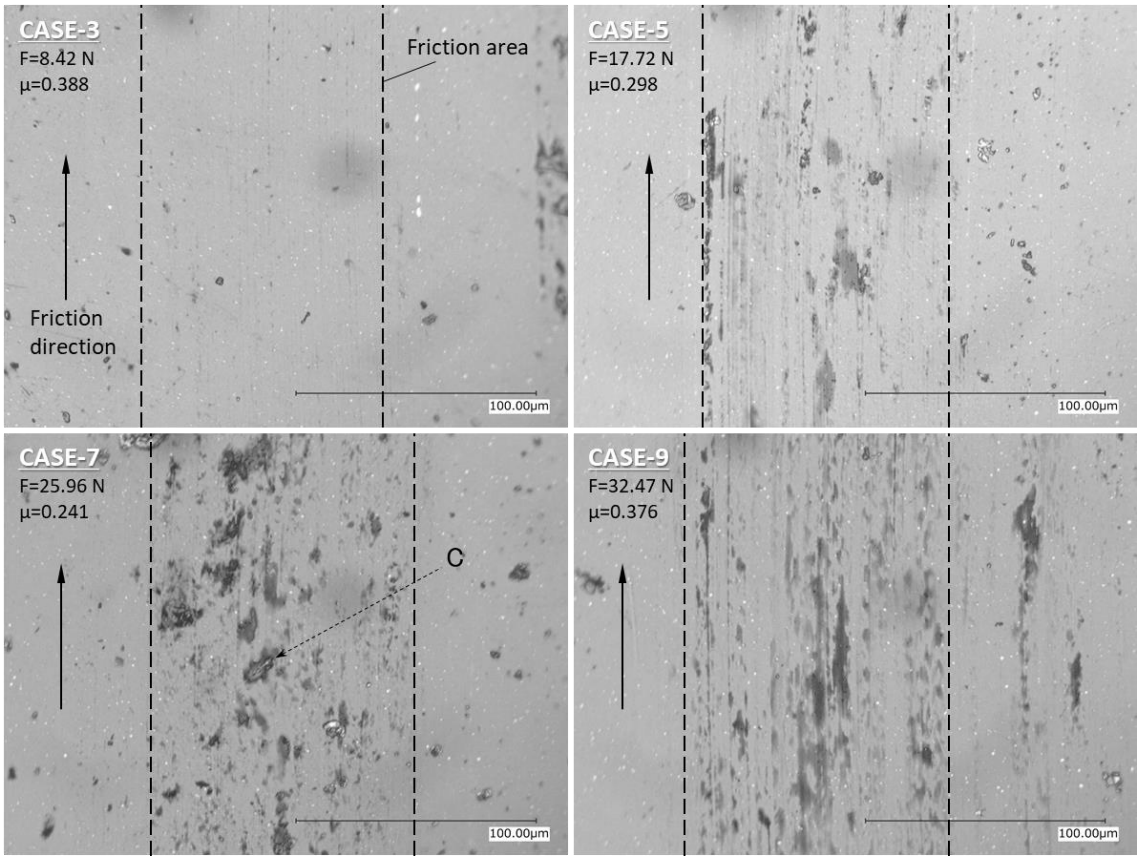

Fig. 75 Microscopic images of friction areas on Si_3N_4 balls.

5.4.2.2. Surface profile analysis

Surface profiles of the stationary balls and the rotating balls were examined by white-light interferometry. The profiles of the stationary balls of representative cases are shown in Fig. 76. The graphs show averaged profiles of the three stationary balls for each test case. Although obvious wear was observed on the stationary balls as shown in the figure, no wear was detected on the rotating balls in all cases including CASE-0. Wear behavior is dependent on material characteristics. Since the wear resistance of Si_3N_4 is much superior to SUS440C, only SUS440C was worn during the SUS440C-Si_3N_4 friction under cryogenic environment.

In all test cases, the wear depth is larger in the center of the friction areas. This depth distribution is caused by the contact pressure distribution where the maximum pressure is located in the center of

contact area considering a contact between spherical objects.

The wear amount of the stationary ball in CASE-0 is much larger than the other cases. In addition, the stationary ball is worn along the shape of the rotating ball which has the same curvature as the stationary balls. To the contrary, wear amounts of the other cases were comparably smaller, and the profiles tend to be flat. These results show that the influence of contact pressure on wear amount is different between cases with and without PTFE lubricant. The better wear-resistance characteristic was caused by an effect of the lubrication film which prevented the stationary balls from sever wear by performing lubricated smooth friction while excessive wear occurred on the stationary balls with higher friction coefficient in CASE-0.

Although the wear depth in all test cases with PTFE lubrication is around 1.0 μm regardless of the normal load conditions, the diameter of the wear marks tends to increase with normal load. This is because the diameter of the initial contact area due to elastic deformation depends on contact pressure. This result is consistent with previous studies that showed that contact area and deformation types in scratch tests are affected by normal contact pressure [81, 82].

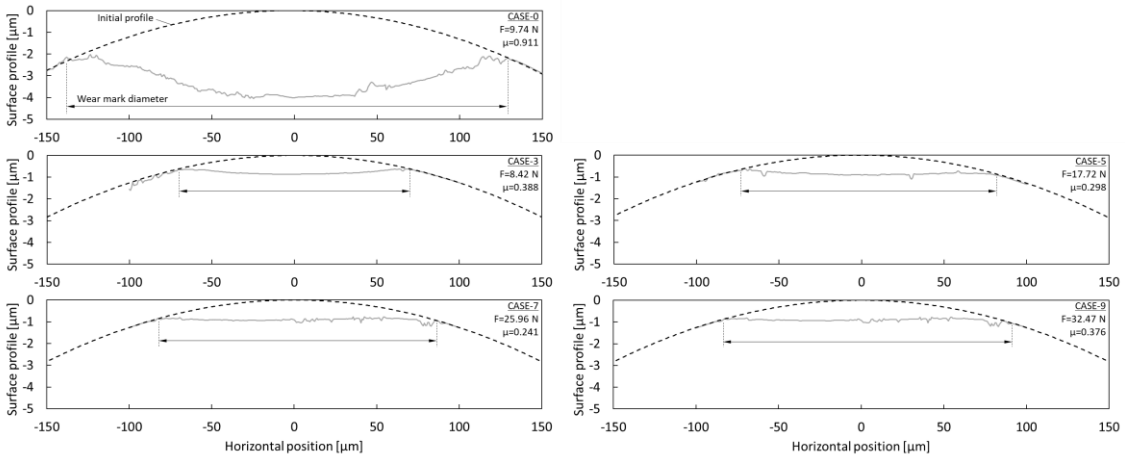

Fig. 76 Surface profiles of friction areas on SUS440C balls.

5.4.2.3. XPS analysis

XPS analysis was performed on the stationary balls and the rotating balls of the representative cases. XPS spectra were acquired by using a monochromatic Al Kα source operating at 150 W. The analysis area was 110 μm diameter circle and included in the friction area. Depth analysis was conducted by etching with Ar-ion gun. The etching duration each time was 5 sec. The etching rate is 20 nm/min of SiO_2 equivalent.

F (1s) spectra of the stationary balls are shown in Fig. 77. PTFE peak which is located around 689.5 eV was mainly detected before the Ar-ion etching in all cases. After one etching, the PTFE peak decreased, and 685.7 eV peak that corresponds to metal fluoride was clearly detected. In addition, 687.7 eV peak that corresponds to C-F which would originate from PTFE was slightly detected. After five times etching, both peaks decreased. Finally, all peaks almost disappeared in all cases after ten times etching. Regarding the metal fluoride peak, possible compositions are iron fluoride and chromium fluoride, considering SUS440C components. However, it is difficult to identify the compositions clearly because their peaks in F (1s) spectra are extremely close and the oxide peaks in Fe (2p) spectra and Cr (2p) spectra are at almost the same positions as the fluoride peaks. From the above, XPS analysis results indicate that PTFE film covers on the surface of the friction area and that metal fluoride exists beneath the PTFE film on the stationary balls' surfaces. The formation process of the metal fluoride is considered to be as follows. PTFE transferred from the pin during the three ball-pin test is broken due to friction energy loaded by the rotating ball. During the break-up, F-ions are generated and react with metal oxide or fresh metal on the surface of the stationary ball. This process is the same as friction tests in room temperature described in section 5.1 even though the friction test in this study was conducted in cryogenic environment.

F (1s) spectra of the rotating balls are shown in Fig. 78. PTFE peak was detected before etching in all cases as well as the stationary balls. Slight peak was also detected around 685.8 eV. It is evident

that the peak is not originated by metal fluoride because no peak was detected in Fe (2p) and Cr (2p) spectra. This peak is considered to be Si-F according to [83, 84]. After etching, Si-F peak was apparently detected in CASE-3 and -9 in addition to 687.4 eV and 689.0 eV which seem to correspond to Si-F_2 and Si-F_3 bindings while the peaks were also slightly observed in CASE-5 and -7. Strong Si-F peak remained in CASE-3 and -9 even after ten times etching though the peak almost disappeared in CASE-5 and -7. These results indicate that, on the outermost surface of the friction area, PTFE film existed in all cases. Beneath the PTFE film, definite Si-F, Si-F_2, and Si-F_3 bindings were present in CASE-3 and -9 and marginally existed in CASE-5 and -7. The formation of those bindings is considered to be caused by direct contact between Si_3N_4 and SUS440C without enough PTFE lubrication. The direct contact would apply larger friction energy to the Si_3N_4 surface, which promote chemical reaction between F-ion and Si_3N_4. The reaction would lead to generating the Si-F, Si-F_2, and Si-F_3 bindings.

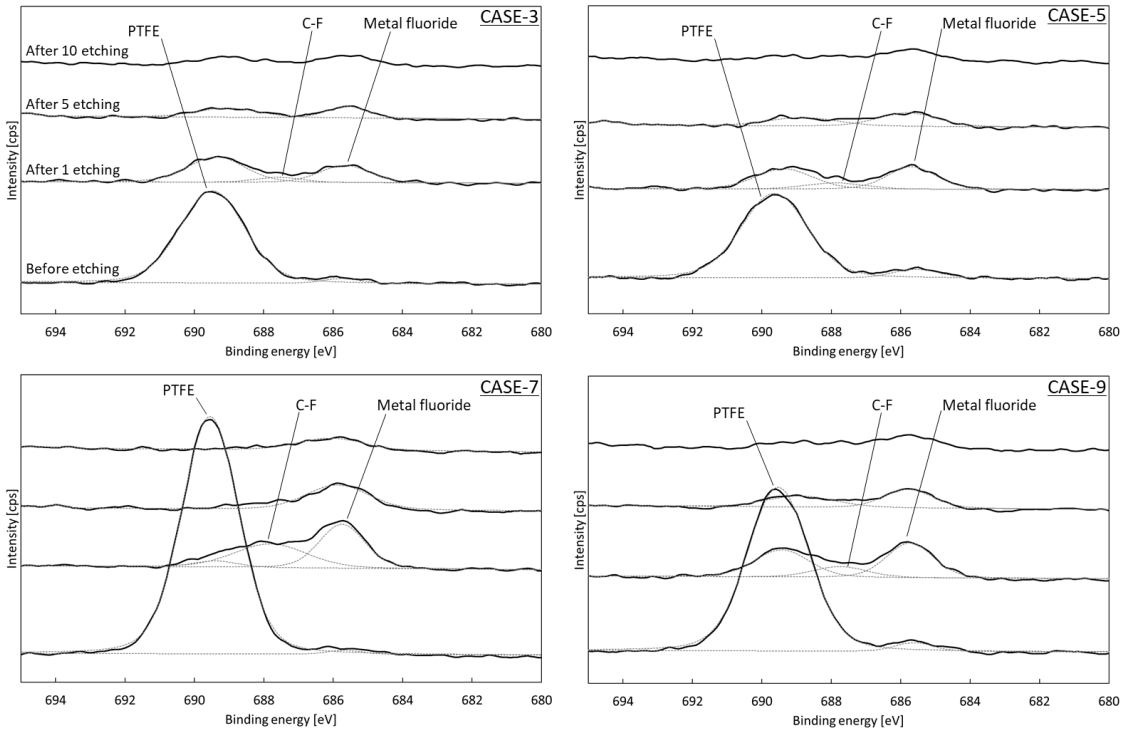

Fig. 77 XPS F (1s) spectra of friction areas on SUS440C balls.

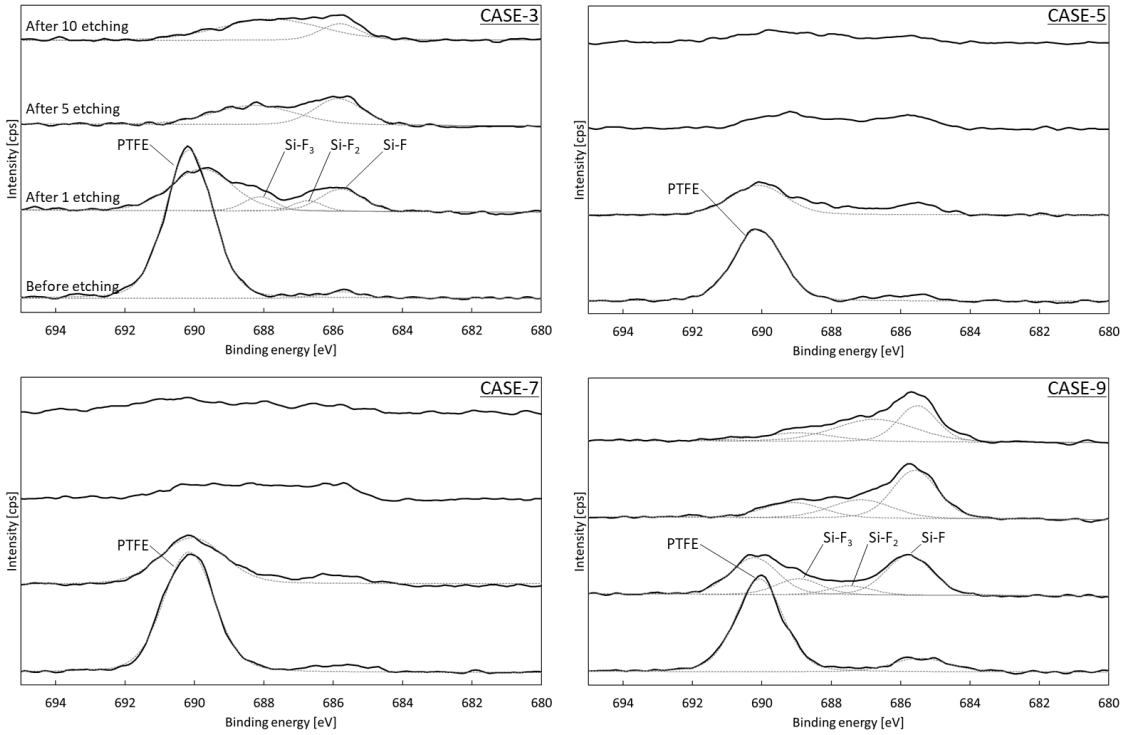

Fig. 78 XPS F (1s) spectra of friction areas on Si_3N_4 balls.

5.4.3. Friction and lubrication mechanisms

Considering the test and analyses results, the PTFE formed on the surface of both the stationary ball and the rotating ball significantly improved the lubrication characteristics of SUS440C-Si_3N_4 friction under cryogenic environment. In addition, the metal fluoride formed on the stationary ball remarkably enhanced the wear resistance performance of SUS440C.

No wear was detected on the stationary ball surface just after the three ball-pin tests which was conducted before each four ball test carrying out SUS440C-Si_3N_4 friction. Additionally, XPS analysis revealed that PTFE film covered the surface and metal fluoride existed beneath the film on the stationary ball surface as well as after four ball tests. Such surface will be rubbed against Si_3N_4 in the four ball tests. Since the analyses results described in section 5.4 showed the detection of wear and the formation of metal fluoride after four ball tests, the stationary balls were worn due to the friction with

Si_3N_4 while metal fluoride was simultaneously formed on the surface. Therefore, the metal fluoride formed in the three ball-pin tests just prevented excessive wear in the early phase of the friction in four ball tests. In the four ball tests, slight wear occurred on the friction area of the stationary ball, gradually generating fresh surface. In the wear process, the metal fluoride was simultaneously formed due to the chemical reaction between the fresh surface and F-ions originated from PTFE and adhered with PTFE. Such PTFE and metal fluoride formed on the stationary ball should perform low friction as shown in Fig. 73.

The tendency of the friction coefficient with normal load could be explained by micro-scale consideration. Schematics of real contact area in friction interface are shown in Fig. 79. In CASE-5 and -7, the friction coefficient was smaller and the Si-F, Si-F_2, and Si-F_3 bindings were barely observed. This suggests that little friction energy was applied to the Si_3N_4 surface. This would be because PTFE was strongly adhered on the SUS440C surface even under friction conditions and covered the SUS440C surface, which prevents the direct contact between the SUS440C and the Si_3N_4 as shown in Fig. 79 (b). Such adhesion of PTFE with SUS440C is considered to cause much lower friction characteristics. Considering that the friction coefficient decreased with normal force on the conditions up to 25.96 N, the strong adhesion of PTFE would occur in conditions of larger friction energy. This is because the binding between PTFE film and SUS440C surface need certain energy to occur since it is formed due to chemical reaction as described above. In CASE-3, it is considered that there was not enough PTFE film on the SUS440C surface which strongly adhered on the SUS440C as shown in Fig. 79 (a) because the friction energy was too small. Therefore, the Si_3N_4 surface directly contacted with the SUS440C, which contributes to generating the Si-F, Si-F_2, and Si-F_3 bindings. In addition, the friction coefficient was higher because such direct friction between the Si_3N_4 and the SUS440C without PTFE film is considered to be larger. In CASE-9, the contact pressure would exceed the ultimate stress of PTFE, and PTFE film which strongly adhered on the SUS440C was broken through

as shown in Fig. 79 (c). Consequently, the Si_3N_4 surface directly contacted with the SUS440C as CASE-3, leading to the larger friction coefficient and generating the Si-F, Si-F_2, and Si-F_3 bindings. In both CASE-3 and -9, the stationary ball surface would be covered by metal fluoride, preventing from adhesion between the SUS440C and the Si_3N_4 which contributes to much larger friction as in CASE-0 and -11. In CASE-11, the metal fluoride was also broken through due to, much larger normal force exceeding the ultimate stress as shown in Fig. 79 (d), and finally the Si_3N_4 severely contacted against fresh metal surface of the SUS440C without the metal fluoride and PTFE, which leads to the adhesion between the SUS440C and the Si_3N_4. In CASE-0, the SUS440C and the Si_3N_4 directly contacted without any lubrication as shown in Fig. 79 (e), and this resulted in much larger friction and excessive wear of the SUS440C.

The formation of metal fluoride during the three ball-pin test is consistent with results of previous studies conducting friction tests and surface analyses with PTFE and metallic material [60, 65-69]. Some of those studies concluded that strong adhesion of PTFE on metallic surface during friction needs friction energy to deform and break PTFE and generate F-ions [60, 69]. Furthermore, the breakdown process of the lubrication film formed on the stationary ball due to larger contact load conditions is also consistent with bearing test results showing the load capacity limitation of lubrication film in hybrid ceramic ball bearings for cryogenic turbopumps [16].

From the above, a significant factor of lower friction characteristics is the PTFE film that strongly adheres on the surface of the stationary ball. The adhesion of the PTFE film is caused by the metal fluoride formed on SUS440C and the moderate friction energy. Therefore, the friction coefficient of SUS440C-Si_3N_4 via PTFE lubrication under cryogenic environment depends on the friction energy which changes with the contact pressure.

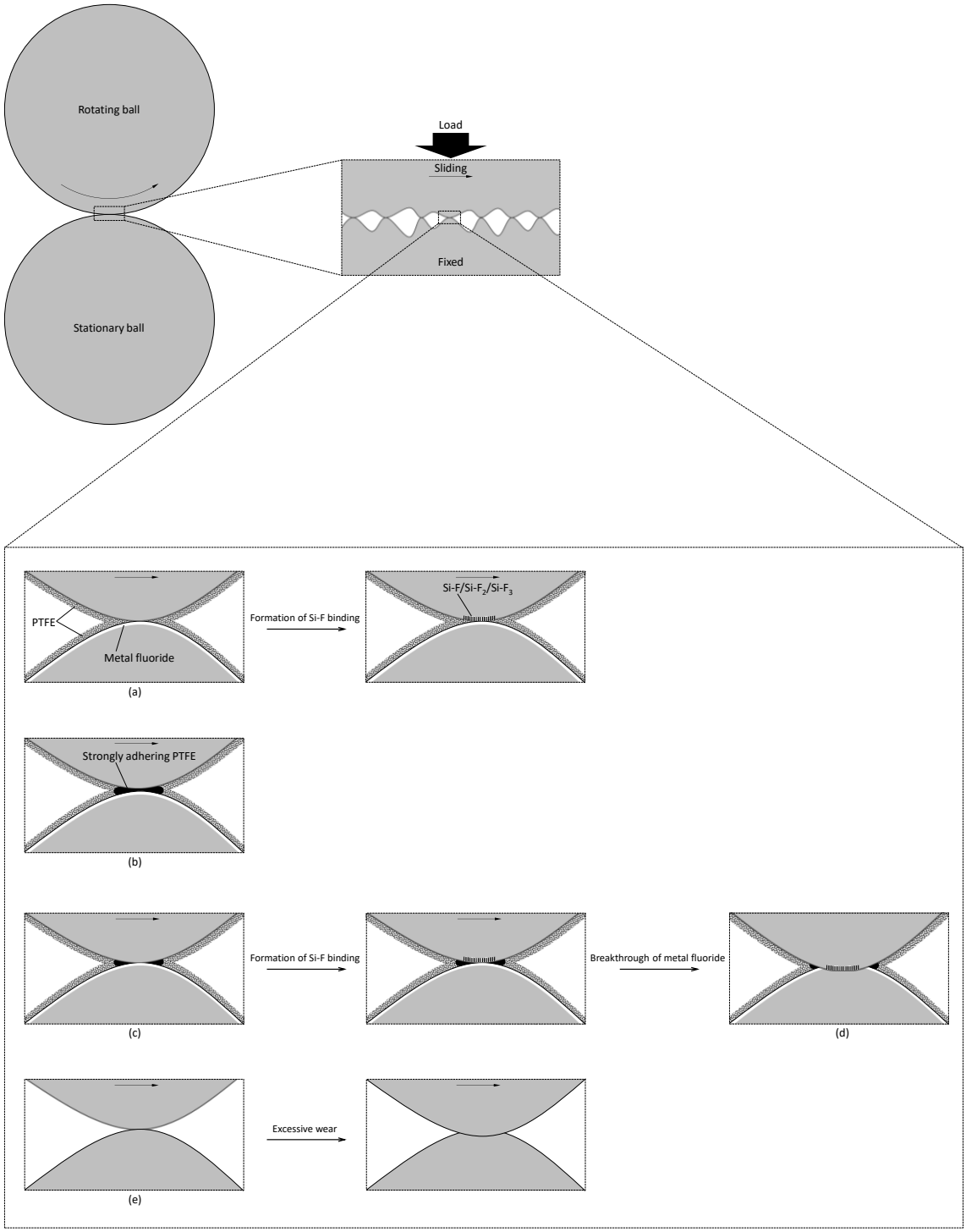

Fig. 79 Schematic of real contact area in friction interface. (a) Test cases of lower load as CASE-3. (b) Test cases of moderate load as CASE-7. (c) Test cases of large load as CASE-9. (d) Test cases of excess load as CASE-11. (e) Test cases without PTFE lubrication as CASE-0.

5.5. Summary

This research experimentally investigated the friction coefficient of bearing materials via PTFE lubrication under cryogenic environment to clarify the friction characteristics of cryogenic turbopump ball bearings. The friction coefficient was clearly dependent on the contact pressure. It decreased with the contact pressure up to 2112 MPa and increased on the pressure conditions more than the value.

The microscopic analysis indicated that lubrication film remained on the friction interface even during the friction process. The surface profiles after the friction tests showed that SUS440C was mainly worn in SUS440C-Si_3N_4 friction under cryogenic environment and that PTFE lubrication improved wear-resistance characteristic of SUS440C by performing lubricated smooth friction and forming metal fluoride on the SUS440C surface. The XPS analysis revealed that metal fluoride was formed in the friction area of SUS440C of all test cases and that Si-F, Si-F_2, and Si-F_3 bindings were present on the friction area of Si_3N_4 of higher friction test cases.

Considering the data on the friction coefficient and the analyses results, the lower friction characteristics are caused by the PTFE film that strongly adheres on the surface of the stationary ball. The better adhesion is led by the metal fluoride formed on the surface and moderate friction energy. PTFE film does not strongly adhere on both too small and excessive friction energy conditions, which contributes to generating Si-F, Si-F_2, and Si-F_3 bindings and larger friction coefficient.

Chapter 6. Modeling of heat generation of cryogenic ball bearing

6.1. Introduction

Performance modeling of heat generation in cryogenic ball bearing will be constructed in this chapter. To construct the modeling, models of fluid heat generation and friction heat generation are needed. The fluid heat generation was calculated by using the results of CFD analysis conducted in Chapter 4. The friction heat generation was calculated by using the results of bearing motion analysis conducted in Chapter 2 and friction characteristics of bearing materials under cryogenic environment investigated in Chapter 6. In this study, the bearing heat generation was modeled as the sum of the fluid heat generation and the friction heat generation. Finally, fidelity of the model was validated by comparing with experimental results investigated in Chapter 3.

6.2. Operating conditions of cryogenic ball bearings for modeling

The modeling conditions are shown in Table 11. Since calculation results obtained by modeling constructed in this chapter will be compared with the experimental results of Chapter 3, modeling conditions were set in accordance with the experimental conditions.

Table 11 Modeling conditions of cryogenic ball bearings.

Parameter	Value			
Bearing	Bearing X		Bearing Y	
Coolant	LCH_4	LN_2	LCH_4	LH_2
Coolant pressure	1.43 MPa	1.11 MPa	1.52 MPa	1.66 MPa
Coolant inlet temperature	120.9 K	94.5 K	120.2 K	27.8 K
Coolant flow rate	0.139 kg/s	0.307 kg/s	0.258 kg/s	0.043 kg/s
Rotational speed	10000 ~ 60000 rpm	10000 ~ 60000 rpm	10000 ~ 50000 rpm	10000 ~ 50000 rpm
Thrust load	1000 N	1000 N	1000 N	1000 N

6.3. Modeling on fluid heat generation (W_f)

As shown in Chapter 4, fluid heat generation of rotating ball bearing is caused by shear force between rotating bearing elements and the surrounding fluid flow. Since the fluid flow structure is remarkably complicated to comprehend by using equations for simple flow, CFD analysis was performed to calculate the fluid heat generation. CFD analysis results of the fluid heat generation of Bearing X in LN_2 and LCH_4 environments are shown in Fig. 53. Ones of Bearing Y in LH_2 and LCH_4 environments are shown in Fig. 67.

6.4. Modeling on friction heat generation

Calculation methods for friction heat generation were explained in section 2.4.1. Friction heat in raceways-ball contact and ball-retainer contact was considered in this study. Friction heat in outer race-retainer contact was not considered in this research because Bearing X and Bearing Y are designed so that they would have enough clearance between the outer race and the retainer without any contact under operating conditions considered in this study. Finally, the friction heat generation of the bearing was calculated as the sum of those friction heat.

6.4.1. Friction heat generation of raceways-ball contact (W_a)

The friction heat generation of raceways-ball contact was calculated according to Equation (33) and Equation (34). Distribution of contact pressure and velocity was calculated as shown in section 2.3.2 and section 2.3.3. Friction coefficient investigated in Chapter 5 was adopted to $\mu_n(x, y)$. Relationship between the normal load and the friction load in the friction tests is shown in Fig. 80. From this relationship, dependence of the friction coefficient on the contact pressure was calculated as shown in Fig. 81. Since these friction data were acquired during steady state condition of the friction experiments, it is reasonable to adopt the data to calculate the friction heat generation in steady state

conditions.

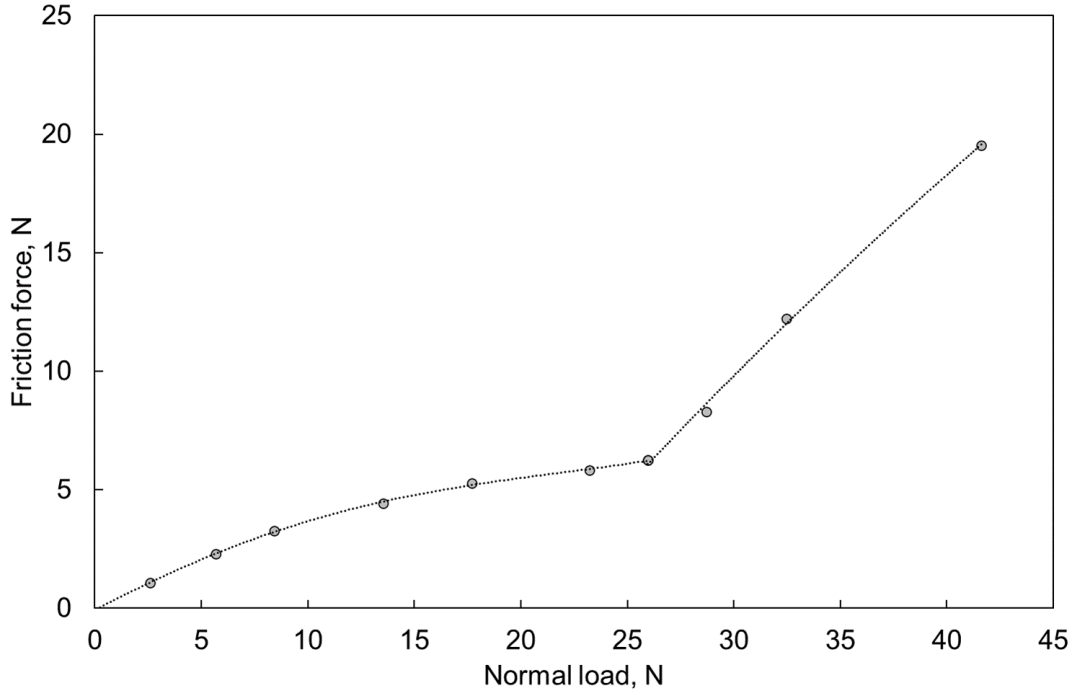

Fig. 80 Friction force data in cryogenic friction tests as a function of normal load.

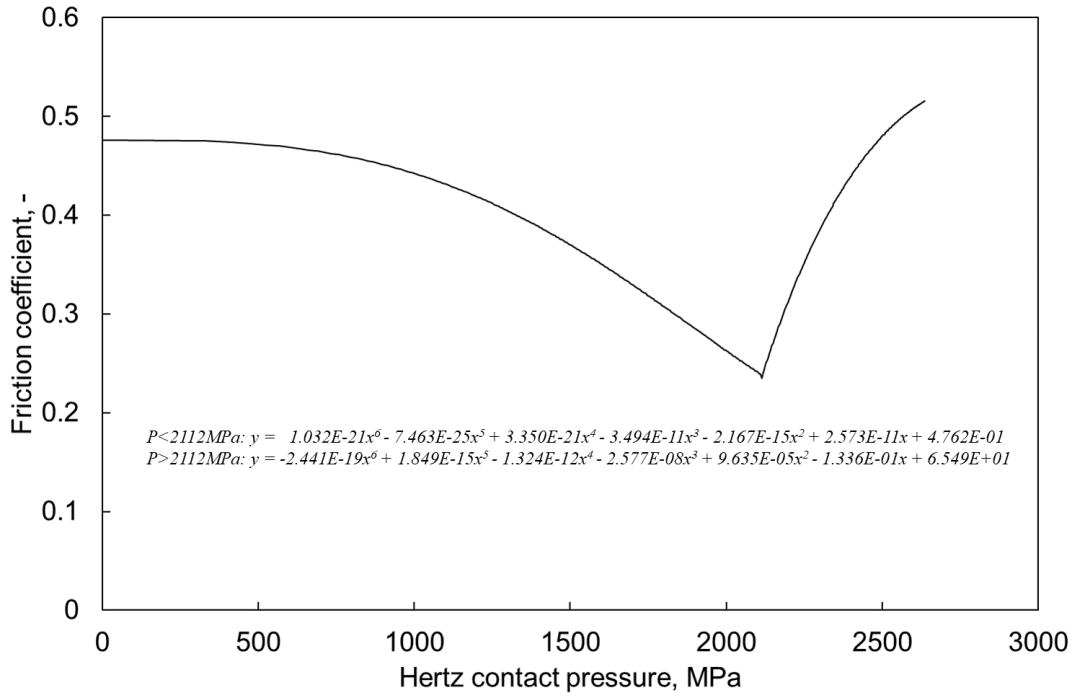

Fig. 81 Friction coefficient calculated by using results of the friction tests as a function of hertz contact pressure.

6.4.2. Friction heat generation of ball-retainer contact (W_b)

The friction heat generation of ball-retainer contact was calculated according to Equation (36). Sliding velocity v_n was calculated by using the results of bearing motion analysis as shown in section 2.3.2. Normal force of ball-retainer contact F_n was assumed to be the sum of the retainer-ball contact loads which is the fluid drag force of the retainer that can be calculated as the results of the CFD analysis described in Chapter 4. Friction coefficient μ_b was investigated by conducting friction experiment as follows.

The friction experiment was conducted by using the same tribometer as one described in Chapter 6. The test procedure was the same as 3 ball-pin test explained in Fig. 72. The material of the 3 stationary balls and the rotating pin was Si_3N_4 and glass cloth-PTFE laminate, respectively, to simulate the friction the ball-retainer friction. Normal load was set around 100 N by deadweight which was the same as the 3 ball-pin tests conducted in Chapter 5. The test result is shown in Fig. 82. Friction coefficient gradually increased from around 0.077 at the start of the friction test (A) to 0.117 at the end (B). This increase was caused by wear of the rotating pin. The pin was gradually worn due to the friction with the balls, which contributes to increasing friction area with the balls and then gaining the friction force. Considering that the friction of ball-retainer contact results in the retainer wear due to the friction with the balls, friction condition in bearings would be same as (B). Therefore, the friction coefficient μ_b was assumed to be 0.117 for Equation (36).

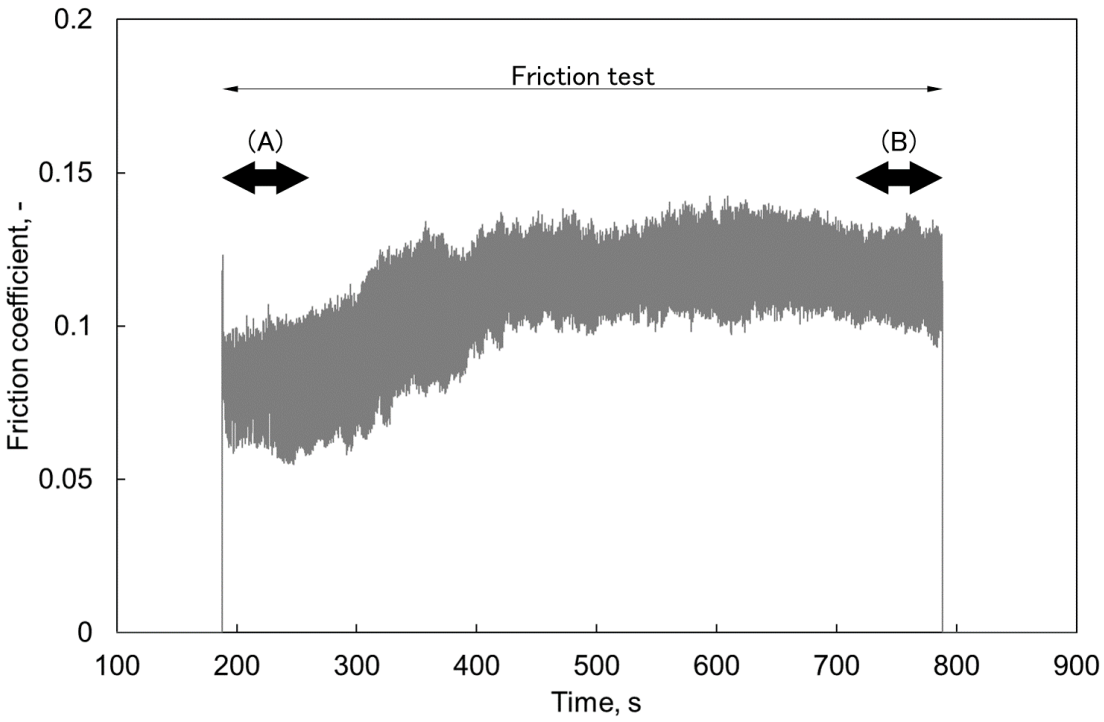

Fig. 82 Time history data of the friction coefficient of 3 ball-pin test using Si_3N_4 balls and glass cloth-PTFE laminate pin.

6.4.3. Friction heat generation

Friction heat generation is shown in Fig. 83 for Bearing X/LCH_4 environment, in Fig. 84 for Bearing X/LN_2 environment, in Fig. 85 for Bearing Y/LCH_4 environment, and in Fig. 86 for Bearing Y/LH_2 environment, respectively. The friction heat generation of ball-retainer contact was larger in higher density coolant since torque around retainer rotation axis was larger. However, it accounted for slight portion of the entire heat generation in all environments. This indicates that the ball-retainer friction was much lighter than the raceways-balls friction. Heat generation of the raceways-balls friction increased with the rotational speed since sliding speed of the friction increased under the same thrust load conditions. The percentage of $W_a(Outer\ race)$ increased with the rotational speed in all conditions while that of $W_a(Inner\ race)$ decreased. It is caused by the dependence of ball load on

the outer race on the rotational speed as shown in Fig. 15 (c) and Fig. 16 (b) which indicate different tendency from that of inner race because of the centrifugal force loading on balls.

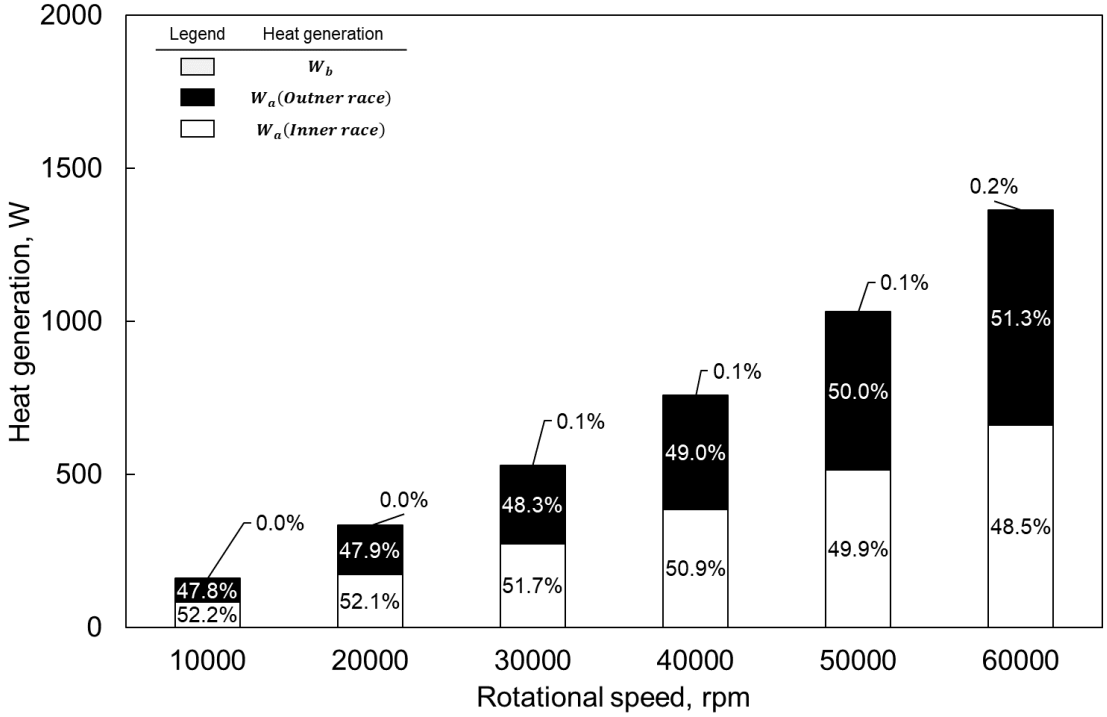

Fig. 83 Friction heat generation of Bearing X in LCH_4 (Calculation result).

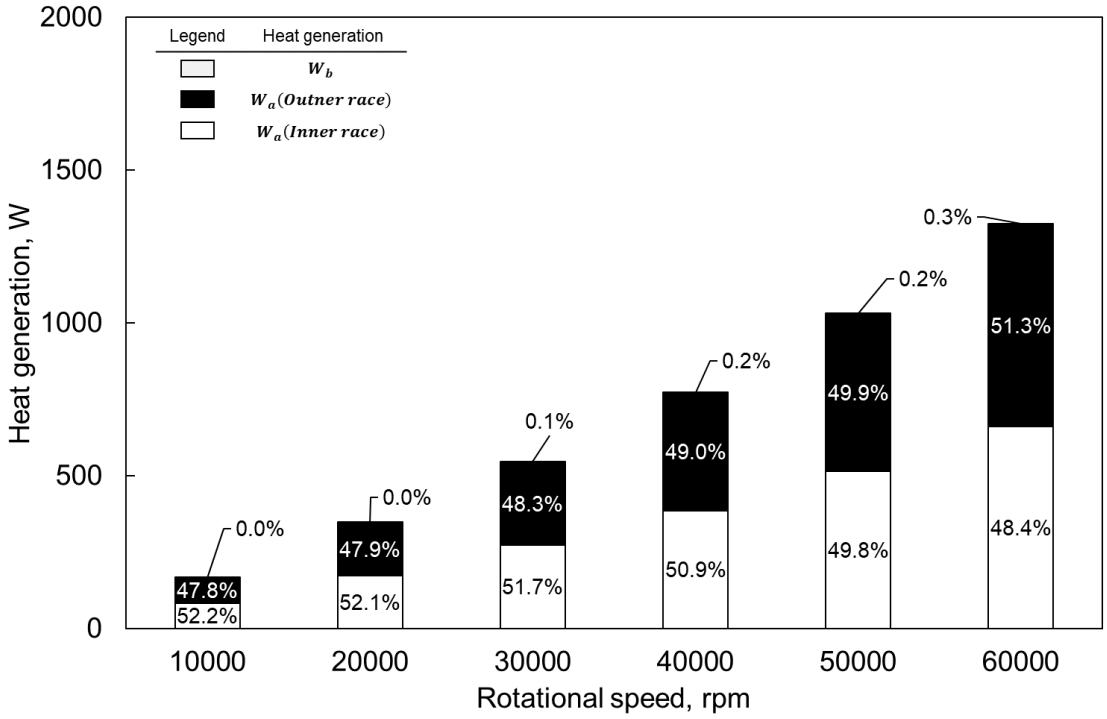

Fig. 84 Friction heat generation of Bearing X in LN_2 (Calculation result).

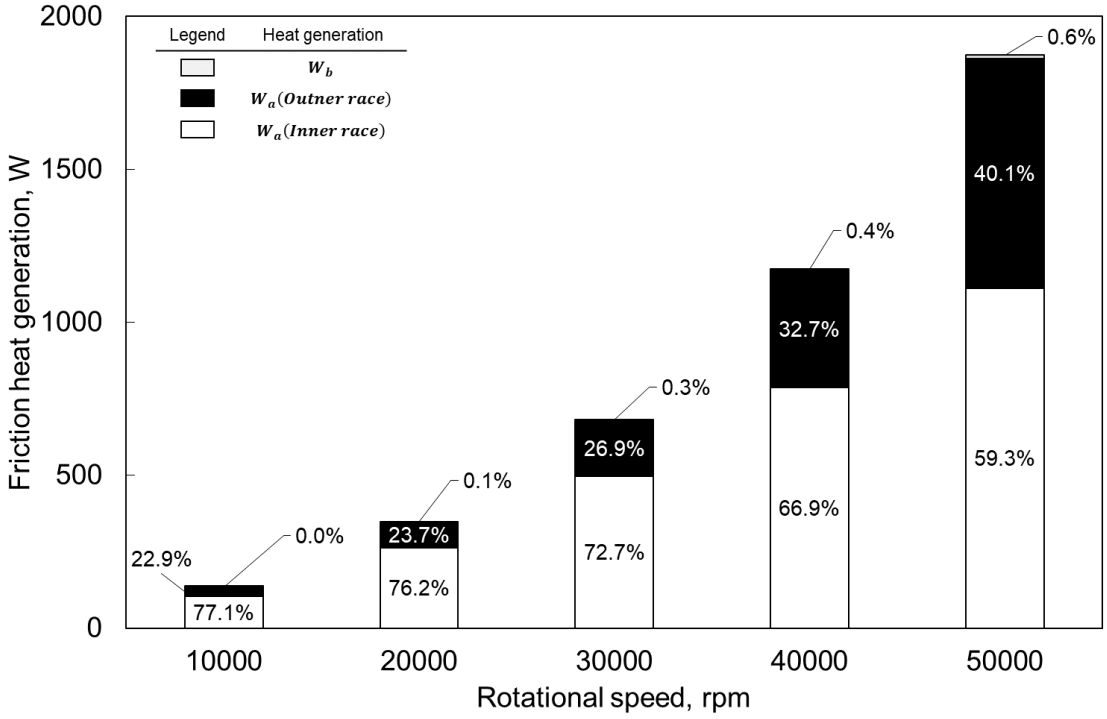

Fig. 85 Friction heat generation of Bearing Y in LCH_4 (Calculation result).

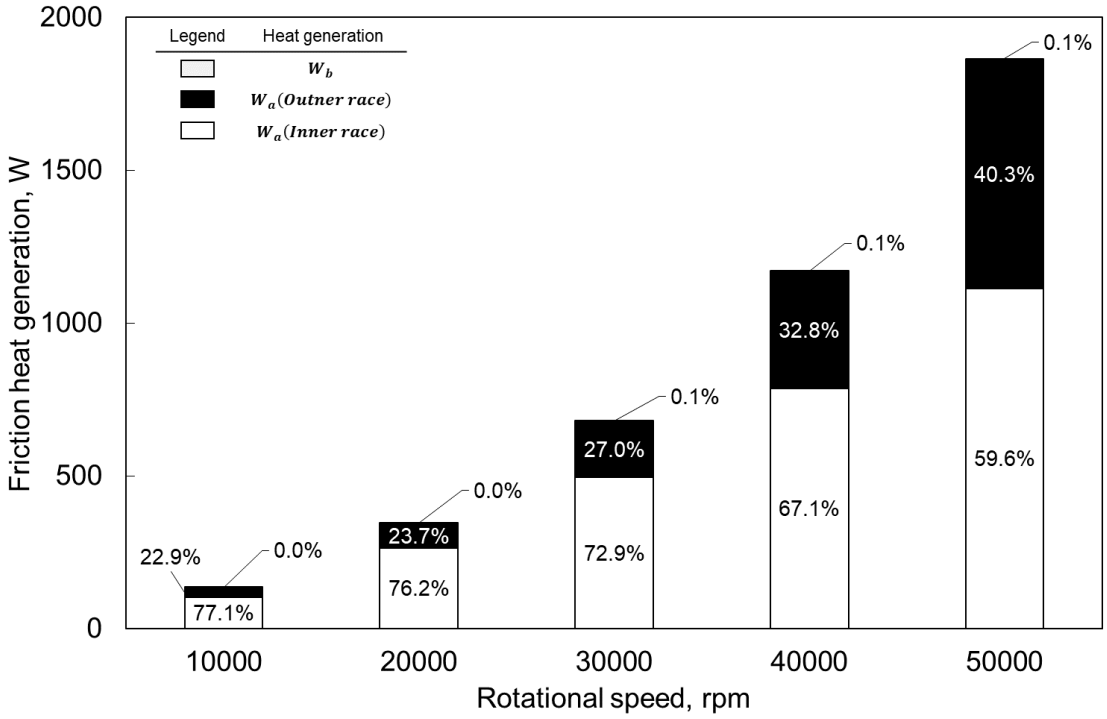

Fig. 86 Friction heat generation of Bearing Y in LH_2 (Calculation result).

6.5. Heat generation model

Heat generation of Bearing X is shown in Fig. 87 for LCH_4 environment and in Fig. 88 for LN_2 environment, respectively. The graphs indicate that fluid heat generation and friction heat generation increased with the rotational speed. The heat generation at 50000 rpm was 1686 W in LCH_4 environment and 2096 W in LN_2 environment, respectively. The fluid heat generation at 50000 rpm accounted for 38.8 % in LCH_4 environment and 50.7 % in LN_2 environment, respectively. These results of the heat generation data in Bearing X suggest that both friction heat and fluid heat are main factors of bearing heat generation.

Heat generation of Bearing Y is shown in Fig. 89 for LCH_4 environment and in Fig. 90 for LH_2 environment, respectively. The graphs indicate that fluid heat generation and friction heat generation

increased with the rotational speed as described above. The heat generation at 50000 rpm was 7597 W in LCH_4 environment and 2639 W in LH_2 environment, respectively. The fluid heat generation at 50000 rpm accounted for 58.6 % in LCH_4 environment and 29.4 % in LH_2 environment, respectively.

Comparing both results, Bearing Y generated 2.68 times heat than Bearing X at 50000 rpm. The difference is caused by bearing design such as bearing element geometry and number of balls. In this case, the friction heat generation was affected by the size of contact areas and the number of the friction area. The fluid heat generation was affected mainly by the surface areas of the bearing elements. Considering that the fluid heat generation of Bearing Y was 4.04 times larger than Bearing X while the difference of the friction heat generation was 1.82 times, the influence of bearing design on the fluid heat generation was significant.

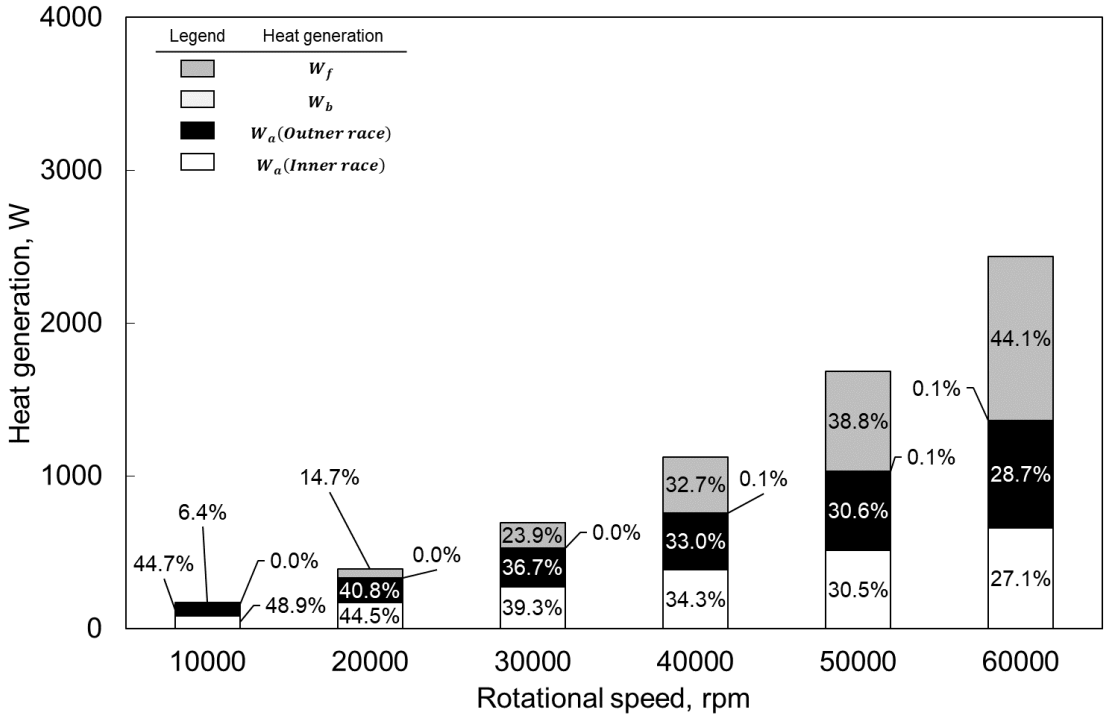

Fig. 87 Heat generation of Bearing X in LCH_4 (Calculation result).

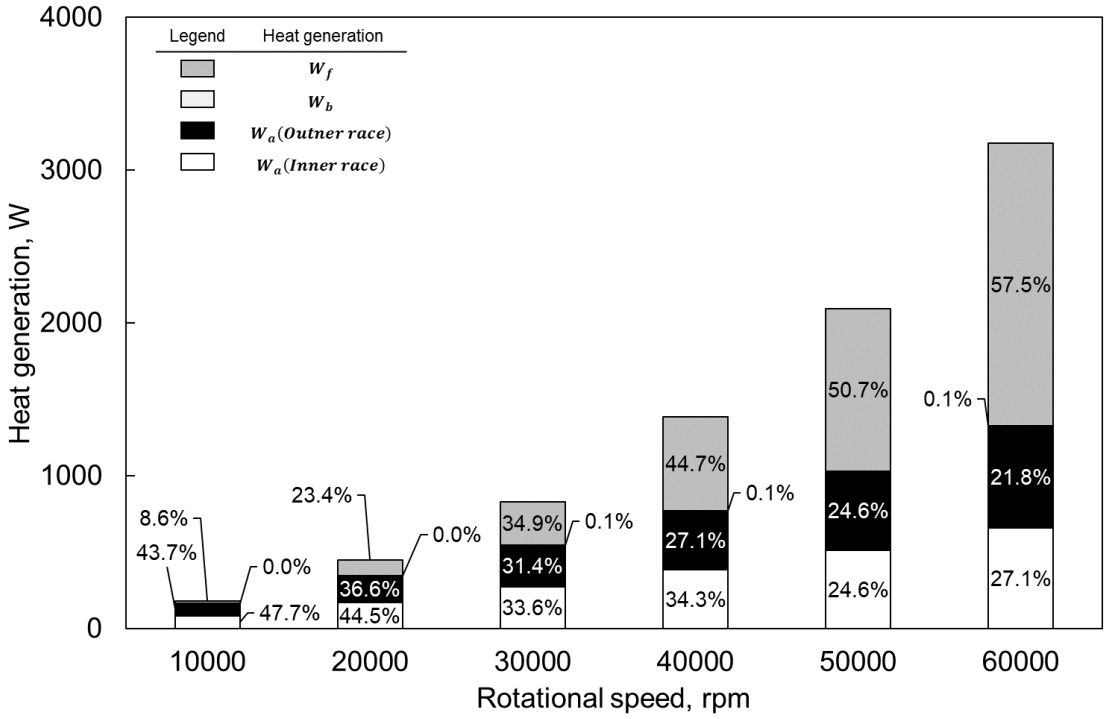

Fig. 88 Heat generation of Bearing X in LN_2 (Calculation result).

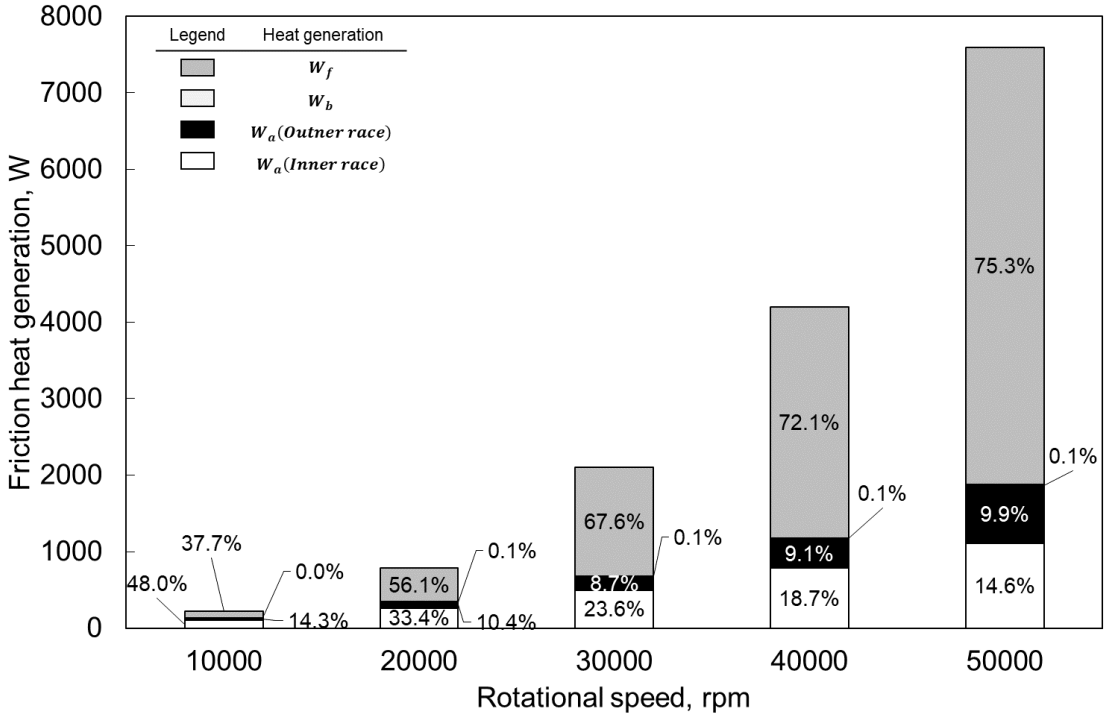

Fig. 89 Heat generation of Bearing Y in LCH_4 (Calculation result).

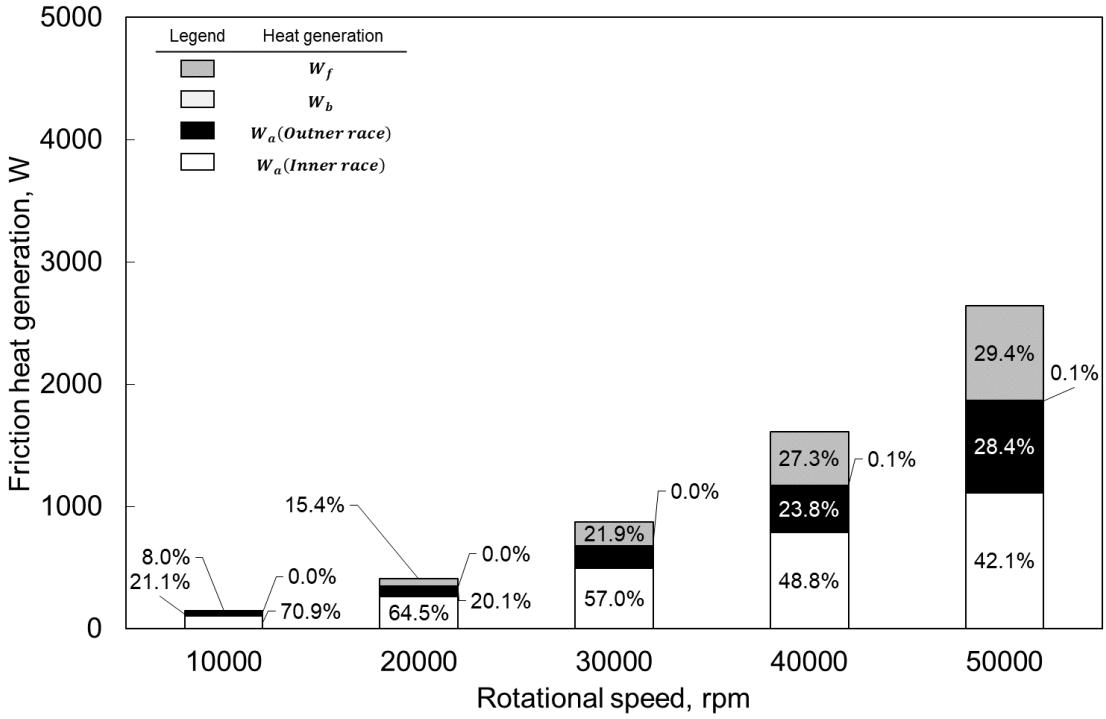

Fig. 90 Heat generation of Bearing Y in LH_2 (Calculation result).

6.6. Comparison of the model with experimental results

Comparison of Bearing X heat generation in LN_2 and LCH_4 environment between experiment and calculation is shown in Fig. 91. The calculation results showed excellent agreement with the experimental results. Error between the calculation results and the experiment results is 18 W at 40000 rpm in LN_2 and 70 W at 52000 rpm in LCH_4, respectively. Comparison of Bearing Y heat generation in LCH_4 and LH_2 environment between experiment and calculation is shown in Fig. 92. The dependency of bearing heat generation on the rotational speed is well simulated by the calculation results in both environments. Error between the calculation results and the experiment results is 210 W at 35000 rpm in LCH_4 and 377 W at 25000 rpm in LH_2, respectively.

The graphs indicate that there were definite errors between both results though the calculation results showed good agreement with the experimental results. Two error factors can be considered. One is

measurement error in experiments as described in section 3.2.1.3. In this study, the measurement error of temperature, pressure, and flowrate had impacts on experimental data of bearing heat generation. Even though state-of-the-art methods for measurement were adopted in the experiments. The other one is calculation method of modeling on bearing heat generation. In this study, the model of bearing heat generation was defined as the sum of all factors of heat generation as described in section 6.4. Therefore, interinfluence between all factors on heat generation was not considered in this study. In particular, it is possible that friction heat generation in bearing elements would have influence on fluid dynamics that relates with fluid heat generation. However, calculation method for solving all factors simultaneously with consideration of interinfluence between them contributes to numerous computational costs which cannot be processed in short time.

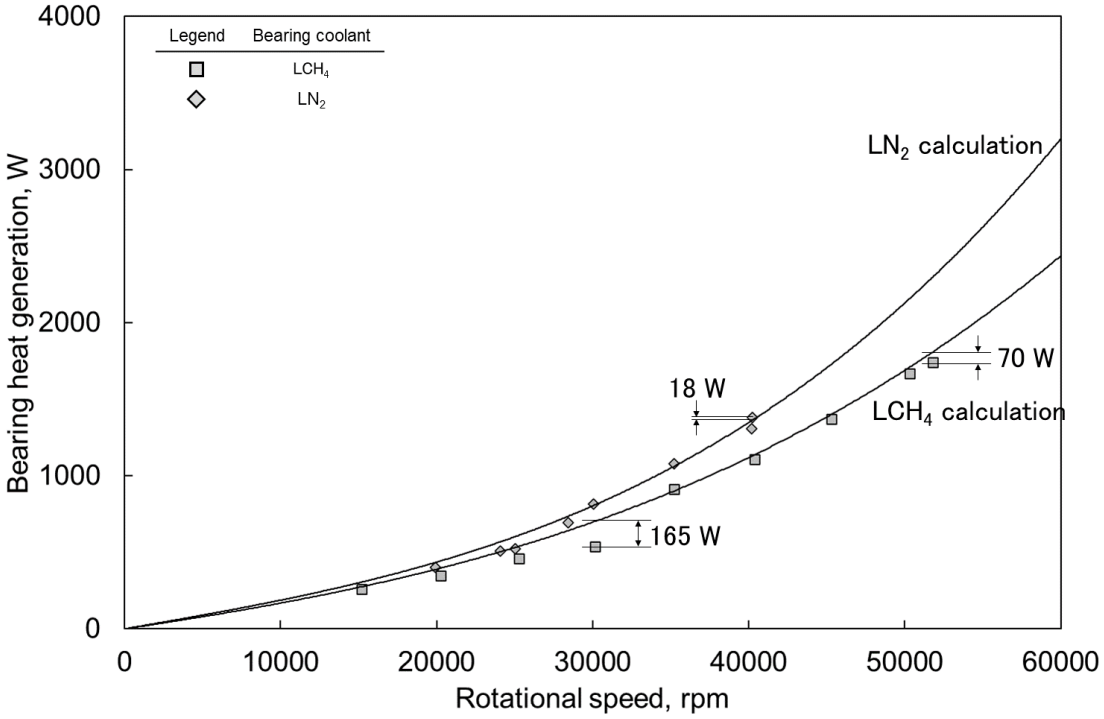

Fig. 91 Comparison of Bearing X heat generation in LN_2 and LCH_4 environment between experiment and calculation.

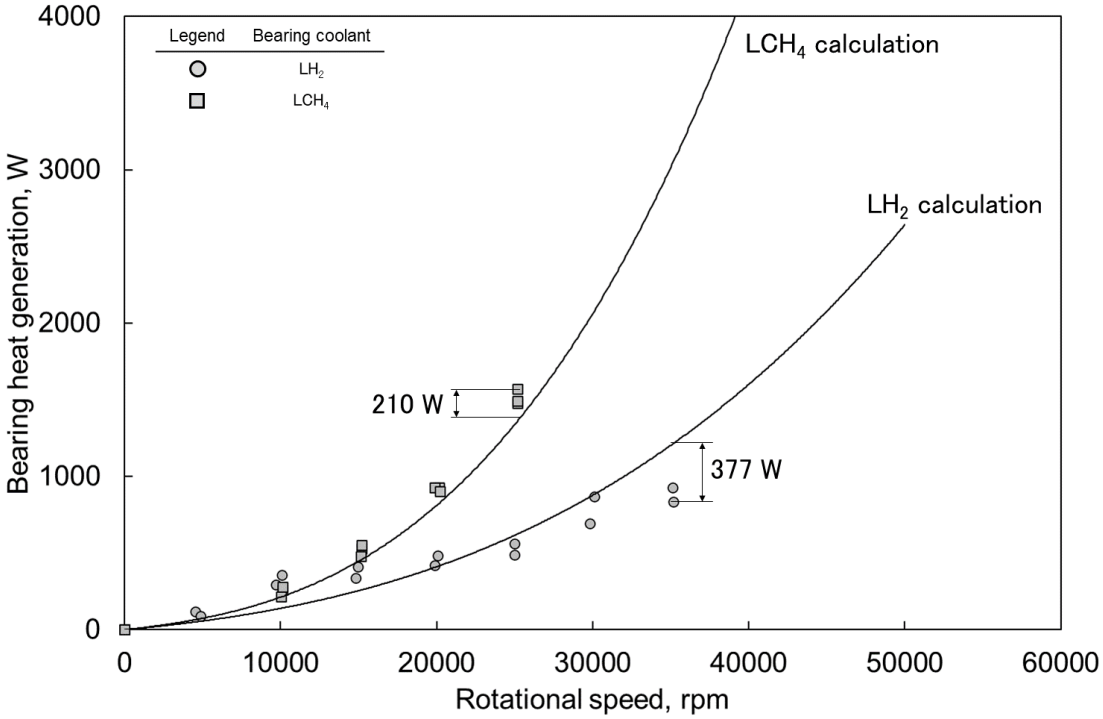

Fig. 92 Comparison of Bearing Y heat generation in LCH_4 and LH_2 environment between experiment and calculation.

6.7. Summary

Modeling on bearing heat generation was constructed by calculating the sum of all heat factors which were researched from Chapter 2 to Chapter 5. Comparing the modeling with the experimental results, the prediction by the modeling showed good agreement with the experimental results and simulated influences of several conditions such as rotational speed, coolant fluid, and bearing size. Although there could be two error factors in the modeling, further improvement of the fidelity is expected by innovation of measurement method and advancement of computational speed.

Chapter 7. Conclusion

This study aimed to construct a high-fidelity modeling of heat generation in turbopump bearings. For that, the friction characteristics of bearing material under cryogenic environment and the fluid flow characteristics of the bearing coolant were mainly investigated. The findings of this study are as follows.

In Chapter 2, the analytical method for calculation of bearing motion and the factors of the heat generation in cryogenic ball bearings were introduced. The analytical method considers the influences of thermal expansion, centrifugal forces, and interference fitting which are unique characteristics of cryogenic ball bearings.

In Chapter 3, bearing heat generation in cryogenic environment were investigated and parametrically summarized and evaluated. Two types of bearings were tested in LH_2, LCH_4, and LN_2 environment and the bearing heat generation was measured. In all bearing types and environments, the heat generation increased with the rotational speed. The gradient to the rotational speed depended on the coolants and increased with the fluid density. This characteristic caused larger bearing heat generation in higher density fluid. The results of Bearing X experiments under LCH_4, and LN_2 environment identified that density and viscosity have strong relationship with the fluid heat generation. Also, by conducting bearing tests under hydrogen environment of several pressure and temperature conditions with Bearing Y, it was identified that density and viscosity significantly influenced the fluid heat generation.

In Chapter 4, the fluid heat generation of cryogenic bearings were investigated by performing CFD analysis. Since the characteristics of the fluid heat generation would be influenced by several conditions such as bearing size, rotational speed, coolant fluid, fluid flow direction, and coolant flowrate, the analysis conditions were set by changing these conditions. Distribution of velocity, temperature, and pressure which have significant impact on fluid heat generation were remarkably complicated and change with operating conditions. The CFD results visualized complex

characteristics of the fluid flow in the vicinity of bearing cavity. In particular, recirculation zones were formed in the downstream and upstream of the bearing cavity on all conditions. Therefore, it was found that the bearing coolant flow is too complicated to predict by adopting simple empirical equations for flat surfaces' fluid flow.

In Chapter 5, the friction coefficient of bearing materials via PTFE lubrication under cryogenic environment was investigated to clarify the friction characteristics of cryogenic turbopump ball bearings. The friction coefficient was clearly dependent on the contact pressure. It decreased with the contact pressure up to 2112 MPa and increased on the pressure conditions more than the value. The microscopic analysis indicated that lubrication film remained on the friction interface even during the friction process. The surface profiles after the friction tests showed that SUS440C was mainly worn in SUS440C- Si_3N_4 friction under cryogenic environment and that PTFE lubrication improved wear-resistance characteristic of SUS440C by performing lubricated smooth friction and forming metal fluoride on the SUS440C surface. XPS analysis revealed that metal fluoride was formed in the friction area of SUS440C of all test cases and that Si-F, Si-F_2, and Si-F_3 bindings were present on the friction area of Si_3N_4 of higher friction test cases. Considering the data on the friction coefficient and the analyses results, the lower friction characteristics are caused by the PTFE film that strongly adheres on the surface of the stationary ball. The better adhesion is led by the metal fluoride formed on the surface and moderate friction energy. PTFE film does not strongly adhere on both too small and excessive friction energy conditions, which contributes to generating Si-F, Si-F_2, and Si-F_3 bindings and larger friction coefficient.

In Chapter 6, modeling on bearing heat generation was constructed by calculating the sum of all heat factors which were researched from Chapter 2 to Chapter 5. Comparing the modeling with the experimental results, the prediction by the modeling showed good agreement with the experimental results and simulated influences of several conditions such as rotational speed, coolant fluid, and

bearing size. Although there could be two error factors in the modeling, further improvement of the fidelity is expected by innovation of measurement method and advancement of computational speed.

References

[1] Sutton, G. P., and Biblarz, O., 2017, "Rocket propulsion elements," Wiley,, Hoboken, New Jersey, p. 1 online resource (792 pages).

[2] Huzel, D. K., and Huang, D. H., 1971, Design of liquid propellant rocket engines, Scientific and Technical Information Office, National Aeronautics and Space Administration; for sale by the National Technical Information Service, Springfield, Washington,.

[3] Sobin, A. J., and Bissell, W. R., 1974, Turbopump systems for liquid rocket engines, National Aeronautics and Space Administration : for sale by the National Technical Information Service, Springfield, Va., Washington.

[4] Marchal, N., Caisso, P., Alliot, P., and Souchier, A., 1992, "Dry lubrication applied to the HM7 engine hydrogen bearing," Journal of Propulsion and Power, 8(5), pp. 968-970.

[5] Bradley, D., and Van Hooser, K., 2011, "Space Shuttle Main Engine - The Relentless Pursuit of Improvement," AIAA SPACE 2011 Conference & Exposition, American Institute of Aeronautics and Astronautics.

[6] Gibson, H. G., 1991, "An evaluation of bearings operating in a cryogenic environment with silicon nitride rolling elements," NASA.

[7] Gibson, H., Thom, R., Moore, C., and Haluch, D., 2010, "History of Space Shuttle Main Engine Turbopump Bearing Testing," 57th JANNAF Joint Propulsion Meeting.

[8] Bursey, R. W., Chin, H., Olinger, J. B., Price, J. L., Tennant, M. T., Moore, L., Thom, R. L., Moore, J., and Marty, D., 1996, "Advanced hybrid rolling element bearings for the Space Shuttle Main Engine high pressure alternate turbopumps," AIAA, ASME, SAE, and ASEE, Joint Propulsion Conference and Exhibit, 32ndLakeBuena Vista, FL.

[9] Subbaraman, M. R., Keba, J. E., and Hadid, A. H., 1992, "Bearing Coolant Flow Optimization, Advanced Earth-to-Orbit Propulsion Technology," NASA CP 3174, pp. 439-449.

[10] Nosaka, M., 1988, "Experimental Study on Lubricating Performance of Self-Lubricating Ball Bearings for Liquid Hydrogen Turbopumps," Lubr. Eng., 44, p. 30.

[11] Nosaka, M., and Kato, T., 2013, "Cryogenic Tribology in High-Speed Bearings and Shaft Seals of Rocket Turbopumps," Tribology, G. Jürgen, ed., IntechOpen, Rijeka.

[12] Nosaka, M., Oike, M., Kikuchi, M., Kamijo, K., and Tajiri, M., 1993, "Self-lubricating performance and durability of ball bearings for the LE-7 liquid oxygen rocket-turbopump," 49:9.

[13] Nosaka, M., Oike, M., Kikuchi, M., Kamijo, K., and Tajiri, M., 1993, "Tribo-Characteristics of Self-Lubricating Ball Bearings for the LE-7 Liquid Hydrogen Rocket-Turbopump," Tribology Transactions, 36(3), pp. 432-442.

[14] Nosaka, M., Oike, M., Kikuchi, M., Nagao, R., and Mayumi, T., 1996, "Evaluation of durability for cryogenic high-speed ball bearings of LE-7 rocket turbopumps," Lubrication Engineering,

52, pp. 221-233.

[15] Nosaka, M., Takada, S., Kikuchi, M., Sudo, T., and Yoshida, M., 2004, "Ultra-High-Speed Performance of Ball Bearings and Annular Seals in Liquid Hydrogen at Up to 3 Million DN (120,000 rpm)©," Tribology Transactions, 47(1), pp. 43-53.

[16] Nosaka, M., Oike, M., Kikuchi, M., and Mayumi, T., 1997, "Tribo-Characteristics of Cryogenic Hybrid Ceramic Ball Bearings for Rocket Turbopumps: Self-Lubricating Performance©," Tribology Transactions, 40(1), pp. 21-30.

[17] Kamijo, K., Yoshida, M., and Tsujimoto, Y., 1993, "Hydraulic and mechanical performance of LE-7 LOX pump inducer," Journal of Propulsion and Power, 9(6), pp. 819-826.

[18] Torii, Y., Sogame, E., Kamijo, K., Ito, T., and Suzuki, K., 1988, "Development status of LE-7," Acta Astronautica, 17(3), pp. 331-340.

[19] Jones, A. B., 1959, "Ball Motion and Sliding Friction in Ball Bearings," Journal of Basic Engineering, 81(1), pp. 1-12.

[20] Jones, A. B., 1960, "A General Theory for Elastically Constrained Ball and Radial Roller Bearings Under Arbitrary Load and Speed Conditions," Journal of Basic Engineering, 82(2), pp. 309-320.

[21] Harris, T. A., and Kotzalas, M. N., 2006, Rolling bearing analysis, CRC/Taylor & Francis, Boca Raton, FL.

[22] Harris, T. A., 1971, "An Analytical Method to Predict Skidding in Thrust-Loaded, Angular-Contact Ball Bearings," Journal of Lubrication Technology, 93(1), pp. 17-23.

[23] Gupta, P. K., 1975, "Transient Ball Motion and Skid in Ball Bearings," Journal of Lubrication Technology, 97(2), pp. 261-269.

[24] Gupta, P. K., 1984, Advanced dynamics of rolling elements, Springer-Verlag, Berlin ; New York.

[25] Gupta, P. K., Dill, J. F., and Bandow, H. E., 1985, "Dynamics of Rolling Element—Bearings Experimental Validation of the DREB and RAPIDREB Computer Programs," Journal of Tribology, 107(1), pp. 132-137.

[26] Gupta, P. K., 1979, "Dynamics of Rolling-Element Bearings—Part I: Cylindrical Roller Bearing Analysis," Journal of Lubrication Technology, 101(3), pp. 293-302.

[27] Gupta, P. K., 1979, "Dynamics of Rolling-Element Bearings—Part II: Cylindrical Roller Bearing Results," Journal of Lubrication Technology, 101(3), pp. 305-311.

[28] Gupta, P. K., 1979, "Dynamics of Rolling-Element Bearings—Part III: Ball Bearing Analysis," Journal of Lubrication Technology, 101(3), pp. 312-318.

[29] Gupta, P. K., 1979, "Dynamics of Rolling-Element Bearings—Part IV: Ball Bearing Results," Journal of Lubrication Technology, 101(3), pp. 319-326.

[30] Dahiwal, R., Thielen, S., and Sauer, B., 2020, "Modeling and Simulation of Cage Wear in Solid-Lubricated Rolling Bearings," Tribology Online, 15(1), pp. 25-35.

[31] Noel, D., Ritou, M., Furet, B., and Le Loch, S., 2013, "Complete Analytical Expression of the Stiffness Matrix of Angular Contact Ball Bearings," Journal of Tribology, 135(4).

[32] Xu, H., Wang, P., Ma, H., He, D., Zhao, X., Bao, Y., and Yang, Y., 2022, "Contact Characteristics Analysis of Deep Groove Ball Bearings Under Combined Angular Misalignments and External Loads," Journal of Tribology, 144(12).

[33] Liu, J., Xu, Z., and An, C., 2022, "An Analysis of the Load Distribution Characteristics of a Cylindrical Roller Bearing Including the Component Deformation and Waviness," Journal of Tribology, 145(2).

[34] Scibbe, H. W., 1968, "Bearings and Seals for Cryogenic Fluids," SAE Transactions, 77, pp. 2307-2320.

[35] Naerheim, Y., and Stocker, P. J., 1989, "Teflon Lubrication Of Liquid Oxygen Turbopump Bearings," Proceedings of the 5th International Congress on Tribology, pp. 289-294.

[36] Nosaka, M., Kikuchi, M., Oike, M., and Kawai, N., 1999, "Tribo-Characteristics of Cryogenic Hybrid Ceramic Ball Bearings for Rocket Turbopumps: Bearing Wear and Transfer Film©," Tribology Transactions, 42(1), pp. 106-115.

[37] Nosaka, M., Kikuchi, M., Kawai, N., and Kikuyama, H., 2000, "Effects of Iron Fluoride Layer on Durability of Cryogenic High-Speed Ball Bearings for Rocket Turbopumps," Tribology Transactions, 43(2), pp. 163-174.

[38] Kawasaki, S., Kimura, T., Uchiumi, M., and Suda, K., 2011, "Numerical Study on Pressure Loss across the Ball Bearing in Rocket Turbopump Coolant Flow," Turbomachinery, 39(6), pp. 358-365.

[39] Gupta, P. K., and Gibson, H. G., 2020, "Real-Time Dynamics Modeling of Cryogenic Ball Bearings With Thermal Coupling," Journal of Tribology, 143(3).

[40] Harris, T. A., and Mindel, M. H., 1973, "Rolling element bearing dynamics," Wear, 23(3), pp. 311-337.

[41] Schwartzberg, F. R., Knight, M., and Martin Marietta Corporation., 1970, Cryogenic materials data handbook, Air Force Materials Laboratory, Air Force Systems Command, Wright-Patterson Air Force Base, Ohio.

[42] Fujii, K., 2000, "Study on High-Speed Rolling Bearings," Meiji University, Tokyo, Ph. D thesis, in Japanese.

[43] Okamoto, J., 2011, Ball bearing design calculation introduction, THE NIKKAN KOGYO SHIMBUN,LTD.

[44] Nosaka, M., Takada, S., Yoshida, M., Kikuchi, M., Sudo, T., and Nakamura, S., 2010, "Effect of Tilted Misalignment on Tribo-Characteristics of High-Speed Ball Bearings in Liquid Hydrogen," Tribology Online, 5(2), pp. 71-79.

[45] Dowson, D., and Higginson, G. R., 1977, "Elasto-Hydrodynamic Lubrication," Pergamon.

[46] Kamijo, K., Sogame, E., and Okayasu, A., 1982, "Development of Liquid Oxygen and

Hydrogen Turbopumps for the LE-5 Rocket Engine," Journal of Spacecraft and Rockets, 19(3), pp. 226-231.

[47] Ohta, T., Fukushima, Y., and Kamijo, K., 1998, "Development on LH2 Turbopump for LE-7 Engine," Journal of the Japan Society for Aeronautical and Space Sciences, 46(539), pp. 705-711.

[48] Yoshida, M., Takada, S., Naruo, Y., and Niu, K., 2009, "Development Status of Reusable Rocket Engine," TRANSACTIONS OF THE JAPAN SOCIETY FOR AERONAUTICAL AND SPACE SCIENCES, SPACE TECHNOLOGY JAPAN, 7(ists26), pp. Ta_13-Ta_18.

[49] Azuma, N., Kojima, M., Kobayashi, T., Okita, K., Motomura, T., and Niiyama, K., 2019, "The Development Status of LE-9 Engine Turbopumps for H3 Launch Vehicle," AIAA Propulsion and Energy 2019 Forum, American Institute of Aeronautics and Astronautics.

[50] Etsion, I., 1984, "A New Concept of Zero-Leakage Noncontacting Mechanical Face Seal," Journal of Tribology, 106(3), pp. 338-343.

[51] Lipschitz, A., 1985, "A Zero-Leakage Film Riding Face Seal," Journal of Tribology, 107(3), pp. 326-330.

[52] Lemmon, E. W., Huber, M. L., and McLinden, M. O., 2007, "NIST Standard Reference Database 23: Reference Fluid Thermodynamic and Transport Properties-REFPROP," National Institute of Standards and Technology.

[53] Schlichting, H., and Gersten, K., 2017, "Boundary-Layer Theory," H. Schlichting, and K. Gersten, eds., Springer Berlin Heidelberg, Berlin, Heidelberg, pp. 83-99.

[54] Kakudo, H., Takada, S., and Hirayama, T., 2021, "Heat Generation in Cryogenic Turbopump Bearing," Tribology Online, 16(4), pp. 271-278.

[55] Addy, J. H., and Schuller, F., 1993, "Lubrication of an 85-mm ball bearing with RP-1," 29th Joint Propulsion Conference and Exhibit, American Institute of Aeronautics and Astronautics.

[56] Bahadur, S., and Tabor, D., 1984, "The wear of filled polytetrafluoroethylene," Wear, 98, pp. 1-13.

[57] Conte, M., and Igartua, A., 2012, "Study of PTFE composites tribological behavior," Wear, 296(1), pp. 568-574.

[58] Xie, T., Zhou, Z., Xu, Z., Yu, J., and Jiao, H., 2013, "Characteristics of the Transfer Film and Tribological Properties of Oxide/PTFE Composites," Advanced Materials Research, 631-632, pp. 172-175.

[59] Pleskachevsky, Y. M., and Smurugov, V. A., 1997, "Thermal fluctuations at PTFE friction and transfer," Wear, 209(1), pp. 123-127.

[60] Jintang, G., 2000, "Tribochemical effects in formation of polymer transfer film," Wear, 245(1), pp. 100-106.

[61] Ye, J., Khare, H. S., and Burris, D. L., 2013, "Transfer film evolution and its role in promoting ultra-low wear of a PTFE nanocomposite," Wear, 297(1), pp. 1095-1102.

[62] Makinson, K. R., and Tabor, D., 1964, "Friction and Transfer of Polytetrafluoroethylene," Nature, 201(4918), pp. 464-466.

[63] Bunn, C. W., Cobbold, A. J., and Palmer, R. P., 1958, "The fine structure of polytetrafluoroethylene," Journal of Polymer Science, 28(117), pp. 365-376.

[64] Speerschneider, C. J., and Li, C. H., 1962, "Some Observations on the Structure of Polytetrafluoroethylene," Journal of Applied Physics, 33(5), pp. 1871-1875.

[65] Cadman, P., and Gossedge, G. M., 1979, "The chemical nature of metal-polytetrafluoroethylene tribological interactions as studied by X-ray photoelectron spectroscopy," Wear, 54(2), pp. 211-215.

[66] De-Li, G., Bing, Z., Qun-Ji, X., and Hong-Li, W., 1990, "Effect of tribochemical reaction of polytetrafluoroethylene transferred film with substrates on its wear behaviour," Wear, 137(2), pp. 267-273.

[67] Deli, G., Bing, Z., Qun-Ji, X., and Hong-Li, W., 1990, "Investigation of adhesion wear of filled polytetrafluoroethylene by ESCA, AES and XRD," Wear, 137(1), pp. 25-39.

[68] Deli, G., Qunji, X., and Hongli, W., 1991, "ESCA study on tribochemical characteristics of filled PTFE," Wear, 148(1), pp. 161-169.

[69] Zuo, Z., Yang, Y., Qi, X., Su, W., and Yang, X., 2014, "Analysis of the chemical composition of the PTFE transfer film produced by sliding against Q235 carbon steel," Wear, 320, pp. 87-93.

[70] Burris, D. L., 2008, "Investigation of the Tribological Behavior of Polytetrafluoroethylene at Cryogenic Temperatures," Tribology Transactions, 51(1), pp. 92-100.

[71] McCook, N. L., Burris, D. L., Dickrell, P. L., and Sawyer, W. G., 2005, "Cryogenic Friction Behavior of PTFE based Solid Lubricant Composites," Tribology Letters, 20(2), pp. 109-113.

[72] Hübner, W., Gradt, T., Schneider, T., and Börner, H., 1998, "Tribological behaviour of materials at cryogenic temperatures," Wear, 216(2), pp. 150-159.

[73] Theiler, G., Hübner, W., Gradt, T., Klein, P., and Friedrich, K., 2002, "Friction and wear of PTFE composites at cryogenic temperatures11Extended version of the paper presented at the 2nd World Tribology Congress, Vienna, 3–7 September 2001," Tribology International, 35(7), pp. 449-458.

[74] Dindar, A., Chimanpure, A. S., and Kahraman, A., 2021, "Mechanical Power Losses of Ball Bearings: Model and Experimental Validation," Journal of Tribology, 144(5).

[75] Nosaka, M., 2011, "Cryogenic Tribology of High-Speed Bearings and Shaft Seals in Liquid Hydrogen," Tribology Online, 6(2), pp. 133-141.

[76] Nosaka, M., Takada, S., and Yoshida, M., 2010, "Research and Development of Cryogenic Tribology of Turbopumps for Rocket Engines," J. of Aeronautical and Space Science Japan, 58(681), pp. 303-313, in Japanese.

[77] Tanaka, K., Uchiyama, Y., and Toyooka, S., 1973, "The mechanism of wear of polytetrafluoroethylene," Wear, 23(2), pp. 153-172.

[78] Du, S., Zhu, Z., Liu, C., Zhang, T., Hossain, M. M., and Sue, H.-J., 2021, "Experimental

observation and finite element method modeling on scratch-induced delamination of multilayer polymeric structures," Polymer Engineering & Science, 61(6), pp. 1742-1754.

[79] Molero, G., Du, S., Mamak, M., Agerton, M., Hossain, M. M., and Sue, H.-J., 2019, "Experimental and numerical determination of adhesive strength in semi-rigid multi-layer polymeric systems," Polymer Testing, 75, pp. 85-92.

[80] Gradt, T., Schneider, T., Hübner, W., and Börner, H., 1998, "Friction and wear at low temperatures," International Journal of Hydrogen Energy, 23(5), pp. 397-403.

[81] Du, S., Mullins, M., Hamdi, M., and Sue, H.-J., 2020, "Quantitative modeling of scratch behavior of amorphous polymers at elevated temperatures," Polymer, 197, p. 122504.

[82] Du, S., Hamdi, M., and Sue, H.-J., 2020, "Experimental and FEM analysis of mar behavior on amorphous polymers," Wear, 444-445, p. 203155.

[83] Takahagi, T., Ishitani, A., Kuroda, H., and Nagasawa, Y., 1991, "Fluorine‐containing species on the hydrofluoric acid etched silicon single‐crystal surface," Journal of Applied Physics, 69(2), pp. 803-807.

[84] Ikeda, M., Rusyanto, T., and Nagashima, N., 1994, "An XPS Study of F and O on the Si (100) Surfaces Dipped in Aqueous Solution of HF," Journal of the Surface Science Society of Japan, 15(3), pp. 164-167, in Japanese.